

**Advances in Digital Gradient Sensing (DGS) Method for Experimental Mechanics**

by

Chengyun Miao

A dissertation submitted to the Graduate Faculty of  
Auburn University  
in partial fulfillment of the  
requirements for the Degree of  
Doctor of Philosophy

Auburn, Alabama  
December 14, 2019

Keywords: experimental mechanics, optical metrology, thin structures, dynamic fracture,  
carbon fiber reinforced polymer composites,

Copyright 2019 by Chengyun Miao

Approved by

Hareesh V. Tippur, Chair, McWane Professor of Mechanical Engineering  
Jeffrey C. Suhling, Quina Distinguished Professor of Mechanical Engineering  
Nima Shamsaei, Associate Professor of Mechanical Engineering  
James S. Davidson, Gottlieb Professor of Civil Engineering

## Abstract

Shape and surface topography evaluation from measured slopes is of considerable engineering significance. These kinematic quantities are often used for metrology and experimental mechanics study of optical and electronic elements, wave front reconstruction and rectification, deformation and damage quantification of structural members, to name a few. In this context, a full-field optical method called *reflection-mode* Digital Gradient Sensing (*r*-DGS) based on random speckle correlation principle capable of measuring extremely small angular deflections of light rays ( $\sim 10^{-4}$  degree) to quantify surface slopes of thin structures is advanced in the first part of this dissertation. The measured quantities from *r*-DGS upon integration can accurately quantify surface topography. Accordingly, a Higher-order Finite-difference-based Least-squares Integration (HFLI) scheme is developed. By combining these tools, high-fidelity quantification of surface topography is demonstrated, and the measurement accuracy is assessed. It is found that the accuracy is influenced by the temporal frequency of the recording device. Ultrahigh-speed digital photography at  $10^6$  frames per second resulted in nanoscale (10-20 nm) out-of-plane deformation measurement accuracy over relatively large ( $75 \times 75$  mm<sup>2</sup>) region-of-interest (ROI) whereas slower recording speeds of  $10^1$  frames per second decreased the accuracy to sub-micron values emphasizing the role random vibrations play in this methodology.

Quantitative visualization of both surface slopes and out-of-plane deformations of thin carbon fiber reinforced plates (CFRP) of different layups subjected to dynamic out-of-plane impact loading at microsecond intervals are made next. Again, challenges of measuring extremely small surface slopes simultaneously in two orthogonal directions with microsecond resolution over relatively large ROI are overcome. Furthermore, the surface slopes, differentiated numerically to determine curvatures, allow estimation of in-plane stresses when used in conjunction with the elastic plate theory.

The loading-rate effects on fracture mechanics of unidirectional CFRP are explored in the next part of this dissertation using *r*-DGS. Fracture responses of single-edge notched multi-layer unidirectional CFRP subjected to symmetric static and dynamic loadings are studied. Effect of different fiber orientations relative to the notch direction is explored. Nominally mode-I fracture occurs when the fiber orientation is  $0^\circ$  whereas mixed-mode (mode-I and -II) fracture ensues in all other fiber orientations ( $15^\circ$ - $60^\circ$ ) studied. An over-deterministic least-squares methodology for extracting stress intensity factors (SIFs) for propagating cracks is developed by exploiting orthogonal surface slopes measured from *r*-DGS. Results show that crack-face fiber-bridges offer significant resistance to growth under quasi-static loading conditions; however, the same is found largely absent under dynamic conditions emphasizing the loading rate effects.

In the next part of this dissertation, two modified Digital Gradient Sensing (DGS) methods of even higher measurement sensitivity suitable for studying ultralow-toughness and high-stiffness transparent solids such as soda-lime glass are proposed. These methods are devised by combining *r*-DGS with the *transmission-mode* DGS (or, *t*-DGS). These methods involve an additional reflective surface behind the transparent substrate, either as

a standalone reflector or as a rear face reflective film deposition. The former approach, designated as  $t^2$ -DGS method, offers measurement sensitivity twice that of  $t$ -DGS whereas the latter called *transmission-reflection* DGS or  $tr$ -DGS results in more than three-fold higher sensitivity. The governing equations of  $tr$ -DGS are developed and demonstrated for measuring angular deflection fields in the crack-tip region during static and fracture events.

Lastly,  $tr$ -DGS and  $t^2$ -DGS methods are extended to examine the fracture mechanics of soda-lime glass, a high stiffness and low toughness material. Extremely high crack speeds (in excess of 1500 m/s), ultralow failure strain ( $\epsilon_f < 0.1\%$ ) and highly localized sub-micron scale deformations are among the challenges overcome in this material. These two new methods are applied to map stress gradients around dynamically growing cracks in glass plates subjected to dynamic impact loading and extract fracture parameters. The  $r$ -DGS method is also implemented to show the need for higher measurement sensitivity to study such challenging materials.

## **Acknowledgements**

I would like to express my deepest respect and gratitude to my advisor, Dr. Hareesh V. Tippur, for his academic guidance and financial support without which this work would not have been successful. I would like to thank my committee members Dr. Jeffrey C. Suhling, Dr. James S. Davidson and Dr. Nima Shamsaei for reviewing this dissertation. Partial financial support for this research from grants (U.S. Army) W31P4Q-14-C-0049, ARMYW911NF-16-1-0093 and W911NF-15-1-0357 (DURIP) are gratefully acknowledged. I would like to thank all my colleagues and friends for the friendship and wonderful time I had in Auburn.

Special thanks to Dr. Lei Huang, Brookhaven National Laboratories, Dr. Dongyeon Lee, Toray Composite Materials America, Inc. Dr. Wesley Hunko and Dr. Lewis N. Payton, Design and Manufacturing Laboratory, for providing guidance on the numerical integration method, supplying CFRP sheets, machining my experimental samples, respectively, for my research.

Last but not least, I would especially like to thank my parents and my wife, Meng Ding, for their invaluable love, support and encouragement throughout my graduate research.

## TABLE OF CONTENTS

LIST OF TABLES .....	ix
LIST OF FIGURES .....	x
Chapter 1. Introduction.....	1
1.1 Motivation .....	1
1.2 Review of full-field optical methods.....	3
1.2.1 Moiré methods .....	3
1.2.2 Electronic Speckle Pattern Interferometry (ESPI).....	4
1.2.3 Shearography .....	5
1.2.4 Coherent Gradient Sensing (CGS).....	7
1.2.5 Digital Gradient Sensing (DGS).....	11
1.3 Integration methods.....	14
1.4 Mechanics of composites .....	15
1.5 Hypotheses and goals .....	19
1.6 Organization of the dissertation .....	21
Chapter 2. Digital Gradient Sensing (DGS) Methods .....	23
2.1 Reflection-mode Digital Gradient Sensing ( <i>r</i> -DGS).....	23
2.2 Transmission-mode Digital Gradient Sensing ( <i>t</i> -DGS) .....	26
Chapter 3. Surface Profile/Topography Measurement from <i>r</i> -DGS .....	30
3.1 Finite-difference based Least-squares Integration (HFLI) Method .....	30
3.2 Algorithm Verification.....	34
3.3 Silicon wafer subjected to central loading .....	35
3.4 Wafer subjected to eccentric loading .....	43
3.5 Dynamic mode-I crack propagation in transparent PMMA.....	45
Chapter 4. Accuracy of Measured Deformations from <i>r</i> -DGS coupled with HFLI Algorithm .....	55
4.1 Ultrahigh-speed Measurements.....	55
4.2 Smallest measurable out-of-plane deformation.....	61
4.2.1 Method-1 .....	62

4.2.2	Method-2.....	63
4.3	Smallest measurable deformation: Quasi-static conditions .....	67
Chapter 5.	Measurement of Deformations and Stresses in Laterally Impacted Composite Plates.....	75
5.1	Demonstration Experiment .....	75
5.2	CFRP Plates Subjected to Dynamic Impact.....	90
5.2.1	Unidirectional CFRP Plate.....	90
5.2.2	Quasi-isotropic CFRP Plate .....	98
5.3	Error Estimation .....	102
5.3.1	Effect of Sub-Image Size .....	102
5.3.2	Effect of Numerical Differentiation.....	106
Chapter 6.	Fracture Behavior of Carbon Fiber Reinforced Polymer Composites: Loading Rate Effects.....	107
6.1	Dynamic Fracture.....	107
6.2	Quasi-Static Fracture.....	120
6.3	Extraction of Stress Intensity Factors (SIFs).....	125
6.4	Results and Discussion.....	128
Chapter 7.	Higher Sensitivity Digital Gradient Sensing Configurations for Transparent Solids	136
7.1	Extensions of <i>r</i> -DGS and <i>t</i> -DGS Methods.....	136
7.1.1	Double/Dual Transmission Digital Gradient Sensing ( <i>t2</i> -DGS) .....	136
7.2	Transmission-Reflection Digital Gradient Sensing ( <i>tr</i> -DGS).....	140
7.2.1	Estimation of Lateral Light Ray Shift in <i>tr</i> -DGS.....	142
7.3	Experimental Verification .....	145
7.3.1	Dynamic fracture experiment .....	145
7.3.2	Static Fracture Experiment .....	155
7.4	Estimation of SIF from <i>tr</i> -DGS and <i>t2</i> -DGS Methods .....	160
Chapter 8.	Dynamic Fracture Behavior of Glass Plates using Modified Digital Gradient Sensing Techniques .....	164
8.1	Dynamic fracture of soda-lime glass studied using <i>r</i> -DGS.....	164
8.2	Dynamic fracture of soda-lime glass studied using higher sensitivity DGS methods.....	170
Chapter 9.	Conclusions.....	183
9.1	Future work .....	189
Reference		190
Appendix A		200

A.1	Disadvantages of current experimental setup of $r$ -DGS .....	200
A.2	Simplified $r$ -DGS setup without beam splitter.....	201
A.3	Demonstration: Silicon wafer subjected to central loading .....	205
A.4	Application to fracture mechanics.....	217

## LIST OF TABLES

Table 5-1: Material properties of 1144 Carbon Steel and PMMA used in finite element simulations .....	89
Table 5-2: Material properties of unidirectional CFRP used in FEA [124] .....	96
Table 6-1: Material properties of T800s/3900-2 unidirectional laminate [124] .....	109
Table 6-2: Material properties of specimens with different $\alpha$ . .....	109
Table 6-3: Compilation of energy release rate ( $G$ ), mode-mixity ( $\psi$ ) and time rate of change of effective SIF ( $\dot{K}_{eff}$ ) .....	134
Table 7-1: Material properties of PMMA [53] [127].....	146
Table 8-1 Material properties of maraging steel and soda-lime glass used in the simulation .....	180

## LIST OF FIGURES

Figure 1.1: Some examples of reflective materials used in engineering. (Image sources: (a) <a href="https://www.electronicweekly.com/news/business/semiconductor-market-top-400bn-2017-07/">https://www.electronicweekly.com/news/business/semiconductor-market-top-400bn-2017-07/</a> , (b) <a href="https://www.digitaltrends.com/cool-tech/scientists-develop-cheap-spray-on-solar-cells/">https://www.digitaltrends.com/cool-tech/scientists-develop-cheap-spray-on-solar-cells/</a> , (c) <a href="https://wasp-planets.net/2017/11/14/wasp-planets-selected-for-james-webb-space-telescope-ers-and-gto/">https://wasp-planets.net/2017/11/14/wasp-planets-selected-for-james-webb-space-telescope-ers-and-gto/</a> ,(d) <a href="https://redmondmag.com/articles/2013/09/10/intel-unveils-new-chips.aspx">https://redmondmag.com/articles/2013/09/10/intel-unveils-new-chips.aspx</a> ).....	1
Figure 1.2: Some examples of CFRP used in engineering area. (Image sources: (a) <a href="https://www.geaviation.com/commercial/engines/genx-engine">https://www.geaviation.com/commercial/engines/genx-engine</a> , (b) <a href="http://compositesmanufacturingmagazine.com/2012/01/structure-sport-style/">http://compositesmanufacturingmagazine.com/2012/01/structure-sport-style/</a> ). ....	2
Figure 1.3: Generic optical setup for ESPI [21]. ....	5
Figure 1.4: Shearography setups using Michelson shearing interferometer (top) [22], and double refractive prism (bottom) [23].....	6
Figure 1.5: Schematic of the experimental setup for reflection CGS [32]. ....	8
Figure 1.6: DIC principle.....	12
Figure 1.7: CC criteria (Table 1) and SSD correlation criteria (Table 2) [58]. ....	13
Figure 2.1: Schematic of experimental setup for reflection DGS ( <i>r</i> -DGS). ....	24
Figure 2.2: Working principle of <i>r</i> -DGS. ....	25
Figure 2.3: Schematic of experimental setup (a) and light ray diagram (b) for <i>t</i> -DGS [53]. .....	27
Figure 3.1: Southwell grid configuration.....	30
Figure 3.2: Verification of HFLI method. (a) Original function, (b) reconstructed function, (c) reconstruction errors, (d) contours of derivatives of the function in the <i>x</i> -direction, (e) contours of derivatives of the function in the <i>y</i> -direction. ....	35
Figure 3.3: The experimental setup used to study out-of-plane deformation of a silicon wafer. ....	36
Figure 3.4: Results from <i>r</i> -DGS for a clamped silicon wafer (30 mm dia., 360 μm thick) subjected to central deflection of 4 μm (left column) and 10 μm (right column). Row 1: contours of $w_{,x}$ ; Row 2: contours of $w_{,y}$ ; Row 3: contours of $w_{,r}$ . Note: (0, 0) is made to coincide with the loading point. Contour increments = $0.5 \times 10^{-4}$ rad and $1 \times 10^{-4}$ rad, respectively. ....	38
Figure 3.5: Comparison of analytical data and experimental data of $\frac{\partial w}{\partial y}$ along the <i>y</i> -axis corresponding to three different imposed out-of-plane deflections.....	39
Figure 3.6: Surface topography calculated via 2D integration using surface slope data and HFLI method: (a) 3D surface representation of reconstructed surface, (b) out-of-plane displacement ( <i>w</i> ) contours (0.5 μm increments). Note: (0, 0) is made to coincide with the loading point; red circle indicates the edge of the circular aperture of the steel washer. .	40
Figure 3.7: Contours of $w_{,y}$ for 20 × 20 pixel sub-images with three different overlap and the corresponding reconstructed figures. ....	42

Figure 3.8: Results from <i>r</i> -DGS for a clamped silicon wafer (30 mm dia., 360 $\mu\text{m}$ thick) subjected to eccentric deflection of 4 $\mu\text{m}$ (left column) and 10 $\mu\text{m}$ (right column). Row 1: contours of $w_{,x}$ ; Row 2: contours of $w_{,y}$ ; Row 3: contours of $w_{,r}$ . Note: (0, 0) is made to coincide with the loading point. Contour increments = $0.5 \times 10^{-4}$ rad and $1 \times 10^{-4}$ rad, respectively. ....	44
Figure 3.9: Surface topography calculated via 2D integration using surface slope data and HFLI method: (a) reconstructed 3D surface, (b) out-of-plane displacement ( $w$ ) contours (0.5 $\mu\text{m}$ increments). Note: (0, 0) is made to coincide with the loading point; red circle is the circular aperture of the steel washer. ....	45
Figure 3.10: Schematic of the experimental setup used for dynamic fracture study. ....	46
Figure 3.11: Speckle images in the undeformed (left) and deformed (right) states recorded by the Cordin 550 high-speed camera through the PMMA specimen. ....	47
Figure 3.12: Angular deflection contour plots (contour interval = $5 \times 10^{-4}$ rad) proportional to stress gradients of $(\sigma_{,x} + \sigma_{,y})$ in the x- and y-directions. ....	49
Figure 3.13: Mode-I and II SIFs for a dynamically growing crack in a monolithic PMMA. ....	51
Figure 3.14: Stress fields of $(\sigma_{,xx} + \sigma_{,yy})$ (contour interval= 0.75 MPa) obtained from a) using $K_I$ and $K_{II}$ measured from the DGS fields along with analytical expression for stress fields and b) using HFLI method applied to measured stress gradients. The black horizontal line represents the growing crack faces. ....	52
Figure 3.15: The 3D surface plot of stress $(\sigma_{,xx} + \sigma_{,yy})$ around a moving crack tip in PMMA reconstructed using HFLI. ....	53
Figure 3.16: The plot of stress $(\sigma_{,xx} + \sigma_{,yy})$ evaluated from integration and by using K-dominant equations from the extracted SIFs for a direction of (a) $0^\circ$ , and (b) $45^\circ$ from the crack growth direction. ....	54
Figure 4.1: Schematic of the experimental setup for dynamic plate impact study. Inset shows the close-up of the optical arrangement. ....	56
Figure 4.2: Evolution of surface slope $w_{,x}$ (left column) and $w_{,y}$ (right column) contours for a clamped glass plate subjected to central impact. Note: (0, 0) is made to coincide with the impact point. Contour increments = $8 \times 10^{-5}$ rad. ....	58
Figure 4.3: Measured surface topography of glass plate at a few select time instants. Left column: reconstructed 3D surface; Right column: out-of-plane displacement ( $w$ ) contours (0.5 $\mu\text{m}$ increment). Note: (0, 0) is made to coincide with the impact point. ....	60
Figure 4.4: The measured profiles for a clamped glass plate subjected to central impact. ....	61
Figure 4.5: Two randomly selected undeformed images. ....	63
Figure 4.6: Surface slopes $w_{,x}$ (left column) and $w_{,y}$ (right column) contours. Contour increments = $1 \times 10^{-5}$ rad. Impact point: row 38, column 45. ....	64
Figure 4.7: Slope in the horizontal direction along three columns (top) and along three rows (bottom). ....	65
Figure 4.8: Reconstructed surface topography. ....	66
Figure 4.9: Out-of-plane deformation along three columns (top) and three rows (bottom). ....	67
Figure 4.10: Experimental setup for <i>r</i> -DGS. Inset shows close-up view of the optical arrangement. ....	69

Figure 4.11: Surface slope $w_{,x}$ (left column) and $w_{,y}$ (right column) contours for a clamped silicon wafer recorded at 0.2 fps. Note: (0, 0) is made to coincide with the center of silicon wafer. Contour increments = $5 \times 10^{-6}$ rad. ....	70
Figure 4.12: Surface slope $w_{,x}$ (left column) and $w_{,y}$ (right column) contours for a clamped silicon wafer recorded at 5 fps. Note: (0, 0) is made to coincide with the center of silicon wafer. Contour increments = $5 \times 10^{-6}$ rad. ....	71
Figure 4.13: Surface topography obtained from integrating surface slopes using HFLI method for a clamped silicon wafer recorded at 0.2 fps. Left column: 3D surface; Right column: out-of-plane displacement ( $w$ ) contours (0.01 $\mu\text{m}$ increments).....	72
Figure 4.14: Surface topography obtained from integrating surface slopes using HFLI method for a clamped silicon wafer recorded at 5 fps. Left column: 3D surface; Right column: out-of-plane displacement ( $w$ ) contours (0.01 $\mu\text{m}$ increments).....	73
Figure 5.1: Schematic of the experimental setup for dynamic plate impact study. Insets show the close-up of the optical arrangement and the strain history due to the compressive pulse measured on the Hopkinson bar. ....	76
Figure 5.2: Recorded speckle images from ultrahigh-speed camera at different time instants. The nominal diameter of the region of interest is 63.5 mm. Disturbance to the recorded speckles is readily evident in the last two images relative to the one at $t = 0$ $\mu\text{s}$ . ....	79
Figure 5.3: Evolution of surface slope $w_{,x}$ (left column) and $w_{,y}$ (right column) contours for a clamped PMMA plate subjected to central impact. The impact point is made to coincide with (0, 0); Contour increments = $2 \times 10^{-4}$ rad. ....	81
Figure 5.4: Evolution of surface slope $w_{,r}$ contours for a clamped PMMA plate subjected to central impact. The impact point is made to coincide with (0, 0); Contour increments = $1.5 \times 10^{-4}$ rad. ....	82
Figure 5.5: Evolution of surface profile of PMMA plate at select time instants. Left column: reconstructed 3D surface; Right column: out-of-plane displacement ( $w$ ) contours (1 $\mu\text{m}$ increment). The impact point is made to coincide with (0, 0). ....	83
Figure 5.6: Results for a clamped PMMA plate subjected to central impact at $t = 2\mu\text{s}$ . Row 1: $w_{,x}$ (left) and $w_{,y}$ (right) contours; Row 2: reconstructed 3D surface (left) and out-of-plane displacement ( $w$ ) contours at 0.05 $\mu\text{m}$ increment (right). The impact point is made to coincide with (0, 0). ....	84
Figure 5.7: The measured transient profiles for a clamped PMMA plate subjected to central impact. (see, Section 5.3 for error estimates).....	85
Figure 5.8: Estimated stresses for a circular clamped PMMA plate subjected to central impact.....	87
Figure 5.9: 3D finite element model used for simulating impact on a clamped PMMA plate. ....	89
Figure 5.10: Comparison of experimental (solid symbols) results with finite element simulations (solid line) at different time instants.....	89
Figure 5.11: Evolution of slopes $w_{,x}$ (left column) and $w_{,y}$ (right column) contours for a clamped unidirectional CFRP plate subjected to central impact. Note: (0, 0) is made to coincide with the impact point. Fiber direction is in the horizontal direction. Contour increments = $2 \times 10^{-4}$ rad. ....	91
Figure 5.12: Evolution of surface topography of unidirectional CFRP plate at a few select time instants. Left column: reconstructed 3D surface; Right column: out-of-plane	

displacement ( $w$ ) contours (0.8 $\mu\text{m}$ increment). Note: (0, 0) is made to coincide with the impact point. Fiber direction is in the horizontal direction.....	92
Figure 5.13: The measured surface profiles for a clamped unidirectional CFRP plate subjected to central impact. (see, Section 5.3 for error estimates) .....	93
Figure 5.14: Estimated stresses for a circular, clamped unidirectional CFRP plate subjected to central impact. Fiber orientation is along the $x$ -axis.....	95
Figure 5.15: Comparison of experimental results with finite element simulations. Solid lines represent values from simulations; solid symbols represent values from the experiment.....	97
Figure 5.16: Evolution of slopes $w_{,x}$ (left column) and $w_{,y}$ (right column) as contours for a clamped quasi-isotropic CFRP plate subjected to central impact. Note: (0, 0) is made to coincide with the impact point. Contour increments = $1 \times 10^{-4}$ rad. ....	99
Figure 5.17: Evolution of surface deformations of a quasi-isotropic CFRP plate at select time instants. Left column: reconstructed 3D surface; Right column: out-of-plane displacement ( $w$ ) contours (0.26 $\mu\text{m}$ increment). Note: (0, 0) is made to coincide with the impact point. ....	100
Figure 5.18: The measured transient surface profiles for a clamped quasi-isotropic CFRP plate subjected to central impact.....	101
Figure 5.19: Evolution of maximum out-of-plane displacement for PMMA, unidirectional CFRP and quasi-isotropic CFRP. ....	101
Figure 5.20: Effect of sub-image sizes for PMMA at $t = 15 \mu\text{s}$ (1) on surface slope $w_{,x}$ ; (2) on out-of-plane deformation; (3) on stress.....	103
Figure 5.21: Estimated stress obtained from different numerical differentiations for 40x40 pixel sub-images, $t = 15 \mu\text{s}$ . ....	104
Figure 5.22: Effect of sub-image sizes for unidirectional CFRP at $t = 15 \mu\text{s}$ : (1) on surface slope $w_{,x}$ ; (2) on out-of-plane deformation; (3) on stress. ....	106
Figure 6.1: Specimen configuration.....	108
Figure 6.2: Schematic (top) and close-up photograph (bottom) of the experimental setup used to study dynamic fracture behavior of CFRP. ....	110
Figure 6.3: Measured surface slopes $w_{,x}$ (left column) and $w_{,y}$ (right column) contours for CFRP of mode-I dynamic fracture. Contour increment = $1 \times 10^{-4}$ rad. Black strips highlight the crack. ....	113
Figure 6.4: Contours of out-of-plane displacements ( $w(x, y)$ ) (0.2 $\mu\text{m}$ intervals) for CFRP during mode-I dynamic fracture at a few select time instants before and after crack initiation ( $t=0$ ). Black strips highlight the crack. Concentration of (+) out-of-plane displacements at the left hand edge is due to impact loading whereas singularity of $w$ -field around the crack tip (-) is due to the discontinuity. ....	114
Figure 6.5: Measured surface slopes $w_{,x}$ contours for CFRP of mixed-mode dynamic fracture. Contour increments = $1 \times 10^{-4}$ rad. (Black strips are overlaid to highlight the crack; broken red line suggests kinked crack growth path.).....	116
Figure 6.6: Contours of out-of-plane displacements ( $w(x, y)$ ) (0.2 $\mu\text{m}$ intervals) for CFRP during mixed-mode dynamic fracture at a few select time instants. (Black strips are overlaid to highlight the crack; broken red line suggests kinked crack growth path.) Concentration of (+) out-of-plane displacements at the left hand edge is due to impact loading whereas singularity of $w$ -field around the crack tip (-) is due to the discontinuity. ....	117

Figure 6.7: Crack growth (a) and velocity (b) histories during dynamic fracture of CFRP with different fiber orientation.....	119
Figure 6.8: Details of quasi-static fracture experiments: (a) Specimen configuration, (b) Schematic of experiment setup.....	121
Figure 6.9: Measured surface slopes of $\frac{\partial w}{\partial x}$ for quasi-static fracture tests on CFRP ( $\alpha = 15^\circ$ ). Contour increments = $2 \times 10^{-4}$ rad. (Black strips are overlaid to highlight the crack; broken red line suggests kinked crack path.).....	123
Figure 6.10: (a) Fracture load variations for different fiber orientations, (b) Load vs. load-point deflection histories.....	124
Figure 6.11: Measured surface slopes for $\alpha = 45^\circ$ in (a) $\frac{\partial w}{\partial x}$ contours, (b) $\frac{\partial w}{\partial x'}$ contours. (Black strip highlights the crack; broken red line suggests kinked crack path.).....	125
Figure 6.12: Compilation of measured stress intensity factor (SIF) histories for CFRP subjected to (a) dynamic loading and (b) quasi-static loading. ( $t = 0$ corresponds to apparent crack initiation.).....	131
Figure 6.13: Cracked faces bridged by fibers in quasi-static experiments. (The random pattern elsewhere is due to the surface texture and angular illumination).....	131
Figure 6.14: Energy release rate histories for CFRP with different fiber orientations (a) dynamic fracture and (b) quasi-static fracture. ( $t = 0$ corresponds to crack initiation.)..	133
Figure 7.1: Specimen configurations for: (a) <i>r</i> -DGS; (b) <i>t2</i> -DGS; (c) <i>tr</i> -DGS. ....	137
Figure 7.2: Light ray diagrams for <i>t2</i> -DGS (a) and <i>tr</i> -DGS (b).....	139
Figure 7.3: Exaggerated light ray diagram for <i>tr</i> -DGS.....	143
Figure 7.4: Back-side of the specimen with and without reflective coating in the upper-half and lower-half, respectively. (Front-side of the specimen faces the camera).....	146
Figure 7.5: Schematic (top) and close-up photography (bottom) of the experimental setup for dynamic plate impact study.....	148
Figure 7.6: Angular deflection contour plots proportional to stress gradients of $(\sigma_x + \sigma_y)$ in the <i>x</i> - and <i>y</i> -directions. Contour increments = $3 \times 10^{-4}$ rad. ....	151
Figure 7.7: Ratio of $\frac{(\phi_{x,y})_{tr-DGS}}{(\phi_{x,y})_{t2-DGS}}$ within $0.5 \leq r/B \leq 1.5$ : (a) along $\pm 45^\circ$ ; (b) along $\pm 90^\circ$ .....	154
Figure 7.8: Mode-I stress intensity factor histories measured by <i>tr</i> -DGS and <i>t2</i> -DGS methods.....	155
Figure 7.9: Schematic of the experimental setup for static fracture study (top). Close-up view of the optical arrangement (bottom).....	157
Figure 7.10: Angular deflection contour plots proportional to stress gradients: (a) $\phi_x$ ; (b) $\phi_y$ . Contour increments = $4 \times 10^{-4}$ rad.....	159
Figure 7.11: Measured ratio of $\frac{(\phi_y)_{tr-DGS}}{(\phi_y)_{t2-DGS}}$ in $0.5 \leq r/B \leq 1.5$ along $\pm 45^\circ$ and $\pm 90^\circ$ .....	159
Figure 7.12: Angular deflection contour plots of $\phi_x$ and $\phi_y$ for four DGS methods corresponding to load of 500 N. Contour increments = $4 \times 10^{-4}$ rad.....	161

Figure 7.13: Measured mode-I stress intensity factors (symbols) at different loads by different DGS methods. The solid line represents the corresponding theoretical values.	163
Figure 8.1: Specimen Configuration.	165
Figure 8.2: Schematic (a) and close-up photograph (b) of the experimental setup used to study dynamic fracture of soda-lime glass.	167
Figure 8.3: Measured angular deflection contours $\phi_x$ (left column) and $\phi_y$ (right column) for dynamic fracture of glass using $r$ -DGS. Contour increment = $10 \times 10^{-6}$ rad. Red stripes highlight the crack.	169
Figure 8.4: Close-up photograph of experimental setup for $t2$ -DGS.	170
Figure 8.5: Measured angular deflection contours $\phi_x$ (left column) and $\phi_y$ (right column) for dynamic fracture of glass using $t2$ -DGS. Contour increment = $20 \times 10^{-6}$ rad. Red stripes highlight the crack.	172
Figure 8.6: Measured angular deflection contours $\phi_x$ (left column) and $\phi_y$ (right column) for dynamic fracture of glass using $tr$ -DGS. Contour increment = $20 \times 10^{-6}$ rad. Red stripes highlight the crack.	173
Figure 8.7: Contours of $(\sigma_x + \sigma_y)$ for dynamic fracture of glass plate at a few select time instants. Contour increment = 1 MPa. White stripes highlight the crack.	174
Figure 8.8: Crack velocity histories for specimens measured using $t2$ -DGS and $tr$ -DGS.	175
Figure 8.9: Fractography showing ‘mirror’, ‘mist’, and ‘hackle’ features. Red arrows show crack propagation direction.	176
Figure 8.10: (a) Discretized finite element model with crack opening displacement contours. (b) The strain history due to the compressive stress pulse measured using the strain gage on the Hopkinson bar.	179
Figure 8.11: Stress intensity factor histories measured by $t2$ -DGS and $tr$ -DGS methods, and finite element analysis prior to crack initiation. $t = 0$ corresponds to crack initiation.	180
Figure 8.12: Plot of dynamic strain energy release rates ( $G^d$ ) with crack velocity ( $V$ ).	182
Figure A1: Light ray diagram of traditional $r$ -DGS depicting loss of light in the apparatus due to the beam splitter.	201
Figure A2: Schematic of experimental setup for simplified $r$ -DGS without beam splitter.	202
Figure A3: Working principle of simplified $r$ -DGS without beam splitter. Inset shows relation between specimen and global coordinate systems.	204
Figure A4: Schematic of the experimental setup for silicon wafer subjected to central loading (a). Images of side view (b) and front view (c) for the setup. (The target plane speckles are visible in bottom-right photograph because the Si wafer surface is reflective.)	207
Figure A5: Speckle images in the reference (a) and deformed (b) states of the silicon wafer subjected to central out-of-plane deformation of 10 $\mu\text{m}$ ; (c) illustration for the measurement of $\Delta$ .	208
Figure A6: Surface slopes $w_{,x}$ (left column) and $w_{,y}$ (right column) for a clamped silicon wafer subjected to out-of-plane deformations. Note: (0, 0) is made to coincide with the center of silicon wafer. Contour increments = $2 \times 10^{-4}$ rad.	210

Figure A7: Comparison of analytical data and experimental data of  $w_x$  along the  $x$ -axis (a), and  $w_y$  along the  $y$ -axis (b) corresponding to three different imposed out-of-plane deformations. .... 211

Figure A8: Surface topography obtained from integrating surface slopes using HFLI method for a clamped silicon wafer subjected to out-of-plane deformations. Left column: 3D surface; Right column: out-of-plane displacement ( $w$ ) contours (1  $\mu\text{m}$  increment). 212

Figure A9: Curvatures  $w_{,xx}$  (left column) and  $w_{,yy}$  (right column) for a clamped silicon wafer subjected to out-of-plane deformations. Note: (0, 0) is made to coincide with the center of silicon wafer. Contour increments =  $9.3 \times 10^{-5} \text{ mm}^{-1}$  ..... 214

Figure A10: Comparison of analytical data and experimental data of  $w_{,xx}$  along the  $x$ -axis (a), and along the  $y$ -axis (b) corresponding to three different imposed out-of-plane deformations. .... 215

Figure A11: Curvatures  $w_{,xy}$  (left column) and  $w_{,yx}$  (right column) for a clamped silicon wafer subjected to out-of-plane deformations. Note: (0, 0) is made to coincide with the center of silicon wafer. Contour increments =  $7.5 \times 10^{-5} \text{ mm}^{-1}$  ..... 217

Figure A12: Schematic of the experimental setup for static fracture study (a). Image of top-view of the setup (b). .... 219

Figure A13: Mode-I crack tip contours of surface slopes  $w_{,x}$  (a) and  $w_{,y}$  (b) corresponding to load of 500 N in 3-point bend PMMA specimen. Contour increments =  $4 \times 10^{-4} \text{ rad}$ . .... 220

Figure A14: Measured stress intensity factors (symbols) from simplified  $r$ -DGS at different load levels. The solid line represents the theoretical prediction. .... 222

# Chapter 1. Introduction

## 1.1 Motivation

Reflective materials are found in many optical and electronic devices (Figure 1.1). The substrate materials used in these are generally stiff and brittle and their surface characteristics (flatness, roughness, etc.) play an important role in their performance. Often, they also suffer deformations or mechanical failure due to thermo-mechanical stresses and shock/impact events. Capability to precisely measure surface features such as topography of these materials and devices, preferably using non-contact full-field methods capable of detecting extremely small deflections, is needed for assuring the mechanical integrity. Some optical sensors such as the Shack–Hartmann wave-front sensor [1], lateral shearing interferometers [2], and pyramid sensors [3] have all been used for this purpose. The current literature indicates that it is more efficient for these sensors to just measure the surface gradients instead of measuring the values of absolute height due to channel capacity limitations [4]. Integration algorithms can then be applied to convert the measured gradients into topographic information. Thus, a highly accurate, non-contact optical method of measuring surface gradients used in conjunction with an accurate integration scheme could satisfactorily reconstruct surface topography.

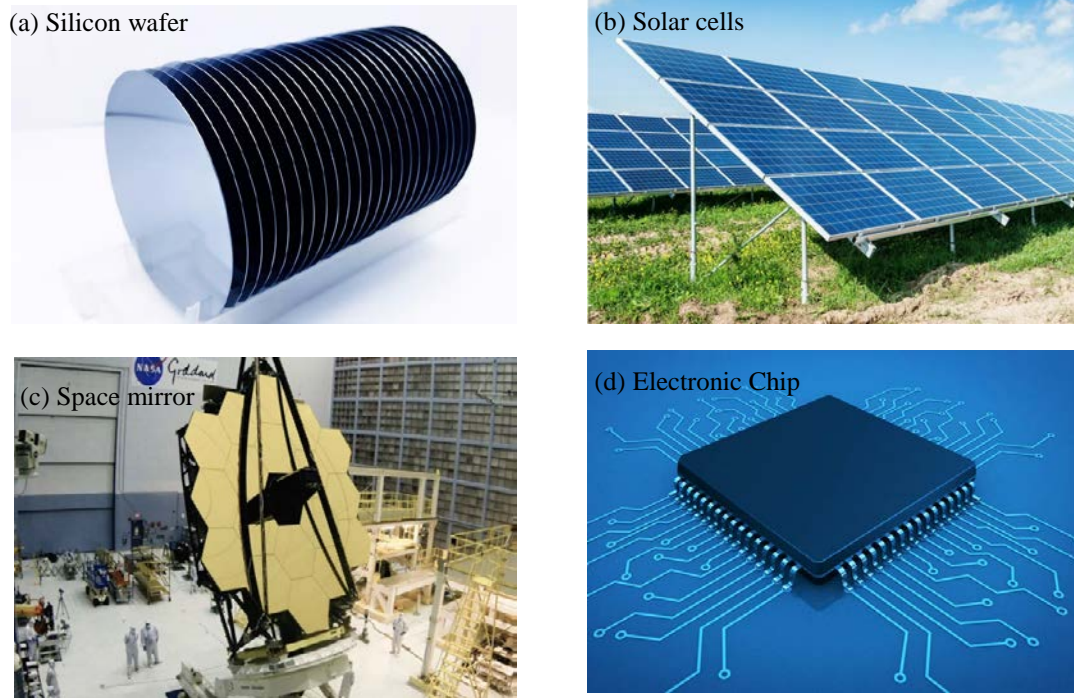


Figure 1.1: Some examples of reflective materials used in engineering. (Image sources: (a) <https://www.electronicweekly.com/news/business/semiconductor-market-top-400bn-2017-07/>, (b) <https://www.digitaltrends.com/cool-tech/scientists-develop-cheap-spray-on-solar-cells/>, (c) <https://wasp-planets.net/2017/11/14/wasp-planets-selected-for-james-webb-space-telescope-ers-and-gto/>, (d) <https://redmondmag.com/articles/2013/09/10/intel-unveils-new-chips.aspx>).

Another group of materials that motivate this research are carbon fiber reinforced polymer (CFRP) structural composites. Their usage in lightweight structures has increased substantially in the past few decades [5, 6, 7] in aerospace, automotive, and transportation industries for both military and civilian purposes due to tailorable stiffness, strength, toughness and high energy absorption characteristics, see Figure 1.2. Yet, these materials are susceptible to stress wave induced events leading to debond formation and fiber/matrix damage due to shock and impact by projectiles, falling objects and/or flying debris during service. Thus compromised CFRP suffer from undesirable reduction of strength and load-bearing capacity [8, 9, 10]. Hence, the ability to quantitatively visualize deformations and

fracture behaviors of CFRP structures under dynamic impact conditions is critical for assuring mechanical integrity and safety.

(a) GE aircraft engine



(b) Sports car



Figure 1.2: Some examples of CFRP used in engineering area. (Image sources: (a) <https://www.geaviation.com/commercial/engines/genx-engine>, (b) <http://compositesmanufacturingmagazine.com/2012/01/structure-sport-style/>).

Motivated by the above, this dissertation advances a full-field optical method called reflection-mode Digital Gradient Sensing (*r*-DGS) to experimental mechanics of stiff, brittle and/or layered materials. This optical method based on random speckle correlation principle can perform metrology of reflective objects by quantifying two orthogonal surface slopes. The simplicity of the experimental setup and its measurement accuracy along with the ubiquity of 2D image correlation algorithms make DGS attractive as the resulting surface slopes can be readily integrated to evaluate deformed surface profiles. A brief review of some of the existing full-field optical methods is presented next. Then, prevalent integration methods are reviewed. This is followed by exploring research of the dynamic impact and fracture mechanics on CFRP.

## **1.2 Review of full-field optical methods**

### **1.2.1 Moiré methods**

Geometric moiré fringes occur when two periodic geometric patterns of nearly same pitch/period are superimposed. The periodic patterns are generally referred to as gratings. Moiré methods can be fashioned to measure in-plane and out-of-plane deformations as well as surface slopes. To measure in-plane deformations on planar surfaces, the in-plane moiré method can be applied by affixing a grating to the specimen surface, so that the specimen grating can follow the in-plane deformations of the specimen. A reference grating when floated over the specimen surface, real-time moiré fringes proportional to in-plane displacement components result. Initially, the reference grating needs to be aligned with the specimen grating under no-load conditions resulting in a zero-order fringe. Subsequent loading the specimen produce moiré fringes representing contours of constant displacement components in real-time. Highest measurement sensitivity achievable using moiré method is 10-50  $\mu\text{m}$  per fringe.

The so-called shadow moiré method can be used to quantitatively visualize out-of-plane deformations. The shadow moiré fringes are produced when geometric interference occurs between a reference grating and its shadow cast on the specimen. Measurement sensitivity of shadow moiré method typically is in the hundred micrometers range. Another variant called the projection moiré method is similar to shadow moiré method in terms of the measured kinematic quantity, but it is used to study relatively large objects such as buckling of aircraft panels. A reference grating in such large size is not generally available; hence, a grating pattern is projected onto the object surface using a light projector in the 'before' and 'after' deformation states to create the geometric interference patterns.

Moiré methods have also been successfully applied to study out-of-plane deformation of thin structure by measuring surface slopes. Lichtenberg [11] proposed a reflection moiré method to determine surface slopes of specular specimen. Rieder and Ritter [12] modified Lichtenberg's experimental setup by introducing a half-mirror (beam splitter) so that a dark spot disrupting the continuity of moiré patterns is avoided. Chiang and Jaisingh [13] extended this method to study dynamic-bending of plates. Asundi [14] improved this method later by using computer-generated gratings which offered greater flexibility in terms of grid generation, manipulation and analysis of interference fringes. Ding *et al.* [15] applied shadow and projection moiré methods to study warpage in electronic package design and manufacturing processes.

### **1.2.2 Electronic Speckle Pattern Interferometry (ESPI)**

Electronic Speckle Pattern Interferometry (ESPI) is a laser based holographic interferometry. The typical ESPI experimental setup is shown in Figure 1.3. It involves the object, laser, beam splitter and a recording device. The initial laser beam gets split into two branches after passing through the beam splitter. The one used to illuminate the object is called the object beam and the other reflected off the beam splitter is called the reference beam. The recording device, generally a CCD camera, is focused on the object to capture the object beam reflected off the object surface. In the meanwhile, the reference beam is also captured by the camera via a group of mirrors. Hence, interference fringes form when there is a path difference between the reference beam and object beam due to out-of-plane deformation of the object.

Initially, the basic principles of ESPI were proposed simultaneously by Butters and Leendertz [16], and Macovski *et. al* [17]. It has been applied to measure out-of-plane deformation [18], slopes [19], and curvatures [20] of deformed objects.

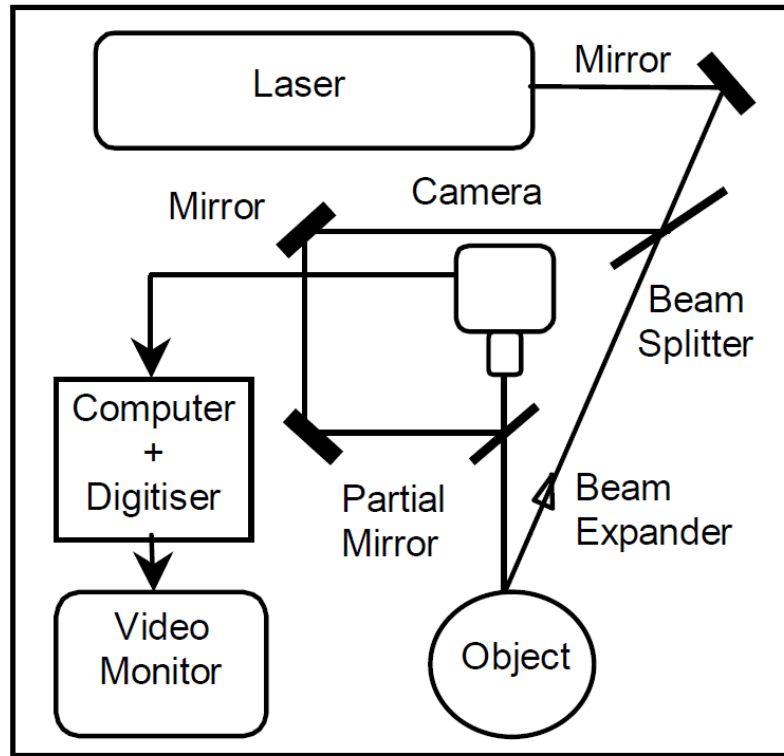


Figure 1.3: Generic optical setup for ESPI [21].

### 1.2.3 Shearography

Shearography is a laser-based full-field interferometric technique used to determine surface slopes. Shearography is similar to Electronic Speckle Pattern Interferometry (ESPI), but the fundamental difference between them is that shearography does not require a reference coherent light beam and it only requires a single laser beam to illuminate the object [21]; the object wave thus generated is spatially sheared by a prism or an optical-wedge that is part of the recording device. Hence, the optical disturbances in ESPI due to reference beam path length changes from environmental and random vibrations are greatly

reduced in shearography. As a result, shearography is a valuable non-destructive testing tool even in industrial/field settings.

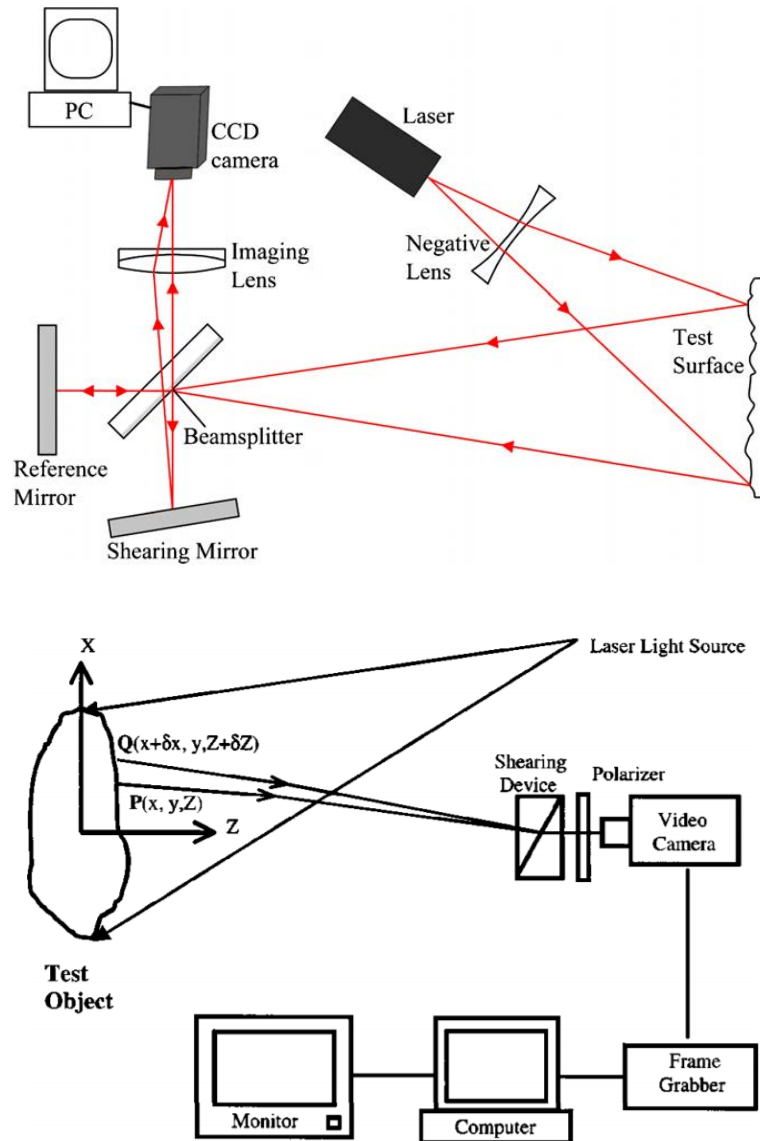


Figure 1.4: Shearography setups using Michelson shearing interferometer (top) [22], and double refractive prism (bottom) [23].

The schematic of an experimental setup for shearography is shown in Figure 1.4. One laser beam is used here to illuminate the sample surface. The reflected laser light, passes through a shearing device (Michelson shearing interferometer or a birefringent

crystal), is photographed by a CCD camera. The shearing device splits the incoming image into two identical but spatially displaced images. An interferometric speckle pattern encoded with the wave front shearing is produced at the sensor of the camera when the two images combine coherently [22].

Shearography has been used widely for surface slope measurement. Hung *et al.* [24] proposed a double-refractive index shearography method to visualize slope contours of an object. In this method, the object is immersed in a refractive medium, and the refractive index of the medium surrounding the object is changed from  $n$  to  $(n + \delta n)$  between digitization [23]. Hung and Liang [25] developed a new image-shearing camera to measure surface slopes by covering half of the camera lens using a glass wedge of small angle. Later on, Hung and Durelli [26] developed a multiple axial image-shearing camera to record the surface slopes with respect to both the  $x$ - and  $y$ -coordinates, simultaneously. With the development of computer technology, digital shearography was invented. Unlike the application of image-shearing camera in conventional shearography, digital shearography utilized a Michelson interferometer or a birefringent crystal as the image-shearing device [23, 27]. Hung *et al.* applied digital shearography as a nondestructive testing technique to evaluate surface slopes, in-plane strains and residual stresses in composite structures [28, 29, 30, 31].

#### **1.2.4 Coherent Gradient Sensing (CGS)**

Coherent Gradient Sensing (CGS) is a full-field lateral shearing interferometric technique for measuring angular deflections of light rays caused by non-uniform stresses in transparent materials, or surface slope changes of specular opaque materials. It has advantages of non-contact, full-field measurement capability and vibration insensitivity.

The experimental setup for CGS in reflection-mode is shown in Figure 1.5. It consists of a specimen with a reflective surface, a beam splitter, two Ronchi gratings and a recording device. The two Ronchi gratings are separated by a known distance and they have identical pitch with principal directions parallel to each other. The reflective specimen surface is illuminated by a collimated coherent beam using a beam splitter. The reflected object beam containing surface features propagates through two Ronchi gratings, undergoing successive diffraction. The resulting diffracted wave fronts are collected by a filtering lens, and then displayed on a filter plane. The interference is obtained by filtering out all but the necessary waves through an aperture. The resulting interference fringes are related to surface slopes of the specimen.

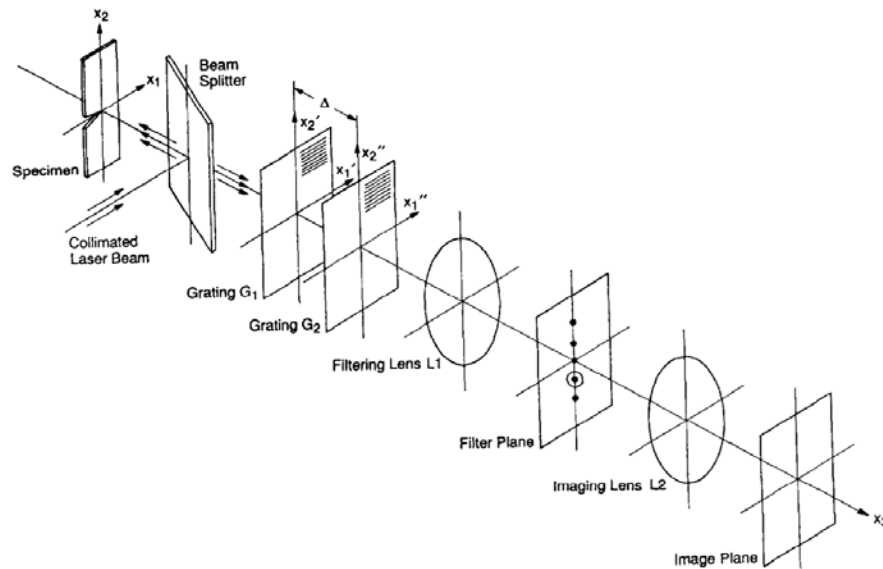


Figure 1.5: Schematic of the experimental setup for reflection CGS [32].

Originally CGS was proposed by Tippur and Rosakis [33, 32] as an optical technique for quasi-static and dynamic fracture mechanics study by measuring stress gradients and surface slopes near cracks to evaluate fracture parameters such as stress intensity factors. Later on, these authors extended transmission CGS to study crack growth

along bimaterial interfaces [34]. Using a bimaterial beam made of PMMA and aluminum bonded along a weak interface, they obtained CGS fringes on the PMMA side of the bimaterial under quasi-static and dynamic conditions and used it to study the interfacial fracture characteristics. Among their ground-breaking observations was an unusually high crack speeds along the interface, approaching the Rayleigh wave speed of PMMA which led a host of new studies on other bimaterial systems and composites and new observations on the possibility of intersonic and supersonic crack growth along weak interfaces. Kimberley and Lambros [35] applied transmission CGS with high-speed photography to study crack kinking behavior along the interface in bimaterials made of PMMA and Homalite-100 polyester. They produced crack kinking at different mode-mixities by varying the impact location. Based on the measurement of fracture parameters from CGS fringes, they concluded that the maximum tensile stress criterion could be used to predict the crack kinking behavior. After the implementation of transmission CGS to study dynamic fracture mechanics, Krishnaswamy *et al.* first applied reflection CGS to measure transient crack-tip deformation fields in steel specimens subjected to dynamic loading by polishing the specimen surface to be mirror finish [36]. Subsequently, reflection CGS was also applied to study fracture behavior of functionally graded materials (FGMs) [37, 38, 39] made of glass-filled epoxy. Rousseau and Tippur [37] investigated mode-I fracture in FGM when cracks were parallel to the elastic gradient. They observed that stress intensification was lower for a crack on the compliant side of the FGM compared with the one with a crack on the stiff side. Later, mixed-mode dynamic fracture in FGM was investigated using CGS and high-speed camera by Kirugulige and Tippur [38, 39]. The single edge notched specimens with crack along the elastic gradient were impact loaded

eccentrically. The results showed that for a crack on the compliant side in FGM, the crack initiated almost self-similarly while the crack initiated with a large kink angle for a crack on the stiff side in FGM. Kitey and Tippur [40] investigated mechanics of interaction between a dynamically propagating crack and a stiff inclusion with different interfacial strengths using reflection CGS and high-speed photography to understand fracture toughness characteristics of particular composites. Their results revealed that a weaker inclusion-matrix interface attracted the propagating crack whereas a stronger interface deflected the crack away.

Reflection CGS was also widely used for characterizing thin films. Since CGS offers slopes directly, the curvatures which are proportional to stresses in thin films can be obtained by differentiating the surface slopes just once and use Stoney's formula [41] to determine the thin film stresses. Rosakis *et al.* [42] demonstrated that CGS was able to measure curvatures in thin films and micro-mechanical structures, the curvatures obtained from CGS were verified with the ones obtained using high-resolution X-ray diffraction. Lee *et al.* [43] measured radial curvatures in thin-film/substrate structures subjected to thermal cycling using CGS. Subsequently, Park *et al.* [44] calculated two principle curvatures and the maximum twist based on the Mohr's circle, and extended CGS to measure these three independent curvature components in thin-film/thicker-substrate structures subjected to large deformations. Brown *et al.* [45] stated that slope and curvature values obtained from CGS matched very well with X-ray micro-diffraction (XRD) counterparts based on the comparison of measurements of discontinuous curvatures in thin film-wafer substrate system using these two methods. CGS was also implemented to

measure thermal stresses and curvatures of thin films at high and low (cryogenic) temperatures [46, 47, 48].

Several modifications have also been introduced to CGS by other researchers. Mishra *et al.* [49] combined CGS with tomography to measure parameters such as temperature, concentration and density, based on time-dependent three-dimensional refractive index variations. Budyansky *et al.* [50] developed CGS microscopy (micro-CGS) to measure microscale curvatures. Recently, Ma and Xie [51, 52] proposed novel phase shifting approaches to CGS to quantify surface slopes accurately.

### **1.2.5 Digital Gradient Sensing (DGS)**

Recently, a new full-field optical method called Digital Gradient Sensing (DGS) based on 2D DIC principles, has been proposed for measuring two orthogonal small angular deflections of light rays [53, 54]. Two variants of DGS, a transmission-mode DGS (*t*-DGS) for measuring stress gradients in transparent solids, and a reflection-mode DGS (*r*-DGS) for measuring surface slopes on optically reflective objects are rather attractive for experimental mechanics investigations due to simplicity of the experimental setup and its measurement accuracy besides the ubiquity of 2D image correlation algorithms.

Before discussing DGS, it is appropriate to describe the principle of 2D Digital Image Correlation (2D DIC) as the former employs principles of the latter. 2D DIC has become popular for measuring full-field surface deformations due to advances in digital recording technologies and image processing algorithms in recent years [55, 56, 57]. It is based on spatial correlation of two random gray scale patterns or speckle images acquired in the ‘reference’ and ‘deformed’ states of an object. During correlation, the images are segmented into sub-images, as shown in Figure 1.6. Subsequently, a sub-image in the

‘deformed’ image is located relative to the ‘reference’ image using a correlation algorithm by maximizing the correlation coefficient, to determine the local displacements  $u$  and  $v$  in the  $x$ - and  $y$ -directions, respectively. To quantify the similarity between sub-images in the ‘deformed’ and ‘reference’ states, a cross-correlation (CC) criterion or sum-squared difference (SSD) correlation criterion is defined initially [58]. In the searching procedure, the position of the deformed sub-image is located by searching the extremum values of the correlation coefficient. The correlation criteria can be divided into two categories, CC criteria and SSD correlation criteria as shown in Figure 1.7 [58, 59, 60, 61]. The attractive features of 2D DIC include simplicity of surface preparation, ordinary white light illumination and digital processing of data.

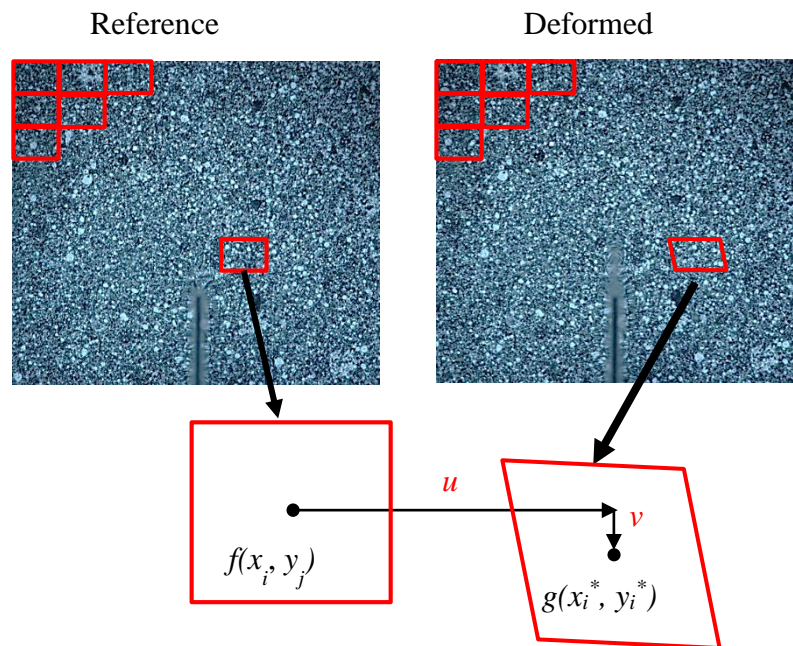


Figure 1.6: DIC principle.

**Table 1.** Commonly used cross-correlation criterion.

CC correlation criterion	Definition
Cross-correlation (CC)	$C_{CC} = \sum_{i=-M}^M \sum_{j=-M}^M [f(x_i, y_j)g(x'_i, y'_j)]$
Normalized cross-correlation (NCC)	$C_{NCC} = \sum_{i=-M}^M \sum_{j=-M}^M \left[ \frac{f(x_i, y_j)g(x'_i, y'_j)}{\bar{f}\bar{g}} \right]$
Zero-normalized cross-correlation (ZNCC)	$C_{ZNCC} = \sum_{i=-M}^M \sum_{j=-M}^M \left\{ \frac{[f(x_i, y_j) - f_m] \times [g(x'_i, y'_j) - g_m]}{\Delta f \Delta g} \right\}$

**Table 2.** Commonly used SSD correlation criterion.

SSD correlation criterion	Definition
Sum of squared differences (SSD)	$C_{SSD} = \sum_{i=-M}^M \sum_{j=-M}^M [f(x_i, y_j) - g(x'_i, y'_j)]^2$
Normalized sum of squared differences (NSSD)	$C_{NSSD} = \sum_{i=-M}^M \sum_{j=-M}^M \left[ \frac{f(x_i, y_j)}{\bar{f}} - \frac{g(x'_i, y'_j)}{\bar{g}} \right]^2$
Zero-normalized sum of squared differences (ZNSSD)	$C_{ZNSSD} = \sum_{i=-M}^M \sum_{j=-M}^M \left[ \frac{f(x_i, y_j) - f_m}{\Delta f} - \frac{g(x'_i, y'_j) - g_m}{\Delta g} \right]^2$

Figure 1.7: CC criteria (Table 1) and SSD correlation criteria (Table 2) [58].

DGS has been applied to study experimental mechanics of materials in recent years. Periasamy and Tippur [62] demonstrated the feasibility of *t*-DGS to study material failure on transparent polymer sheet subjected to quasi-static and dynamic line loadings. The same authors [63] also demonstrated that *t*-DGS can be used as a nondestructive optical inspection tool for evaluating transparent sheets. Hao *et al.* [64] have followed up with a report investigating fiber pull-out problem using *t*-DGS. Zhang *et al.* [65] applied *r*-DGS to measure surface topography and thin film stresses at elevated temperatures. Jain and Tippur [66] explored static and dynamic fracture mechanics in polymer plates using *r*-DGS. Later on, the same authors [67] extended *r*-DGS to study transient deformations and damage in planar solids. Pasumarthy and Tippur [68] conducted mechanical and optical characterization of polymer gel using *t*-DGS. Dai *et al.* [69] evaluated the thermal residual

stress distribution in a transparent specimen using lateral shearing interferometry and  $t$ -DGS, and concluded that  $t$ -DGS is more practical relative to the interferometric counterpart.

### **1.3 Integration methods**

The measured slopes when integrated can provide surface profile or topography information. Furthermore, numerical integration methods are rather robust when compared to differentiation of experimental data. Accordingly, a brief review of various integration methods is appropriate here. There are several 2D integration schemes reported in the literature. Broadly, they can be divided into two types: path dependent integration methods [70, 71, 72] and path independent integration methods [4, 73, 74, 75, 76, 77]. Path dependent integration methods such as trapezoidal rule or Simpson's rule calculate the local height increments by directly integrating the slope function. These methods are easy to implement due to simplicity and efficiency of computing. However, the accuracy of results from these methods depends heavily on integration paths. Noise in the measured data can also propagate and accumulate along the integration path. Such errors can be mitigated in path independent integration methods because gradient data have global influence on the solution procedures and errors get uniformly dispersed over the whole surface [78].

Methods based on Fourier transforms [73] are a family of path independent integration methods which are fast and accurate. However, these methods cannot deal with irregular surface shapes which make them not very practical. Another family of path independent integration methods, which can also be fast and highly accurate, is least-squares based integration methods [74, 76, 75, 77]. Hudgin [74] proposed a least-squares

recursive algorithm for wave-front reconstruction from phase difference and studied the propagation of noise. Southwell [76] proposed a more detailed least-squares integration algorithm for wave-front reconstruction based on a rectangular grid configuration. Huang *et al.* [75] pointed out that the assumption of biquadratic functions in Southwell grid configuration limited the accuracy of the algorithm. They proposed an optimized algorithm by implementing iterative compensations. Li *et al.* [77] pointed out that although the accuracy of reconstruction was significantly improved by Huang's algorithm, it was rather time consuming. Hence, they proposed a more accurate and less time intense approach. Ettl *et al.* [4] proposed another kind of integration method by using radial basis functions which showed robustness and high accuracy. However, compared with Li's method, it was found time consuming, especially with incomplete datasets. Huang *et al.* [79] compared three families of two-dimensional integration methods: (a) the finite-difference-based least-squares integration methods, (b) the transform-based integration methods and (c) the radial basis function based integration methods. The performance, advantages and weaknesses of each are discussed in detail for specific cases. Based on their conclusion, Li *et al.*'s algorithm [77] is selected later in this work.

#### **1.4 Mechanics of composites**

Another aspect addressed in this dissertation is failure behavior of carbon fiber reinforced polymer (CFRP) composites. This material system has become the choice in many aerospace and automotive structures [80, 81]. The high strength, high stiffness, impact resistant and lightweight characteristics have made them very popular in these and other applications. However, fiber reinforced plastics (FRP) in general are comprised of weak matrix-fiber interfaces and hence prone to debonds/disbonds and crack-like defects

during fabrication or service. As a result, crack initiation and growth originated from such defects under different loading conditions and loading rates is a distinct possibility. Composites are also susceptible to dynamic impact during their life span by foreign objects; e.g., flying debris, tool drops, etc. As a result, the delamination may occur in CFRP and cause reduction of load-bearing capacity and strength [8, 9, 10]. Hence, it is critical to quantitatively visualize deformations of CFRP under dynamic impact loading, and to quantify failure characteristics by understanding the mechanisms that control the fracture behaviors of CFRP under different loading rates.

Several optical techniques which offer full-field, non-contact measurements have been proposed and used for quantitative visualization of mechanical response of composite materials [82]. They can be broadly classified into coherent and incoherent methods based on the type of illumination used. Quinn *et al.* [83] investigated distribution of surface strains on 3D woven composites subjected to tensile loading using Electronic Speckle Pattern Interferometry (ESPI). The same method was employed in conjunction with embedded fiber optic sensors to study deformation behavior of cross-ply composite laminates under three-point bending by Bosia *et al.* [84]. Tippur *et al.* [33] proposed a lateral shearing interferometry, called the Coherent Gradient Sensing (CGS), which can be applied to measure real-time surface slopes of thin films and structures [43, 85]. Among the incoherent methods, techniques based on moiré phenomena have been applied in several forms. Ritter [86] proposed the reflection moiré method to study the dynamic plate bending. Cairns *et al.* [87] studied the mechanical response of composite laminates under compression by using shadow moiré method. The same method was used by Karthikeyan *et al.* to study the ballistic response of laminated composite plates [88] undergoing large

deformations and lamina failure. In recent years, Digital Image Correlation (DIC) methods have become very popular for measuring structural deformations [89, 90, 91, 92, 93]. Koerber *et al.* [89] conducted an investigation of transverse compression and in-plane shear properties of unidirectional polymer composites under quasi-static and dynamic loading by using 2D DIC. Yamada *et al.* [90] carried out 3D measurements to evaluate the mechanical performance of CFRP during rapid loading by using 3D DIC and two high-speed cameras to measure in-plane as well as out-of-plane deformations. Although using two high-speed cameras has its advantages, it increases the hardware cost and the complexity of the experimental setup including synchronization of the two cameras and subsequent data analysis. Hence, 3D DIC approaches based on a single high-speed camera have been introduced [91, 92]. Pan *et al.* [93] investigated the full-field transient 3D deformation of braided composites plates during ballistic impact by using 3D DIC with a single high-speed camera coupled with a clever light path modification.

The fracture behaviors of polymer composites subjected to quasi-static and dynamic (impact) loads have also been studied by several researchers [94, 95, 96]. Those studies are often based on globally measured mechanical quantities (e.g., far-field loads and/or deflections) and fractography of the fractured surfaces. May [97] has reviewed different testing geometries to measure rate-dependent mode I fracture toughness of composites to conclude that wedge-loaded Double Cantilever Beam (DCB) is suitable for measuring the mode I fracture toughness. Beckermann [98] and Seyhan [99] conducted DCB tests and End Notched Flexure (ENF) tests to study mode I and mode II fracture toughness of different composites (unidirectional carbon/epoxy composite and glass fiber/carbon nanotube reinforced composite). Their results were based on measurement of

loads imposed in the far-field. Shukla *et al.* [100, 101] developed strain-gage methods to measure strains and hence fracture parameters in glass fiber reinforced epoxy laminate  $[0_2/90]_{2s}$ .

Full-field optical methods have distinct advantages relative to global load or displacement measurement techniques as they allow quantitative visualization of mechanical quantities in the entire region-of-interest (ROI) via non-contact means and hence preferable to study fracture mechanics of various materials including fiber reinforced composites. Freire *et al.* investigated the stress state in glass fiber reinforced polyester laminated composites using reflection photoelasticity [102]. Shukla and Khanna also studied crack growth in different unidirectional composites reinforced with glass fibers and metal fibers photoelastically and have noted that fiber bridges reduced the stress intensification and crack velocity [103]. Liu *et al.* extended the optical method of Coherent Gradient Sensing (CGS) [33] to study static and dynamic fracture behaviors of graphite/epoxy unidirectional fiber-reinforced composites (IM7/8551-7) [104, 105]. Hatta *et al.* applied Electronic Speckle Pattern Interferometry (ESPI) to evaluate fracture process in cross-ply carbon fiber reinforced composite laminates and concluded that ESPI was effective in identifying small-scale delaminations [106]. In recent years, due to advances in digital recording technologies and image processing algorithms, Digital Image Correlation (DIC) methods have become popular for measuring full-field surface deformations [58, 107, 108, 109, 110, 111, 112, 113, 114]. Mekky and Nicholson [107] explored crack opening displacement extraction in ceramic/metal composite laminates using DIC. Kirugulige *et al.* [109, 108] were the first to demonstrate DIC in conjunction with ultrahigh-speed photography to study dynamic fracture of polymers and structural

foams. Lee *et al.* [110, 111] extended the idea to investigate crack growth in unidirectional CFRP composites (T800/3900-2) coupons subjected to dynamic impact. More recently, Bedsole *et al.* [112] investigated interlaminar vs. intralaminar dynamic fracture characteristics of unidirectional CFRP using DIC. 3D-DIC has been adopted by Mallon *et al.* [113] to study fracture behavior of pre-stressed orthotropic woven glass fiber-reinforced composites under out-of-plane shock tube loading up to crack initiation. Hoffmann *et al.* [114] applied DIC to study strain field around a crack tip in composite laminates (unidirectional carbon fiber reinforced prepreg stacked with  $[(90,0)_8,90]_s$  lay-up) under quasi-static and high-rate loading conditions and noted that the strain-energy release rate of a composite laminate under high-rate loading was lower than its quasi-static counterpart.

Understanding the dynamic crack growth in fiber reinforced composites continues to be rather challenging from the perspective of full-field measurement of mechanical fields. In addition to the obvious issues of lack of optical transparency or the need for specimen surface preparation required to implement legacy optical methods, the abundance of weak fiber-matrix interfaces and large directional stiffness result in relatively high crack speeds (500-1000 m/s) accompanied by small deformations (a few micrometers) pose challenges to experimental investigations. Difficulty of identifying crack-tip location precisely for accurate evaluation of fracture parameters is among the issues for vision-based investigations [110] of in-plane, non-singular displacements.

## **1.5 Hypotheses and goals**

In this dissertation, it is hypothesized that the full-field optical method - reflection-mode Digital Gradient Sensing or *r*-DGS - (a) can be coupled with robust 2D integration schemes to evaluate surface topography of specular solids at sub-micron scales over

large/macroscale regions-of-interest (ROI), (b) can be advanced to study mechanical deformations and fracture behavior of fiber reinforced composites under quasi-static and dynamic loading conditions, (c) can be coupled with other variants of DGS to improve its measurement sensitivity to study dynamic failure of high-stiffness, low-toughness materials such as soda-lime glass.

To tackle these hypotheses, research is carried out to meet the following goals:

- Implement a Higher-order Finite-difference-based Least-squares Integration (HFLI) method in conjunction with  $r$ -DGS measurements for surface profile evaluation,
- Investigate the accuracy of measured surface profiles from  $r$ -DGS coupled with HFLI in static and dynamic loading experiments,
- Quantitatively visualize out-of-plane deformations and curvatures over relatively large ROI in fiber reinforced polymer composite plates subjected to dynamic impact using  $r$ -DGS,
- Demonstrate the feasibility of  $r$ -DGS to study fracture mechanics of fiber reinforced composites in the pre- and post-crack initiation regimes under static and dynamic loading by conducting fracture experiments on composites with different fiber orientations relative to the initial notch,
- Explore the possibility of new DGS configurations capable of higher measurement sensitivity to study fast fracture in ultralow-toughness, high-stiffness materials such as soda-lime glass relative to the existing  $r$ -DGS approach.

## 1.6 Organization of the dissertation

This dissertation is organized into nine chapters including the current introductory chapter. In Chapter 2, the experimental setups and working principles of  $t$ -DGS and  $r$ -DGS methods this dissertation is based on are described. In Chapter 3, a 2D integration method called the Higher-order Finite-difference based Least-squares Integration (HFLI) is introduced. The experimental details to investigate the feasibility of HFLI when used in conjunction with  $r$ -DGS are discussed. The accuracy of the smallest measurable surface deformations in both static and dynamic loading conditions using DGS in conjunction with HFLI algorithm is explored in Chapter 4.

In Chapter 5, visualization and quantification of impact induced surface topography and stresses evolution in carbon fiber reinforced polymer composites using  $r$ -DGS are explored. The ability of  $r$ -DGS to quantify surface slopes at micro-radian scales and at microsecond intervals with the aid of ultrahigh-speed photography is demonstrated. The  $r$ -DGS approach is advanced to static and dynamic fracture study of unidirectional CFRP laminates in Chapter 6. Mode-I and mixed-mode fractures of composite specimens with different fiber orientations relative to the initial notch are discussed based on the measured fracture parameters from surface slopes associated with stationary and propagating cracks.

In Chapter 7, two new variants of DGS that offer significantly higher measurement sensitivity relative to  $r$ -DGS are proposed for quantifying extremely small stress gradients in transparent solids. The experimental setup details, working principles and their governing equations are derived and verified. Dynamic fracture of soda-lime glass plates is studied using the newly proposed DGS methods in Chapter 8. The experimental details

of applying the new methods with ultrahigh-speed photography besides extraction of fracture parameter histories are described.

In Chapter 9, major conclusions of this dissertation are presented and a few potential future applications of the DGS methods are noted.

## Chapter 2. Digital Gradient Sensing (DGS) Methods

In this chapter, variants of Digital Gradient Sensing (DGS) methods in transmission and reflection modes are described. DGS is based on 2D Digital Image Correlation (DIC) commonly used for quantifying in-plane motion of decorated speckles to measure angular deflections of light rays in the whole field. In the reflection-mode Digital Gradient Sensing or *r*-DGS, the angular deflections of light rays are related to surface slopes, whereas in transmission-mode Digital Gradient Sensing or *t*-DGS, the angular deflections of light rays are related to the gradients of in-plane normal stresses.

### 2.1 Reflection-mode Digital Gradient Sensing (*r*-DGS)

A schematic of the experimental setup for reflection-mode Digital Gradient Sensing (*r*-DGS) to measure surface slopes is shown in Figure 2.1. A digital camera is used to record random speckles on a target plane via the reflective specimen surface. To achieve this, the specimen and the target plate are placed perpendicular to each other, and the beam splitter is placed at 45° relative to the specimen and target plate, respectively. The target plate is coated with random black and white spray painted speckles, and is illuminated uniformly using a broad spectrum (white) light. The specimen surface is made reflective using vapor deposition of aluminum film or using the film transfer technique [115]. When the specimen is in the undeformed state, the gray scale at a generic point P on the target

plate is photographed by a camera pixel through point O on the specimen plane. Thus recorded speckle image at that time instant and/or load level is the reference image. After the specimen, say, suffers deformation due to the applied load, the gray scale at a neighboring point of P, namely Q on the target plate, is photographed by the same pixel through the same point O on the specimen surface. The corresponding image of the specimen in the deformed state is recorded next. The *local* orthogonal speckle displacements identified as  $\delta_{y;x}$  in Figure 2.2 can be obtained by performing a 2D correlation of the reference and deformed images. The corresponding angles  $\phi_{x;y}$  representing two orthogonal angular deflections of light rays can then be obtained as shown in Figure 2.2.

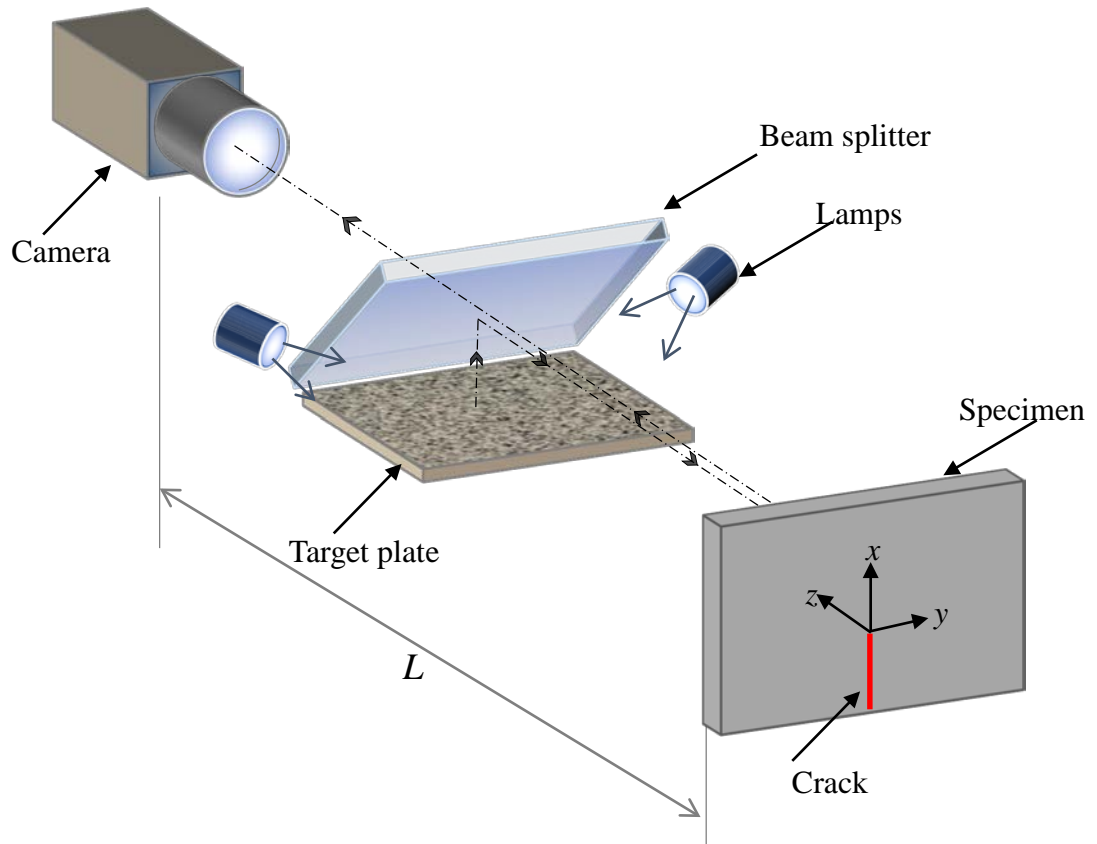


Figure 2.1: Schematic of experimental setup for reflection DGS (*r*-DGS).

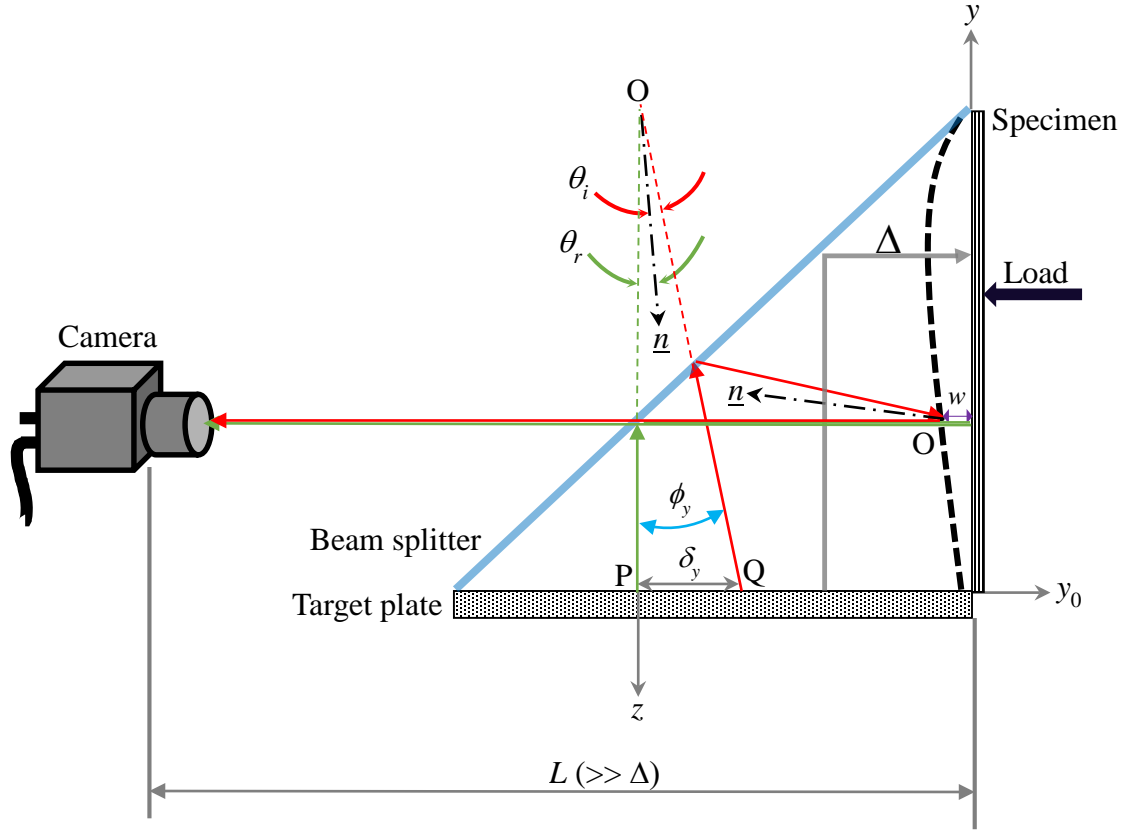


Figure 2.2: Working principle of  $r$ -DGS.

For simplicity, only the angular deflections of light rays in the  $y$ - $z$  plane are shown in Figure 2.2. Here,  $OQ$  makes an angle  $\phi_y$  with  $OP$ . Further,  $\phi_y = \theta_i + \theta_r$  where  $\theta_i$  and  $\theta_r$  ( $=\theta_i$ ) are incident and reflected angles relative to the normal to the specimen and  $\underline{n}$  denotes the local normal to the deformed surface. A similar relationship in the  $x$ - $z$  plane can be obtained as well. Then, the two orthogonal surface slopes of the surface can be related to

$\phi_{y;x}$  as  $\frac{\partial w}{\partial y;x} = \frac{1}{2} \tan(\phi_{y;x})$ . The governing equations for  $r$ -DGS thus are [54],

$$\frac{\partial w}{\partial y;x} = \frac{1}{2} \tan(\phi_{y;x}) \approx \frac{1}{2}(\phi_{y;x}) \approx \frac{1}{2} \left( \frac{\delta_{y;x}}{\Delta} \right) \quad (2.1)$$

where  $\Delta$  is the distance or the gap between the specimen and target planes and small angle approx. is used. It is important to note that the coordinates of the specimen plane are utilized for describing the governing equations and the camera is focused on the target plane during photography. Therefore, coordinate mapping is needed to transfer the target plane locations to the specimen plane. This can be done using the pin-hole camera approximation,  $(x; y) = \frac{L}{L + \Delta}(x_0; y_0)$ , where  $(x; y)$  and  $(x_0; y_0)$  represent the coordinates of the specimen and target planes, respectively, and  $L$  is the distance between the specimen and the camera [53].

## 2.2 Transmission-mode Digital Gradient Sensing (*t*-DGS)

A schematic of the experimental setup for transmission-mode digital gradient sensing (*t*-DGS) method is shown in Figure 2.3(a). Unlike in the *r*-DGS setup, a random speckle pattern on the target plate is recorded through a transparent specimen in *t*-DGS. As in *r*-DGS, a reference image is recorded first. That is, the gray level at point P on the target plane corresponding to point O on the specimen plane is recorded initially by a camera pixel. The refractive index and thickness of the specimen change after imposing a mechanical load on the specimen. As a result, the light rays deviate from their initial path due to the so-called elasto-optical effect. In the deformed state of the specimen, another image is recorded with the gray scale at a neighboring point of P, namely Q, on the target plane, recorded by the same pixel through O on the specimen plane. The local speckle displacements  $\delta_{x,y}$  can be quantified by correlating the reference image with the deformed image of the specimen. The angles  $\phi_{x,y}$  are the two orthogonal angular deflections of light rays, and can be explained as follows:

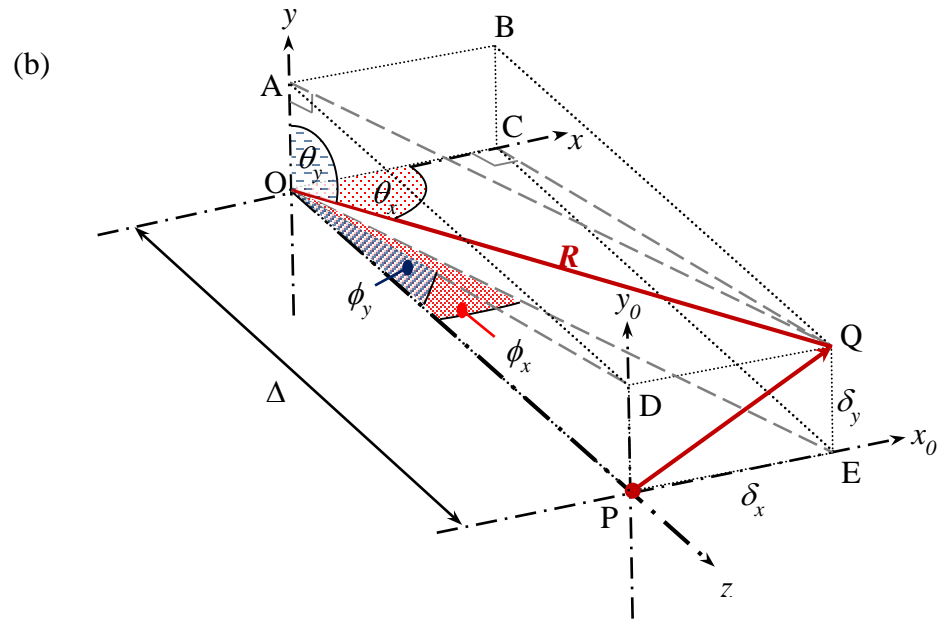
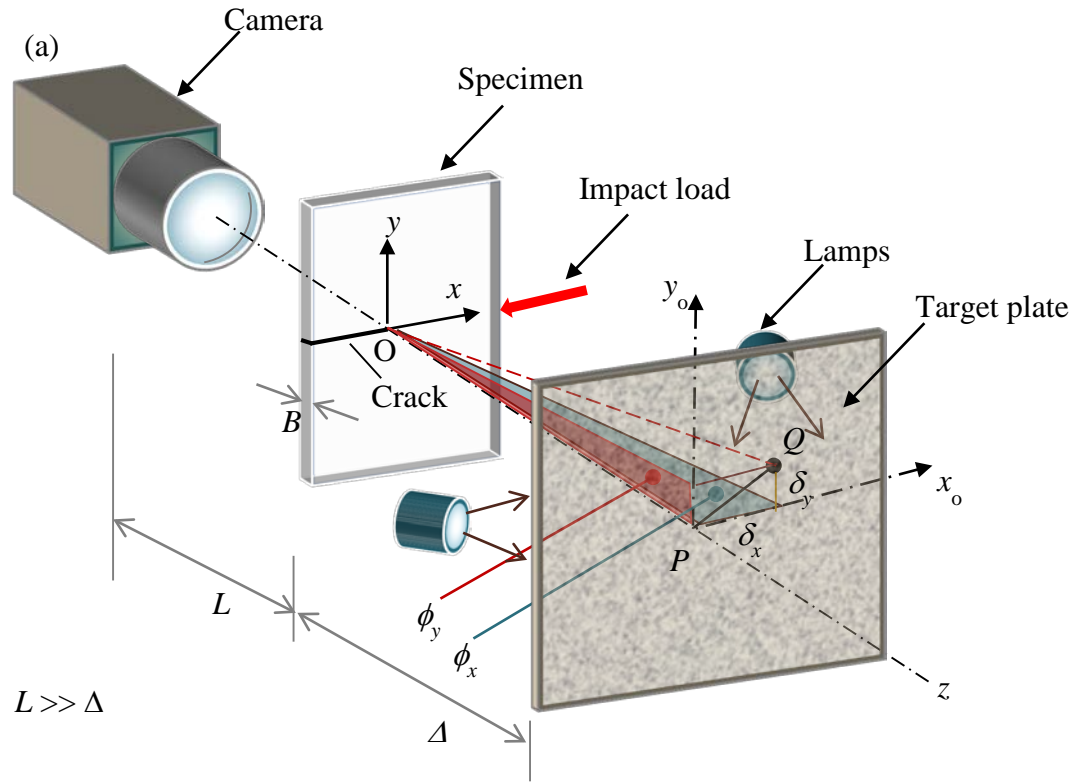


Figure 2.3: Schematic of experimental setup (a) and light ray diagram (b) for  $t$ -DGS [53].

The optical path change,  $\delta S$ , between the original light ray OP and deflected light ray OQ caused by the deformation of the specimen, can be expressed as [33]:

$$\delta S(x, y) = 2B(n-1) \int_0^{1/2} \varepsilon_{zz} d(z/B) + 2B \int_0^{1/2} \delta n d(z/B) \quad (2.2)$$

The two integrals on the right hand side of the above equation represent the contributions of the normal strain in the thickness direction,  $\varepsilon_{zz}$ , and the change in the refractive index,  $\delta n$ , to the overall optical path, respectively. The Maxwell-Neumann relationship [116] states that the refractive index change is proportional to the local state of normal stresses in the specimen. The strain,  $\varepsilon_{zz}$ , can be related to the normal stresses using the generalized Hooke's law for an isotropic, linear elastic solid. Thus, for plane stress conditions, Eq. (2.2) reduces to [53],

$$\delta S(x, y) = C_\sigma B (\sigma_{xx} + \sigma_{yy}), \quad (2.3)$$

where  $C_\sigma = D_1 - (\nu/E)(n-1)$  is the elasto-optic constant of the specimen material.

The deflected light ray OQ make solid angles  $\theta_x$  and  $\theta_y$  with the  $x$ - and  $y$ -axes, respectively, as shown in Figure 2.3(b). It is evident from the above equations that, for small angular deflections, the direction cosines of OQ,  $\cos \theta_{x,y}$ , are related to the in-plane stress gradients as,

$$\cos \theta_{x,y} = \frac{\partial(\delta S)}{\partial(x; y)} = C_\sigma B \frac{\partial(\sigma_{xx} + \sigma_{yy})}{\partial(x; y)}, \quad (2.4)$$

Referring to the planes defined by points OAQ and OCQ shown in Figure 2.3(b),

$$\cos \theta_{x,y} = \frac{\delta_{x,y}}{R}, \quad (2.5)$$

where  $R (= \sqrt{\Delta^2 + \delta_x^2 + \delta_y^2})$  is the distance between points O and Q,  $\Delta$  is the distance between the specimen and target planes. For small angular deflections, or  $\delta_{x,y} \ll \Delta$ , the two angular deflections of light rays,  $\phi_{x,y}$ , are related to the in-plane stress gradients as [53],

$$\phi_{x,y} \approx \frac{\delta_{x,y}}{\Delta} \approx \cos \theta_{x,y} = C_{\sigma} B \frac{\partial(\sigma_{xx} + \sigma_{yy})}{\partial(x; y)}. \quad (2.6)$$

Again, as in  $r$ -DGS, the pin-hole camera mapping function needs to be used here to transfer the coordinates of the target plane to the specimen plane.

## Chapter 3. Surface Profile/Topography Measurement from $r$ -DGS

In this chapter, a 2D integration method which is called Higher-order Finite-difference based Least-squares Integration (HFLI) is introduced. The surface slopes measured by  $r$ -DGS can be integrated using HFLI to get the surface topography. The feasibility of HFLI used in conjunction with  $r$ -DGS is described in this chapter.

### 3.1 Finite-difference based Least-squares Integration (HFLI) Method

In the field of surface profile reconstruction from slope data, 2D integration based on finite-difference is widely used to compute topographic values by least-squares procedures. A robust Higher-order Finite-difference-based Least-squares Integration (HFLI) scheme in the so-called Southwell configuration is developed during this work to reconstruct the surface topography. The feasibility of  $r$ -DGS in conjunction with HFLI to measure the surface topography is demonstrated in this part of the research.

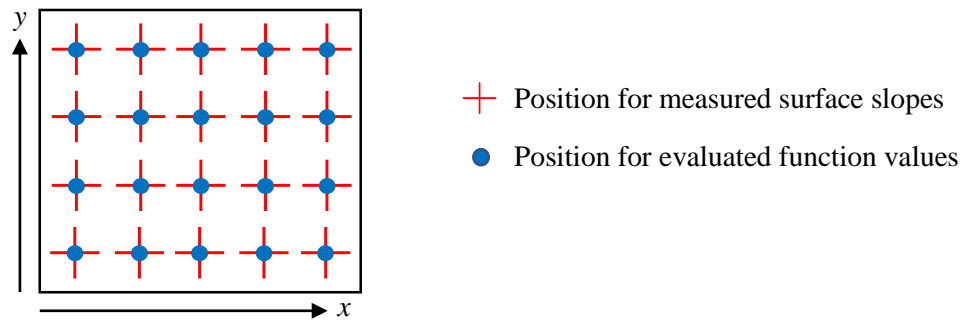


Figure 3.1: Southwell grid configuration.

Southwell proposed a Traditional Finite-difference-based Least-squares Integration or TFLI algorithm based on a rectangular grid configuration, as shown in Figure 3.1, requiring the measured surface slopes and the evaluated topographic values are at the same spatial position [76, 79]. The relation between the slopes and the evaluated function values in a  $M \times N$  matrix in this approach can be expressed as [117, 79],

$$\left\{ \begin{array}{l} \frac{f_{m,n+1} - f_{m,n}}{x_{m,n+1} - x_{m,n}} = \frac{s_{m,n+1}^x + s_{m,n}^x}{2}, \quad \begin{array}{l} m = 1, 2, \dots, M, \\ n = 1, 2, \dots, N-1. \end{array} \\ \frac{f_{m+1,n} - f_{m,n}}{y_{m+1,n} - y_{m,n}} = \frac{s_{m+1,n}^y + s_{m,n}^y}{2}, \quad \begin{array}{l} m = 1, 2, \dots, M-1, \\ n = 1, 2, \dots, N. \end{array} \end{array} \right. \quad (3.1)$$

where  $x, y$  are the local coordinates,  $s$  denotes the spatial gradients/slopes,  $f$  is the value of the function at  $(x, y)$ . Eq. (3.1) can be converted into a matrix form,

$$\mathbf{D}\mathbf{F} = \mathbf{G}, \quad (3.2)$$

where,

$$\mathbf{D} = \begin{bmatrix} D^x \\ D^y \end{bmatrix} = \begin{bmatrix} -1 & 0 & \dots & 0 & 1 & 0 & \dots & \dots & 0 \\ 0 & -1 & 0 & \dots & 0 & 1 & 0 & \dots & 0 \\ \vdots & \vdots \\ 0 & \dots & \dots & 0 & -1 & 0 & \dots & 0 & 1 \\ \hline -1 & 1 & 0 & \dots & \dots & \dots & \dots & \dots & 0 \\ 0 & -1 & 1 & 0 & \dots & \dots & \dots & \dots & 0 \\ \vdots & \vdots \\ 0 & \dots & \dots & \dots & \dots & \dots & 0 & -1 & 1 \end{bmatrix}_{[M(N-1)+(M-1)N] \times MN} \quad (3.3)$$

$$\mathbf{F} = \begin{bmatrix} f_{1,1} \\ f_{2,1} \\ \vdots \\ f_{M,N} \end{bmatrix}_{MN \times 1} \quad (3.4)$$

$$\mathbf{G} = \begin{bmatrix} \mathbf{G}^x \\ \mathbf{G}^y \end{bmatrix} = \frac{1}{2} \begin{bmatrix} (s_{1,2}^x + s_{1,1}^x)(x_{1,2} - x_{1,1}) \\ (s_{2,2}^x + s_{2,1}^x)(x_{2,2} - x_{2,1}) \\ \vdots \\ (s_{M,N}^x + s_{M,N-1}^x)(x_{M,N} - x_{M,N-1}) \\ \hline (s_{2,1}^y + s_{1,1}^y)(y_{2,1} - y_{1,1}) \\ (s_{3,1}^y + s_{2,1}^y)(y_{3,1} - y_{2,1}) \\ \vdots \\ (s_{M,N}^y + s_{M-1,N}^y)(y_{M,N} - y_{M-1,N}) \end{bmatrix}_{[M(N-1)+(M-1)N] \times 1} \quad (3.5)$$

Eq. (3.2) can be solved to get  $\mathbf{F}$  as,

$$\mathbf{F} = (\mathbf{D}^T \mathbf{D})^{-1} \mathbf{D}^T \mathbf{G} \quad (3.6)$$

where  $\mathbf{D}^T$  denotes the transpose of  $\mathbf{D}$ .

The TFLI method is widely used due to its simplicity [76]. It has an algorithmic error of  $O(h^3)$  where  $h$  indicates the interval between two adjacent grid points used in Taylor's expansion as noted by Li *et al.* [77]. A more accurate approach is proposed by incorporating higher order terms in the Taylor's expansion and two additional neighboring slopes into the integration scheme resulting in an algorithmic error of  $O(h^5)$ . This approach is called the Higher-order Finite-difference-based Least-squares Integration or the HFLI method. In this method, the  $\mathbf{G}$  matrix mentioned earlier is expressed as:

$$\mathbf{G} = \begin{bmatrix} \mathbf{G}^x \\ \mathbf{G}^y \end{bmatrix} \quad (3.7)$$

$$G^x = \frac{1}{24} \begin{bmatrix} 12(s_{1,2}^x + s_{1,1}^x)(x_{1,2} - x_{1,1}) \\ 12(s_{2,2}^x + s_{2,1}^x)(x_{2,2} - x_{2,1}) \\ \vdots \\ 12(s_{M,2}^x + s_{M,1}^x)(x_{M,2} - x_{M,1}) \\ (-s_{1,4}^x + 13s_{1,3}^x + 13s_{1,2}^x - s_{1,1}^x)(x_{1,3} - x_{1,2}) \\ (-s_{2,4}^x + 13s_{2,3}^x + 13s_{2,2}^x - s_{2,1}^x)(x_{2,3} - x_{2,2}) \\ \vdots \\ (-s_{M,4}^x + 13s_{M,3}^x + 13s_{M,2}^x - s_{M,1}^x)(x_{M,3} - x_{M,2}) \\ (-s_{1,5}^x + 13s_{1,4}^x + 13s_{1,3}^x - s_{1,2}^x)(x_{1,4} - x_{1,3}) \\ \vdots \\ (-s_{M,5}^x + 13s_{M,4}^x + 13s_{M,3}^x - s_{M,2}^x)(x_{M,4} - x_{M,3}) \\ \vdots \\ (-s_{M,N}^x + 13s_{M,N-1}^x + 13s_{M,N-2}^x - s_{M,N-3}^x)(x_{M,N-1} - x_{M,N-2}) \\ 12(s_{1,N}^x + s_{1,N-1}^x)(x_{1,N} - x_{1,N-1}) \\ 12(s_{2,N}^x + s_{2,N-1}^x)(x_{2,N} - x_{2,N-1}) \\ \vdots \\ 12(s_{M,N}^x + s_{M,N-1}^x)(x_{M,N} - x_{M,N-1}) \end{bmatrix}_{[M(N-1)] \times 1} \quad (3.8)$$

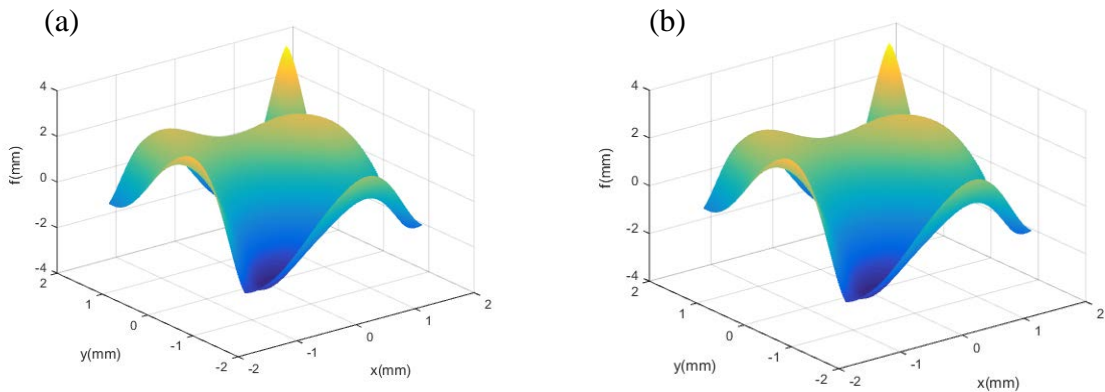
$$G^y = \frac{1}{24} \begin{bmatrix} 12(s_{2,1}^y + s_{1,1}^y)(y_{2,1} - y_{1,1}) \\ (-s_{4,1}^y + 13s_{3,1}^y + 13s_{2,1}^y - s_{1,1}^y)(y_{3,1} - y_{2,1}) \\ (-s_{5,1}^y + 13s_{4,1}^y + 13s_{3,1}^y - s_{2,1}^y)(y_{4,1} - y_{3,1}) \\ \vdots \\ (-s_{M-1,1}^y + 13s_{M-2,1}^y + 13s_{M-3,1}^y - s_{M-2,1}^y)(y_{M-2,1} - y_{M-3,1}) \\ 12(s_{M,1}^y + s_{M-1,1}^y)(y_{M,1} - y_{M-1,1}) \\ 12(s_{2,2}^y + s_{1,2}^y)(y_{2,2} - y_{1,2}) \\ (-s_{4,2}^y + 13s_{3,2}^y + 13s_{2,2}^y - s_{1,2}^y)(y_{3,2} - y_{2,2}) \\ \vdots \\ (-s_{M-1,2}^y + 13s_{M-2,2}^y + 13s_{M-3,2}^y - s_{M-2,2}^y)(y_{M-2,2} - y_{M-3,2}) \\ 12(s_{M,2}^y + s_{M-1,2}^y)(y_{M,2} - y_{M-1,2}) \\ 12(s_{2,3}^y + s_{1,3}^y)(y_{2,3} - y_{1,3}) \\ (-s_{4,3}^y + 13s_{3,3}^y + 13s_{2,3}^y - s_{1,3}^y)(y_{3,3} - y_{2,3}) \\ \vdots \\ 12(s_{M,N}^y + s_{M-1,N}^y)(y_{M,N} - y_{M-1,N}) \end{bmatrix}_{[(M-1)N] \times 1} \quad (3.9)$$

### 3.2 Algorithm Verification

To verify the accuracy of HFLI method independently, a function  $f(x, y)$  was defined as follows:

$$f(x, y) = (x + y) \cos(x^2 - y^2) + 2 \sin(x^2 + y) \cos(xy + y) \quad (3.10)$$

The chosen range for  $x$  and  $y$  coordinates for this demonstration were from -1.5 to 1.5 mm with an interval of 0.01 mm, resulting in a  $300 \times 300$  data array. As evident from Figure 3.2(a) the function includes significant complexities in its features. The corresponding slope contours in the  $x$ - and  $y$ -directions are shown in Figure 3.2(d) and (e), respectively. After removing the piston errors [118], the reconstructed function using HFLI algorithm is shown in Figure 3.2(b). The integration errors shown in Figure 3.2(c) indicate the high accuracy of the HFLI method. The integration errors on the edges of the domain are somewhat higher because of the lack of two adjacent slopes along the edges as evident from Eqs. (3.8) and (3.9). The mean values of errors in the region away from the edges are essentially zero or negligible.



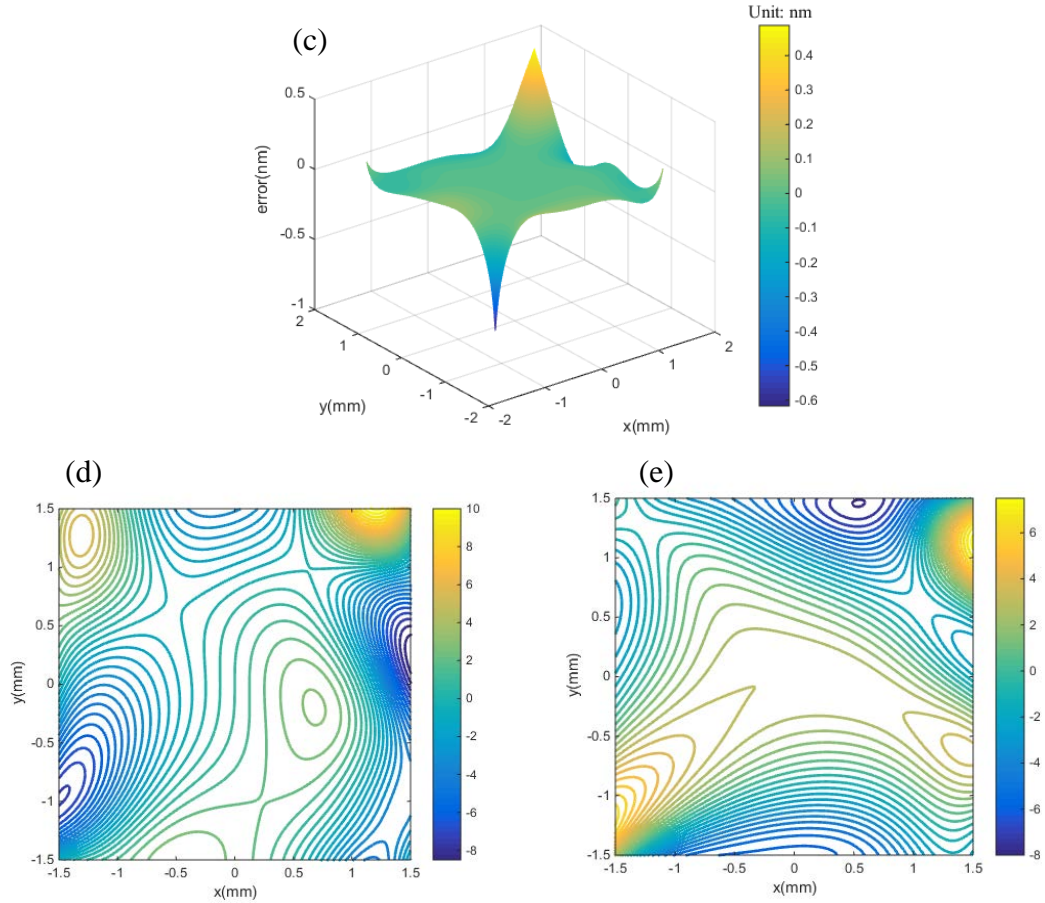


Figure 3.2: Verification of HFLI method. (a) Original function, (b) reconstructed function, (c) reconstruction errors, (d) contours of derivatives of the function in the  $x$ -direction, (e) contours of derivatives of the function in the  $y$ -direction.

### 3.3 Silicon wafer subjected to central loading

The feasibility of HFLI method used in conjunction with  $r$ -DGS to obtain mechanically induced out-of-plane deformation maps for a deformed thin silicon wafer subjected to central loading was considered for demonstration of the approach to study experimental mechanics problems. A single-face polished  $360\ \mu\text{m}$  thick silicon wafer of diameter  $50.8\ \text{mm}$  was used in the experiment. The unpolished face was bonded to a thick ( $1.65\ \text{mm}$ ) steel washer with a circular aperture of  $30\ \text{mm}$  using a slow curing epoxy in order to simulate a thin circular plate with a circular clamped boundary. Another steel plate

fitted with a micrometer at its center was positioned directly behind the silicon wafer. These two steel plates were secured in a cylindrical lens holder. A target plate, decorated with random black and white speckles, was placed horizontally at  $90^\circ$  to the silicon wafer. The target was illuminated by two cool LED lamps to minimize thermal currents. A beam splitter was placed at  $45^\circ$  relative to both the silicon wafer and the target plate. It was also at  $45^\circ$  to the optical axis of the camera (see Figure 3.3). The distance ( $\Delta$ ) between the silicon wafer surface and the target plate along the optical axis was 62 mm.

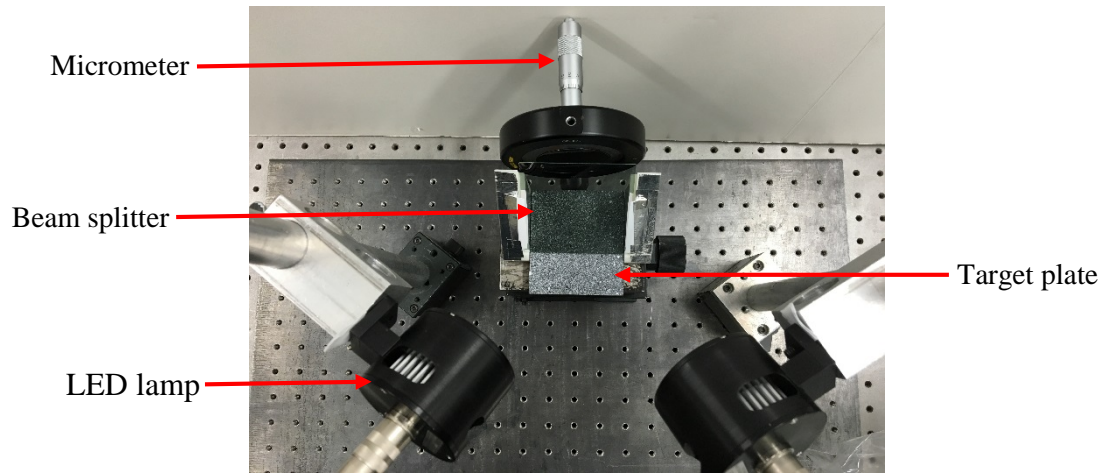


Figure 3.3: The experimental setup used to study out-of-plane deformation of a silicon wafer.

A Nikon D100 digital SLR camera was focused on the target via the polished face of the silicon wafer. The camera was fitted with a 70-300 mm macro lens and an adjustable bellows. A small aperture ( $F^\# = 22$ ) was selected for recording the speckles with a good focus. The distance between the silicon wafer and the end of lens ( $L$ ) was 1403 mm. When the silicon wafer was under no load, an 8-bit reference image of speckle pattern was recorded with a resolution of  $1504 \times 1000$  pixels (1 pixel =  $43.9 \mu\text{m}$  on the target plane). Then, different but known central out-of-plane displacements,  $w$ , were imposed on the

silicon wafer using the micrometer tip and speckle images corresponding to the deformed states of the wafer were recorded. By correlating each of these speckle images with the reference image, the local displacements  $\delta_{y;x}$  in the region of interest were measured. During correlation (using ARAMIS image analysis software), the images were sub-divided into  $20 \times 20$  pixels with 10 pixel overlap in the  $x$ - and  $y$ -directions, resulting in  $97 \times 133$  matrix of data points in the entire field.

Two sets of orthogonal surface slope contours,  $\frac{\partial w}{\partial x}$  and  $\frac{\partial w}{\partial y}$  measured from  $r$ -

DGS are shown in Figure 3.4 for two imposed central deflections,  $4 \pm 1 \mu\text{m}$  and  $10 \pm 1 \mu\text{m}$ .

For completeness, contours of  $\frac{\partial w}{\partial r} \left( = \sqrt{\left(\frac{\partial w}{\partial x}\right)^2 + \left(\frac{\partial w}{\partial y}\right)^2} \right)$  are also shown, where  $r$  is the

radial distance from the center (loading point) of the wafer. The contours are plotted at increments of 50 and 100 micro-radians in the two cases, respectively. It can be observed

that the magnitude of contours of  $\frac{\partial w}{\partial x}$  and  $\frac{\partial w}{\partial y}$  are symmetric about  $x=0$  and  $y=0$  with

a high concentration of contours near the loading point. The contours of  $\frac{\partial w}{\partial r}$  show circular

symmetry, again with a higher concentration of contours around the loading point and near the clamped edges with fewer contours in the intermediate zone. As expected, slopes are zero along the circular edge (and beyond) of the Si wafer in the glued portion and near the loading point with a gradual transition in the intermediate region.

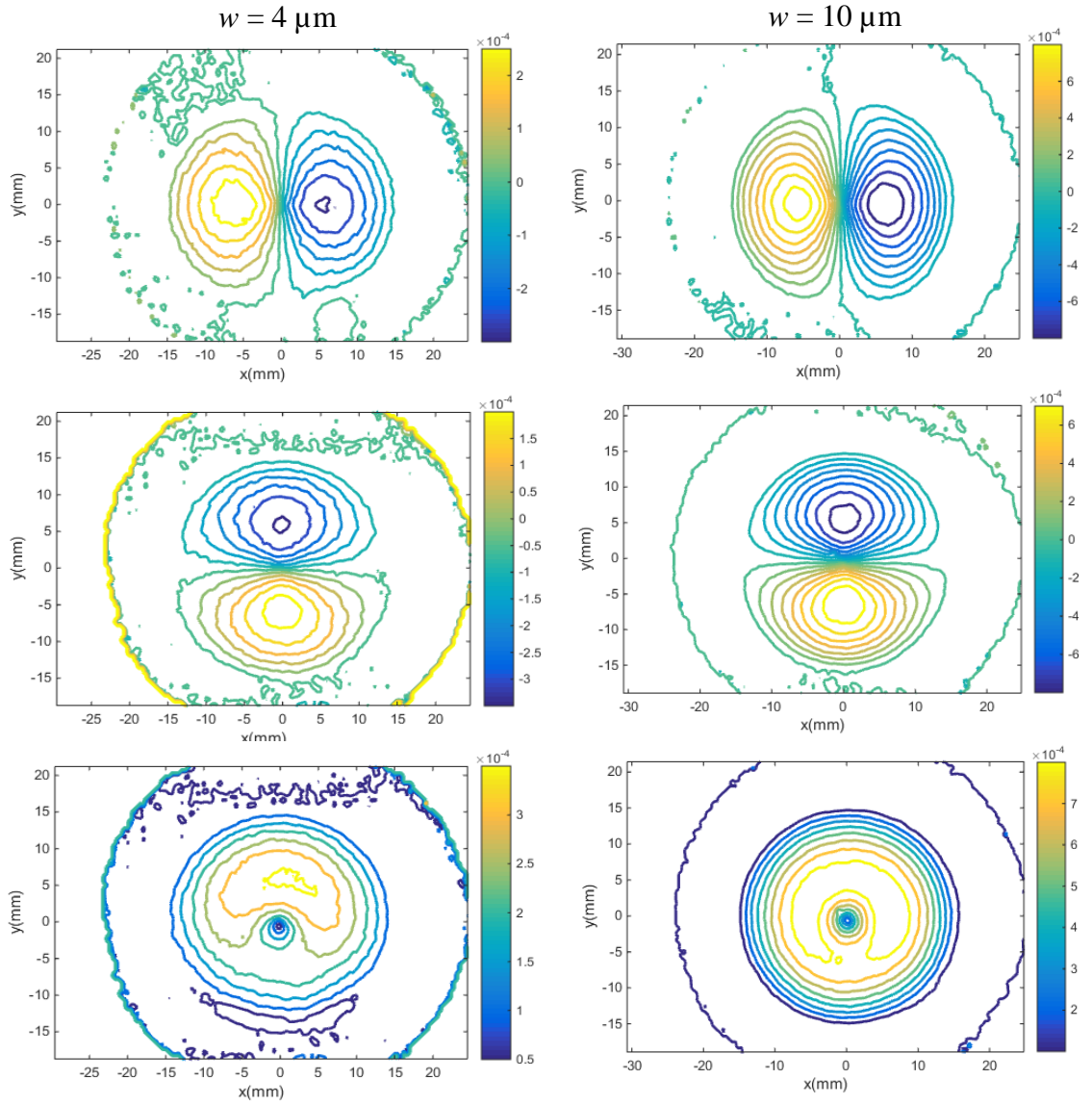


Figure 3.4: Results from  $r$ -DGS for a clamped silicon wafer (30 mm dia., 360  $\mu\text{m}$  thick) subjected to central deflection of 4  $\mu\text{m}$  (left column) and 10  $\mu\text{m}$  (right column). Row 1: contours of  $w,x$ ; Row 2: contours of  $w,y$ ; Row 3: contours of  $w,r$ . Note: (0, 0) is made to coincide with the loading point. Contour increments =  $0.5 \times 10^{-4}$  rad and  $1 \times 10^{-4}$  rad, respectively.

The measurements from  $r$ -DGS are compared directly with the closed-form solutions for an elastic thin circular plate with a clamped boundary subjected to a centrally applied deflection using,

$$\frac{\partial w}{\partial y} = \frac{4yw}{R^2} \log\left(\frac{\sqrt{x^2 + y^2}}{R}\right) \quad (3.11)$$

where  $w$  is the out-of-plane deformation and  $R$  is the radius of the circular plate.

The comparisons shown in Figure 3.5 are made between experimental and analytical data sets along the  $y$ -axis for different magnitudes of out-of-plane deformations. The least count of the micrometer used being  $2 \mu\text{m}$ , results from  $w = 2 \mu\text{m}$  is also added to this comparison. It can be readily observed that there is a good agreement between the two data sets with percentage error decreasing as imposed deflection is increased.

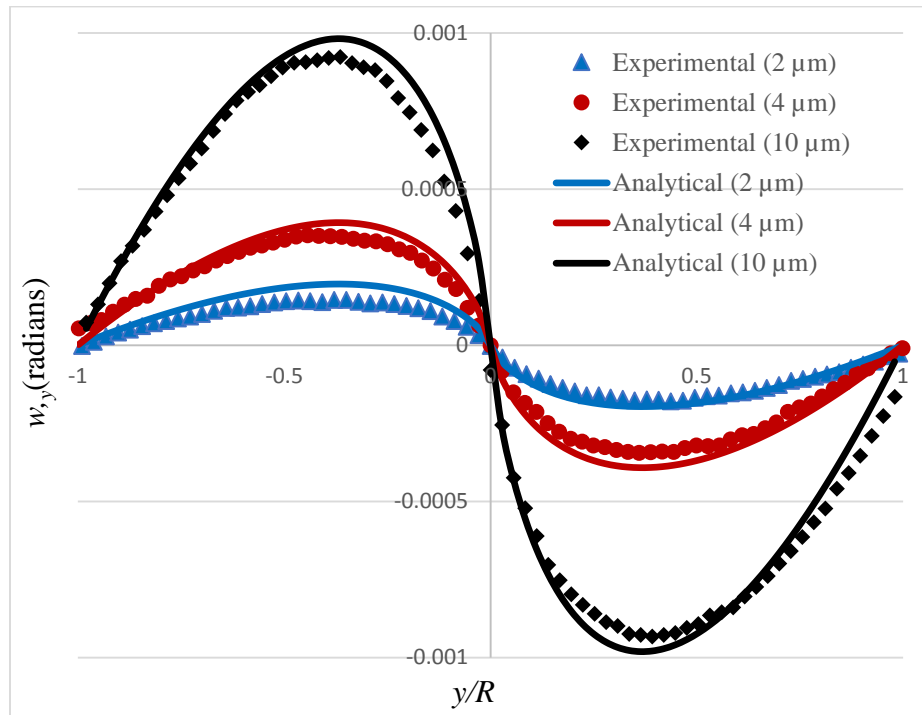


Figure 3.5: Comparison of analytical data and experimental data of  $\frac{\partial w}{\partial y}$  along the  $y$ -axis corresponding to three different imposed out-of-plane deflections.

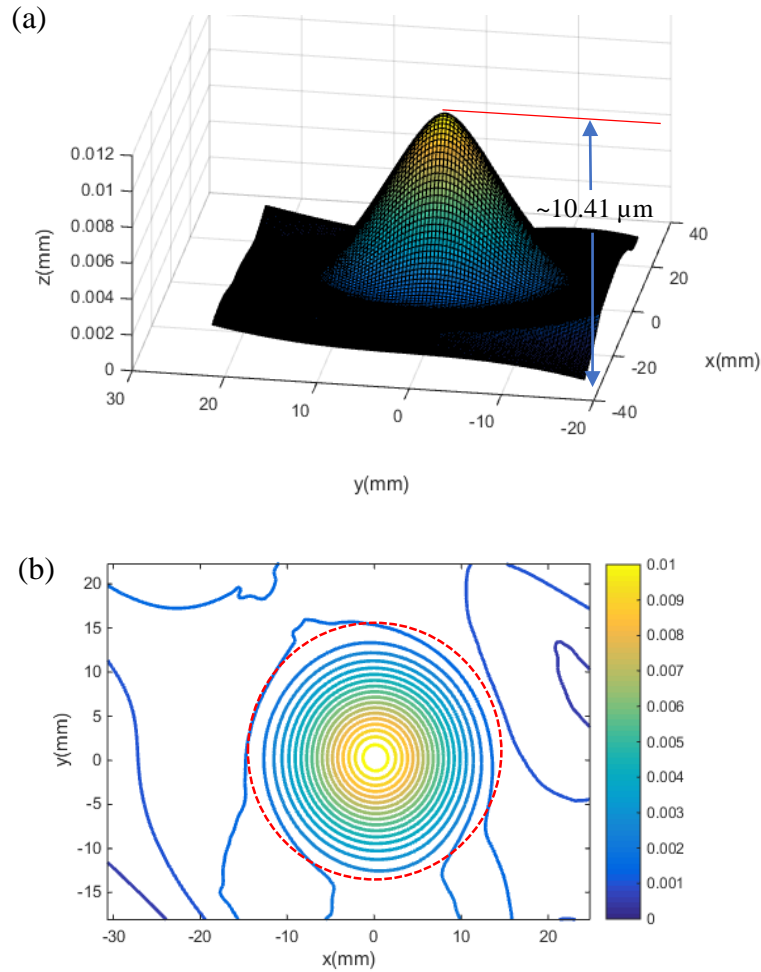


Figure 3.6: Surface topography calculated via 2D integration using surface slope data and HFLI method: (a) 3D surface representation of reconstructed surface, (b) out-of-plane displacement ( $w$ ) contours ( $0.5 \mu\text{m}$  increments). Note:  $(0, 0)$  is made to coincide with the loading point; red circle indicates the edge of the circular aperture of the steel washer.

The reconstructed 3D surface computed using integration of surface slope data and HFLI computations is plotted in Figure 3.6(a) for the  $10 \mu\text{m}$  deflection case. Figure 3.6(b) shows the corresponding contours of out-of-plane displacements ( $w$ ) at  $0.5 \mu\text{m}$  increments. The circular contours in Figure 3.6(b) demonstrate that the shape of the reconstructed figure matches well with the reality attempted in the experiment, both qualitatively and quantitatively. (Note that for all the plots in Figure 3.4 and Figure 3.6, the origin is made

to coincide with the loading point.) The peak value of the height of the reconstructed 3D surface is  $10.41 \mu\text{m}$  with an acceptable error of 4.1%. (The reconstruction for the smaller imposed deflection of  $4 \mu\text{m}$ , not shown here for brevity, led to a peak value of  $4.81 \mu\text{m}$ , a deviation of 20.2%. Given the uncertainty of the imposed deflection of  $\pm 1 \mu\text{m}$ , the reconstructed peak value is deemed reasonable despite a higher error.) The errors are attributed to a combined effect of (a) micrometer backlash and human errors while imposing the out-of-plane displacement, (b) the non-uniformity and finite compliance of the epoxy adhesive used to ‘clamp’ the Si wafer to the steel plate, (c) errors due to DGS measurements as well as integration errors in the HFLI method. Although it is beneficial to isolate each of these effects, it is difficult to do so practically. It should also be mentioned that the reconstructed surface along the glued boundary of the wafer shows non-zero deflection (approximately  $1 \mu\text{m}$  instead of zero). This is attributed to a combination of reconstruction errors as well as compliance of the epoxy glue layer alluded to earlier.

The accuracy of HFLI method relies on the interval between two neighboring grid points. And, this interval in turn depends on the choice of sub-image size and pixel overlap used during correlation of the reference and deformed images while implementing *r*-DGS. Further, the overlap was selected for achieving correlation at all points in the region-of-interest with minimum noise in the plotted data. Therefore, the tradeoffs if any due to different interval choices on HFLI outcome was examined. Figure 3.7 shows the measured contours of  $\frac{\partial w}{\partial y}$  for  $20 \times 20$  pixels sub-images with three different overlaps of 0, 10, 15 pixels and the corresponding reconstructed surfaces. Higher number of overlapping pixels resulted in the interval (*h*) between two neighboring grid points getting smaller. In Figure 3.7, it can be observed that the slope contours are generally in good agreement with each

other with minor differences between the slope contours near the wafer boundary where the slopes are expected to be zero. That is, the interval ( $h$ ) for 0 pixel overlap and 15 pixel overlap cases are different by a factor of 2 and 0.5 relative to the 10 pixel overlap case. The reconstructed surfaces for each of these cases are shown in Figure 3.7. (Note that the plots appear darker as the grid density increases.) The difference of the peak values of out-of-plane displacement for the three cases relative to the imposed value range between 3.2% and 4.5% suggesting the robustness of the reconstruction algorithm. The height of the reconstructed surface for the zero pixel overlap case is the closest to  $10\ \mu\text{m}$ , however, it is less accurate due to the larger interval between neighboring grid points. As a result, 10 pixel overlap was judged appropriate for subsequent analyses.

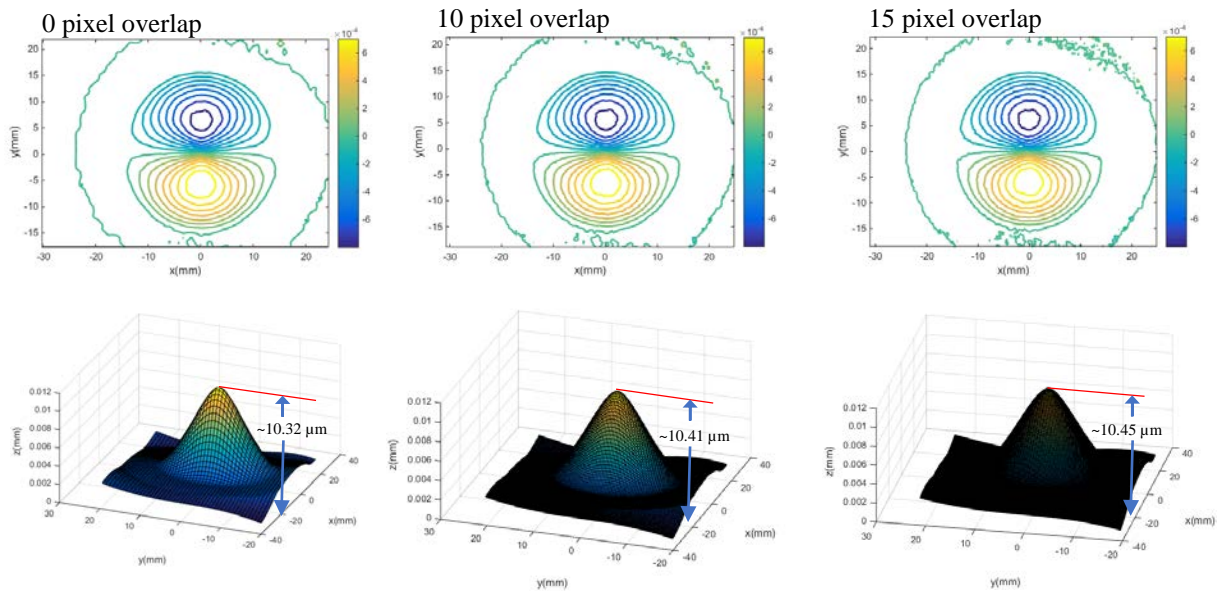


Figure 3.7: Contours of  $w,y$  for  $20 \times 20$  pixel sub-images with three different overlap and the corresponding reconstructed figures.

### 3.4 Wafer subjected to eccentric loading

The measurement of slopes and reconstruction of out-of-plane deformations of a silicon wafer subjected to eccentric loading was attempted next. In this experiment, again out-of-plane displacements,  $w = 4 \pm 1 \mu\text{m}$  and  $10 \pm 1 \mu\text{m}$ , were imposed on the silicon wafer eccentrically at a distance of 5 mm away from the center of the wafer along the  $y$ -axis. Otherwise, the optical setup in this experiment was the same one used in the previous experiment. A  $20 \times 20$  sub-image size with 10 pixel overlap was also used here to correlate the images in the deformed and undeformed states to get displacements  $\delta_{y,x}$ .

The two orthogonal surface slope contours,  $\frac{\partial w}{\partial x}$  and  $\frac{\partial w}{\partial y}$  for each of these imposed displacements are shown in Figure 3.8. The contours of  $\frac{\partial w}{\partial r}$  are also provided. As in the central loading case, all the contours are plotted with increments of 50 and 100 micro-radians for the  $4 \mu\text{m}$  and  $10 \mu\text{m}$  cases, respectively. It can be observed that the contours of  $\frac{\partial w}{\partial x}$  and  $\frac{\partial w}{\partial y}$  are symmetric in terms of magnitude about  $x = 0$ , but asymmetric about  $y = 0$ . Accordingly, the contours of  $\frac{\partial w}{\partial x}$ ,  $\frac{\partial w}{\partial y}$  and  $\frac{\partial w}{\partial r}$  are relatively crowded in the positive  $y$ -direction. The noise at the circular clamped boundary and its vicinity in the figures are attributed to measurement errors in  $r$ -DGS.

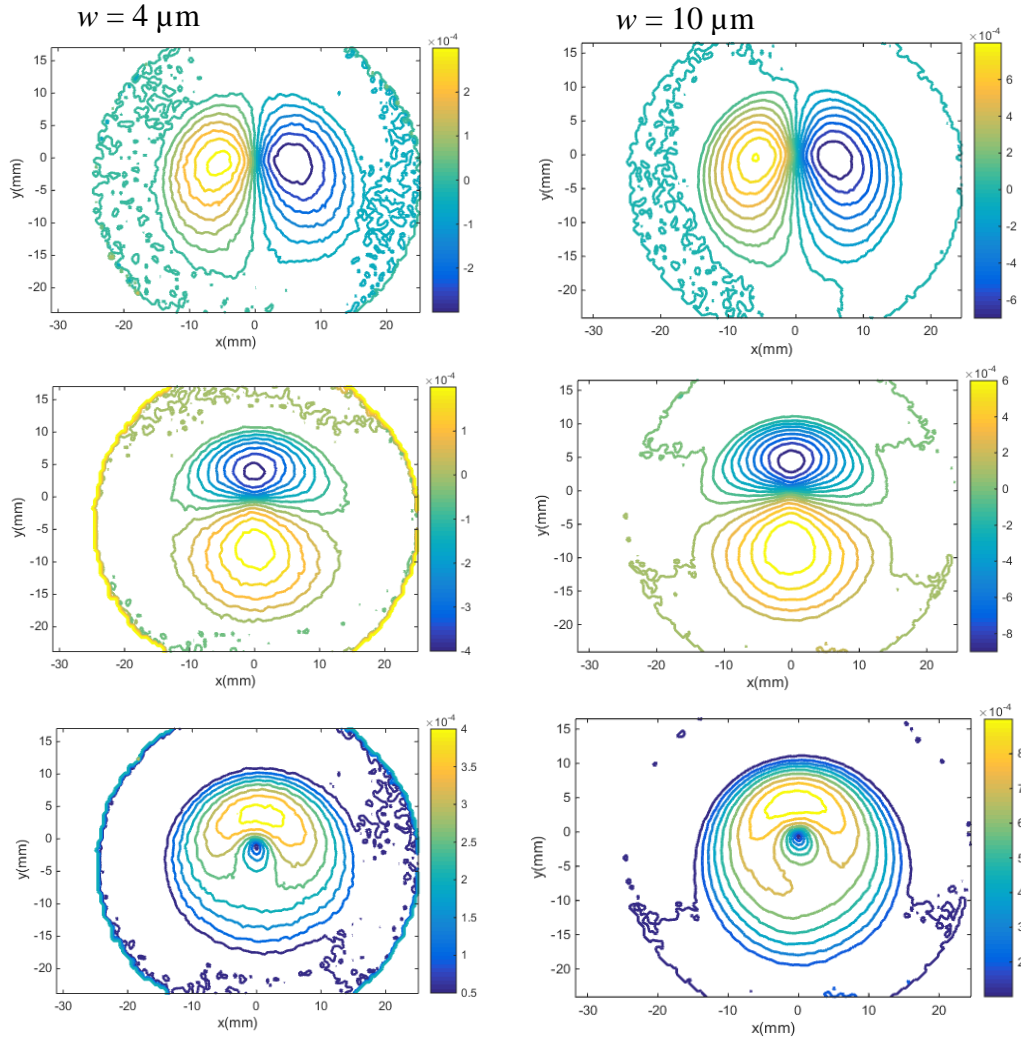


Figure 3.8: Results from  $r$ -DGS for a clamped silicon wafer (30 mm dia., 360  $\mu\text{m}$  thick) subjected to eccentric deflection of 4  $\mu\text{m}$  (left column) and 10  $\mu\text{m}$  (right column). Row 1: contours of  $w_{,x}$ ; Row 2: contours of  $w_{,y}$ ; Row 3: contours of  $w_{,r}$ . Note: (0, 0) is made to coincide with the loading point. Contour increments =  $0.5 \times 10^{-4}$  rad and  $1 \times 10^{-4}$  rad, respectively.

The reconstructed 3D surface calculated from HFLI is plotted in Figure 3.9(a). Figure 3.9(b) shows the corresponding contours of out-of-plane displacement ( $w$ ) at 0.5  $\mu\text{m}$  increments. These plots demonstrate that the shape of the reconstructed surface match the reality of the experiment. Again, in Figure 3.8 and Figure 3.9, (0, 0) is made to coincide with the loading point. The peak value of the height of the reconstructed 3D surface is approximately 10.53  $\mu\text{m}$ . Based on the elasticity theory for a circular plate loaded by an

eccentric concentrated force [119], the peak value of deflection is  $10.16 \mu\text{m}$ . Further, the location of the theoretical peak value is at  $(x = 0, y = -0.8)$  or  $0.8 \text{ mm}$  away from the loading point along the  $-y$  direction. Compared with this theoretical value, the reconstruction error is an acceptable  $3.6\%$ . The sources of errors are the same as the ones discussed in the previous experiment. Evidently, the reconstructed surface shows asymmetry as expected along with an obvious tilt due to higher stresses and deformation suffered by the epoxy adhesive layer along the boundary close to the loading point relative to the far away edges. That is, the reconstructed shape is tilted towards the positive  $y$ -direction, in agreement with the load point eccentricity relative to the center of the wafer.

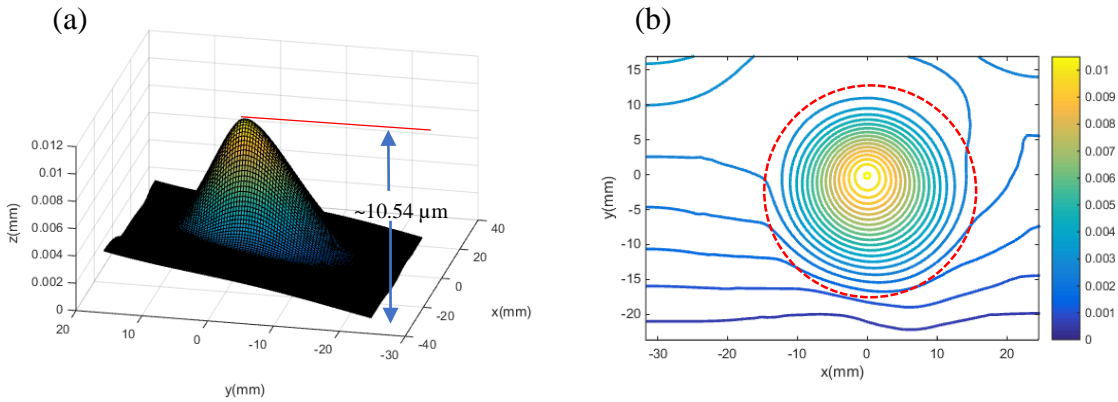


Figure 3.9: Surface topography calculated via 2D integration using surface slope data and HFLI method: (a) reconstructed 3D surface, (b) out-of-plane displacement ( $w$ ) contours ( $0.5 \mu\text{m}$  increments). Note:  $(0, 0)$  is made to coincide with the loading point; red circle is the circular aperture of the steel washer.

### 3.5 Dynamic mode-I crack propagation in transparent PMMA

The previous two experiments demonstrated the feasibility of coupling  $r$ -DGS methodology with HFLI approach for reconstructing surface profile due to mechanical deformation. Next, the method was extended to transmission-mode DGS (or,  $t$ -DGS) to

extract stress field data from measured orthogonal stress gradient data to study dynamic crack propagation in brittle polymers such as PMMA. First, the dynamic crack growth in PMMA sheets was studied using  $t$ -DGS technique in conjunction with ultrahigh-speed digital photography. The schematic of the experimental setup employed is shown in Figure 3.10. A Hopkinson pressure bar (a 25 mm dia., 1.8 m long 7075-T6 aluminum bar) was used for subjecting a pre-notched ( $40^\circ$  V-notch) PMMA specimen to wedge-loading using a gas-gun to launch a striker bar (a 25 mm dia. and 225 mm long aluminum rod). A Cordin 550 ultrahigh-speed digital camera with 32 independent  $1000 \times 1000$  pixels sensors was used for recording the speckle images during the dynamic fracture event. The specimen was at a distance of approximately 850 mm in front of the camera. A target plate decorated with random black and white speckles was placed behind the specimen at a distance ( $\Delta$ ) 29.3 mm away from the mid-plane of the specimen. The region-of-interest in this study was in the crack tip neighborhood (52 mm x 52 mm).

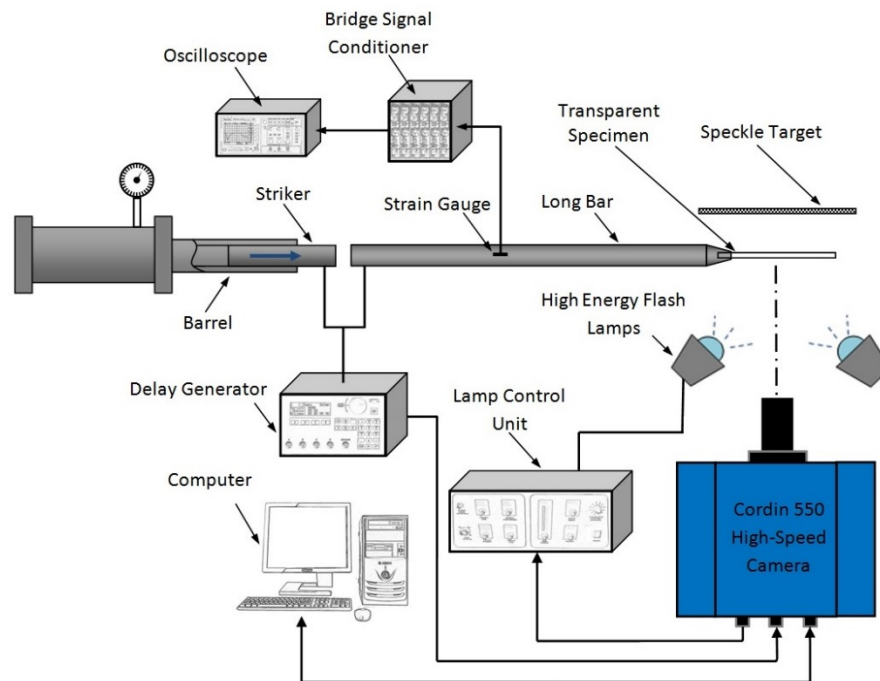


Figure 3.10: Schematic of the experimental setup used for dynamic fracture study.

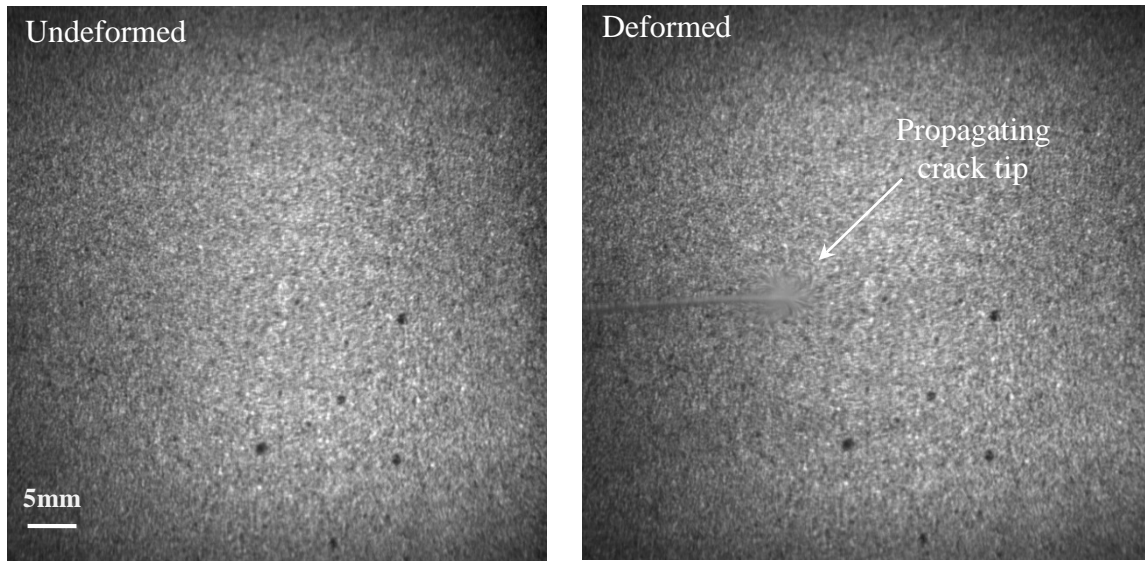
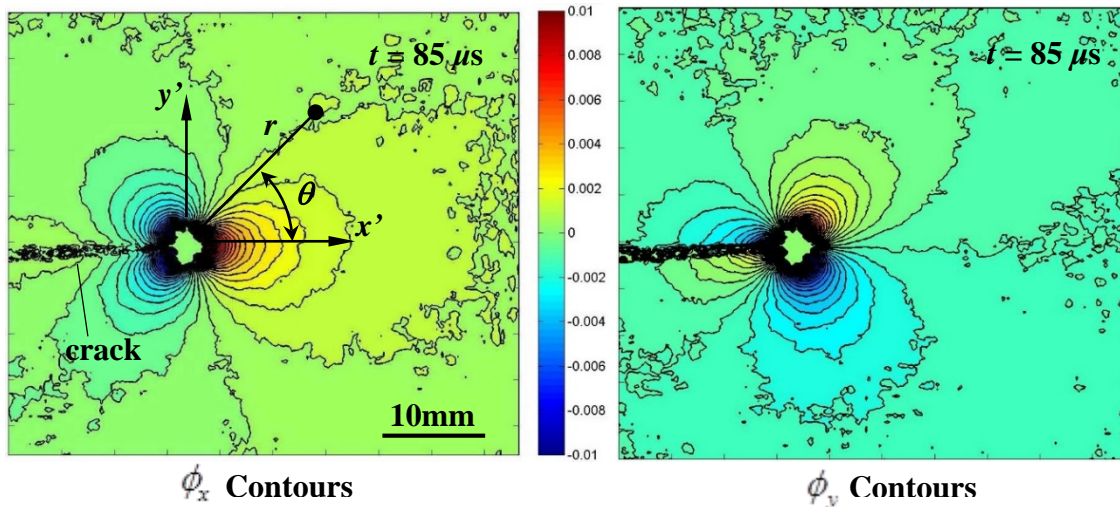


Figure 3.11: Speckle images in the undeformed (left) and deformed (right) states recorded by the Cordin 550 high-speed camera through the PMMA specimen.

A pair of heavy dots (Figure 3.11) marked on the target plate were used to relate the dimension on the image to the actual specimen/target dimensions. Prior to loading the specimen, a set of 32 speckle images were recorded at 200,000 frames per second through the specimen in its undeformed state. Next, without altering any of the camera settings, the specimen was dynamically loaded by impacting the long-bar with the striker bar (striker velocity  $\sim 14$  m/sec). The impact event triggered recording of a second set of 32 images in the deformed state at the same framing rate. Thus, a total of 32 pairs of images in the deformed and undeformed (reference) states were recorded at 5  $\mu$ s intervals between successive images. Two representative speckle images in the region-of-interest, one in the undeformed state and the other in the deformed state are shown in Figure 3.11(a) and (b), respectively. The speckle pattern shown in Figure 3.11(b) corresponds to a time instant 95  $\mu$ sec after crack initiation at the initial notch tip. It can be seen that the speckles are

noticeably distorted in the near vicinity of the propagating crack tip (in the deformed image) whereas they seem largely unaffected in the far-field. The corresponding image pairs from each sensor were correlated separately. Further details of the experiment are previously reported by Sundaram and Tippur [120].

During image correlation<sup>1</sup>, each image was segmented into  $25 \times 25$  pixels sub-images. An overlap of 20 pixels (i.e., a step size of 5 pixels) was used during analysis. This resulted in  $194 \times 194$  matrix of data points in the region of interest for each of the two orthogonal displacement fields. The corresponding angular deflections of light rays were subsequently determined using the known distance  $\Delta$  between the specimen and the target planes. Figure 3.12 shows the angular deflection plots at three select time instants. The crack velocity history for such a crack growth has been previously reported in [120].



<sup>1</sup>The image correlation was carried out in r-DGS also using the image analysis software ARAMIS®.

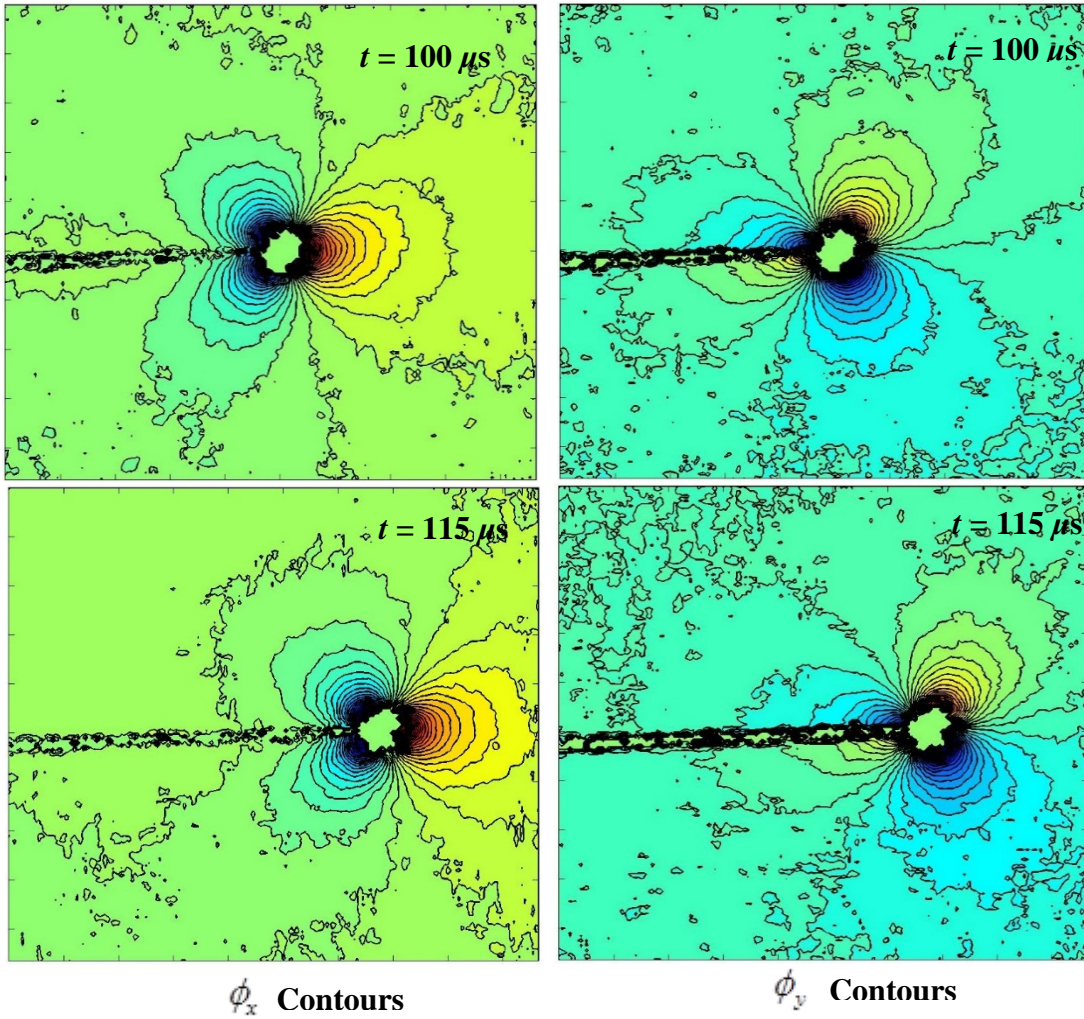


Figure 3.12: Angular deflection contour plots (contour interval =  $5 \times 10^{-4}$  rad) proportional to stress gradients of  $(\sigma_x + \sigma_y)$  in the x- and y-directions.

Using the angular deflection fields along the  $x$ -direction mode-I and mode-II SIFs were evaluated using an over-deterministic least-squares analysis based on the asymptotic expressions for the measured stress gradients (See [120] for details),

$$\phi_x(t) = C_\sigma B \left[ \begin{array}{l} -\frac{1}{2} r_l^{\frac{3}{2}} \left\{ \begin{array}{l} f(V; C_L; C_S) A_1(t) \cos\left(\frac{3\theta_l}{2}\right) \\ + g(V; C_L; C_S) D_1(t) \sin\left(-\frac{3\theta_l}{2}\right) \end{array} \right\} \\ + \sum_{N=2}^{\infty} \left\{ \begin{array}{l} A_N(t) \left(\frac{N}{2}-1\right) r_l^{\left(\frac{N}{2}-2\right)} \cos\left(\left(\frac{N}{2}-2\right)\theta_l\right) \\ + D_N(t) \left(\frac{N}{2}-1\right) r_l^{\left(\frac{N}{2}-2\right)} \sin\left(\left(\frac{N}{2}-2\right)\theta_l\right) \end{array} \right\} \end{array} \right] \quad (3.12)$$

where  $f$  and  $g$  denote functions of instantaneous crack velocity, and  $(r_l, \theta_l)$  denote the contracted crack tip polar coordinates for a growing crack,  $C_\sigma$  is the elasto-optic constant of the material ( $1.08 \times 10^{-10} \text{ m}^2/\text{N}$ ), and  $B$  is its initial thickness. Further,  $(r_l, \theta_l)$  can be expressed in the local Cartesian coordinates  $(x', y')$  as,  $r_l = \left\{ (x')^2 + \alpha_L^2 (y')^2 \right\}^{1/2}$  and  $\theta_l = \tan^{-1} \left( \frac{\alpha_L y'}{x'} \right)$ . The coefficients of  $A_1(t)$  and  $D_1(t)$  in the asymptotic series are related to the mode-I and mode-II Stress Intensity Factors (SIF)  $K_I(t)$  and  $K_{II}(t)$ , respectively, as  $A_1(t) = K_I(t) \sqrt{2/\pi}$  and  $D_1(t) = K_{II}(t) \sqrt{2/\pi}$ . The functions  $f$  and  $g$  are [120],

$$\begin{aligned} f(V; C_L, C_S) &= \left( \frac{1+\nu}{1-\nu} \right) \frac{(1+\alpha_S^2)(1-\alpha_L^2)}{4\alpha_L\alpha_S - (1+\alpha_S^2)^2}, \\ g(V; C_L, C_S) &= \left( \frac{1+\nu}{1-\nu} \right) \frac{2\alpha_S(1-\alpha_L^2)}{4\alpha_L\alpha_S - (1+\alpha_S^2)^2} \end{aligned} \quad (3.13)$$

where  $\alpha_L = \left[ 1 - \frac{\rho(1-\nu)}{2\mu} V^2 \right]^{\frac{1}{2}}$  and  $\alpha_S = \left[ 1 - \frac{\rho}{\mu} V^2 \right]^{\frac{1}{2}}$  for plane stress. Data in the region  $(0.25 < r/B < 0.75)$  and  $(-135^\circ < \theta < 135^\circ)$  near the crack tip was used for analysis. Figure 3.13 shows the plot of SIF history evaluated. As this is a mode-I crack growth,  $K_{II}$  is

expected to be relatively small if not zero. Further, it can be seen that the  $K_I$  remains approximately same throughout the window of observation.

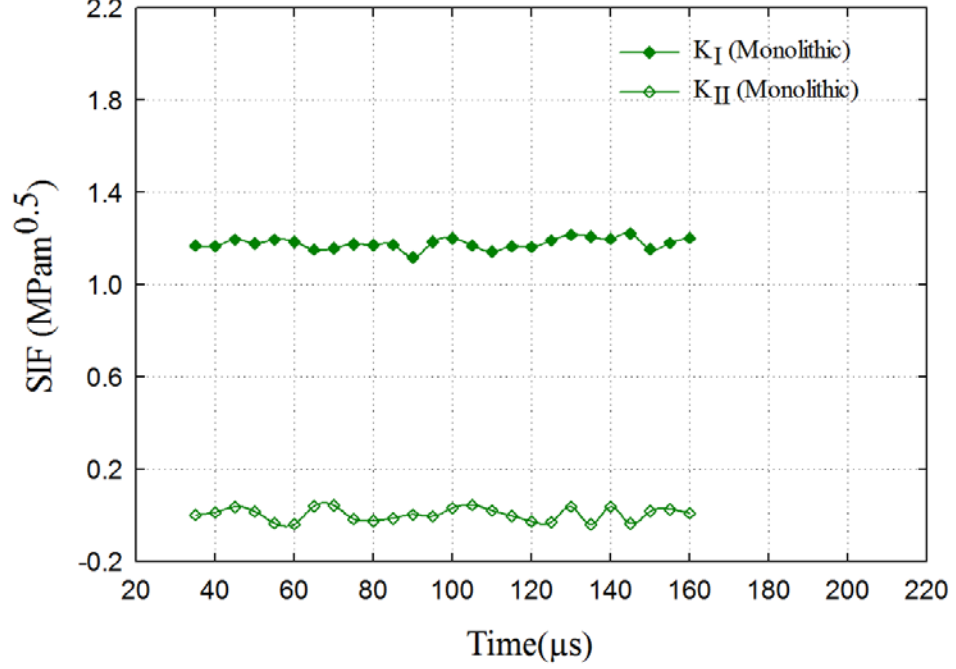


Figure 3.13: Mode-I and II SIFs for a dynamically growing crack in a monolithic PMMA.

Using the SIFs evaluated from the stress gradient fields, the  $(\sigma_{xx} + \sigma_{yy})$  fields around the moving crack tip were obtained using the mode-I  $K$ -dominant expression for stresses as [121],

$$(\sigma_{xx} + \sigma_{yy}) = \frac{K_I(t)}{\sqrt{2\pi r}} f(\theta = 0, V), \quad (3.14)$$

where  $V$  is the crack velocity,

$$f(\theta; V) = \frac{1}{D} \frac{2\alpha_L^2(1+\alpha_S^2)}{\sqrt{\gamma_L}} \cos\left(\frac{\theta_L}{2}\right), \quad D = 4\alpha_S\alpha_L - (1+\alpha_S^2)^2, \quad \alpha_{S:L} = \sqrt{1 - \left(\frac{V}{C_{S:L}}\right)^2},$$

$$\gamma_{S:L} = \sqrt{1 - \left( \frac{V \sin \theta}{C_{S:L}} \right)^2}, \quad \tan \theta_{S:L} = \alpha_{S:L} \tan \theta \quad \text{and} \quad C_{S:L} \text{ denote the shear and longitudinal}$$

wave speeds of the material. Contour plots of constant  $(\sigma_{xx} + \sigma_{yy})$  for a time instant 100  $\mu\text{sec}$  after crack initiation are shown in Figure 3.14(a).

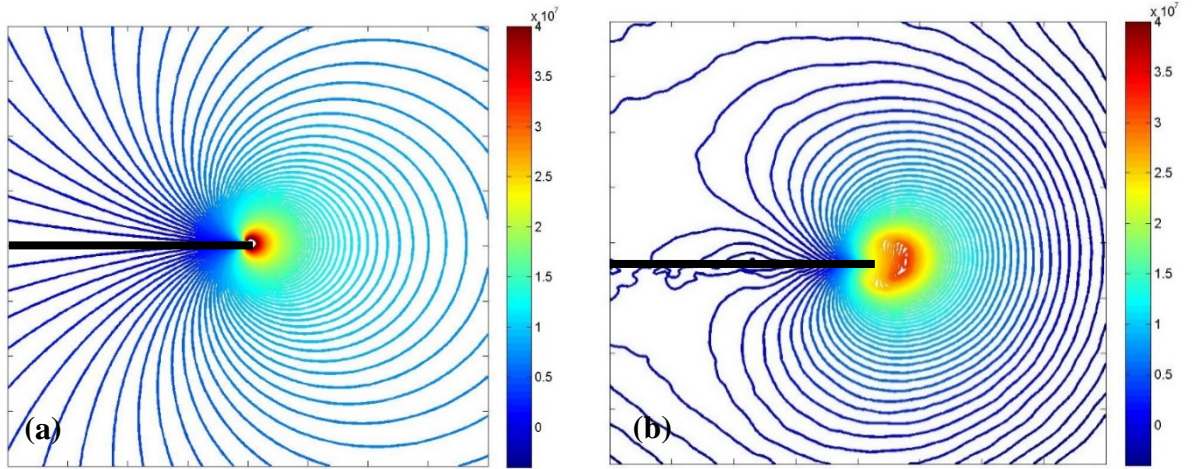


Figure 3.14: Stress fields of  $(\sigma_{xx} + \sigma_{yy})$  (contour interval= 0.75 MPa) obtained from a) using  $K_I$  and  $K_{II}$  measured from the DGS fields along with analytical expression for stress fields and b) using HFLI method applied to measured stress gradients. The black horizontal line represents the growing crack faces.

The  $(\sigma_{xx} + \sigma_{yy})$  fields around the moving crack tip were also obtained by integrating the measured orthogonal stress gradient fields and HFLI method. Figure 3.14(b) shows the  $(\sigma_{xx} + \sigma_{yy})$  fields from HFLI algorithm at a select time instant of 100  $\mu\text{sec}$  during dynamic crack growth corresponding to the stress gradient contours shown in Figure 3.14(a). It can be seen that both the stress fields have qualitative similarities near the crack tip vicinity. However, it should be emphasized that the reconstructed stresses, unlike the theoretical counterpart, encompass all the far-field effects (or, the higher order terms). In light of this, the contours do deviate both qualitatively and quantitatively from the ones

shown in Figure 3.14(a) based on  $K$ -dominant (one-term description) in Eq. (3.14). The 3D surface plot of reconstructed stress around the crack tip is shown in Figure 3.15 that indicates severe stress amplification in the immediate crack tip vicinity.

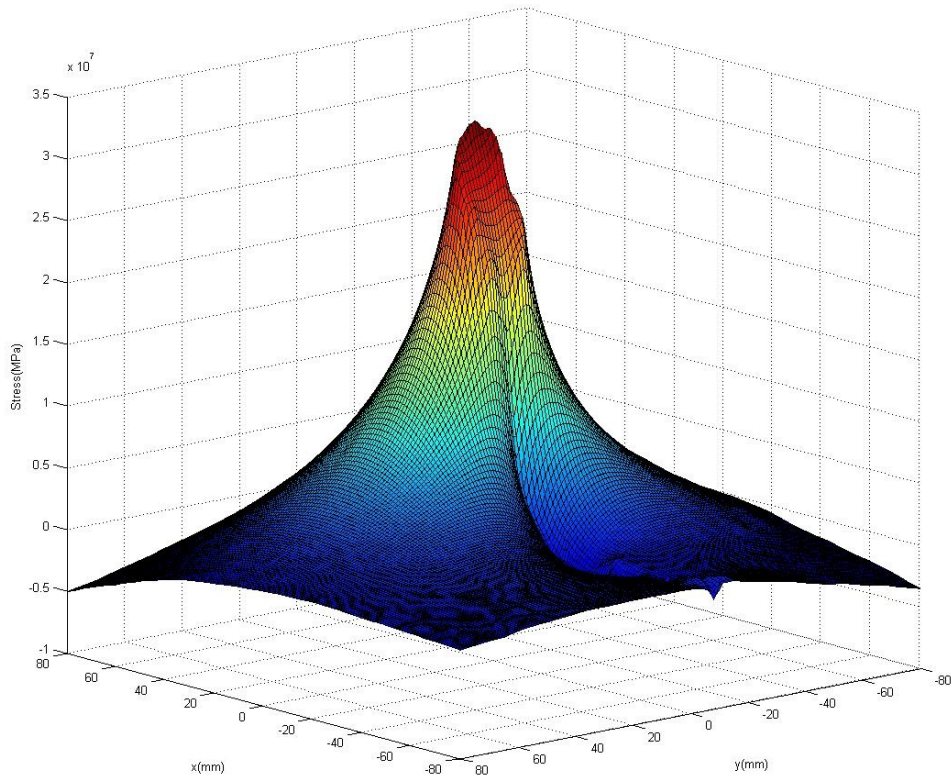


Figure 3.15: The 3D surface plot of stress ( $\sigma_{xx} + \sigma_{yy}$ ) around a moving crack tip in PMMA reconstructed using HFLI.

To compare the  $(\sigma_{xx} + \sigma_{yy})$  fields obtained from these two methods more effectively,  $(\sigma_{xx} + \sigma_{yy})$  values were evaluated at select directions namely  $(r, \theta = 0^\circ)$  and  $(r, \theta = 45^\circ)$  relative to the crack tip ( $\theta = 0^\circ$  denotes crack growth direction) are plotted in Figure 3.16. We can see a good agreement between the two plots in the region  $(0.25 < r/B$

< 0.75) where the data was selected for performing the least-squares analysis. For  $r/B > 0.75$  the  $K$ -dominance is lost and for  $r/B < 0.25$  there is significant stress triaxiality whereas contours based on Eq. (3.14) are based on 2D (plane stress) assumptions.

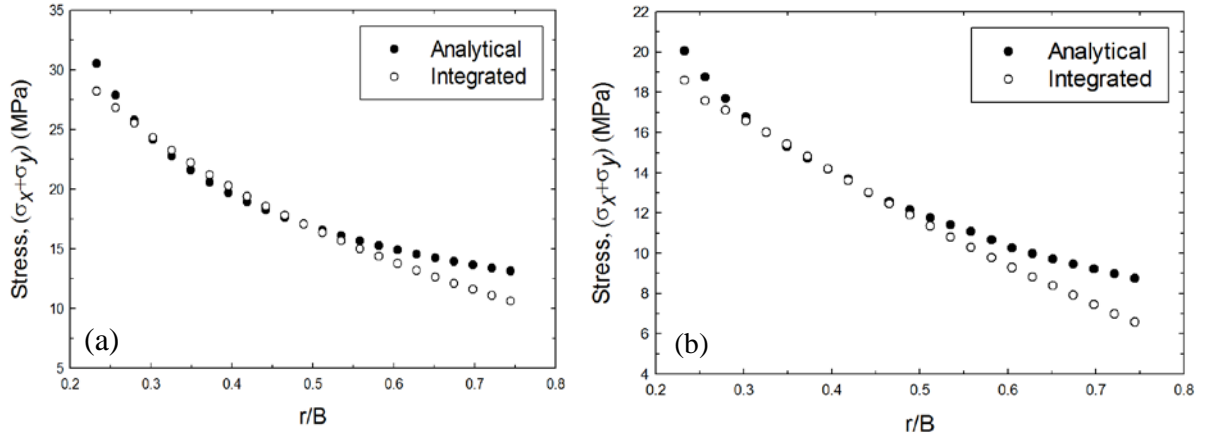


Figure 3.16: The plot of stress ( $\sigma_{xx} + \sigma_{yy}$ ) evaluated from integration and by using  $K$ -dominant equations from the extracted SIFs for a direction of (a)  $0^\circ$ , and (b)  $45^\circ$  from the crack growth direction.

## **Chapter 4. Accuracy of Measured Deformations from *r*-DGS coupled with HFLI Algorithm**

In this chapter, the accuracy of smallest measurable out-of-plane deformation using DGS when used in conjunction with HFLI algorithm is explored. Both quasi-static and dynamic experiments are considered separately. In both experiments, two images in two time-lapsed, undeformed states are correlated to explore the smallest out-of-plane deformation.

### **4.1 Ultrahigh-speed Measurements**

The accuracy of measurements was assessed using an experiment involving the backside impact of a soda lime glass plate monitored using *r*-DGS in conjunction with ultrahigh-speed digital photography using a single sensor camera. (It should be emphasized that performing the same experiment without subjecting the specimen to impact is sufficient for accuracy assessment.) A 152.4 mm × 101.6 mm rectangular glass specimen of 4.6 mm thickness was used in the experiment. One of the two 152.4 × 101.6 mm<sup>2</sup> faces of the specimen was deposited with a thin aluminum using vapor deposition to make the surface reflective.

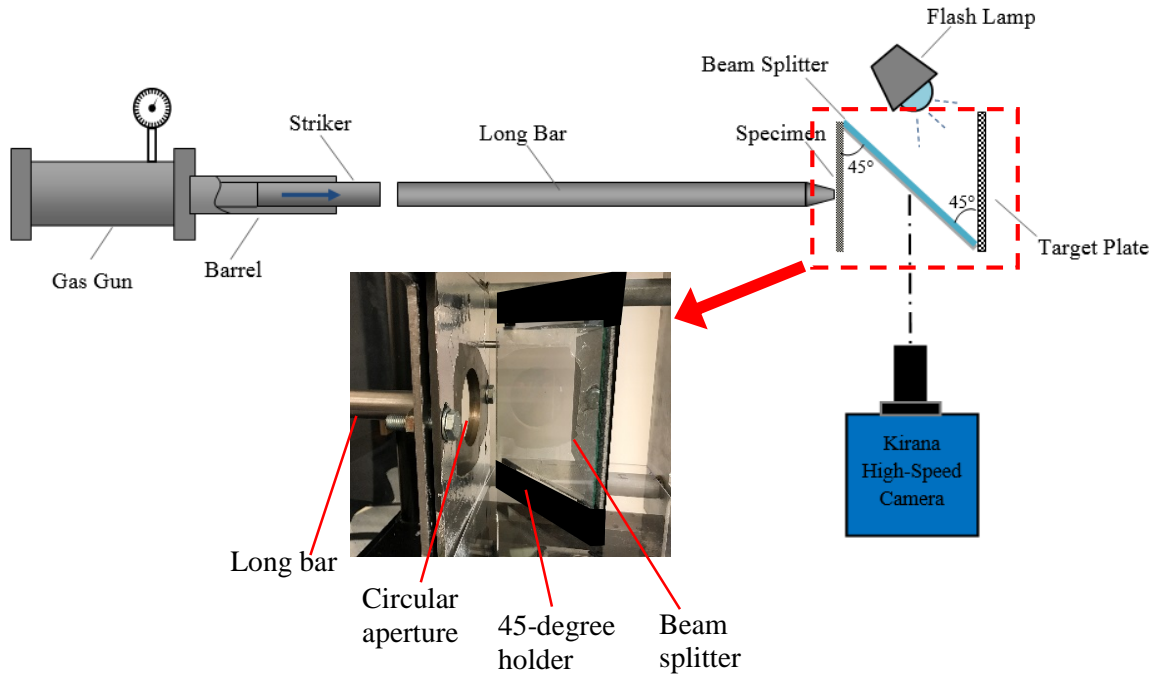


Figure 4.1: Schematic of the experimental setup for dynamic plate impact study. Inset shows the close-up of the optical arrangement.

The schematic of the experimental setup used is shown in Figure 4.1. A modified Hopkinson pressure bar (or simply a ‘long-bar’) was used for loading the uncoated backside of the specimen. The long-bar was a 1.83 m steel rod of 25.4 mm diameter with a tapered end of 3 mm diameter impacting the backside of the specimen. A 305 mm long, 25.4 mm diameter steel striker placed in the barrel of a gas-gun was co-axially aligned with the long-bar at the start of the experiment. The striker was launched towards the long-bar at a velocity of  $\sim 2.5$  m/s during the tests. The specimen was clamped using a fixture containing two steel plates with circular apertures, see Figure 4.1. The 63.5 mm in diameter apertures were coaxial allowing optical observations and measurements in this region. The loading point was chosen to be at the center of the aperture. A beam splitter and the speckle target plate were placed in a 45° holder, housed within the cage of the specimen holding fixture, so that the speckle pattern on the target plate was viewed via the reflective face of

the specimen. The deformations on the front face of the specimen were photographed by a Kirana-05M ultrahigh-speed digital camera assisted by a pair of high energy flash lamps (Cordin mode 659) to illuminate the target. This high-speed camera is a single sensor camera, capable of recording 180 10-bit images at a maximum rate of up to 5 million frames per second at a spatial resolution of  $924 \times 768$  pixels per image. The camera and the two flash lamps were triggered using a variable delay circuit relative to the striker impacting the long-bar and the duration required for the stress waves to travel the length of 1.83 m along the steel rod.

A Nikon 70 – 300 mm focal length macro zoom lens with an adjustable bellows was used with the camera to record the images. A good exposure and focus were achieved by stopping down the lens aperture to F#8 after focusing. The distance between the specimen and the camera lens plane (L) was ~950 mm and the one between the specimen mid-plane and the target plane ( $\Delta$ ) was 102 mm. A total of 180 images, some in the undeformed and others in the deformed states were recorded at 1.25 million frames per second (inter frame period  $0.8 \mu s$ ) in each experiment. When the long-bar was impacted by the striker, a compressive stress wave was generated that propagated along the long-bar. The fixture used to house the specimen was mounted on a pair of rails so that it can travel away from the long-bar when the specimen was loaded by the stress waves. However, the inertia of the fixture was substantially higher than that of the specimen and hence it took several milliseconds for the fixture to move away from the long-bar whereas, and the images corresponding to specimen deformations were recorded over approx. 50 microseconds. One undeformed image right before the start of deformation was selected as the reference image ( $t = 0 \mu s$ ). Subsequent deformed images were correlated with the

reference image by using ARAMIS<sup>®</sup> image analysis software. During correlation, a sub-image size of  $25 \times 25$  pixels (1 pixel = 83.68  $\mu\text{m}$ ) with 15 pixels overlap was used to extract the local displacements  $\delta_{y;x}$  in the region-of-interest using 2D DIC.

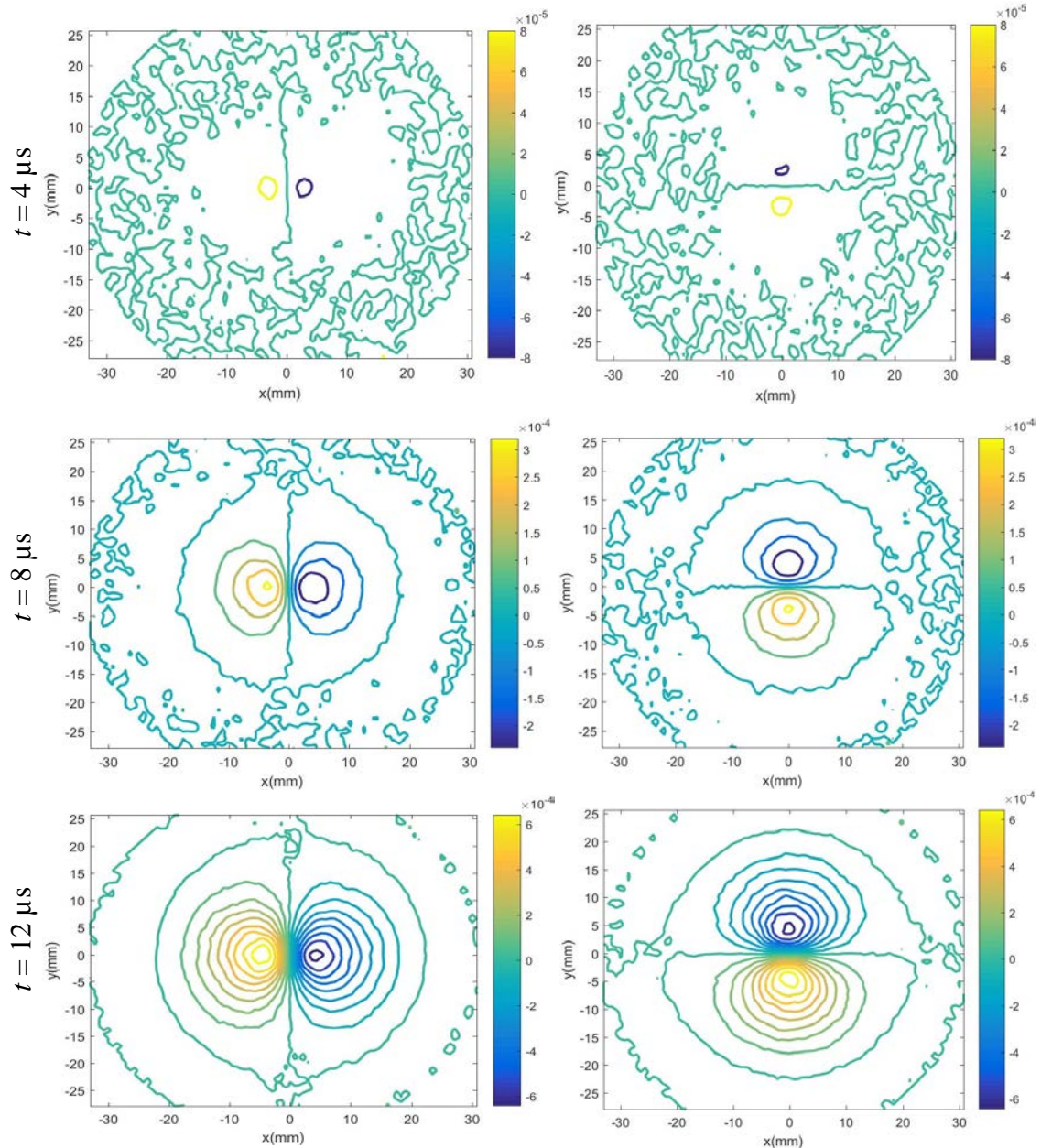


Figure 4.2: Evolution of surface slope  $w_{,x}$  (left column) and  $w_{,y}$  (right column) contours for a clamped glass plate subjected to central impact. Note: (0, 0) is made to coincide with the impact point. Contour increments =  $8 \times 10^{-5}$  rad.

The time-resolved orthogonal surface slope contours of  $\frac{\partial w}{\partial x}$  and  $\frac{\partial w}{\partial y}$  due to transient stress wave propagation in the glass plate are shown in Figure 4.2 at a few select time instants. Once the compressive stress waves from long-bar enter the glass plate, the impact induced longitudinal stress waves radiating from the contact point will propagate along the thickness direction to reach the outer surface of glass plate. Then, they will propagate back (reflected waves) to return to the contact point, selected as the origin in these images. In the early stages of impact, deformations are concentrated close to the center of the plate resulting in small surface slope contours. With the passage of time, the contours get denser and larger with a higher concentration of contours near the contact point. The reconstructed 3D surfaces computed from 2D integration by using surface slope data from  $r$ -DGS in conjunction with HFLI are plotted in Figure 4.3. The corresponding contours of out-of-plane displacements ( $w$ ) at  $0.5 \mu m$  increment are shown in the right column of Figure 4.3. The out-of-plane deformation is approx.  $0.63 \mu m$  at  $t = 4 \mu s$ , which shows that *this method is able to detect sub-micron deformations in glass plates at sub-microsecond intervals*. The circular contours in the right column demonstrate that the reconstructed shape matches well with the reality of the experiment both qualitatively and quantitatively. The cross-sectional out-of-plane deformation along  $x = 0$  at selected time instants is plotted in Figure 4.4. The radius  $R$  here is measured from the impact point,  $(0,0)$ . With the passage of time the out-of-plane deformations expand outwards from the impact point and propagate towards the outer clamped region of the plate.

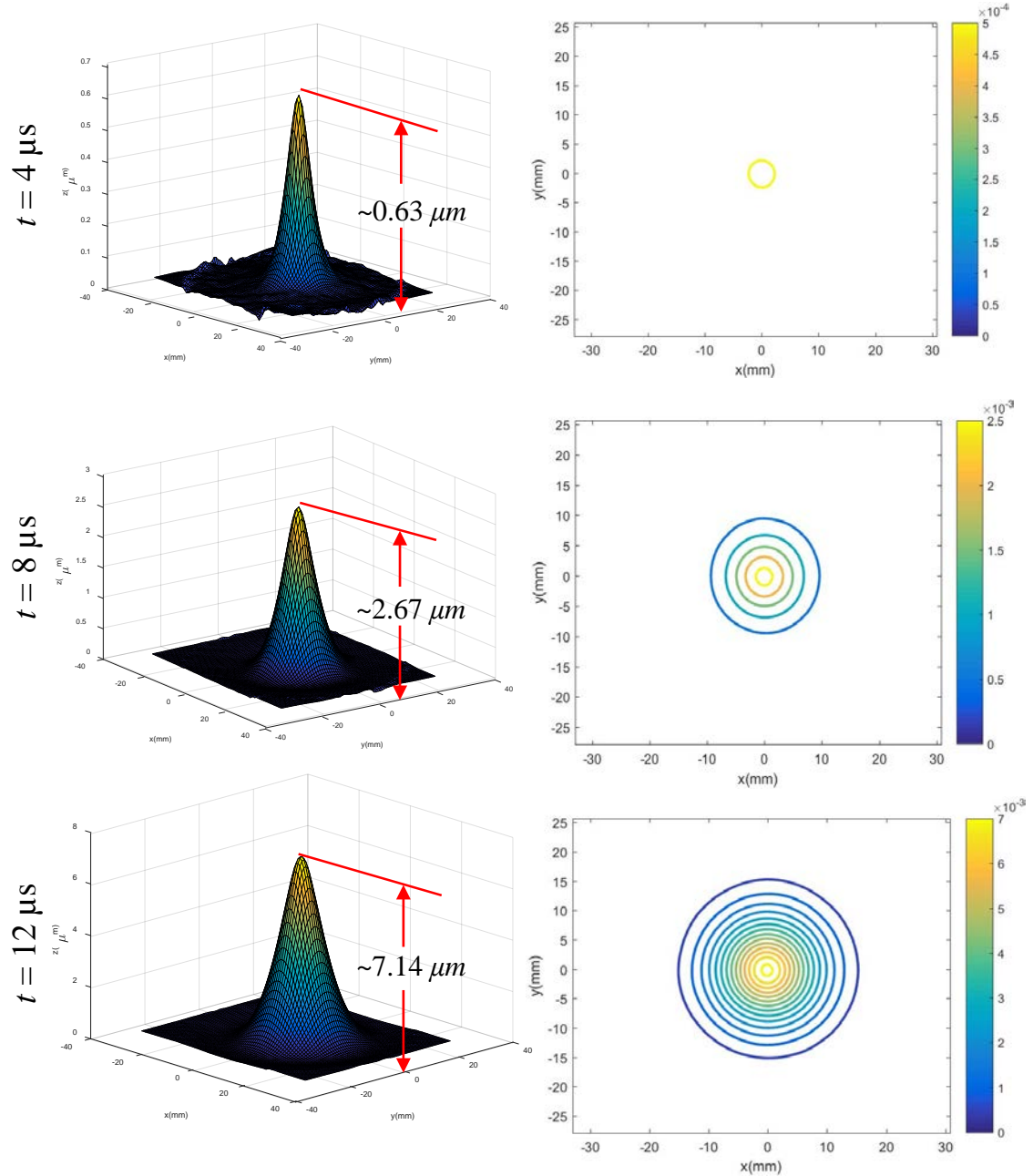


Figure 4.3: Measured surface topography of glass plate at a few select time instants. Left column: reconstructed 3D surface; Right column: out-of-plane displacement ( $w$ ) contours ( $0.5 \mu\text{m}$  increment). Note:  $(0, 0)$  is made to coincide with the impact point.

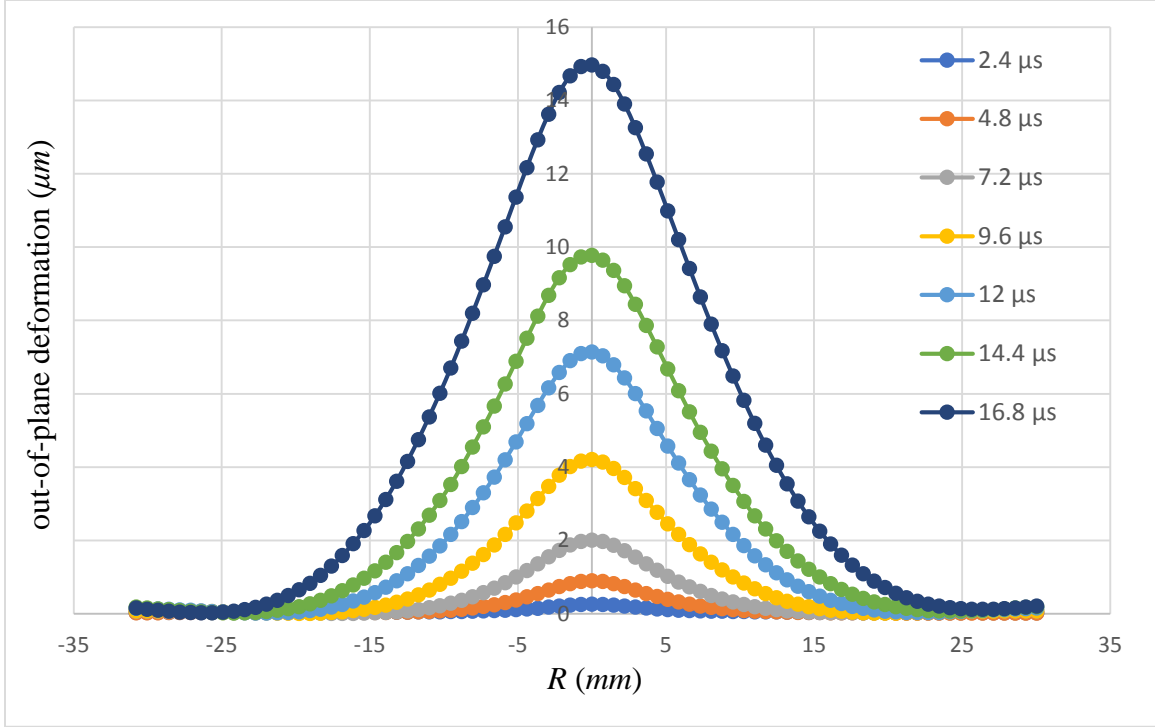


Figure 4.4: The measured profiles for a clamped glass plate subjected to central impact.

## 4.2 Smallest measurable out-of-plane deformation

The previous part states that the application of  $r$ -DGS with HFLI is able to detect sub-micron scale deformations at sub-micro-second intervals during a stress wave loading event over a large, 62.5 mm diameter, field-of-view (FOV). Therefore, it is pertinent that the smallest measurable out-of-plane deformation be quantified to justify the validity of such measurements. Two aspects were considered for validating these observations; one was based on an accepted estimate of the smallest measurable displacement from the prevailing 2D DIC algorithms, and the other was by correlating two speckle images in the undeformed state but recorded by the camera with a time lapse. The latter provided a good estimate of measurement noise due to the combined effect of electronic noise of the

imaging device as well as the measurement environment (e.g., random vibrations, thermal currents in the optical path, etc.).

#### 4.2.1 Method-1

The out-of-plane deformation was integrated from the slope data measured by  $r$ -DGS, and the slope data were obtained by dividing the in-plane displacements of speckles from DIC by the optical lever  $\Delta$  (the distance or the gap between the specimen and target plane). Hence, the smallest out-of-plane deformation was determined by the smallest measurable in-plane displacement from DIC. As noted in Ref. [58] that the smallest measurable in-plane displacement from DIC is  $\sim 1\%$  of one pixel. Accordingly,  $2\%$  of one pixel was assumed here as the smallest measurable in-plane displacement from DIC to assess the accuracy of  $r$ -DGS. In this experiment, 1 pixel corresponded to  $83.68 \mu\text{m}$  on the target plane. Hence, the smallest measurable in-plane displacement,  $\delta$ , was  $83.68 \times 10^{-6} \times 2\% \approx 1.67 \times 10^{-6} \text{m}$ . The corresponding slope was  $\frac{\delta}{\Delta}$ . Thus, the smallest measurable slope =  $(1.67 \times 10^{-6}) \div (119 \times 10^{-3}) \approx 1.4 \times 10^{-5} \text{rad}$ . In this experiment, the sub-image overlap or facet step was 10 pixels. Therefore the distance between two neighboring sub-images,  $d_x$ , was,  $d_x = 10 \times 83.68 \times 10^{-6} = 83.68 \times 10^{-5} \text{m}$ . Then the smallest out-of-plane deformation,  $w$ , based on the trapezoidal rule-of-integration was,  $w = (1.4 \times 10^{-5}) \times (83.68 \times 10^{-5}) \approx 1.17 \times 10^{-8} \text{m}$ , or 11.7 nm.

Under the assumption of plane stress and using Hooke's law, the out-of-plane deformation can be related to in-plane normal stresses as,

$$w \approx -\frac{\nu B}{2E} (\sigma_{xx} + \sigma_{yy}) \quad (4.1)$$

where  $\nu$  is the Poisson's ratio,  $B$  is the undeformed thickness, and  $E$  is the elastic modulus of the specimen. Hence, the smallest measurable  $(\sigma_{xx} + \sigma_{yy})$  can be obtained from the estimated smallest measurable  $w$ . For a 4.6 mm thick soda-lime glass,  $\nu = 0.22$ ,  $E = 70$  GPa, the smallest measurable  $(\sigma_{xx} + \sigma_{yy}) \approx 1.6$  MPa.

#### 4.2.2 Method-2

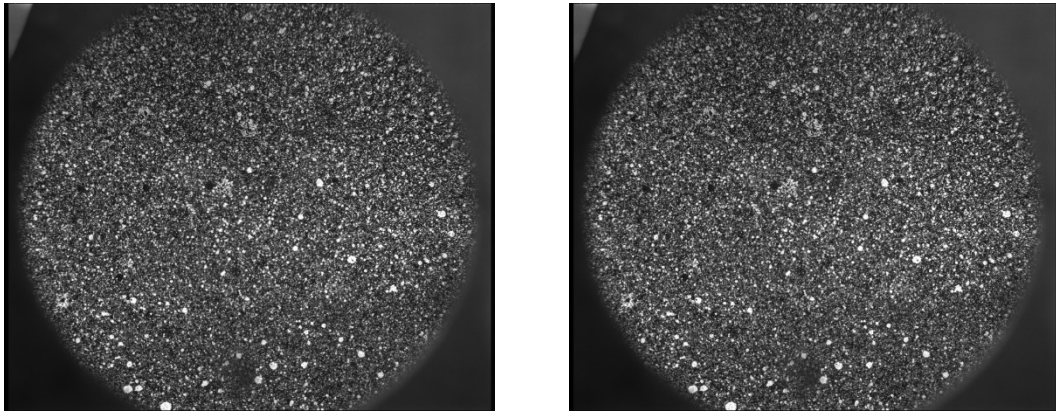


Figure 4.5: Two randomly selected undeformed images.

The second method to check the smallest measurable  $w$  was to correlate two undeformed images recorded with a time lapse. Figure 4.5 shows two randomly selected speckle images, both in the undeformed state. Theoretically, the in-plane displacements obtained by correlating these two undeformed images should be zero. However, due to various experimental deficiencies such as electronic noise of the imaging system, random vibrations, thermal fluctuations and shortcoming of the correlation algorithm, the in-plane speckle displacements extracted will not be zero. The corresponding slopes thus obtained after dividing the in-plane displacements by the optical-lever  $\Delta$  will be affected as well. A pair of surface slope components of angular deflections is shown in Figure 4.6. The contour increments here were intentionally kept very small,  $1 \times 10^{-5}$  rad (eight times smaller than

the one in Figure 4.2), so that the slope contours obtained from noise could be observed. The red dot in Figure 4.6 indicates the impact point or the origin at row 38, column 45 of the processed  $74 \times 88$  data array. It can be observed from Figure 4.6 that the slopes are very small and random in most regions, while they are relatively large along the edges, highlighting the periphery of the specimen/region-of-interest.

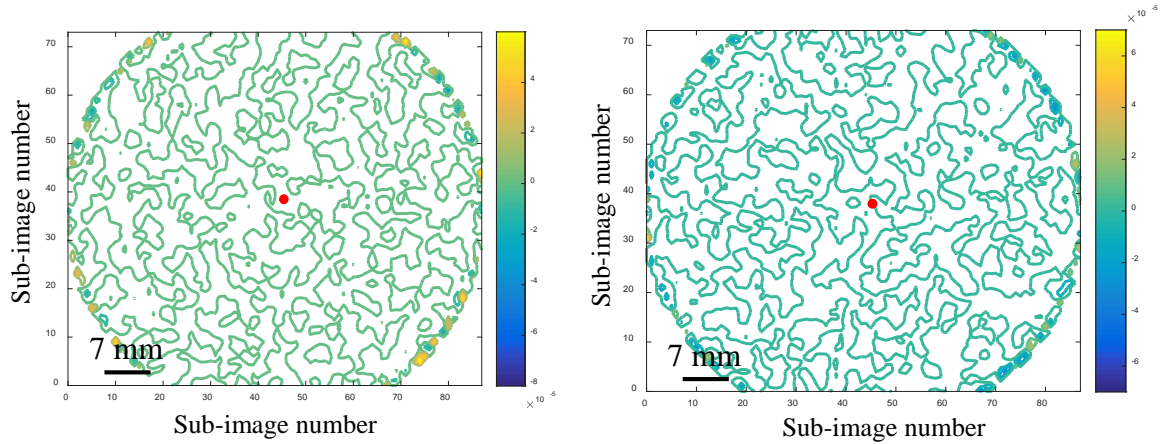


Figure 4.6: Surface slopes  $w_x$  (left column) and  $w_y$  (right column) contours. Contour increments =  $1 \times 10^{-5}$  rad. Impact point: row 38, column 45.

To quantify the noise level better, the horizontal slope along three rows and three columns, which are inclusive of the impact point, are extracted and plotted in Figure 4.7. It should be noted here that five data points at the two ends of the diameter were removed from the plot as they are close to the specimen edges containing much larger noise levels. It can be observed from Figure 4.7 that most of the noise is spread within  $-2 \times 10^{-6}$  to  $2 \times 10^{-6}$  rad range, suggesting that *r*-DGS is capable of detecting slopes in the micro radian range.

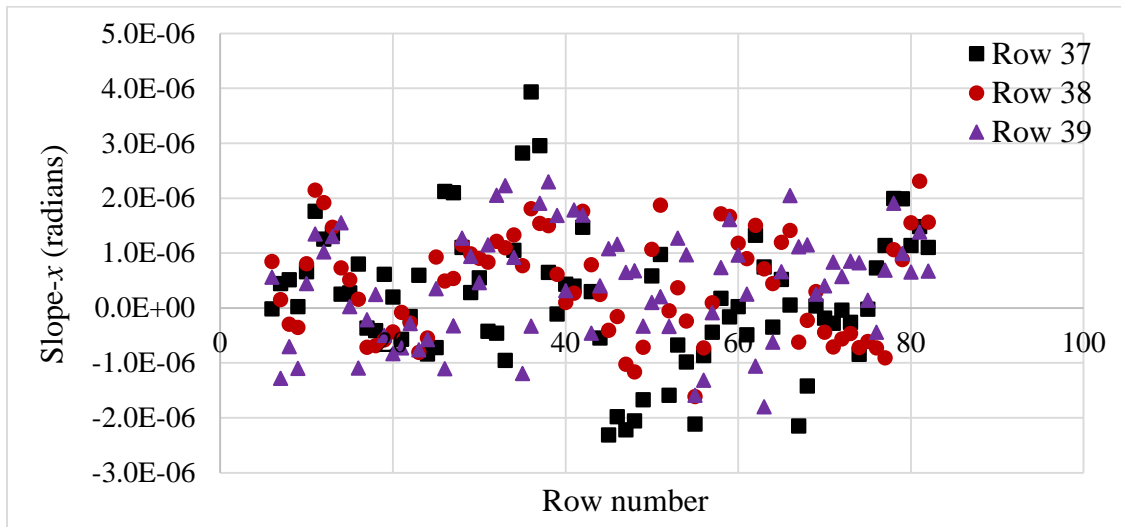
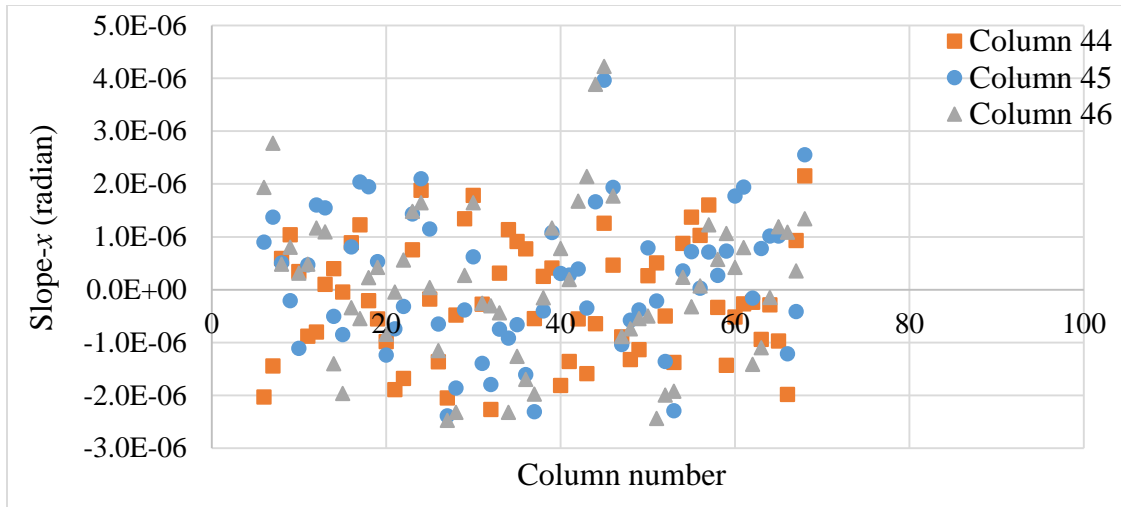


Figure 4.7: Slope in the horizontal direction along three columns (top) and along three rows (bottom).

The surface slopes such as the one shown in Figure 4.6 were integrated using HFLI to obtain the topographic information, see Figure 4.8. The units of the vertical axis in Figure 4.8 are plotted as  $\mu\text{m}$ , whereas the two horizontal axes are in the matrix format which corresponds to the one in Figure 4.6. It can be observed from Figure 4.8 that the reconstructed surface is textured and ‘rough’ in appearance and the noise along the edge is relatively large. Note that the algorithmic error of HFLI is included in the noise. Hence, the surface topography obtained here contains three noise contributors namely, the

experimental apparatus including the imaging system, the speckle correlation and integration algorithms. The out-of-plane deformation along three rows and three columns inclusive of the impact point/origin, are extracted and plotted in Figure 4.9. Once again, five data points at the two ends have been truncated in this plot. It can be observed from Figure 4.9 that the largest noise value,  $w$ , is 7 nm. Based on Hooke's law and plane stress approximation, the corresponding  $(\sigma_{xx} + \sigma_{yy})$  is  $\sim 1$  MPa. These values are in the same range as the ones obtained from Method-1 discussed earlier. Thus, it can be concluded that, under dynamic experimental conditions, with micro-second time lapse period, the smallest measurable  $w$  from  $r$ -DGS with HFLI is approx. 10 nm over a large FOV using the current state-of-the-art imaging equipment.

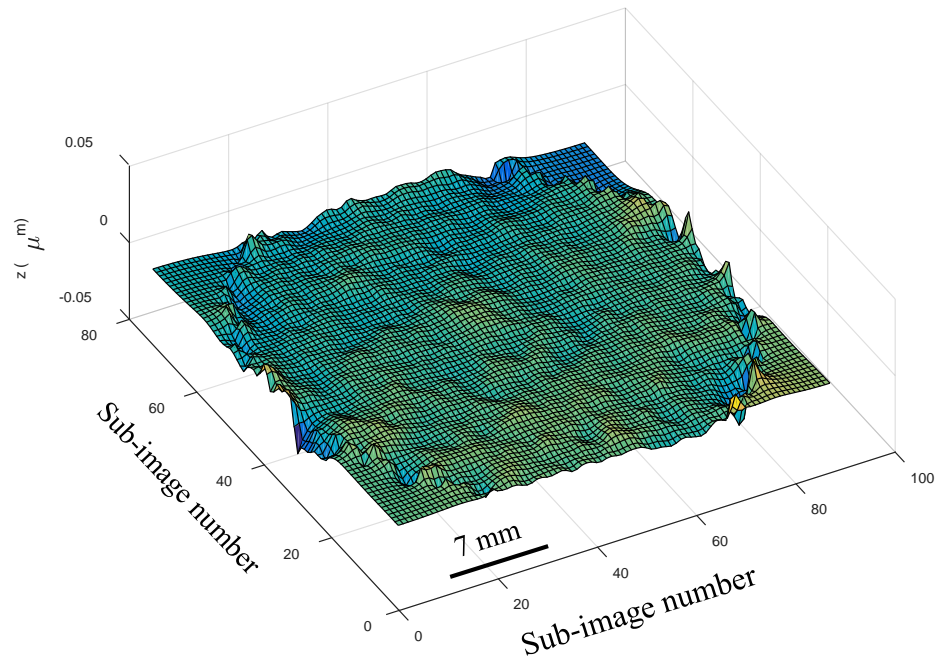


Figure 4.8: Reconstructed surface topography.

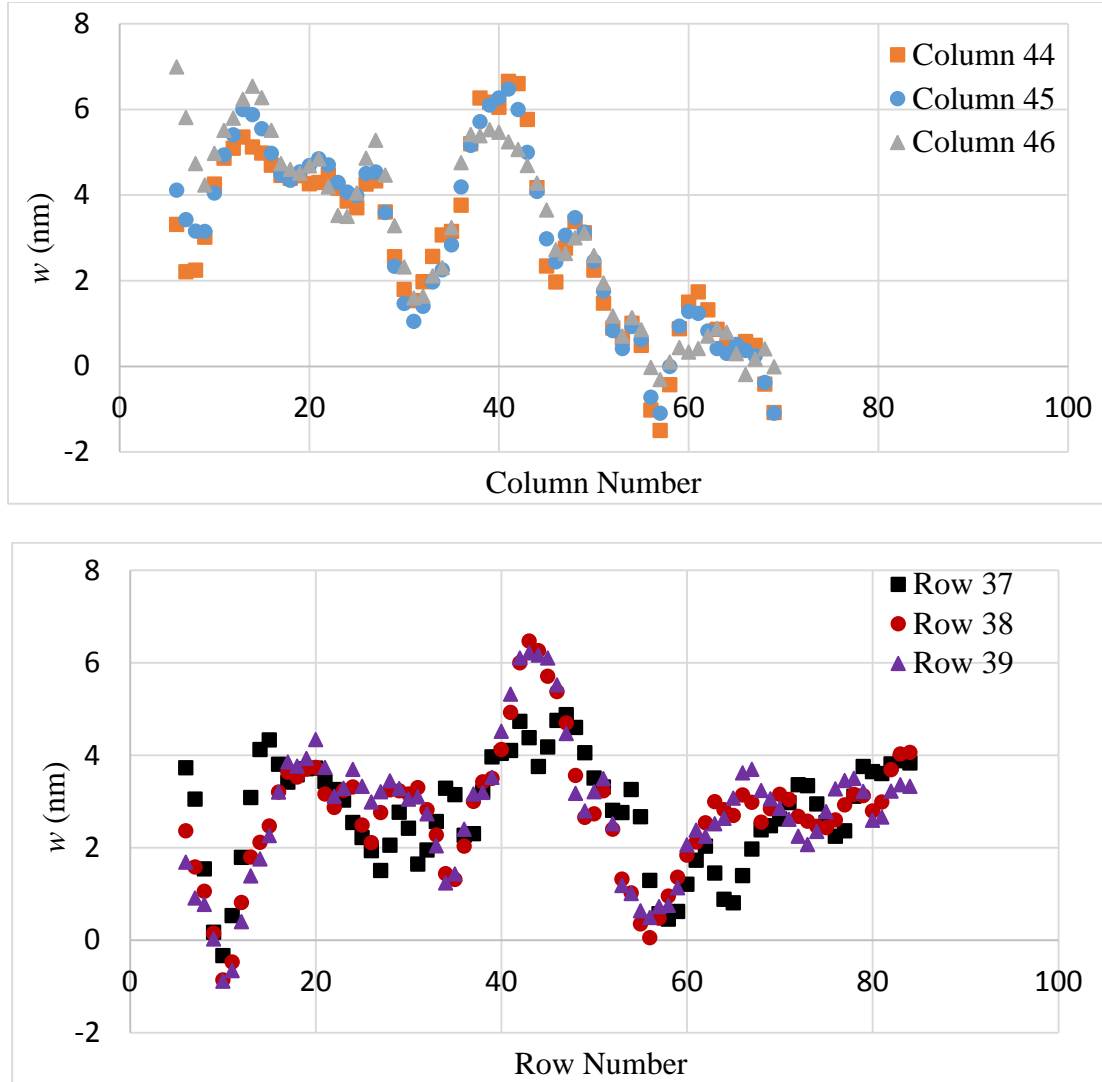


Figure 4.9: Out-of-plane deformation along three columns (top) and three rows (bottom).

### 4.3 Smallest measurable deformation: Quasi-static conditions

Miao *et al.* [117] demonstrated the feasibility of *r*-DGS used in conjunction with HFLI to map surface topography of a ‘clamped’ reflective Si wafer subjected to out-of-plane concentrated load. The work showed that the recovered values deviated approximately 5% of the expected value during static manual loading using a micrometer. However, the work did not dwell into the smallest measurable out-of-plane deformation.

Accordingly, the experiment was repeated to check the smallest measurable out-of-plane deformation under static loading conditions. The experimental details are as follows:

A single-face polished, silicon wafer of diameter of 50.8 mm and 360  $\mu\text{m}$  thickness was used in the experiment. (Note that any reflective specimen should suffice, although an existing setup was utilized for this demonstration.) The unpolished face was bonded to a thick steel washer with a circular aperture of 30 mm using slow curing epoxy. The steel washer was secured in a cylindrical holder. A target plate, decorated with random black and white speckles, was placed at  $90^\circ$  to the silicon wafer. The target plate was illuminated by a cool LED lamp. A beam splitter was placed at  $45^\circ$  to both the silicon wafer and the target plate (see Figure 4.10). The distance ( $\Delta$ ) between the silicon wafer surface and the target plate was 112 mm. A Point Grey digital camera with a Nikon 70-300 mm macro lens and an adjustable bellows was used to record speckles on the target plate through the beam splitter via the reflective silicon wafer surface. The distance between the silicon wafer and the end of lens ( $L$ ) was  $\sim 1445$  mm.

First, the silicon wafer was under no load condition, and the digital speckle images ( $2048 \times 2048$  pixels) were recorded at two different rates - 0.2 frames per second and 5 frames per second. In each experiment, one of the images were selected as the reference image ( $t = 0 \mu\text{s}$ ), and the rest images were correlated with the reference image by using ARAMIS<sup>®</sup> image analysis software. During correlation, a sub-image size of  $25 \times 25$  pixels (1 pixel = 23.16  $\mu\text{m}$ ) with 15 pixels overlap was used to extract the local displacements  $\delta_{y;x}$  in the region-of-interest using 2D DIC.

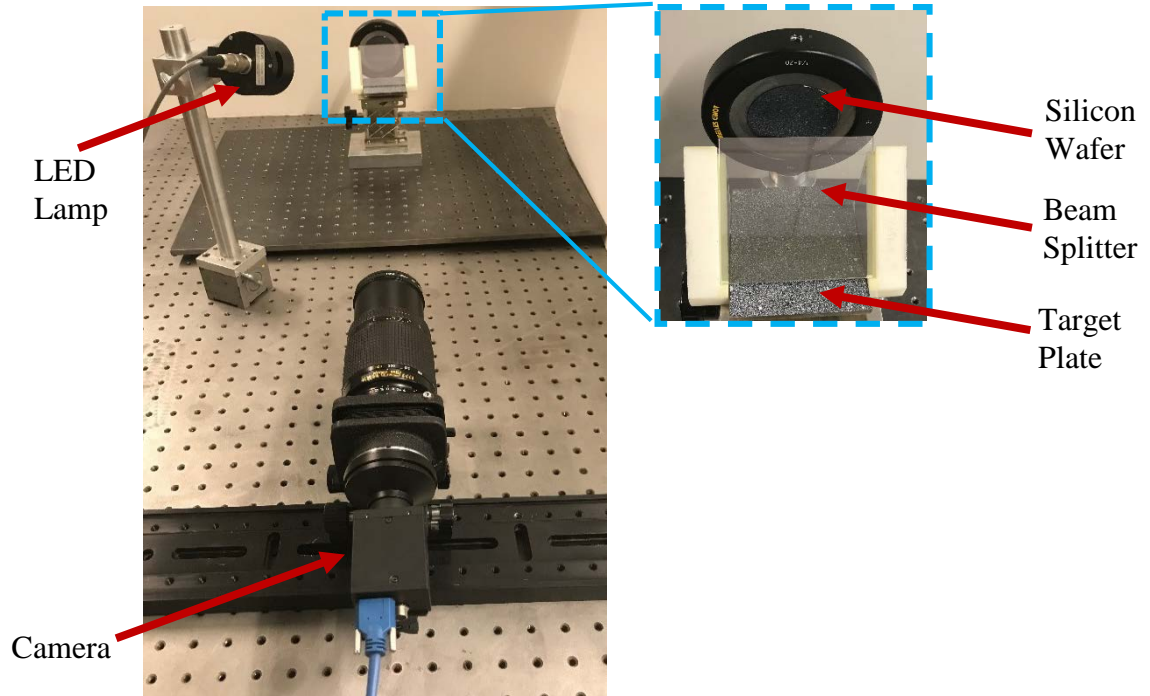


Figure 4.10: Experimental setup for  $r$ -DGS. Inset shows close-up view of the optical arrangement.

The time-resolved orthogonal surface slope contours of  $\frac{\partial w}{\partial x; y}$  are plotted in Figure 4.11 and Figure 4.12, which corresponds to framing rates of 0.2 fps and 5 fps, respectively. During the experiment, the silicon wafer was not subjected to any load at all. Therefore, the surface slopes should be uniformly zero in the region-of-interest. However, due to experimental noise, the non-zero slope values occur throughout the region-of-interest. The contour increments here are  $5 \times 10^{-6}$  rad, as a result, extremely small slopes can be observed. The random slopes are spread in  $-3 \times 10^{-6}$  to  $3 \times 10^{-6}$  rad range.

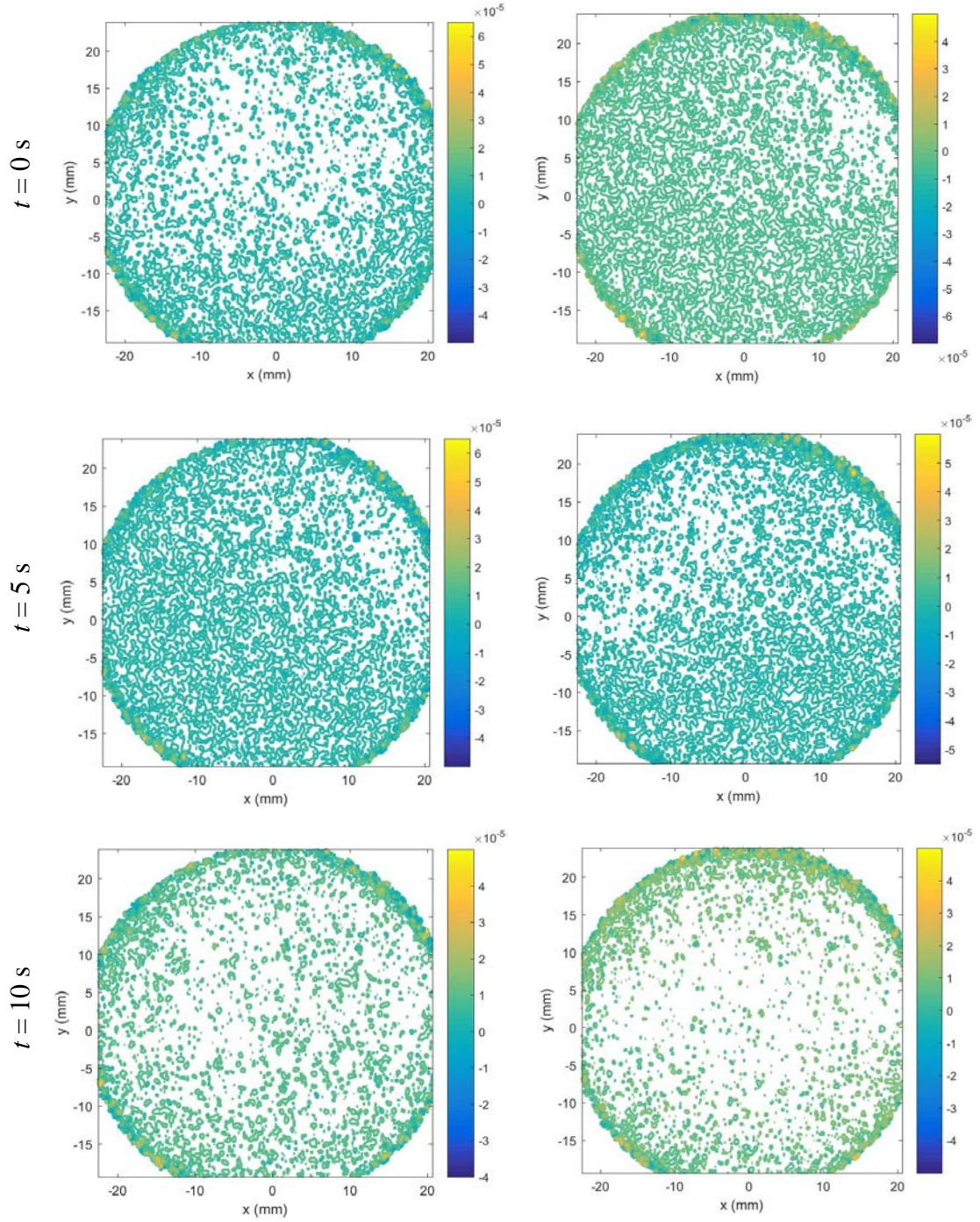


Figure 4.11: Surface slope  $w_x$  (left column) and  $w_y$  (right column) contours for a clamped silicon wafer recorded at 0.2 fps. Note: (0, 0) is made to coincide with the center of silicon wafer. Contour increments =  $5 \times 10^{-6}$  rad.

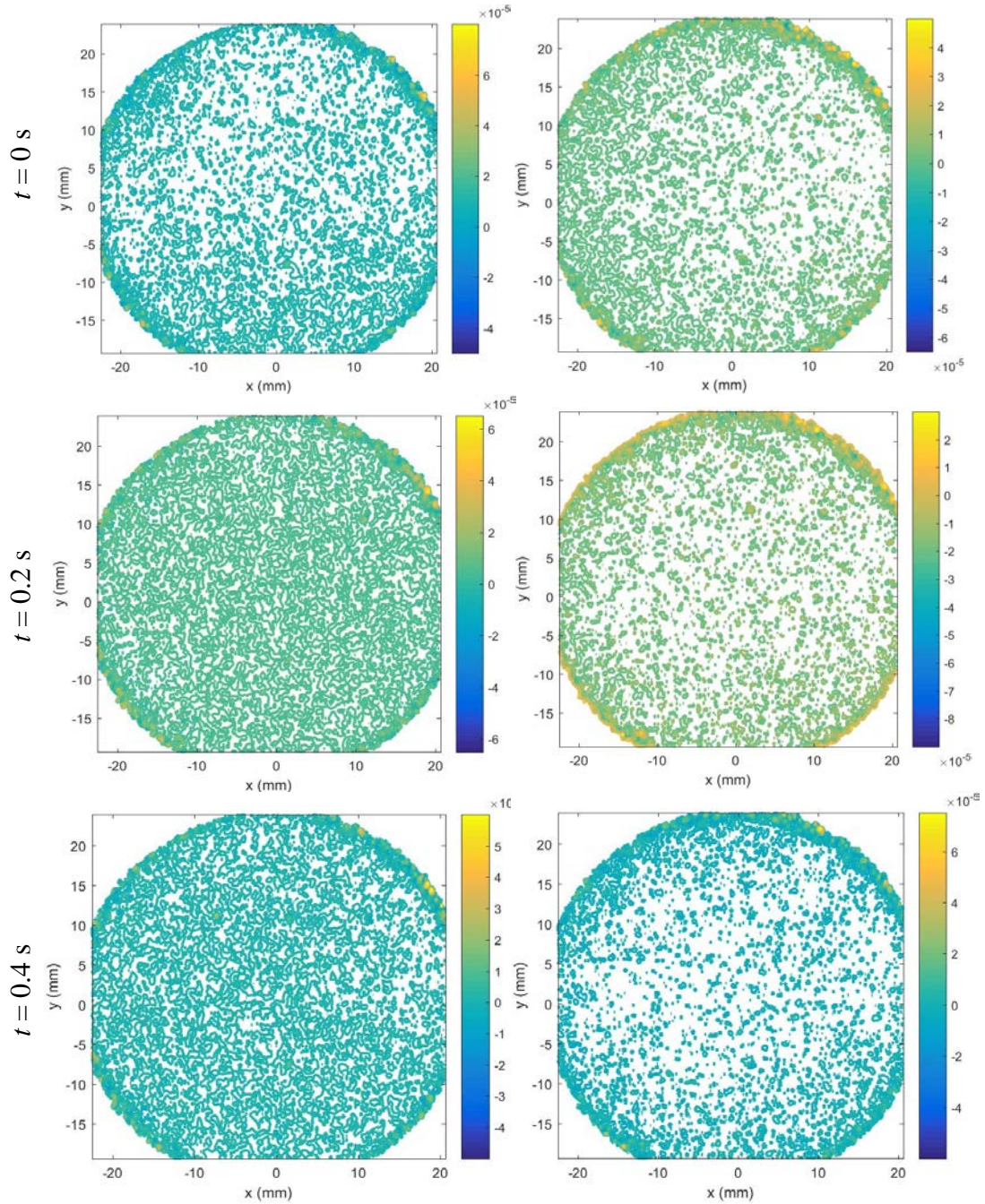


Figure 4.12: Surface slope  $w_{,x}$  (left column) and  $w_{,y}$  (right column) contours for a clamped silicon wafer recorded at 5 fps. Note: (0, 0) is made to coincide with the center of silicon wafer. Contour increments =  $5 \times 10^{-6}$  rad.

The surface slopes in Figure 4.11 and Figure 4.12 were numerically integrated using HFLI methodology to obtain the surface topography, and are plotted in Figure 4.13

and Figure 4.14, respectively. The left columns in Figure 4.13 and Figure 4.14 represent the 3D surfaces at different time instants, the right columns represent the out-of-plane displacement ( $w$ ) contours corresponding to the 3D surface in left columns.

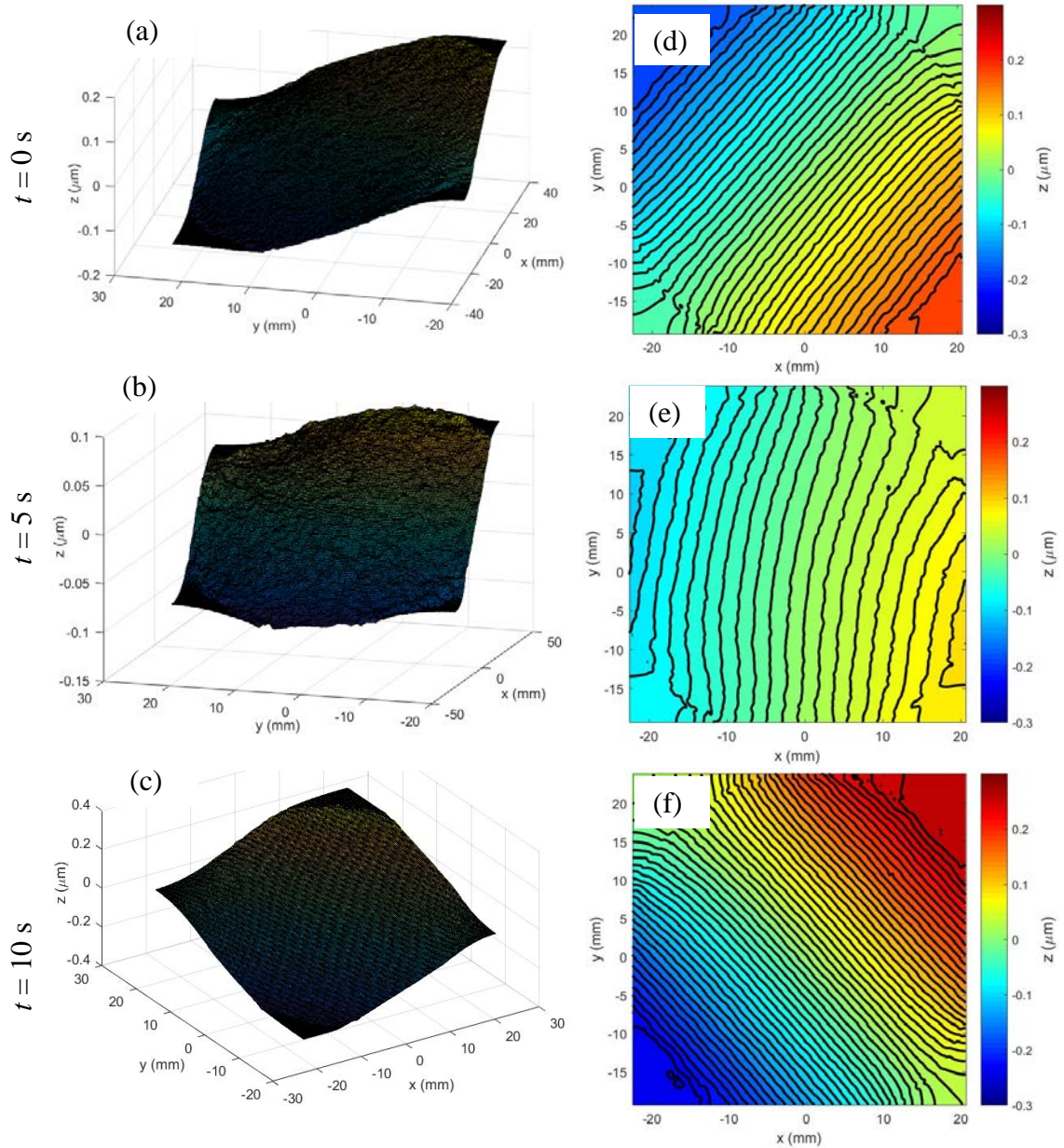


Figure 4.13: Surface topography obtained from integrating surface slopes using HFLI method for a clamped silicon wafer recorded at 0.2 fps. Left column: 3D surface; Right column: out-of-plane displacement ( $w$ ) contours ( $0.01 \mu\text{m}$  increments).

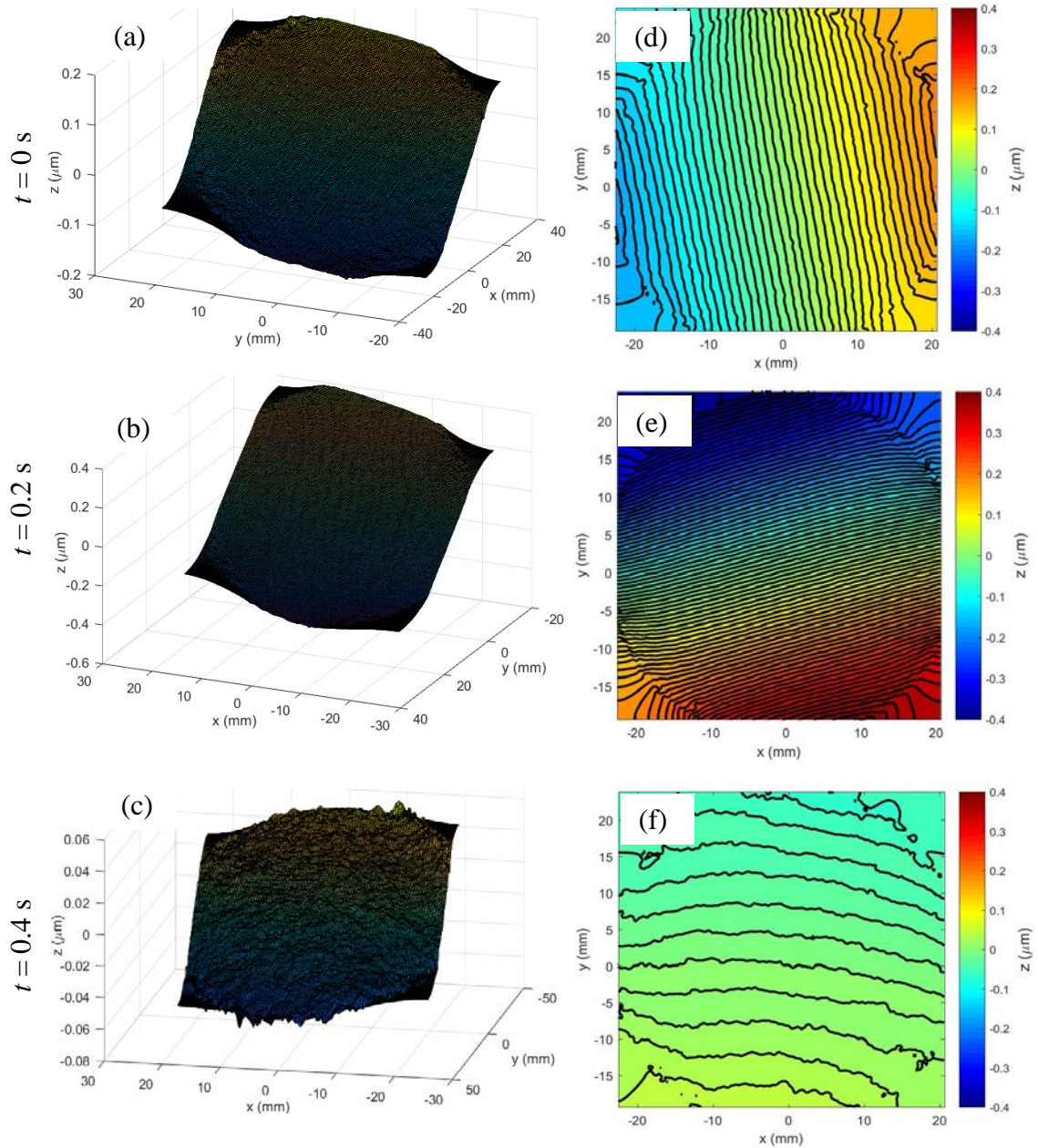


Figure 4.14: Surface topography obtained from integrating surface slopes using HFLI method for a clamped silicon wafer recorded at 5 fps. Left column: 3D surface; Right column: out-of-plane displacement ( $w$ ) contours ( $0.01 \mu\text{m}$  increments).

The 3D surfaces in Figure 4.13 and Figure 4.14 are plotted from different azimuth angles to best present the surface characteristics. It should be noted that the horizontal axes are in mm, while the vertical axes are in  $\mu\text{m}$ . Accordingly, all the 3D surfaces plotted here

are tilted at significant angles, though theoretically they should be flat devoid of contours. The contour increments for the out-of-plane displacement ( $w$ ) in the right column are set as  $0.01\ \mu\text{m}$  or  $10\ \text{nm}$ . The texture ('roughness') of the reconstructed surface due to experimental noise can be observed from the wrinkles on each contour. The out-of-plane displacement ( $w$ ) contours better reveal the phenomenon that all the 3D surfaces are tilted in different special directions. This is different with the reconstructed flat surface in Figure 4.8. It should be noted that since the laboratory where these experiments were performed is on the top floor of a four-story building, at close proximity to a passenger elevator, mechanical vibrations expectedly influence during the time lapse photography in addition to electronic noise and thermal currents within the recording column. Considering the measurement in the previous dynamic experiment conducted using this optical method could be in the nanometer range over a large region of observation using a short inter frame period ( $0.8\ \mu\text{s}$  or sub-micro second), the role of mechanical vibrations in the current slow-speed, quasi-static experiment is significant. The fact that the reconstructed surfaces are arbitrarily tilted in space at the instant of recording matches the reality that mechanical vibrations affected the measurements. Evidently, the smallest out-of-plane deformation ranges from  $-0.06\ \mu\text{m}$  to  $0.06\ \mu\text{m}$  in Figure 4.14 (c) and (f), whereas the largest spread is within  $-0.4\ \mu\text{m}$  to  $0.4\ \mu\text{m}$  in Figure 4.14 (b) and (e). Note that the higher errors at 5 fps when compared to 0.2 fps further emphasize the effect of random vibrations at lower imaging speeds influencing the measurements. This also indicates that the  $r$ -DGS is able to measure out-of-plane deformation in the sub-micron range over a relatively large FOV even under quasi-static conditions without special vibration isolation of the apparatus.

## **Chapter 5. Measurement of Deformations and Stresses in Laterally Impacted Composite Plates**

In this chapter, both out-of-plane deformations and in-plane stresses in thin composite plates subjected to lateral impact are studied. First, the feasibility of measuring surface slopes at the micro-radian scale and microsecond temporal resolution is demonstrated using *r*-DGS method with ultrahigh-speed photography. Subsequently, the measured surface slopes are integrated using HFLI methodology detailed earlier to evaluate out-of-plane deformations at the micron and sub-micron scales. The same surface slopes, differentiated numerically to determine curvatures allow estimation of in-plane stresses when used in conjunction with the classical plate theory.

### **5.1 Demonstration Experiment**

The dynamic impact of a PMMA plate was studied using *r*-DGS in conjunction with ultrahigh-speed single sensor digital camera. A 152.4 mm × 101.6 mm rectangular PMMA plate of 8.5 mm thickness was employed in the experiment. A 152.4 × 101.6 mm<sup>2</sup> face of the specimen was deposited with a thin aluminum film to make the surface reflective.

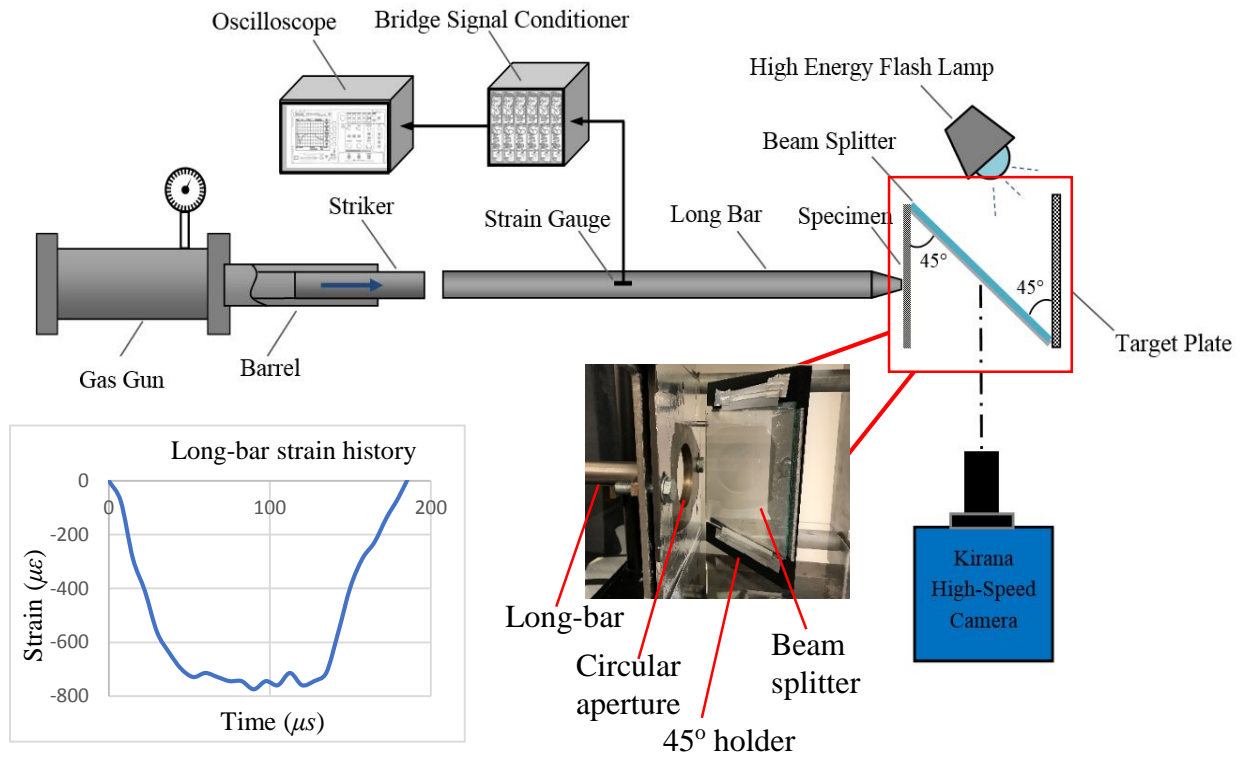


Figure 5.1: Schematic of the experimental setup for dynamic plate impact study. Insets show the close-up of the optical arrangement and the strain history due to the compressive pulse measured on the Hopkinson bar.

The schematic of the experimental setup used is shown in Figure 5.1. A modified Hopkinson pressure bar (or simply a ‘long-bar’) was used for loading the uncoated backside of the specimen. The long-bar was a 1.83 m steel rod of 25.4 mm diameter with a conical tip of 3 mm diameter impacting the backside of the specimen. A 305 mm long, 25.4 mm diameter steel striker placed in the barrel of a gas-gun was co-axially aligned with the long-bar at the start of the experiment. The striker was launched towards the long-bar at a velocity of  $\sim 8.5$  m/s and the corresponding strain history due to wave propagation in the long-bar due to the impact event was measured by a strain gage affixed to the long-bar. The specimen was clamped using a fixture containing two steel plates with circular apertures, see Figure 5.1. The apertures were 63.5 mm in diameter and coaxial facilitating

optical measurements over a relatively large ROI. Loading point was at the center of the aperture. A beam splitter and the speckle target plate were placed in a 45° holder, housed within the cage of the specimen holding the fixture, so that the speckle pattern on the target plate could be viewed via the reflective face of the specimen. The deformations on the front surface of the specimen were photographed by a Kirana-05M ultrahigh-speed digital camera assisted by a pair of Cordin-659 high energy flash lamps to illuminate the target. This camera is a single sensor camera, capable of recording 180 10-bit gray scale images at a maximum rate of 5 million frames per second and at a spatial resolution of  $924 \times 768$  pixels per image. The camera and the two flash lamps were triggered using a variable delay circuit relative to the time instant the striker impacts the long-bar and the duration required for the stress waves to travel the length of 1.83 m along the steel rod.

A Nikon 70-300 mm focal length macro zoom lens with an adjustable bellows was used with the camera for recording the images. A good exposure and focus were achieved by stopping down the lens aperture to F/8 after focusing. The distance between the specimen and the camera lens plane ( $L$ ) was ~950 mm and the one between the specimen mid-plane and the target plane ( $\Delta$ ) was 102 mm. A total of 180 images, some in the undeformed state and others in the deformed state, were recorded at 1 million frames per second. When the long-bar was impacted by the striker, a compressive stress wave was generated and it propagated along the bar. The fixture/cage used to house the specimen at the other end of the long-bar was mounted on a pair of guide-rails so that it can slide away from the long-bar when the specimen was loaded by the stress waves. However, the inertia of the fixture was substantially higher than that of the specimen and hence it took several milliseconds for the fixture to move away from the long-bar whereas the images

corresponding to specimen deformations were recorded over approx. 100 microseconds. Thus, the specimen was nominally in contact with the long-bar throughout the measurement history. Four select speckle images at different time instants are shown in Figure 5.2. In these,  $t = 0 \mu s$  corresponds to the start of the loading event on the plate. The distortion/displacement of the speckles due to the out-of-plane deformation evident in the central part of the images is caused by the out-of-plane deformations of the PMMA plate. However, no distortion of speckles can be observed in the image at  $t = 5 \mu s$  as out-of-plane deformation of the PMMA plate is extremely small to discern. One of the undeformed images before the start of deformation was selected as the reference image. Subsequent deformed images were correlated with the reference image by using ARAMIS<sup>®</sup> image analysis software. During image analysis, a sub-image size of  $40 \times 40$  pixels (1 pixel =  $83.31 \mu m$ ) with 30 pixels overlap was used to extract the local speckle displacements  $\delta_{x,y}$  in the ROI. In order to achieve correlation over the entire image and over the deformation range, a relatively large sub-image size was selected in favor of smaller sub-images<sup>2</sup>. The displacement fields were then used to compute the two orthogonal angular deflection fields of light rays ( $\phi_{x,y}$ ).

---

<sup>2</sup> The role of sub-image size in the range  $20 \times 20$  to  $40 \times 40$  pixels, each with the same step size, on the measurement of angular deflections are included in Section 5.3 (Figure 5.20(1)) for a time instant  $t = 15 \mu s$  for completeness. The magnitude of maximum slope difference between  $20 \times 20$  and  $40 \times 40$  sub-image size choice was approx. 6.1%. The larger sub-image size results in a smaller magnitude slope relative to smaller sub-image due to smoothing effect. The latter produces noisier variation of slopes relative to the former.

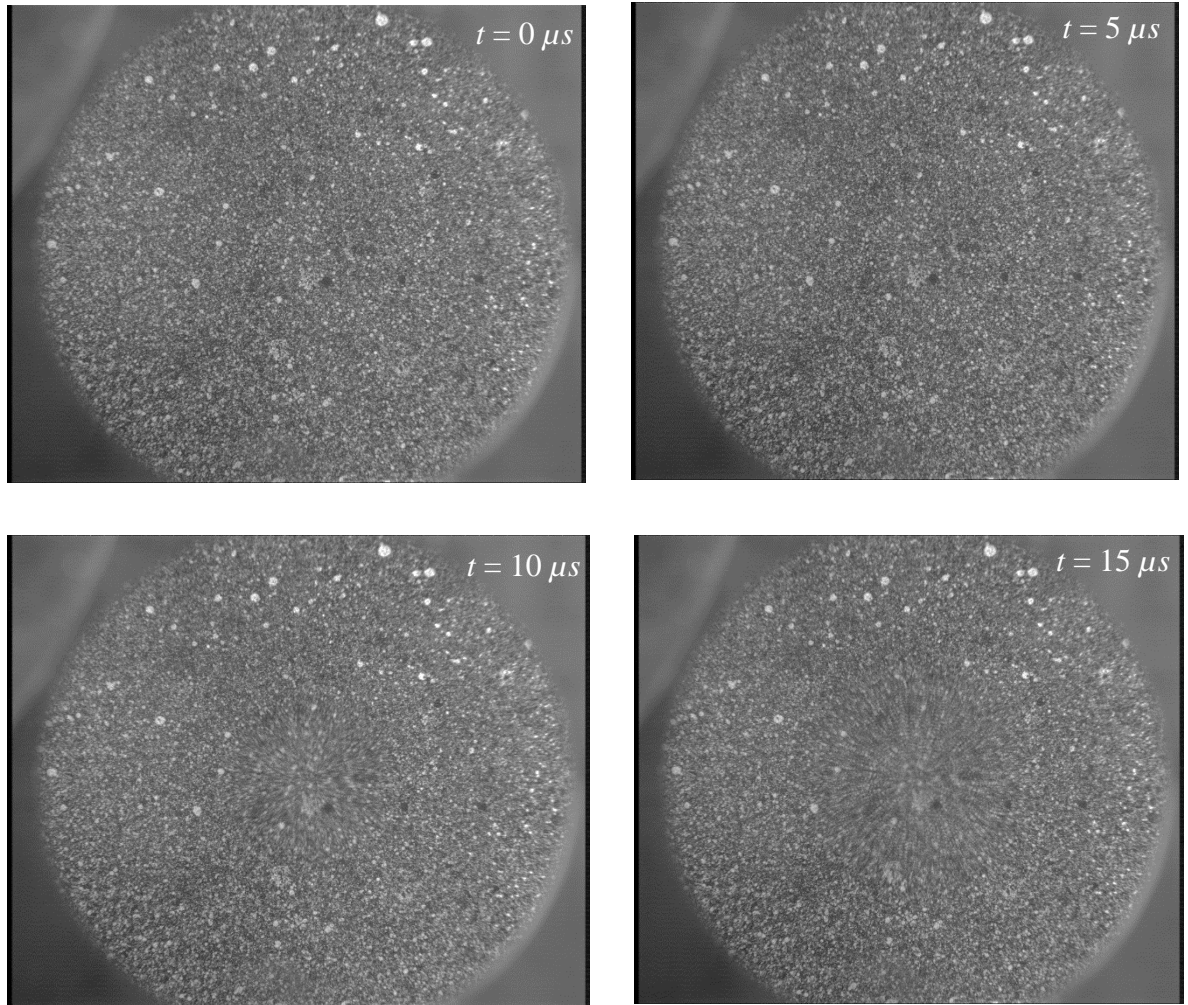
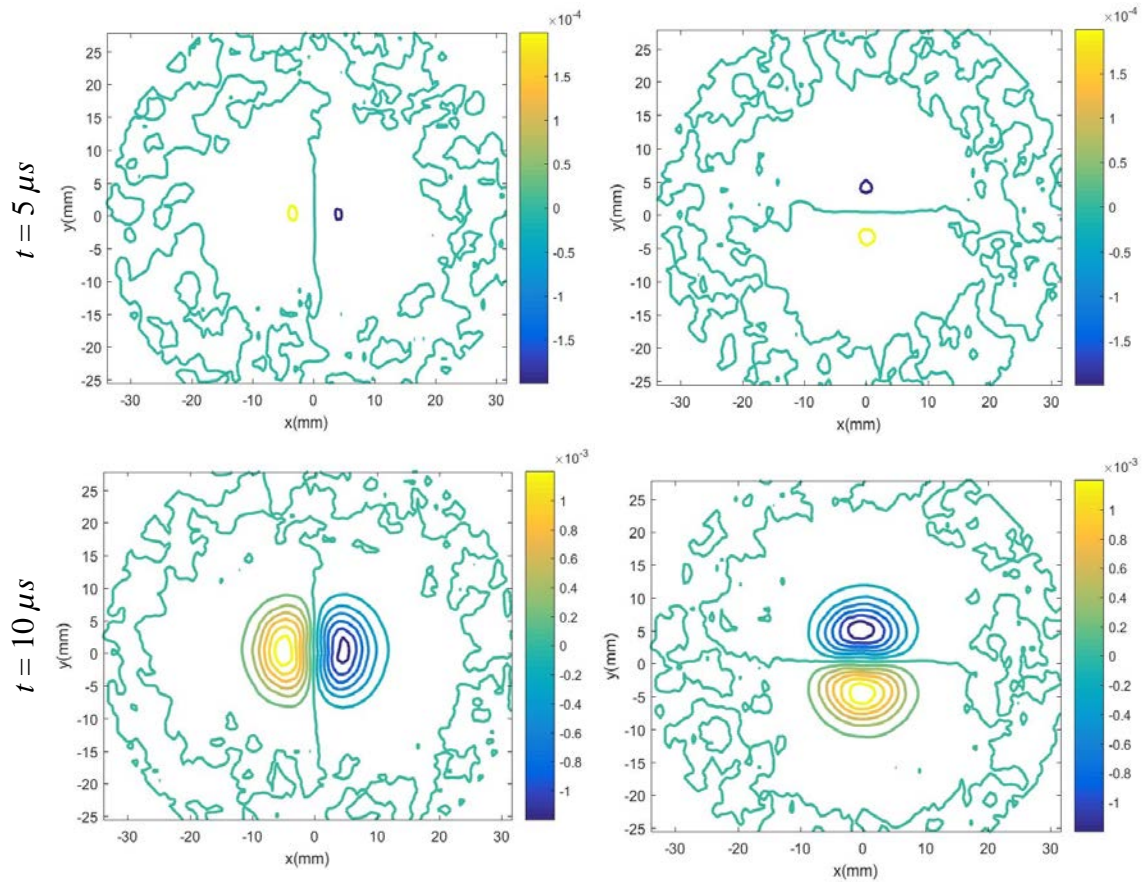


Figure 5.2: Recorded speckle images from ultrahigh-speed camera at different time instants. The nominal diameter of the region of interest is 63.5 mm. Disturbance to the recorded speckles is readily evident in the last two images relative to the one at  $t = 0 \mu s$ .

The time-resolved orthogonal surface slope contours  $\frac{\partial w}{\partial x}$  and  $\frac{\partial w}{\partial y}$  due to stress wave propagation in the PMMA plate are shown in Figure 5.3 at a few select time instants. The undeformed/reference image mentioned earlier was selected from a sequence of 10-20 images recorded before the start of the impact event or  $t = 0 \mu s$ . Once the compressive stress wave from the long-bar enter the PMMA plate, the impact induced stress waves

propagate through the plate thickness (8.5 mm) from the contact point to reach the outer surface of the plate being monitored. During the early stages of impact, deformations are concentrated close to the center of the plate (chosen as the origin) resulting in small surface slopes and sparse contours. The rest of the plate is undeformed as stress waves are yet to reach those outer regions and hence surface slopes are vanishingly small, below the measurement sensitivity of the method. With the passage of time, the contours get denser and larger with a higher concentration of contours near the contact point. The vertical line of symmetry in  $\frac{\partial w}{\partial x}$  contours and the horizontal line of symmetry in  $\frac{\partial w}{\partial y}$  contours indicate the zero surface slope as to be expected of the single point impact at the center of the plate.



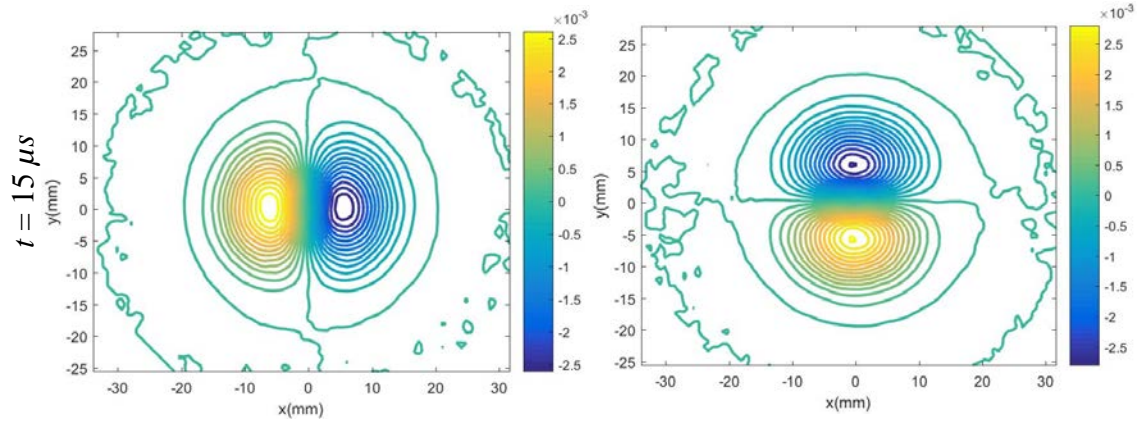
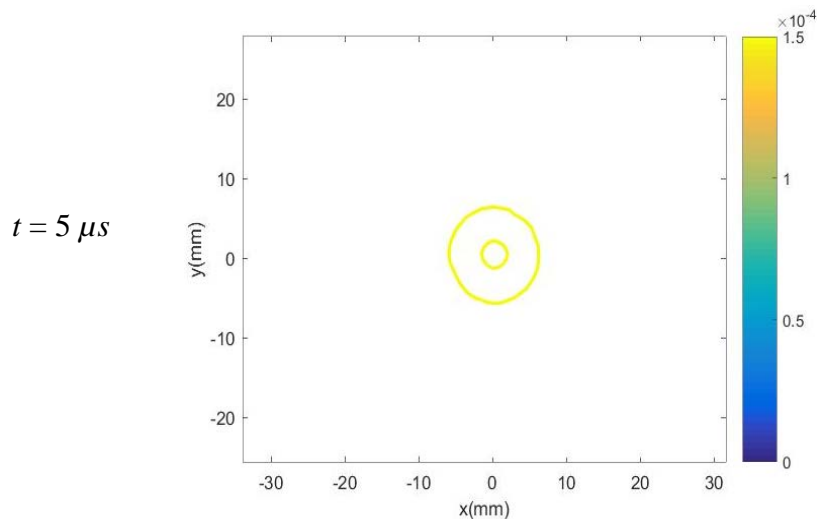


Figure 5.3: Evolution of surface slope  $w_{,x}$  (left column) and  $w_{,y}$  (right column) contours for a clamped PMMA plate subjected to central impact. The impact point is made to coincide with  $(0, 0)$ ; Contour increments =  $2 \times 10^{-4}$  rad.

The contours of  $\frac{\partial w}{\partial r} \left( = \sqrt{\left(\frac{\partial w}{\partial x}\right)^2 + \left(\frac{\partial w}{\partial y}\right)^2} \right)$  are also shown in Figure 5.4, where  $r$

is the radial distance from the contact point. These show very high degree of axisymmetry and also a higher concentration of contours near the impact point which become relatively sparse first before becoming dense again in the area away from the origin. This is because the slopes  $\frac{\partial w}{\partial r}$  vary substantially in the regions around the impact point and near the clamped edge, while they are nearly constant in the intermediate region.



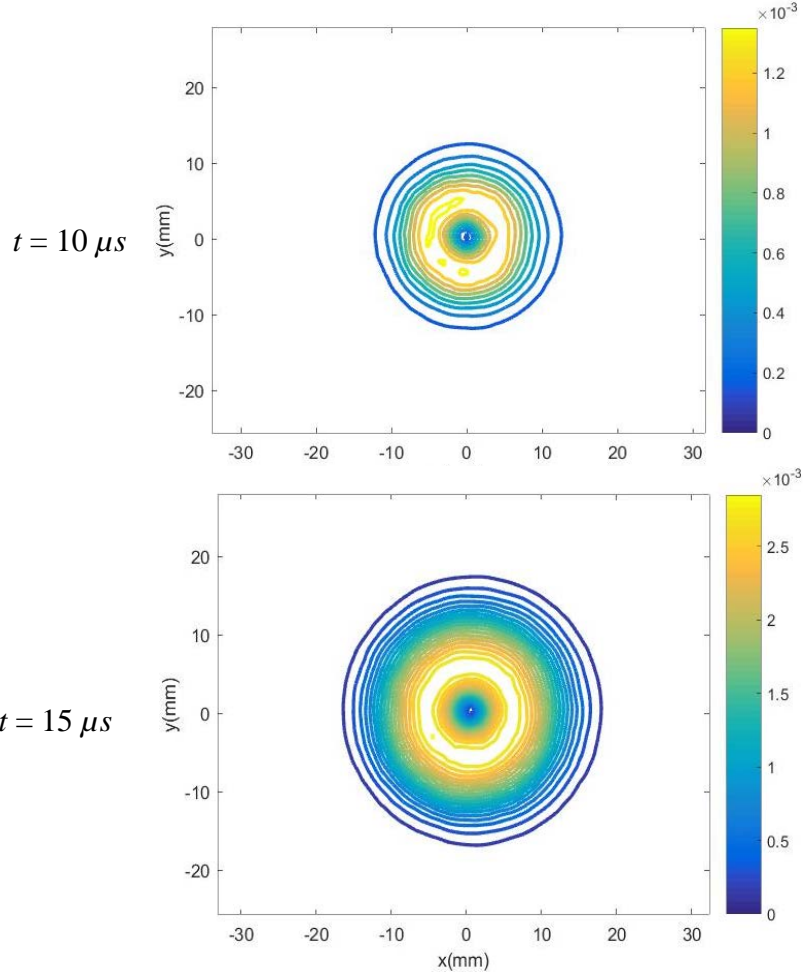


Figure 5.4: Evolution of surface slope  $w,r$  contours for a clamped PMMA plate subjected to central impact. The impact point is made to coincide with  $(0, 0)$ ; Contour increments =  $1.5 \times 10^{-4}$  rad.

The reconstructed 3D surfaces computed through 2D integration using slope data from  $r$ -DGS in conjunction with HFLI algorithm are plotted in Figure 5.5. The corresponding contours of out-of-plane displacements ( $w$ ) at  $1 \mu m$  increment are shown in Figure 5.5(b), (d) and (f). It can be observed that the out-of-plane deformations are very small in the early stages of impact, and they increase with time. The circular contours in the right column demonstrate that the reconstructed shape matches very well with the reality of the experiment both qualitatively and quantitatively.

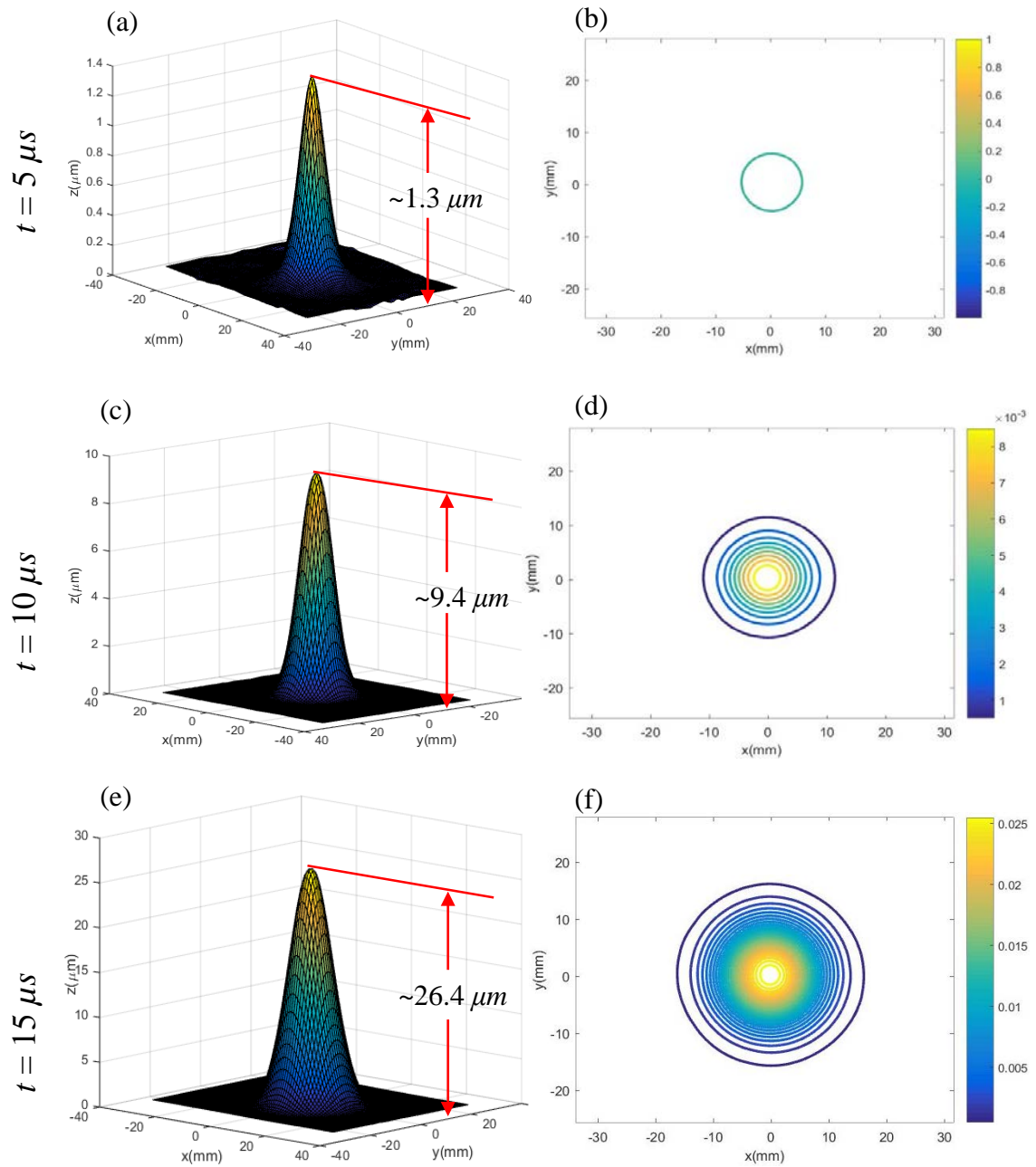


Figure 5.5: Evolution of surface profile of PMMA plate at select time instants. Left column: reconstructed 3D surface; Right column: out-of-plane displacement ( $w$ ) contours ( $1 \mu\text{m}$  increment). The impact point is made to coincide with  $(0, 0)$ .

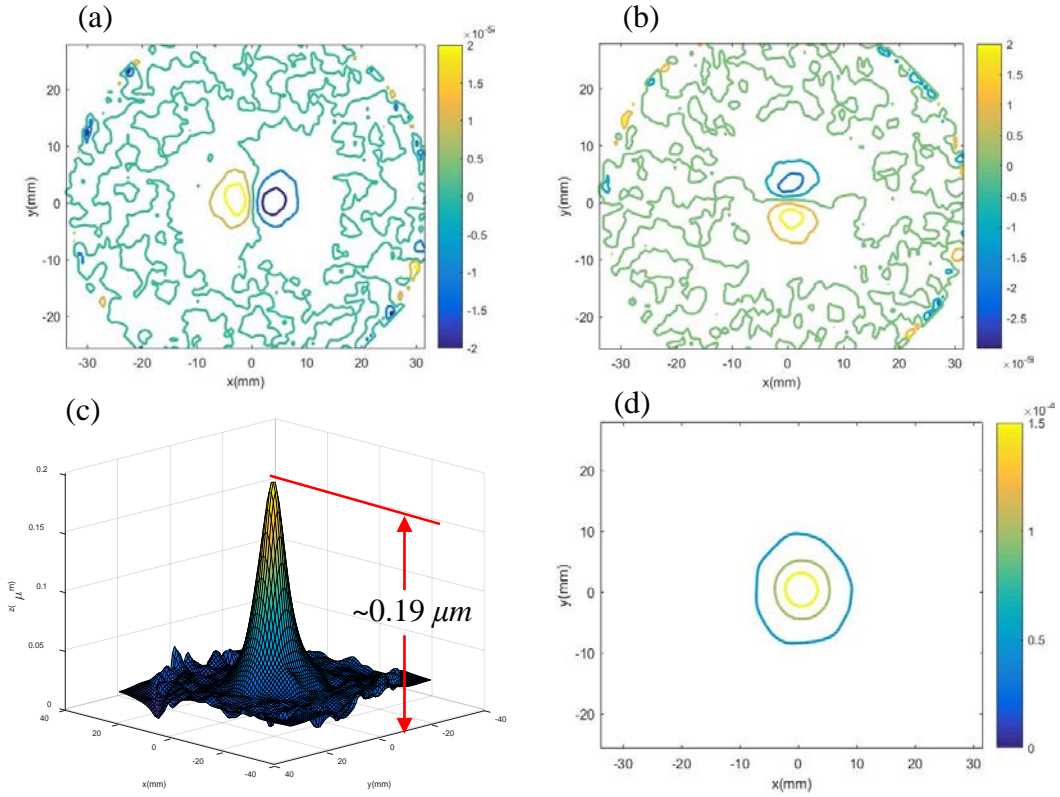


Figure 5.6: Results for a clamped PMMA plate subjected to central impact at  $t = 2 \mu s$ . Row 1:  $w_{,x}$  (left) and  $w_{,y}$  (right) contours; Row 2: reconstructed 3D surface (left) and out-of-plane displacement ( $w$ ) contours at  $0.05 \mu m$  increment (right). The impact point is made to coincide with  $(0, 0)$ .

The surface slope contours  $\frac{\partial w}{\partial x}$  and  $\frac{\partial w}{\partial y}$  at  $t = 2 \mu s$  are plotted in Figure 5.6(a) and

(b). The contour increments here are  $1 \times 10^{-5}$  rad (or  $\sim 5.7 \times 10^{-4}$  deg.), approx. equal to the generally accepted 1% of the pixel scaling as the accuracy limit of DIC method. Hence, the experimental noise is somewhat more evident in the figure relative to the one in Figure 5.3. However, at the center of the figure, slope contours can be clearly discerned. After integrating the surface slope data using the HFLI scheme, the reconstructed 3D surface and the corresponding contour representation of out-of-plane displacements ( $w$ ) in  $50 \text{ nm}$  increments are plotted in the second row (Figure 5.6(c) and (d)). Unlike differentiation, the

numerical integration of measured data produces a smoothing effect on the resulting out-of-plane displacements. More importantly, deformation in the sub-micron scale ( $w \sim 190\text{nm}$ ) are discernable using  $r$ -DGS when used in conjunction with the HFLI algorithm. The circular contours at the bottom right figure also demonstrate that the reconstructed shape qualitatively matches well with the reality of the experiment.

The out-of-plane deformations along  $x = 0$  at a few select time instants are plotted in Figure 5.7<sup>3</sup>. The radius  $R$  was measured from the impact point. In all the cases, due to stress wave propagation through the plate thickness from the impact point to reach the observed surface of the plate, the out-of-plane deformations emanate from the contact point and propagate outwards towards the clamped edge. It was observed that the out-of-plane deformations monotonically increase but somewhat rapidly after  $6\ \mu\text{s}$ .

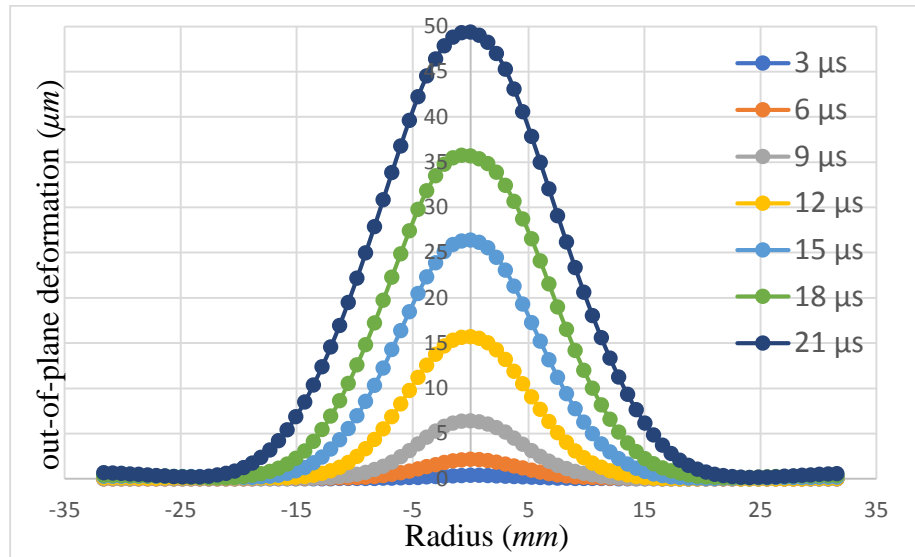


Figure 5.7: The measured transient profiles for a clamped PMMA plate subjected to central impact. (see, Section 5.3 for error estimates)

<sup>3</sup> The role of the sub-image size ( $20 \times 20$  to  $40 \times 40$  pixels) on the out-of-plane deformation is included in Section 5.3 (Figure 5.20(2)) for a time instant  $t = 15\ \mu\text{s}$  for completeness. The differences between the maximum displacement estimates however reduce significantly ( $< 1\%$ ) when integrated using HFLI.

Since  $r$ -DGS is able to measure instantaneous orthogonal surface slopes  $\frac{\partial w}{\partial x}$  and

$\frac{\partial w}{\partial y}$  in the entire field, the evaluation of instantaneous curvatures  $\frac{\partial^2 w}{\partial x^2}$ ,  $\frac{\partial^2 w}{\partial y^2}$  and  $\frac{\partial^2 w}{\partial x \partial y}$

require just one additional differentiation of the measured data<sup>4</sup>. Now, by recognizing that stresses in thin plates are related to curvatures in Kirchhoff plate theory [122] as,

$$\begin{pmatrix} \sigma_{xx} \\ \sigma_{yy} \\ \sigma_{xy} \end{pmatrix} = \begin{bmatrix} C_{11} & C_{12} & C_{13} \\ C_{21} & C_{22} & C_{23} \\ C_{31} & C_{32} & C_{33} \end{bmatrix} \begin{pmatrix} \varepsilon_{xx} \\ \varepsilon_{yy} \\ 2\varepsilon_{xy} \end{pmatrix} = -z \begin{bmatrix} C_{11} & C_{12} & C_{13} \\ C_{21} & C_{22} & C_{23} \\ C_{31} & C_{32} & C_{33} \end{bmatrix} \begin{pmatrix} \frac{\partial^2 w}{\partial x^2} \\ \frac{\partial^2 w}{\partial y^2} \\ 2\frac{\partial^2 w}{\partial x \partial y} \end{pmatrix} \quad (5.1)$$

where  $C_{ij}$  ( $i, j=1, \dots, 3$ ) are the elements of the stiffness matrix for the material. Under the assumption that the functional form of Kirchhoff plate theory holds for transient conditions, instantaneous stresses were estimated. That is, the slope data was differentiated using central difference scheme<sup>5</sup> to obtain local curvatures and the corresponding stresses over the entire ROI. Thus estimated values of  $\sigma_{xx}$  and  $\sigma_{xy}$  at  $t = 20 \mu s$  are plotted in Figure 5.8 as stress surfaces. (The  $\sigma_{yy}$  plots are avoided here due to its similarity with  $\sigma_{xx}$  field but offset by  $90^\circ$ .)

<sup>4</sup> As it is well known that differentiation exaggerates noise in the experimental data, single differentiation is obviously very desirable instead of performing two successive differentiations of measured out-of-plane deformations as it would be case in, say, 3D-DIC or shadow moiré methods, a subtle but significant issue for estimating stresses.

<sup>5</sup> The role of the sub-image size ( $20 \times 20$  to  $40 \times 40$  pixels) on the stress estimation is included in Section 5.3 (Figure 5.20(3)) for a time instant  $t = 15 \mu s$  for completeness. A difference in the peak value of stress  $\sigma_{xx}$  of approx. 13% is evident between the smallest and the largest sub-image size. Furthermore, two types of central difference schemes, one with an algorithmic error of  $O(h^2)$  and another  $O(h^4)$  where  $h$  is the step-size, were attempted. A representative result at a time instant  $t = 15 \mu s$  is shown in Session 5.3, Figure 5.21.

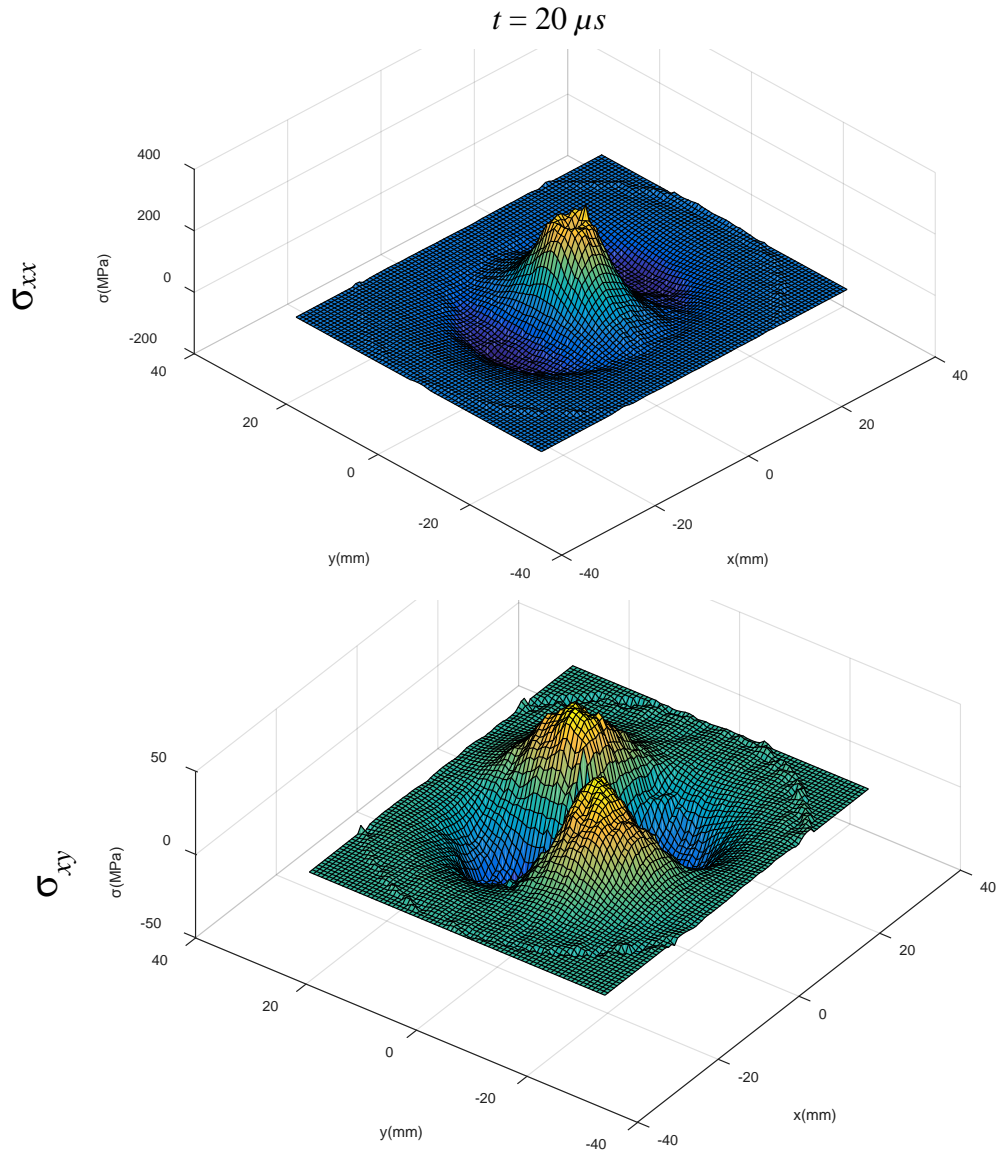


Figure 5.8: Estimated stresses for a circular clamped PMMA plate subjected to central impact.

The distribution of normal stress  $\sigma_{xx}$ , approaching a tensile peak ( $\sim 280 \pm 18$  MPa) at the origin<sup>6</sup>. The tensile stresses rapidly decrease into a torus shaped valley of

---

<sup>6</sup> Note that the peak stress cannot be evaluated precisely due to numerical differentiation errors and the finite sub-image size used during image analysis. These, however, can be expected to greatly improve with the advent of higher pixel count sensors of smaller pixel size and better fill-factor in high-speed cameras.

compressive stresses before becoming negligibly small far away from the impact point. The shear stress distribution of  $\sigma_{xy}$ , on the other hand, is skewed along  $\pm 45^\circ$  directions with dual equidistant positive and negative peaks away from the origin.

To complement the experimental results, a 3D elasto-dynamic finite element simulation was carried out using ABAQUS<sup>®</sup> structural analysis software. A quarter-model of the plate, as shown in Figure 5.9, was simulated. The specimen and the end of steel long-bar were discretized into 202,215 and 7,580 eight-node hexahedral elements, respectively. The regions corresponding to the clamped region were restrained in the out-of-plane direction and a kinematic contact condition was imposed between the PMMA plate and the tip of the steel long-bar. The dynamic elastic modulus (4.92 GPa) and Poisson's ratio (0.32) of PMMA were used in the simulation based on ultrasonic measurement of longitudinal and shear wave speeds [123]. The elastic properties of 1144 carbon steel were used in the simulation of the long-bar (see Table 5-1). The particle velocity history ( $V = c\varepsilon$ , where  $c$  is the bar wave speed of steel and  $\varepsilon$  the strain), obtained from a measured strain gage history on the long-bar during the experiment, was used as an input into the numerical simulations. The out-of-plane displacements along the radius in the region-of-interest were extracted every 5  $\mu s$  to compare with the corresponding results of the reconstructed 3D surface in Figure 5.10. The solid lines represent values from numerical simulations and the solid symbols are the experimental counterparts. It can be observed that there is a rather good agreement between the two data sets. Moreover, the ability of the methodology to detect sub-micron deformations at microsecond temporal resolution is evident and noteworthy.

Table 5-1: Material properties of 1144 Carbon Steel and PMMA used in finite element simulations

	1144 Carbon Steel	PMMA
Density ( $\text{kg/m}^3$ )	7870	1100
Elastic modulus (GPa)	200	4.92
Poisson's ratio	0.29	0.32

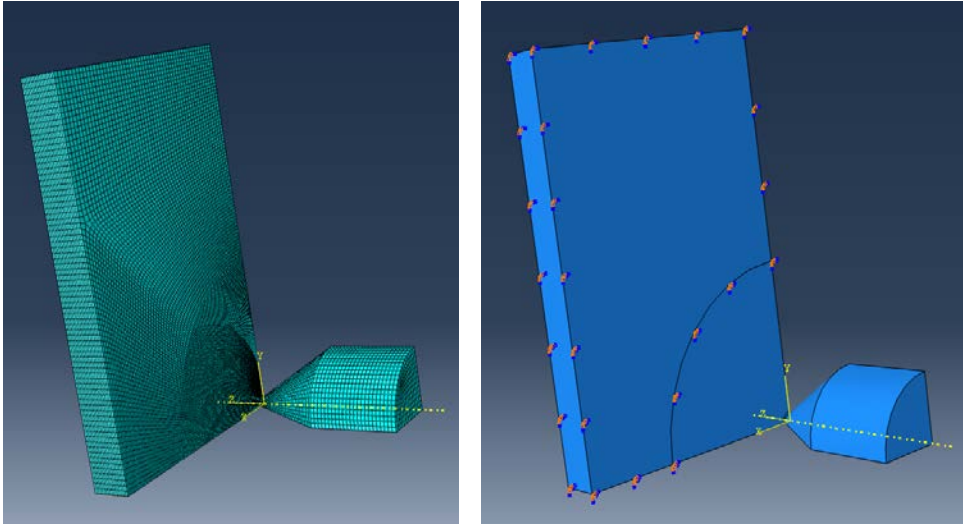


Figure 5.9: 3D finite element model used for simulating impact on a clamped PMMA plate.

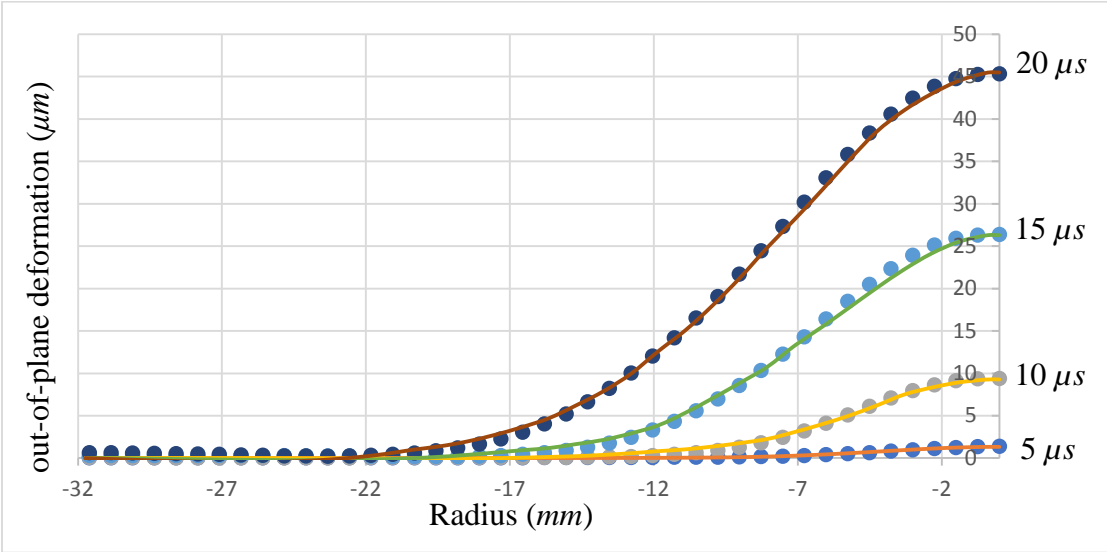


Figure 5.10: Comparison of experimental (solid symbols) results with finite element simulations (solid line) at different time instants.

## 5.2 CFRP Plates Subjected to Dynamic Impact<sup>7</sup>

Two types of CFRP plates subjected to dynamic impact were studied next. One was an orthotropic CFRP plate made of T800s/3900-2 unidirectional laminate with a  $[0_{24}]$  lay-up, the second was a quasi-isotropic CFRP plate made of the same unidirectional laminae in  $[(+45/90/-45/0)_3]_s$  lay-up (Toray Composite America, Inc.). For the unidirectional CFRP plate subjected to impact, the fiber direction coincided with the horizontal axis. The plate specimens were  $152.4 \text{ mm} \times 101.6 \text{ mm} \times 4.5 \text{ mm}$  made specularly reflective by using the aluminum film transfer technique. As in case of PMMA, the plates were clamped in the fixture beyond 63.5 mm diameter. A striker velocity of  $\sim 8.5 \text{ m/s}$  was used in these experiments as well. A total of 180 images in the undeformed and deformed states were recorded at 1 million frames per second.

### 5.2.1 Unidirectional CFRP Plate

The time-resolved orthogonal surface slope contours representing  $\frac{\partial w}{\partial x}$  and  $\frac{\partial w}{\partial y}$  due to transient stress wave propagation in the unidirectional CFRP plate are shown in Figure 5.11 at a few select time instants.

---

<sup>7</sup> The effects of sub-image size on surface slopes, out-of-plane deformation and stresses for CFRP were studied along the lines described for PMMA. The corresponding results are shown in Section 5.3 (Figure 5.22(1)-(3)). The maximum (magnitude) slope difference between  $20 \times 20$  and  $40 \times 40$  sub-image size choice was approx. 6.9%. The larger sub-image size results in a smaller magnitude slope relative to smaller sub-image. The latter produces noisier variation of slopes relative to the former. As in case of PMMA, the differences in maximum out-of-plane deformations are significantly reduced ( $< 0.5\%$ ) upon numerical integration of the slope data whereas maximum stress  $\sigma_{xx}$  (along the fibers) shows 3.5% difference between  $20 \times 20$  and  $40 \times 40$  sub-image size.

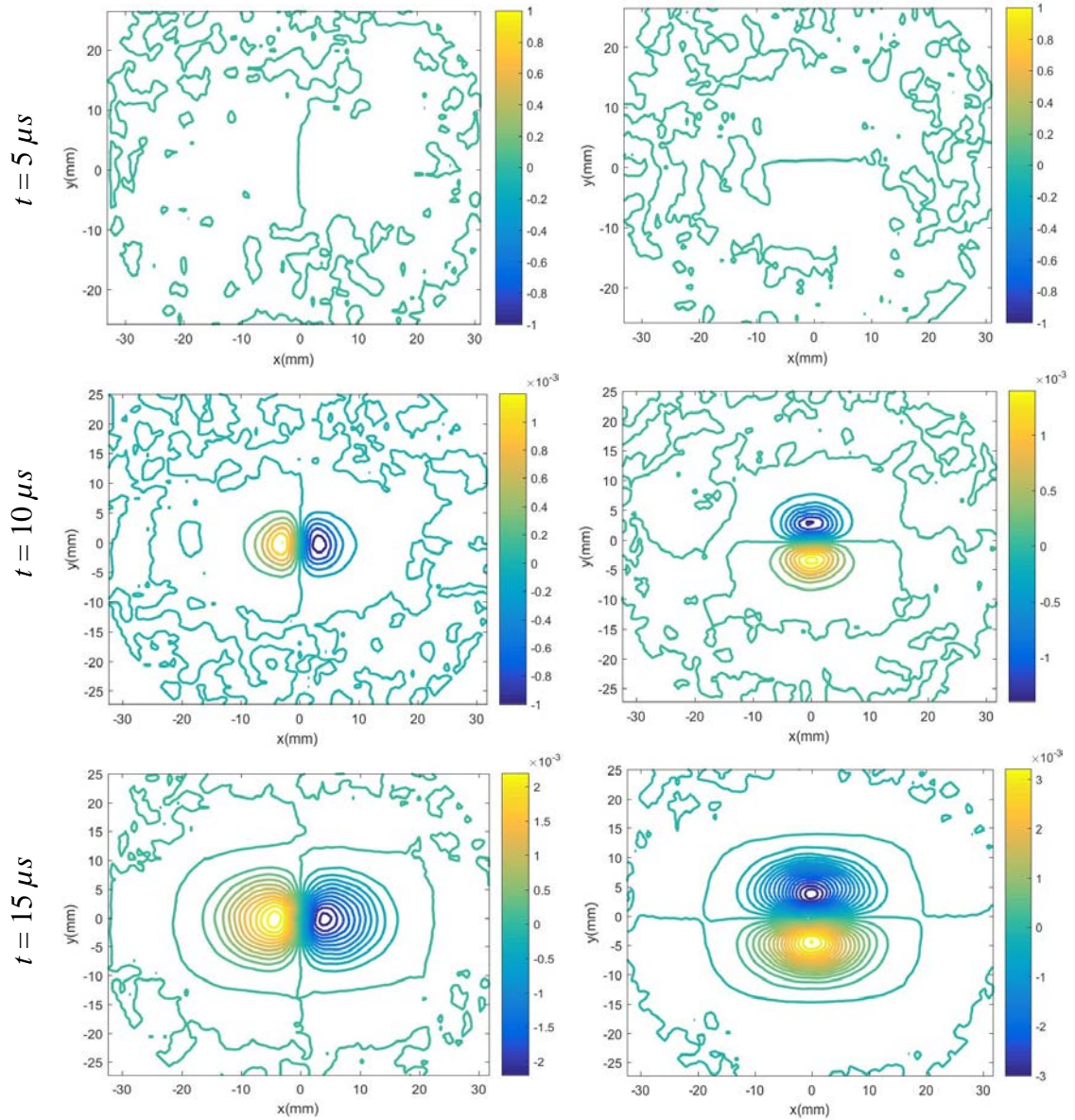


Figure 5.11: Evolution of slopes  $w_x$  (left column) and  $w_y$  (right column) contours for a clamped unidirectional CFRP plate subjected to central impact. Note:  $(0, 0)$  is made to coincide with the impact point. Fiber direction is in the horizontal direction. Contour increments =  $2 \times 10^{-4}$  rad.

Unlike PMMA plates, the slope contours here are visibly stretched in the horizontal direction, which corresponds to the fiber direction of this unidirectional composite along which the stress waves propagate faster relative to the normal to the fiber direction. At  $t = 15 \mu s$ , the outermost discernable contour corresponding to the zero surface slope is

nearly rectangular in shape in contrast to the one for PMMA (see Figure 5.3), which are circular due to isotropy.

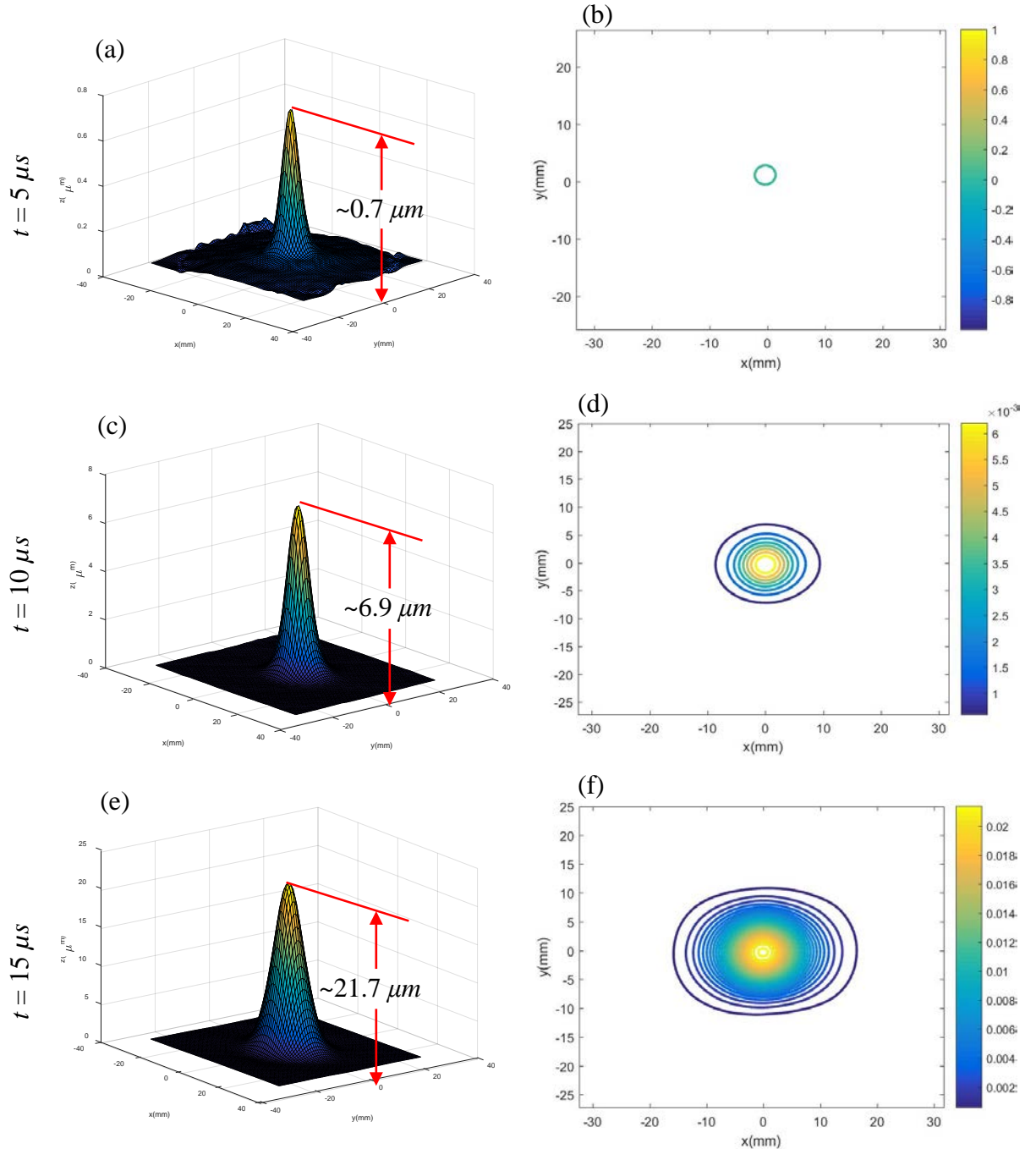


Figure 5.12: Evolution of surface topography of unidirectional CFRP plate at a few select time instants. Left column: reconstructed 3D surface; Right column: out-of-plane displacement ( $w$ ) contours ( $0.8 \mu m$  increment). Note:  $(0, 0)$  is made to coincide with the impact point. Fiber direction is in the horizontal direction.

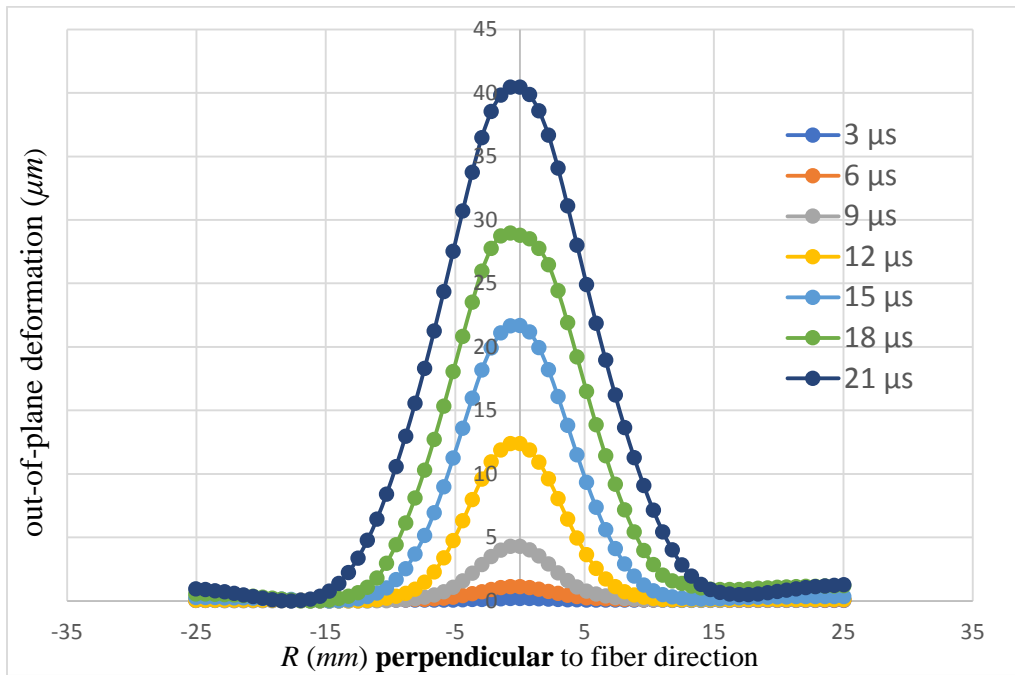
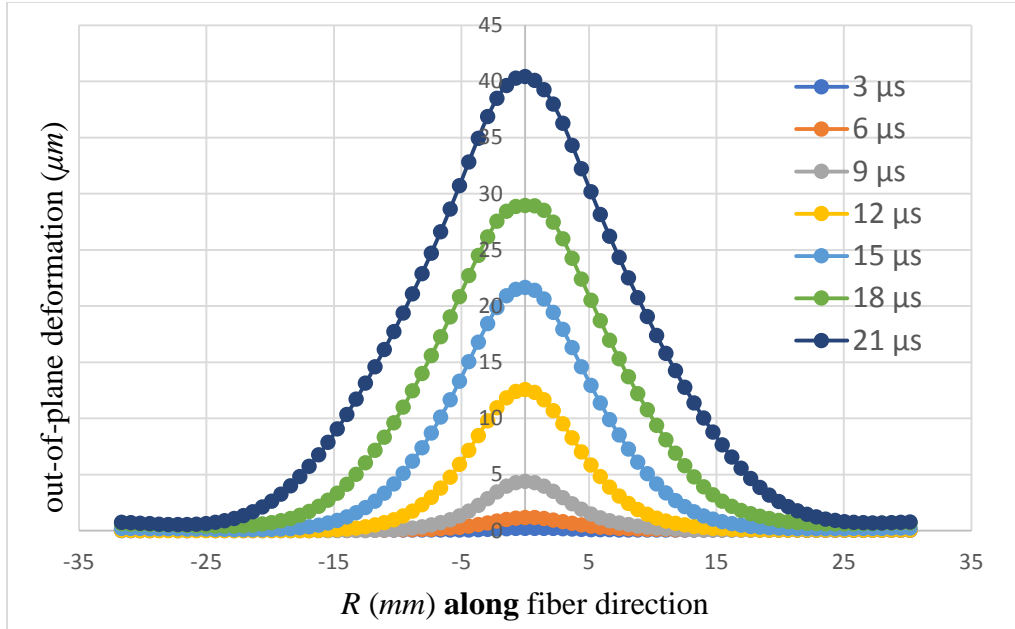


Figure 5.13: The measured surface profiles for a clamped unidirectional CFRP plate subjected to central impact. (see, Section 5.3 for error estimates)

The reconstructed 3D surfaces obtained via 2D integration of surface slope data from  $r$ -DGS in conjunction with HFLI scheme are plotted in Figure 5.12. The corresponding contours of out-of-plane displacements ( $w$ ) at  $0.8 \mu\text{m}$  increments are shown

in Figure 5.12(b), (d) and (f). A sub-micron deformation of  $0.7 \mu m$  can be observed at  $t = 5 \mu s$ . The oblong contours in Figure 5.12(b), (d) and (f) demonstrate that the reconstructed shape is qualitatively consistent with the reality of the experiment. The cross-sectional out-of-plane deformations, along and normal to the fiber directions, at a few select time instants are plotted in Figure 5.13. The radius  $R$  here again is measured from the impact point, (0, 0). It can be observed that the radial extent of the out-of-plane deformations perpendicular to the fiber direction is narrower than the ones along fiber direction, consistent with the reality of the experiment.

As in case of the PMMA plate, transient values of stresses in unidirectional CFRP were obtained. Thus estimated distribution of  $\sigma_{xx}$ ,  $\sigma_{yy}$  and  $\sigma_{xy}$  at  $t = 20 \mu s$  are plotted in Figure 5.14 as stress surfaces. These are relatively noisy when compared to the corresponding PMMA ones due to the fibrous nature of the composite besides numerical differentiation of slopes to obtain curvatures. Furthermore, the directionality of stress magnitudes is also readily evident in these plots. At this time instant, the normal stress  $\sigma_{xx}$  distribution approaches a local tensile peak of  $\sim 3500$  MPa at the origin. These stresses rapidly decay to compressive values before becoming negligibly small far away from the impact point. The distribution of normal stress  $\sigma_{yy}$  perpendicular to the fibers, on the other hand, also approaches a tensile peak of  $\sim 350$  MPa at the origin, an order of magnitude lower than that for  $\sigma_{xx}$ . This too decays, but slowly normal to the fibers vs. more steeply along the fibers, to compressive values before becoming negligible far away from the impact point. The shear stress  $\sigma_{xy}$  distribution is again skewed relative to the  $x$ - $y$  axes, with

two positive and negative peaks of  $\sim 65$  MPa magnitude occurring along approximately  $\pm 45^\circ$  directions away from the origin in the surface plot.

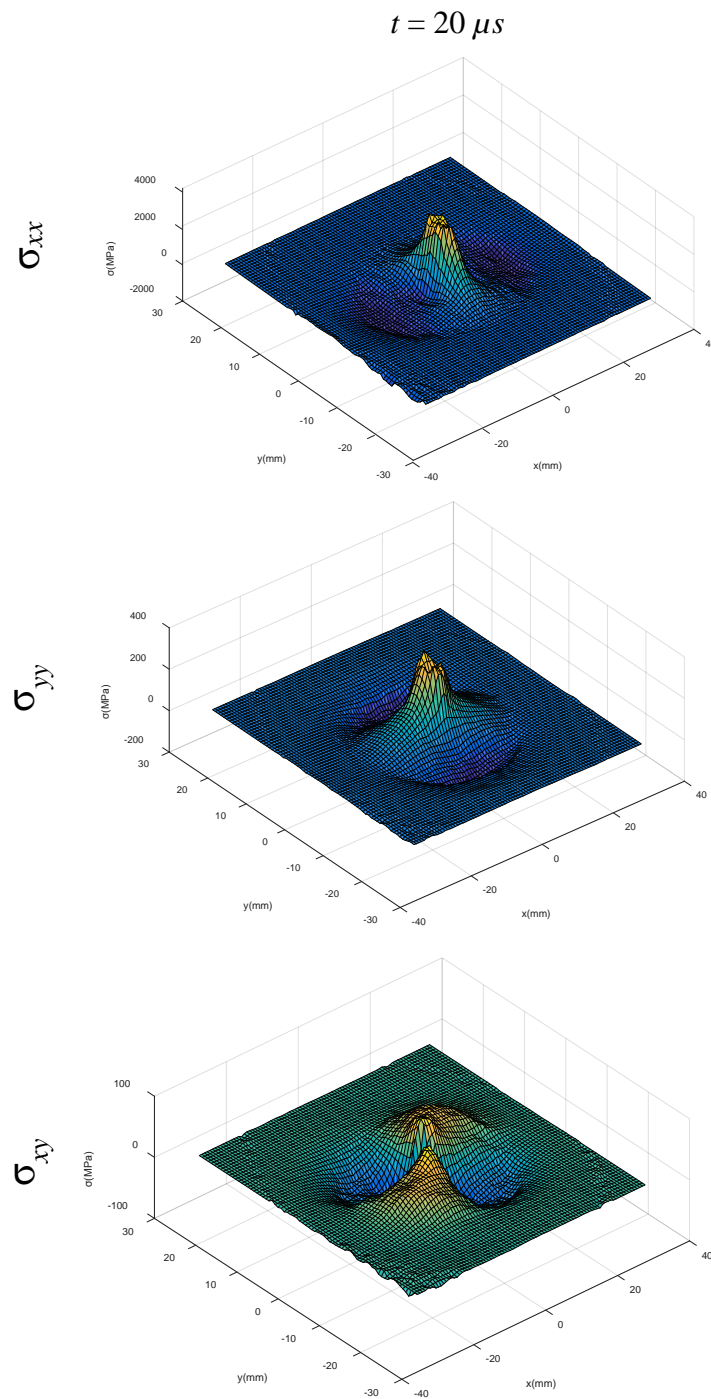


Figure 5.14: Estimated stresses for a circular, clamped unidirectional CFRP plate subjected to central impact. Fiber orientation is along the  $x$ -axis.

The experimental results obtained above are complemented using a 3D elasto-dynamic finite element simulation carried out using ABAQUS® structural analysis software. As in the PMMA plate case, a quarter-model was simulated. The specimen and the end of steel long-bar were discretized into 511,608 and 7,620 eight-node hexahedral elements, respectively. Kinematic contact was imposed between the CFRP plate and the steel long-bar tip. The material properties of CFRP used in these simulations are listed in Table 5-2 [124]. The out-of-plane displacements were extracted every 5  $\mu s$  to compare with the corresponding experimental results (see Figure 5.15). The solid lines represent values from the numerical simulation, and the solid symbols are from the experiment. It can be observed that there is a reasonably good agreement between the two data sets, demonstrating the feasibility of *r*-DGS and HFLI based measurements made during the dynamic impact experiment. It should also be noted that somewhat larger deviations between the two data sets is attributed to elastic properties used in the simulations as they were not measured by the authors but borrowed from a published report under quasi-static loading conditions.

Table 5-2: Material properties of unidirectional CFRP used in FEA [124]

$E_1$ (GPa)	$E_2$ (GPa)	$E_3$ (GPa)	$G_{12}$ (GPa)	$G_{23}$ (GPa)	$G_{13}$ (GPa)	$\nu_{12}$	$\nu_{23}$	$\nu_{13}$	Density(kg/m <sup>3</sup> )
152	8	8	4	2.75	4	0.34	0.45	0.34	1632

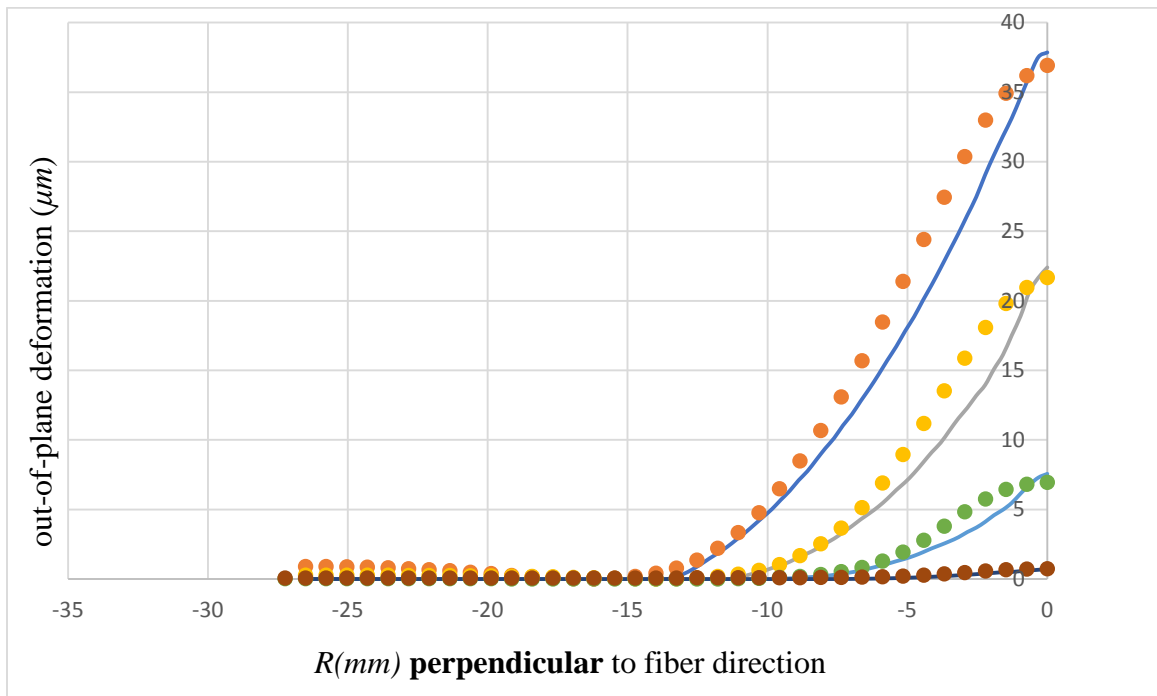
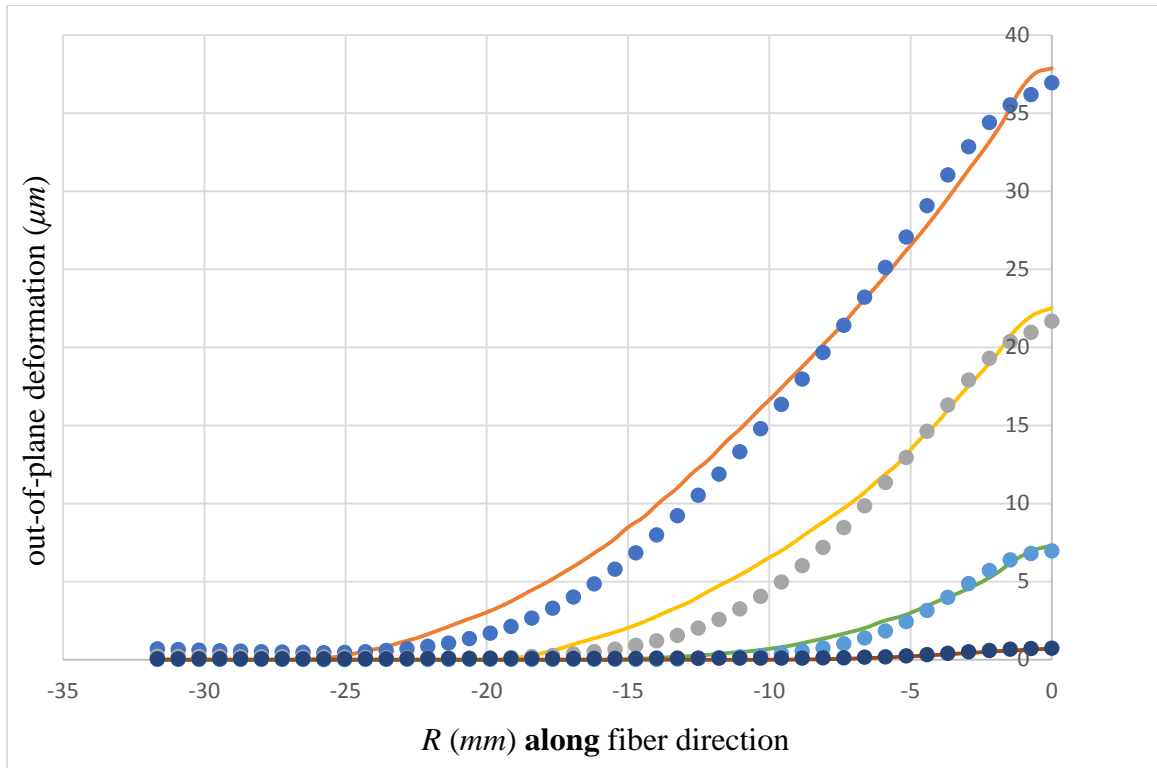


Figure 5.15: Comparison of experimental results with finite element simulations. Solid lines represent values from simulations; solid symbols represent values from the experiment.

### 5.2.2 Quasi-isotropic CFRP Plate

Lastly, the time-resolved orthogonal surface slope contours of  $\frac{\partial w}{\partial x}$  and  $\frac{\partial w}{\partial y}$  during stress wave propagation in the quasi-isotropic CFRP plate are shown in Figure 5.16 at a few select time instants. It can be observed that the contours here are somewhat similar to those of PMMA due to quasi-isotropy. The reconstructed 3D surfaces computed through 2D integration of surface slope data from  $r$ -DGS used in conjunction with HFLI scheme are plotted in Figure 5.17. The corresponding contours of out-of-plane displacements ( $w$ ) at  $0.26 \mu\text{m}$  increment are shown in Figure 5.17(b), (d) and (f). At  $t = 5 \mu\text{s}$ , a sub-micron magnitude peak deformation of  $\sim 0.2 \mu\text{m}$  was recovered at the impact point. The noise level in the reconstructed surface profile at this time instant is relatively higher than the isotropic counterparts due to a combination of extremely small out-of-plane deformations and material anisotropy. Further, it can be observed that at the same time frame, the out-of-plane deformations of quasi-isotropic CFRP plate are much smaller than those of unidirectional CFRP counterpart, although they are both subjected to the same impact velocity. This is consistent with the higher stiffness components of the quasi-isotropic CFRP plate relative to the unidirectional counterpart of the same number of plies. The out-of-plane deformations along  $x = 0$  at selected time instants are plotted in Figure 5.18 and the deformations at  $t = 3 \mu\text{s}$  and  $t = 6 \mu\text{s}$  are rather small. This is different when compared to deformations of PMMA at the same time instant, although the PMMA plate studied was thicker (8.5 mm vs. 4.5 mm) than the CFRP plate.

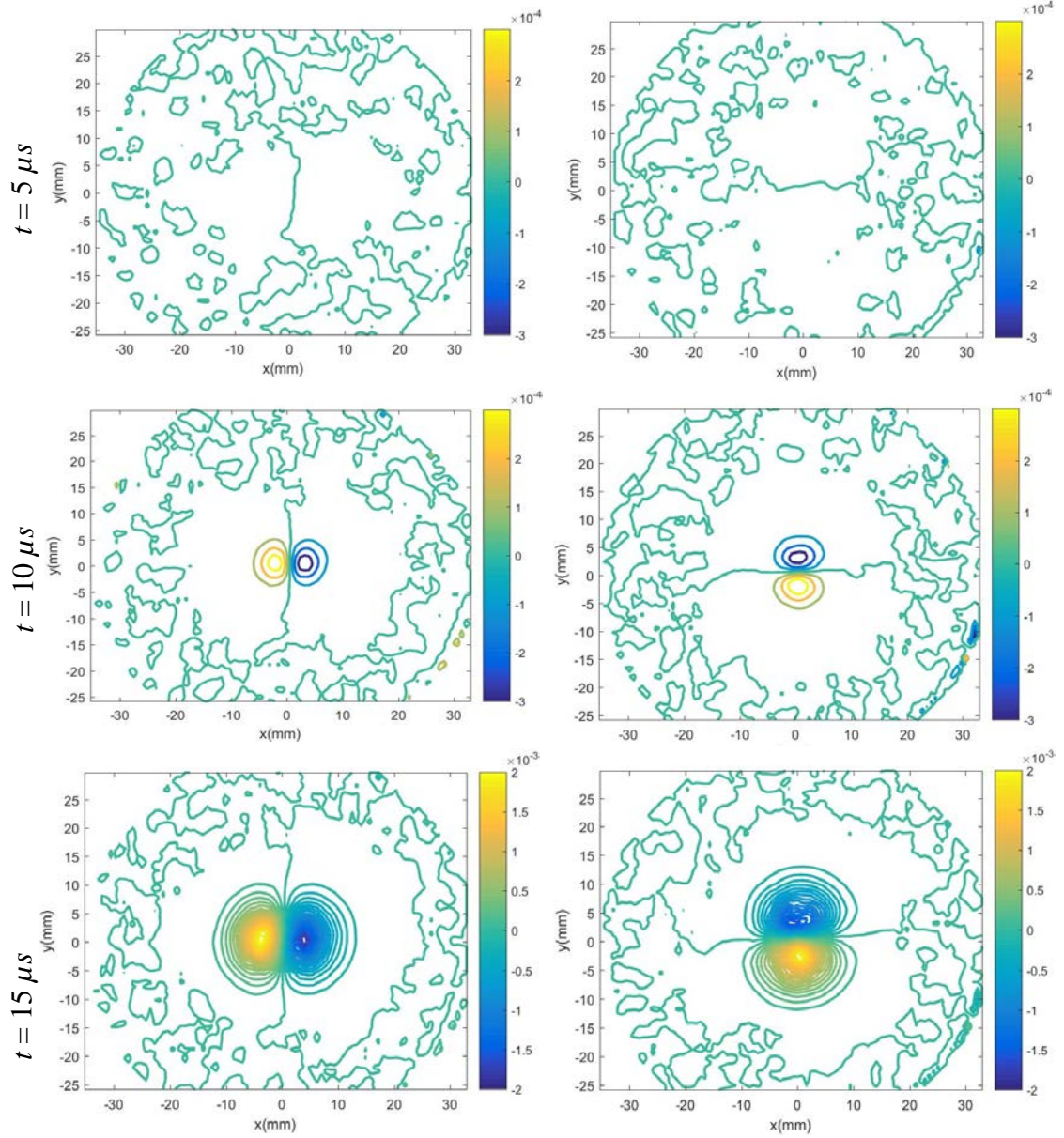


Figure 5.16: Evolution of slopes  $w_x$  (left column) and  $w_y$  (right column) as contours for a clamped quasi-isotropic CFRP plate subjected to central impact. Note:  $(0, 0)$  is made to coincide with the impact point. Contour increments =  $1 \times 10^{-4}$  rad.

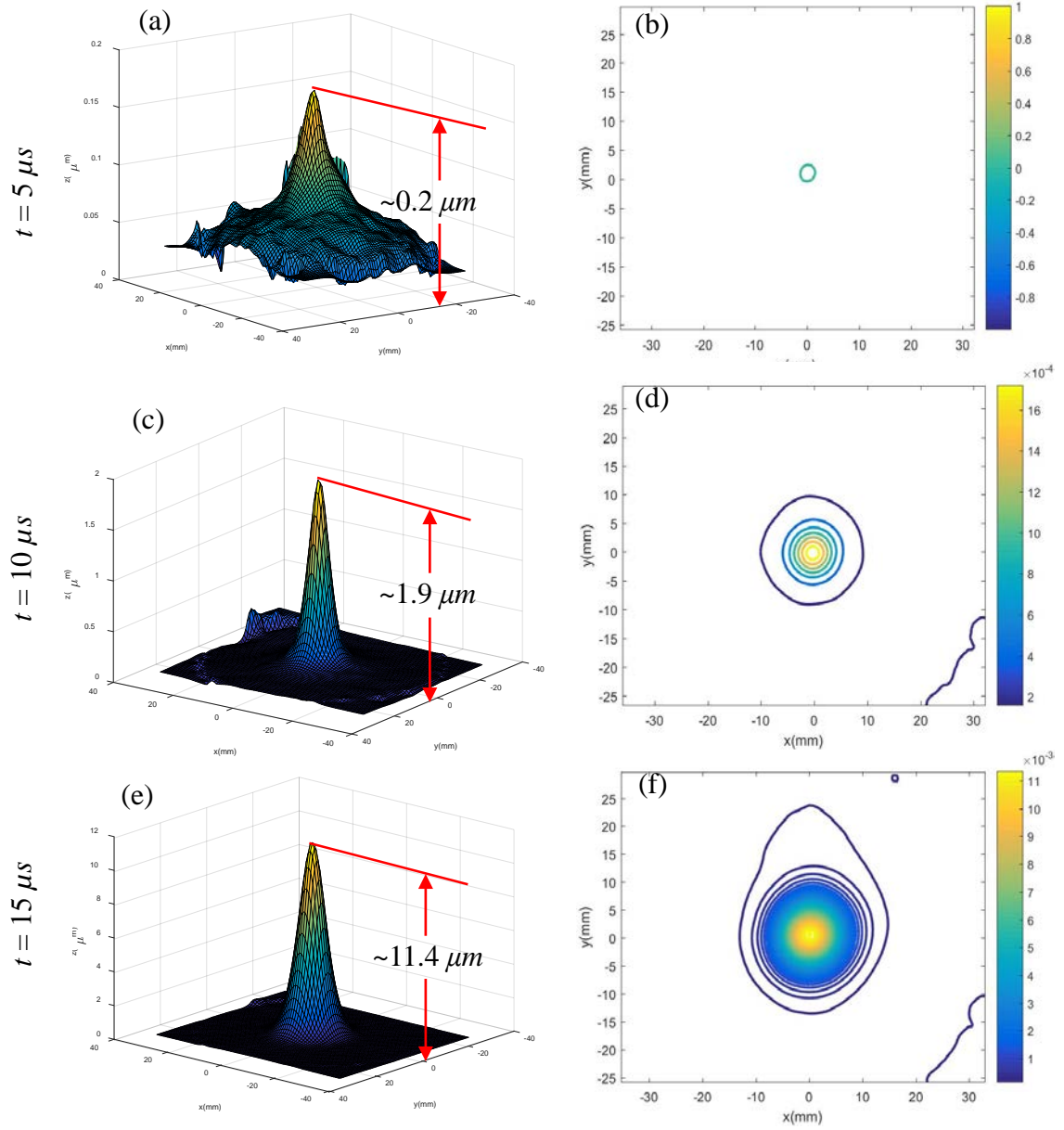


Figure 5.17: Evolution of surface deformations of a quasi-isotropic CFRP plate at select time instants. Left column: reconstructed 3D surface; Right column: out-of-plane displacement ( $w$ ) contours ( $0.26 \mu\text{m}$  increment). Note:  $(0, 0)$  is made to coincide with the impact point.

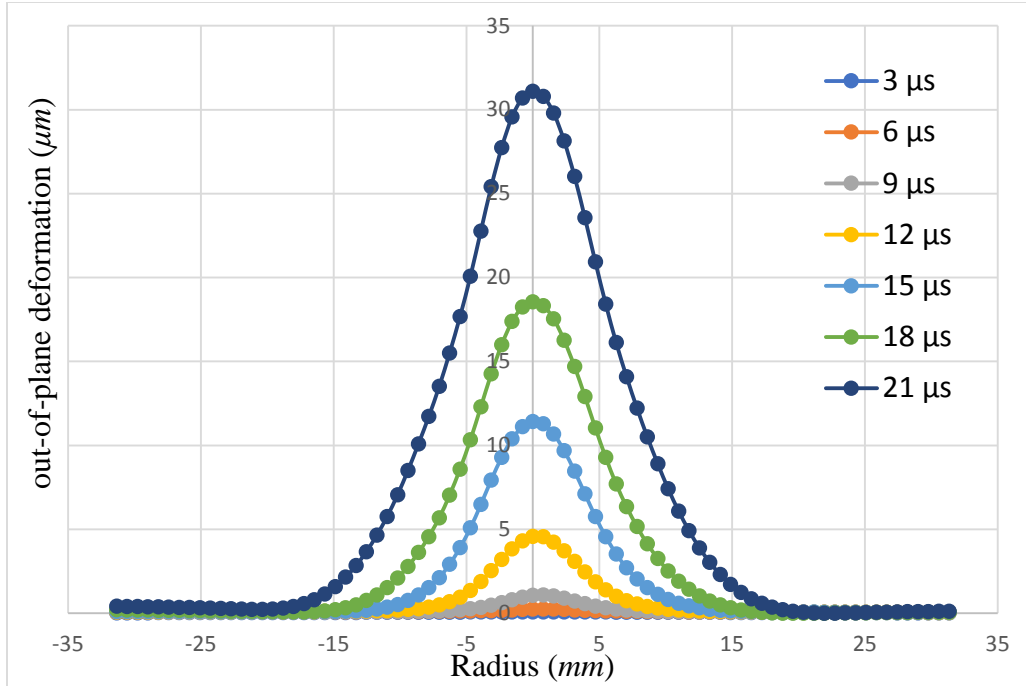


Figure 5.18: The measured transient surface profiles for a clamped quasi-isotropic CFRP plate subjected to central impact.

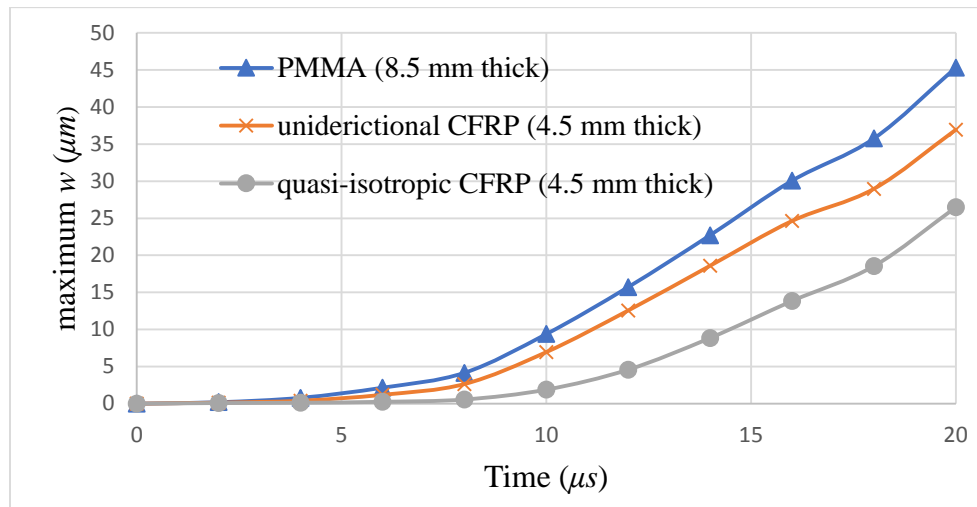


Figure 5.19: Evolution of maximum out-of-plane displacement for PMMA, unidirectional CFRP and quasi-isotropic CFRP.

To compare the histories of maximum out-of-plane deformation ( $w_{max}$ ) of PMMA, unidirectional CFRP and quasi-isotropic CFRP plates, all impacted with a striker velocity

of 8.5 *m/s*, the experimental data are plotted in Figure 5.19. The deformations increase in each of these cases monotonically during the window of observation. The deformations for PMMA are the largest at each time instant even though it is twice as thick as the CFRP plates. The magnitude of deformation of the PMMA plate is followed by unidirectional CFRP and quasi-isotropic CFRP, respectively.

### 5.3 Error Estimation

#### 5.3.1 Effect of Sub-Image Size

PMMA: To verify the effect of sub-image size on measured surface slope and subsequently the surface topography, three different sub-image sizes, 20×20, 30×30, and 40×40 pixels and step-size of 10 pixels were considered. Experimental results for the impact loaded PMMA plate at a time instant of  $t = 15\mu s$  after impact are plotted in Figure 5.20. Figure 5.20(1) corresponds to the measured slope  $\frac{\partial w}{\partial x}$  along the *x*-axis, Figure 5.20(2) shows the integrated out-of-plane deformation along the radius, Figure 5.20(3) shows the estimated stress component  $\sigma_{xx}$  along the *x*-axis, each corresponding to different sub-image sizes considered. It can be observed from Figure 5.20(1) that small differences in slope data (difference between 20×20 to 40×40 pixels for maximum  $\frac{\partial w}{\partial x}$  is 6.1%) for different sub-image sizes occur. It is also clear that larger sub-image size producing smoother variation relative to the smaller counterpart. In Figure 5.20(2), out-of-plane deformations obtained via HFLI algorithm show a smoothing effect, altering the peak value of *w* at the impact point by less than 1%.

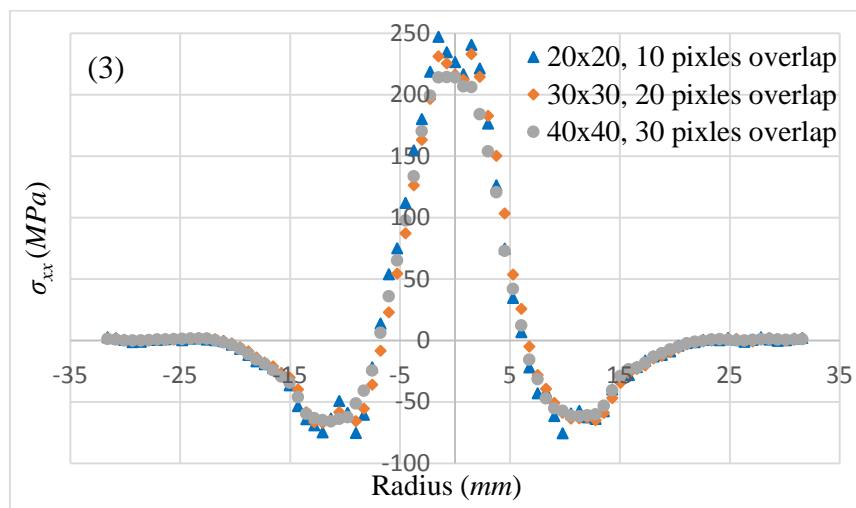
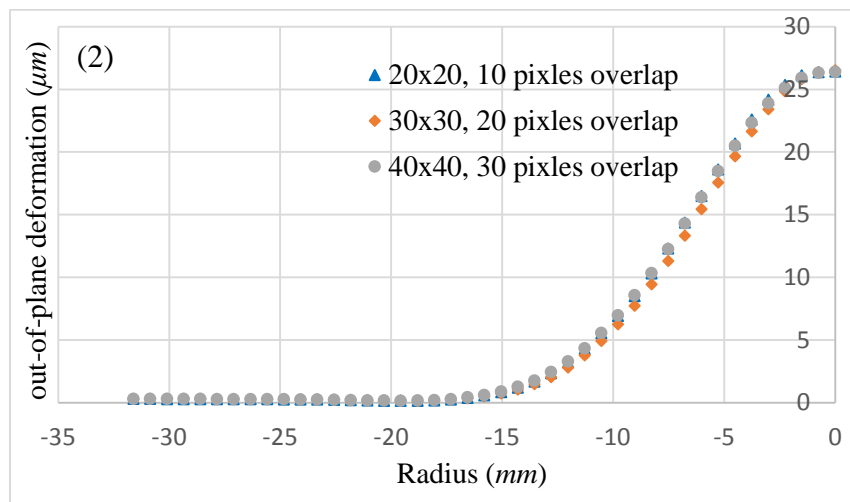
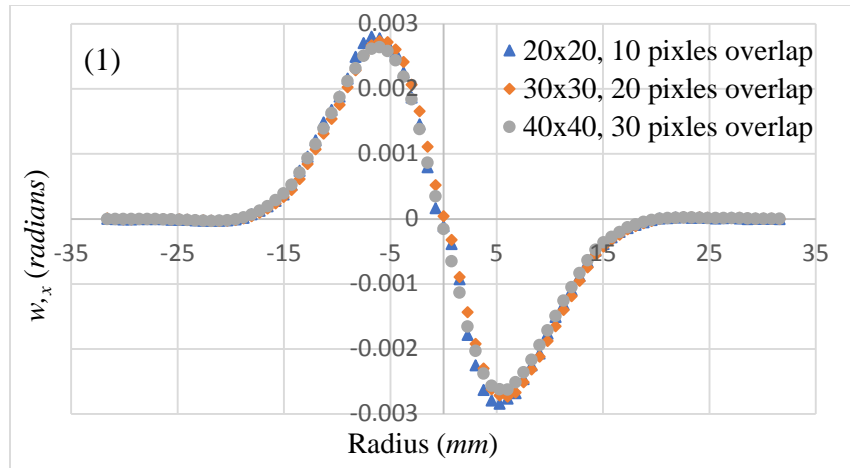


Figure 5.20: Effect of sub-image sizes for PMMA at  $t = 15 \mu\text{s}$  (1) on surface slope  $w_x$ ; (2) on out-of-plane deformation; (3) on stress.

The estimated stress  $\sigma_{xx}$  was obtained from curvatures by differentiating the slope data. Once again, the effect of different sub-image sizes was observed to be acceptable. The smaller sub-image size produced noisier variation relative to the larger sub-image; approx. 13% in the peak stress value between the smallest and largest sub-image sizes is evident. Furthermore, the two different numerical differentiation schemes tested did not show significant effect on the outcome with values deviating between 4-5% (see Figure 5.21).

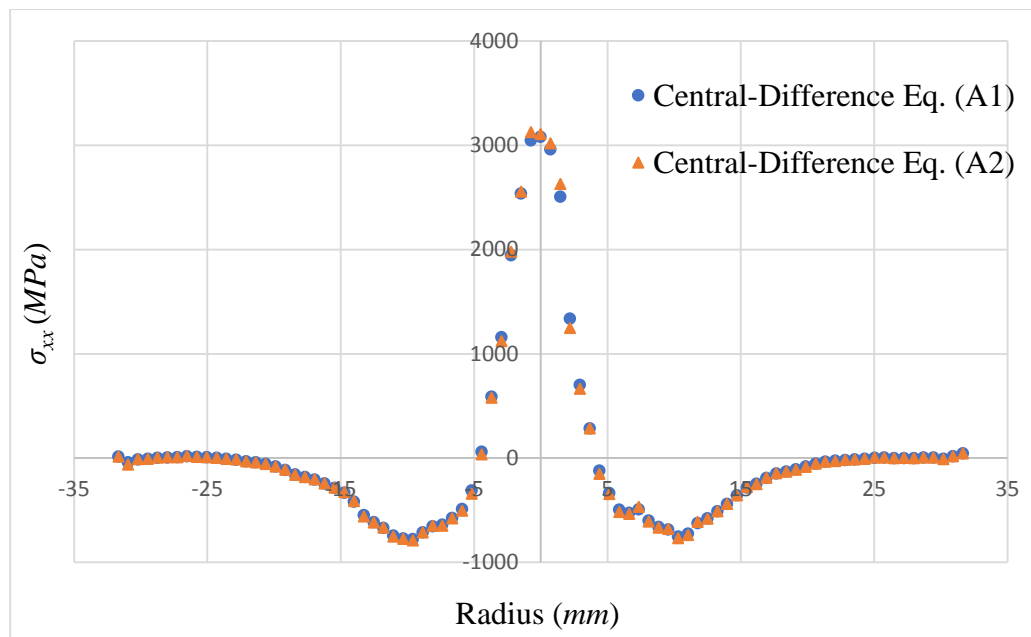
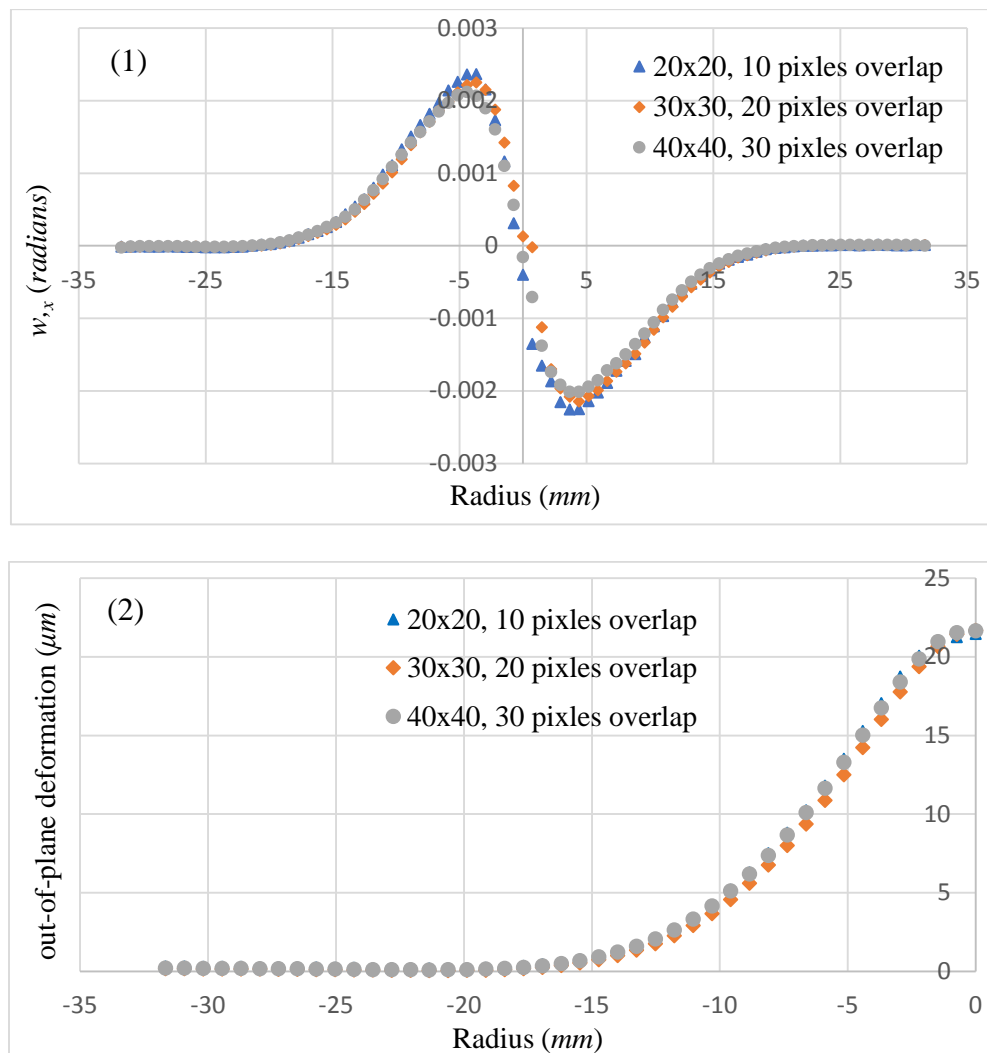


Figure 5.21: Estimated stress obtained from different numerical differentiations for 40x40 pixel sub-images,  $t = 15 \mu s$ .

CFRP: Experimental results for unidirectional CFRP along the fiber direction, again at  $t = 15 \mu s$  after impact, are plotted in Figure 5.22. Similar effects of sub-image sizes can be observed in measured surface slope, and post-processed out-of-plane deformation and stress data shown in Figure 5.22(1)-(3), respectively. The maximum

(magnitude) slope difference between 20×20 and 40×40 sub-image size choice was approx. 6.9%. The larger sub-image size resulted in a smaller magnitude of maximum slopes relative to smaller sub-image size. Again, the latter produced noisier variation of slopes relative to the former. The difference in maximum out-of-plane deformations were significantly reduced (< 0.5%) upon numerical integration whereas maximum stress  $\sigma_{xx}$  (along the fibers) showed 3.5% difference between 20×20 and 40×40 sub-image size.



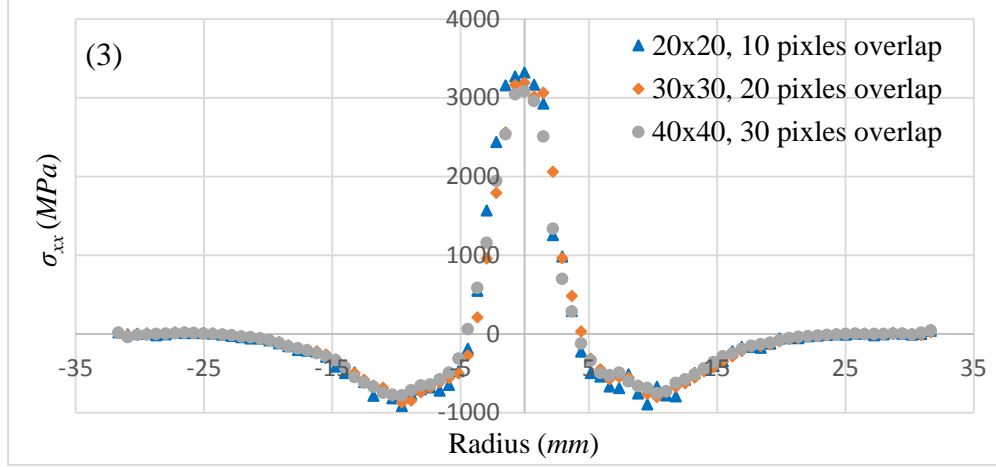


Figure 5.22: Effect of sub-image sizes for unidirectional CFRP at  $t = 15 \mu\text{s}$ : (1) on surface slope  $w_{,x}$ ; (2) on out-of-plane deformation; (3) on stress.

### 5.3.2 Effect of Numerical Differentiation

To verify the effect of different differentiation on the estimated stress, the measured slopes of unidirectional CFRP at  $t = 15 \mu\text{s}$  were differentiated using two classical central difference schemes [125],

$$f''(x) \approx \frac{f'(x+h) - f'(x-h)}{2h} \quad (5.2)$$

$$f''(x) \approx \frac{-f'(x+2h) + 8f'(x+h) - 8f'(x-h) + f'(x-2h)}{12h} \quad (5.3)$$

to obtain the local curvatures, where  $h$  is the interval between two neighboring data points of  $f'$ . The stresses shown in Figure 5.8 and Figure 5.14 were obtained using Eq. (5.2). The algorithmic error of Eq. (5.2) is of order  $O(h^2)$ , while for Eq. (5.3), the algorithmic error is  $O(h^4)$  [125]. The estimated stress component  $\sigma_{xx}$  along the  $x$ -axis corresponding to these two formulas is plotted in Figure 5.21. Evidently, the two sets of data nearly overlay with each other suggesting minimum influence of the numerical differentiation scheme in the range of 4-5%.

## Chapter 6. Fracture Behavior of Carbon Fiber Reinforced Polymer Composites: Loading Rate Effects

In this chapter, crack initiation and growth in single-edge notched unidirectional T800s/3900-2 CFRP laminates are studied under stress wave and quasi-static loading conditions. The effect of fiber orientation in the range  $0^\circ$ - $60^\circ$  relative to the initial notch and two loading rates are investigated. Extraction of crack-tip parameters - the instantaneous crack speed and stress intensity factor (SIFs) histories - associated with the stationary and propagating cracks using measured surface slopes is presented.

### 6.1 Dynamic Fracture

Fracture behavior of CFRP plates made of T800s/3900-2 unidirectional laminate with a  $[0_{36}]$  lay-up (Toray Composites America, Inc.) were studied first. The specimens were cut into  $152 \text{ mm} \times 76 \text{ mm} \times 6.8 \text{ mm}$  plates of five different fiber orientations,  $\alpha = 0^\circ$ ,  $15^\circ$ ,  $30^\circ$ ,  $45^\circ$  and  $60^\circ$  with respect to the initial edge crack direction, as depicted in Figure 6.1. The elastic properties of T800s/3900-2 unidirectional laminate are listed in Table 6-1 [124] where subscripts 1 and 2 represent directions along and normal to the fiber direction, respectively, and subscript 3 represents the out-of-plane direction. For specimens with different fiber orientations, elastic moduli and Poisson's ratios, corresponding to the global coordinate system shown in Figure 6.1, were computed by rotational transformations and are listed in Table 6-2. The so-called degree-of-anisotropy,  $\frac{E_{xx}}{E_{yy}}$ , for different specimens

are also listed in Table 6-2. For each specimen, a 10 mm long horizontal pre-notch was cut at the middle of the long edge using a 300  $\mu\text{m}$  thick diamond saw and then sharpened using a razor blade. The impact load was also imposed at the middle of the edge opposite to the cracked edge. That is, when  $\alpha = 0^\circ$  nominally mode-I fracture conditions occur whereas mixed-mode (mode-I + II) conditions arise for all other non-zero angles. One of the two 152 mm  $\times$  76 mm faces of each specimen was made reflective by using the aluminum film transfer technique to implement *r*-DGS.

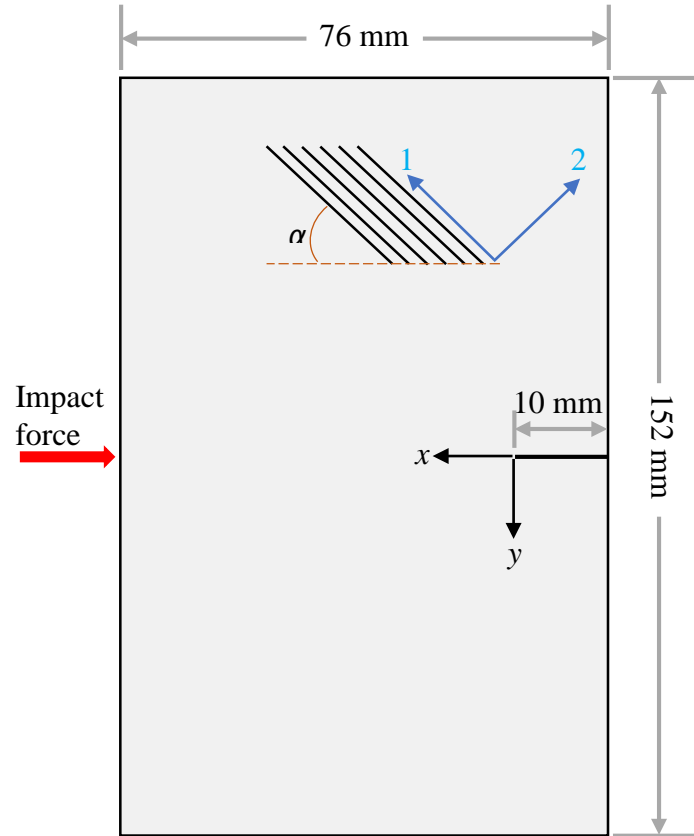


Figure 6.1: Specimen configuration.

Table 6-1: Material properties of T800s/3900-2 unidirectional laminate [124]

$E_1$ (GPa)	$E_2$ (GPa)	$G_{12}$ (GPa)	$\nu_{12}$	$\nu_{13}$	$\nu_{23}$
152.0	8.0	4.0	0.34	0.34	0.45

Table 6-2: Material properties of specimens with different  $\alpha$ .

	$\alpha = 0^\circ$	$\alpha = 15^\circ$	$\alpha = 30^\circ$	$\alpha = 45^\circ$	$\alpha = 60^\circ$
$E_{xx}$ (GPa)	152.0	46.2	17.4	10.6	8.6
$E_{yy}$ (GPa)	8.0	8.1	8.6	10.6	17.4
$G_{xy}$ (GPa)	4.0	4.5	6.1	7.5	6.1
$\nu_{xy}$	0.34	0.43	0.41	0.33	0.20
$E_{xx}/E_{yy}$	19.0	5.7	2.0	1.0	0.5

The schematic of the experimental setup used is shown in Figure 6.2. A modified Hopkinson pressure bar, or simply a ‘long-bar’, was used for loading the edge-cracked composite specimens. The long-bar was a 1.83 m steel rod of 25.4 mm diameter with a polished wedge-shaped tip for impacting an unconstrained CFRP plate on the edge opposite to the cracked edge. A 305 mm long, 25.4 mm diameter steel striker placed in the barrel of a gas-gun was co-axially aligned with the long-bar at the start of the experiment. The striker was launched towards the long-bar at a velocity of approx. 6 m/s during tests. A close-up view of the optical arrangement is also shown in Figure 6.2. Initially, the long-bar tip was kept in contact with the specimen. The specimen was positioned on the platform using a rectangular soft putty strip to prevent direct contact with the platform. To achieve symmetry in terms of acoustic impedance relative to the loading axis, another putty strip was pressed onto the top edge of the specimen. The lower putty strip isolated the specimen from the support to create an approximately ‘free surface’ condition away from the loading point. A beam splitter and the speckle target plate were placed in a specially designed  $45^\circ$  holder so that the camera could be focused on the speckles through the beam splitter via

the reflective specimen surface. The speckle images were photographed by a Kirana-05M ultrahigh-speed digital camera, a single sensor camera capable of recording 180 10-bit gray scale images at a maximum rate of 5 million frames per second and spatial resolution of  $924 \times 768$  pixels per image. The speckles on the target plate were illuminated using a pair of Cordin-659 high energy flash lamps.

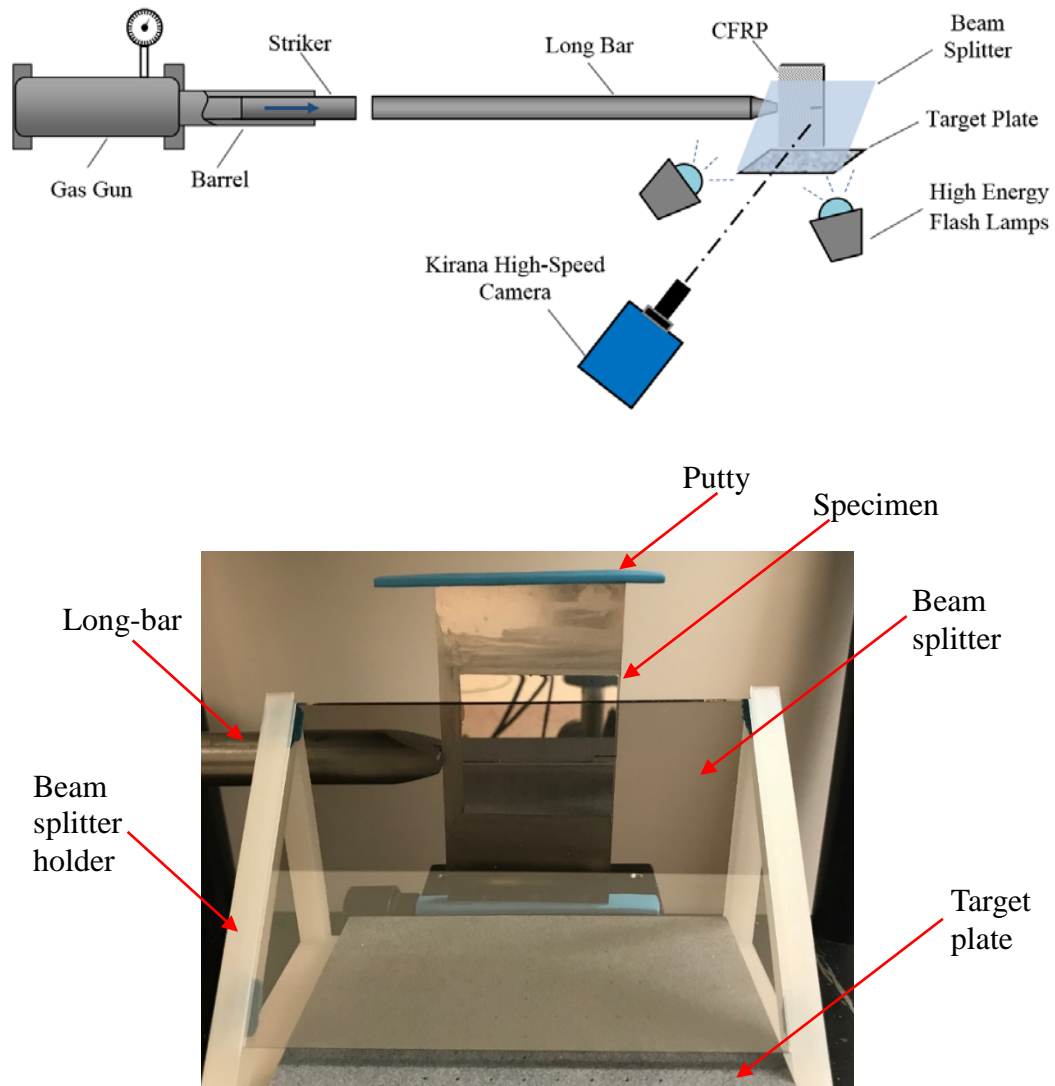


Figure 6.2: Schematic (top) and close-up photograph (bottom) of the experimental setup used to study dynamic fracture behavior of CFRP.

A Nikon 70-300 mm focal length zoom lens with an adjustable bellows was used with the camera to record the speckle images from a long distance. An optimum sensor exposure and focus were achieved by stopping down the lens aperture to F<sup>#</sup>11 after focusing. The distance between the specimen and the lens plane ( $L$ ) was ~780 mm and the one between the specimen mid-plane and the target plane ( $\Delta$ ) was ~70 mm. With these settings, the camera recorded information from a rectangular region of approximately 40 mm  $\times$  35 mm on the specimen plane in the vicinity of the pre-notch tip as the region-of-interest (ROI). When the long-bar was impacted by the striker, a compressive stress wave was set off and it propagated the entire length of the bar. Also, a trigger pulse was generated at the moment of impact to start recording the speckle images by the camera with a prescribed delay. A total of 180 images, some in the undeformed state and others in the deformed state of the specimen, were recorded at 500,000 frames per second (inter frame period 2  $\mu$ s). One image just before the start of deformation was selected as the reference image. Subsequent images corresponding to the deformed state were correlated with the reference image using ARAMIS<sup>®</sup> image analysis software. During analysis, a sub-image size of 30  $\times$  30 pixels (1 pixel = 45.68  $\mu$ m<sup>8</sup> on the specimen) with 25 pixels overlap was used to extract the local displacements  $\delta_{x;y}$  in the ROI<sup>9</sup>. The displacement fields were

then used to compute the two orthogonal surface slopes,  $\frac{\partial w}{\partial x; y}$ .

---

<sup>8</sup> The lower limit of measurable in-plane displacements using DIC being  $\pm 1-2\%$  of the scale factor, under ideal conditions the smallest measurable angular deflection is  $\sim \pm 1.3 \times 10^{-5}$  rad.

<sup>9</sup> The effect of sub-image size and step size chosen for this optical setup are reported in Chapter 5 and Ref. [139].

Measured surface slopes of  $\frac{\partial w}{\partial x; y}$  around a dynamically loaded mode-I crack for  $\alpha = 0^\circ$  are shown in Figure 6.3 at a few select time instants. In these plots,  $t = 0 \mu s$  corresponds to crack initiation at the original notch-tip. It can be observed that, due to the symmetric nature of mode-I fracture, the crack propagates along a horizontal path (from right to left in these images) and hence the contours are generally symmetric in shape relative to the initial crack. The increasing size of  $\frac{\partial w}{\partial x; y}$  contours during propagation qualitatively indicates an increase in stress intensity factors during crack propagation. It can be observed that contours of  $\frac{\partial w}{\partial x}$  are rather well-defined when compared to those for  $\frac{\partial w}{\partial y}$ , especially after crack initiation. This is because the fiber orientation being along the horizontal direction,  $\frac{\partial w}{\partial x}$  contours are affected to a lesser extent by the fibers when compared with the  $\frac{\partial w}{\partial y}$  counterparts. The contours near the left-hand edge in these plots are attributed to the concentration of deformations due to the impact load imposed on that edge (outside the ROI).

For completeness, the contours of out-of-plane displacements ( $w(x, y)$ ) computed by 2D integration of slope data from  $r$ -DGS in conjunction with Higher-order Finite-difference-based Least-squares Integration (HFLI) algorithm [117] are plotted in Figure 6.4<sup>10</sup>. The singular crack-tip deformations (negative values) before crack initiation and

---

<sup>10</sup> Based on the smallest measurable angular deflection, quantifiable out-of-plane displacement from the least-squares integration scheme is well below  $\pm 0.2 \mu m$ .

during crack growth are clearly evident. A noticeable concentration of positive  $w(x, y)$  along the left hand edge is again attributed to the impact loading on the coupon.

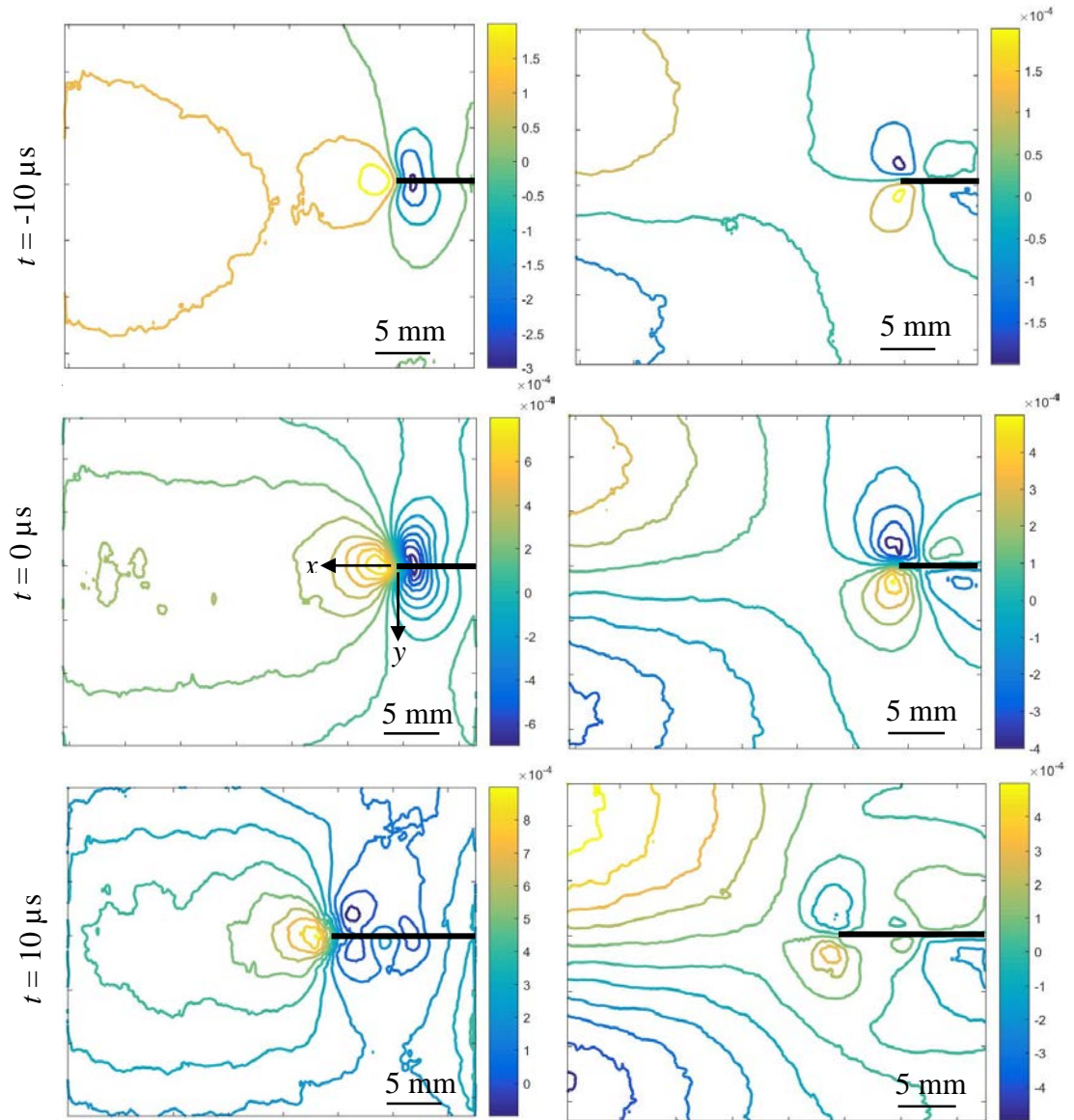


Figure 6.3: Measured surface slopes  $w_x$  (left column) and  $w_y$  (right column) contours for CFRP of mode-I dynamic fracture. Contour increment =  $1 \times 10^{-4}$  rad. Black strips highlight the crack.

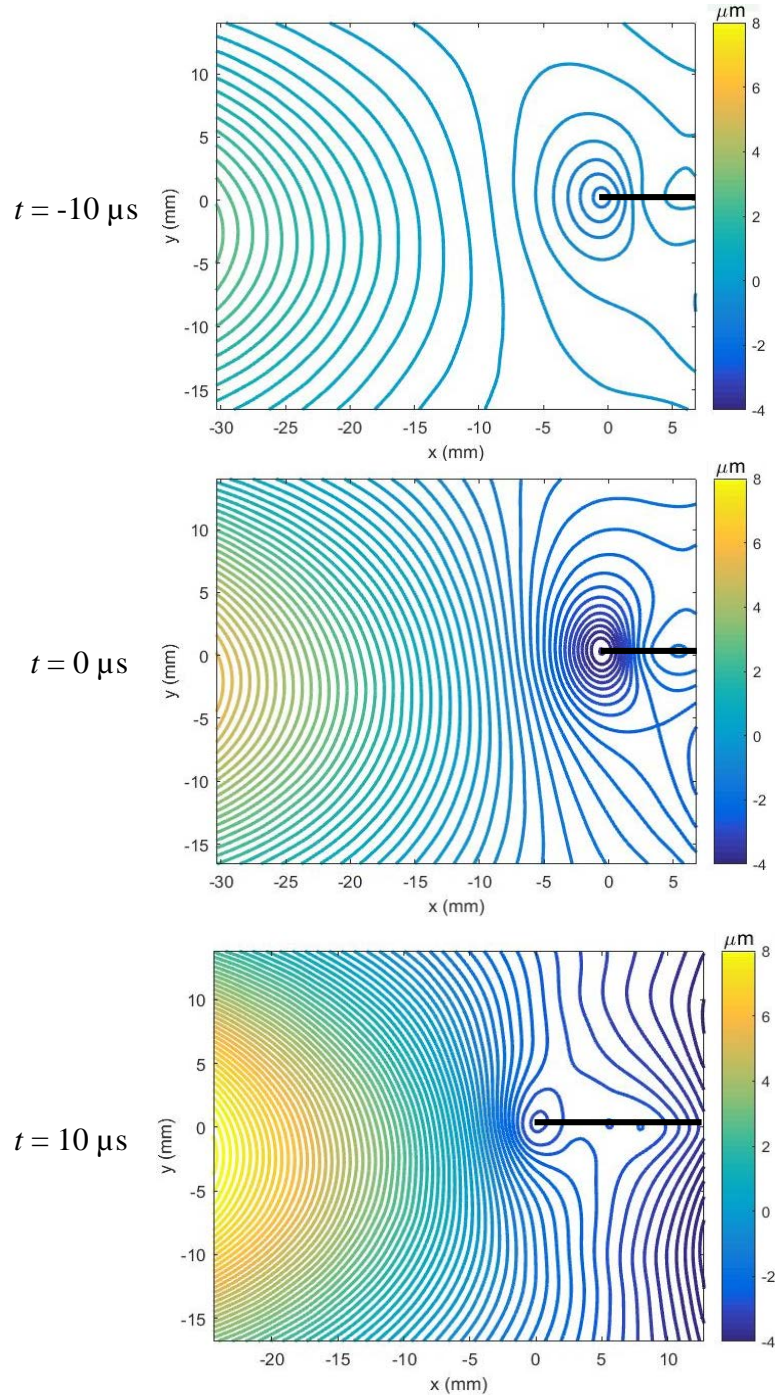


Figure 6.4: Contours of out-of-plane displacements ( $w(x, y)$ ) ( $0.2 \mu\text{m}$  intervals) for CFRP during mode-I dynamic fracture at a few select time instants before and after crack initiation ( $t=0$ ). Black strips highlight the crack. Concentration of (+) out-of-plane displacements at the left hand edge is due to impact loading whereas singularity of  $w$ -field around the crack tip (-) is due to the discontinuity.

The measured surface slopes of  $\frac{\partial w}{\partial x}$  around the dynamically loaded cracks for  $\alpha = 15^\circ, 30^\circ, 45^\circ, 60^\circ$  are shown in Figure 6.5 at a few select time instants. It should be noted that, all the contours depicted in Figure 6.5(b) are plotted in the coordinates  $(x, y)$ . The mixed-mode fracture behaviors can be readily observed here due to the fiber orientations being not along the loading direction namely the  $-x$ -axis. Figure 6.5(a)-(d) correspond to  $\frac{\partial w}{\partial x}$  of each specimen at  $t = 0 \mu s$  or just before crack initiation; it can be observed in these plots that these contours generally lack symmetry relative to the initial crack orientation and become more tilted as the fiber orientation increases. Figure 6.5(e)-(h) correspond to  $\frac{\partial w}{\partial x}$  of each specimen at  $t = 20 \mu s$ , or when the cracks have propagated for  $20 \mu s$  after crack initiation in each case. The dominant contours are at the current crack-tip whereas those at the original notch-tip represent residual/unrecovered deformations. The dotted lines indicate the crack path after initiation and solid lines represent the initial crack direction in these plots. It can be observed that the crack propagation occurs along the fiber direction as expected although they are subjected to identical geometrically symmetric impact loading. Furthermore, the specimen with  $\alpha = 15^\circ$  has the longest crack growth at  $t = 20 \mu s$  and the amount of crack growth is lower with increasing angles of fiber orientation relative to loading direction.

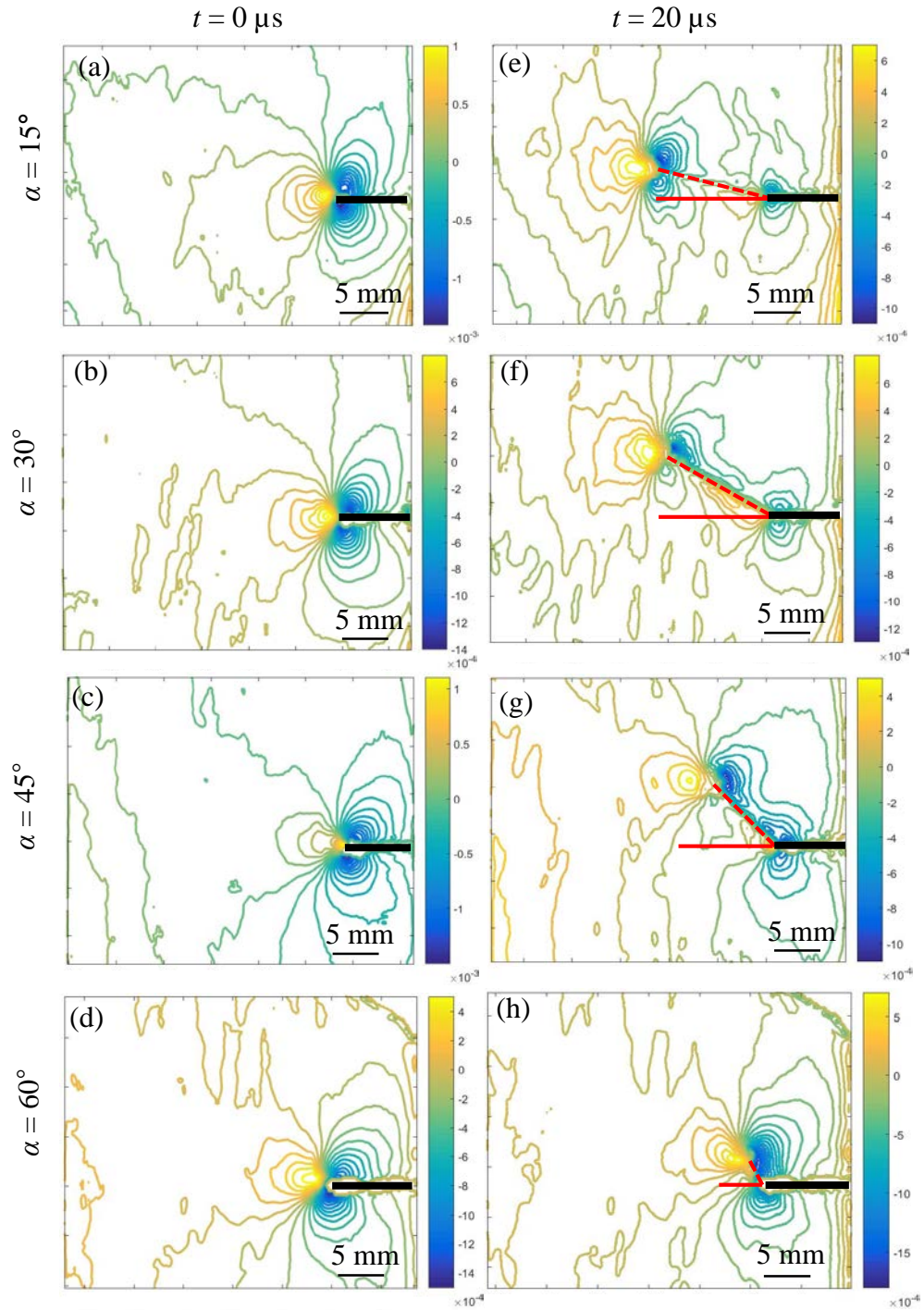


Figure 6.5: Measured surface slopes  $w_{,x}$  contours for CFRP of mixed-mode dynamic fracture. Contour increments =  $1 \times 10^{-4}$  rad. (Black strips are overlaid to highlight the crack; broken red line suggests kinked crack growth path.)

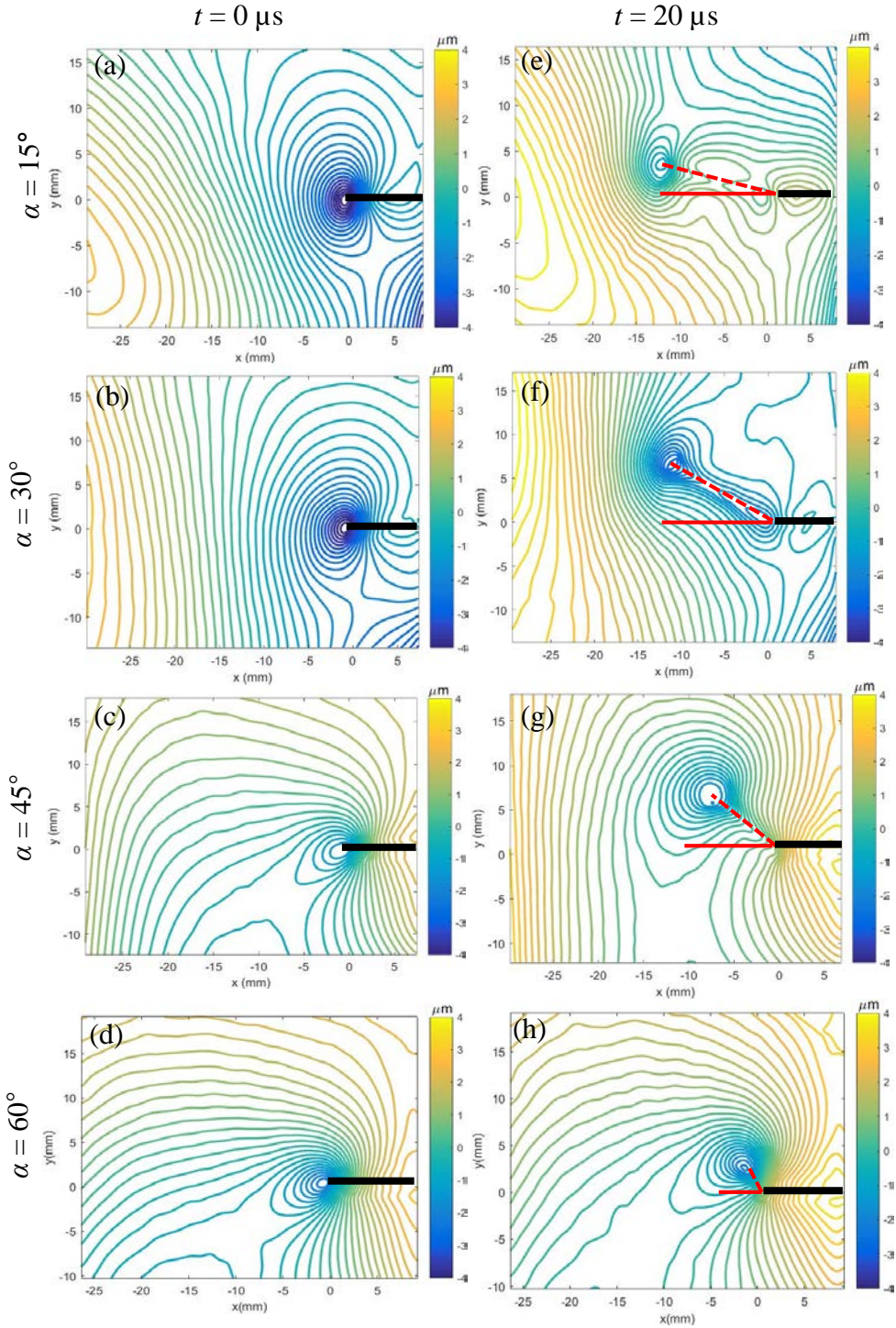


Figure 6.6: Contours of out-of-plane displacements ( $w(x, y)$ ) ( $0.2 \mu\text{m}$  intervals) for CFRP during mixed-mode dynamic fracture at a few select time instants. (Black strips are overlaid to highlight the crack; broken red line suggests kinked crack growth path.) Concentration of (+) out-of-plane displacements at the left hand edge is due to impact loading whereas singularity of  $w$ -field around the crack tip (-) is due to the discontinuity.

Again, for completeness, the contours of out-of-plane displacements ( $w(x, y)$ ), corresponding to the plots in Figure 6.5, computed using the 2D least-squares integration, are plotted in Figure 6.6. Concentrations of singular crack-tip deformations (negative) before crack initiation and during crack growth are clearly evident. Evidently, higher concentration of  $w(x, y)$  at crack initiation relative to the one during propagation qualitatively suggests a drop in the stress intensification during dynamic growth. Additionally, it can be observed in Figure 6.6(a)-(d) that these out-of-plane displacements are somewhat more inclined as the fiber orientation increases, same as the phenomenon observed in Figure 6.5(a)-(d).

The crack growth histories during dynamic crack growth are plotted in Figure 6.7(a). Quadratic Bezier curves [126] with 0.5 as the control point were fitted to the instantaneous crack length (symbols) data resulting in smoothed crack growth histories (solid lines) shown in Figure 6.7(a). The crack speed histories are plotted in Figure 6.7(b). These generally show that after crack initiation the crack accelerates to a steady-state condition within 2-3 time steps. The averaged crack speed during steady state growth part was calculated in each case. Evidently, for  $\alpha = 0^\circ, 15^\circ$  and  $30^\circ$  cases the crack growth histories bunch up in a narrow range. That is, their average crack speeds are between 690-720 m/s. However, for  $\alpha = 45^\circ$ , a significant drop in speed to  $\sim 518$  m/s. For  $\alpha = 60^\circ$ , the crack growth occurred at the lowest speed of 200 m/s following initiation and decelerated to less than 100 m/s at later stages of growth.

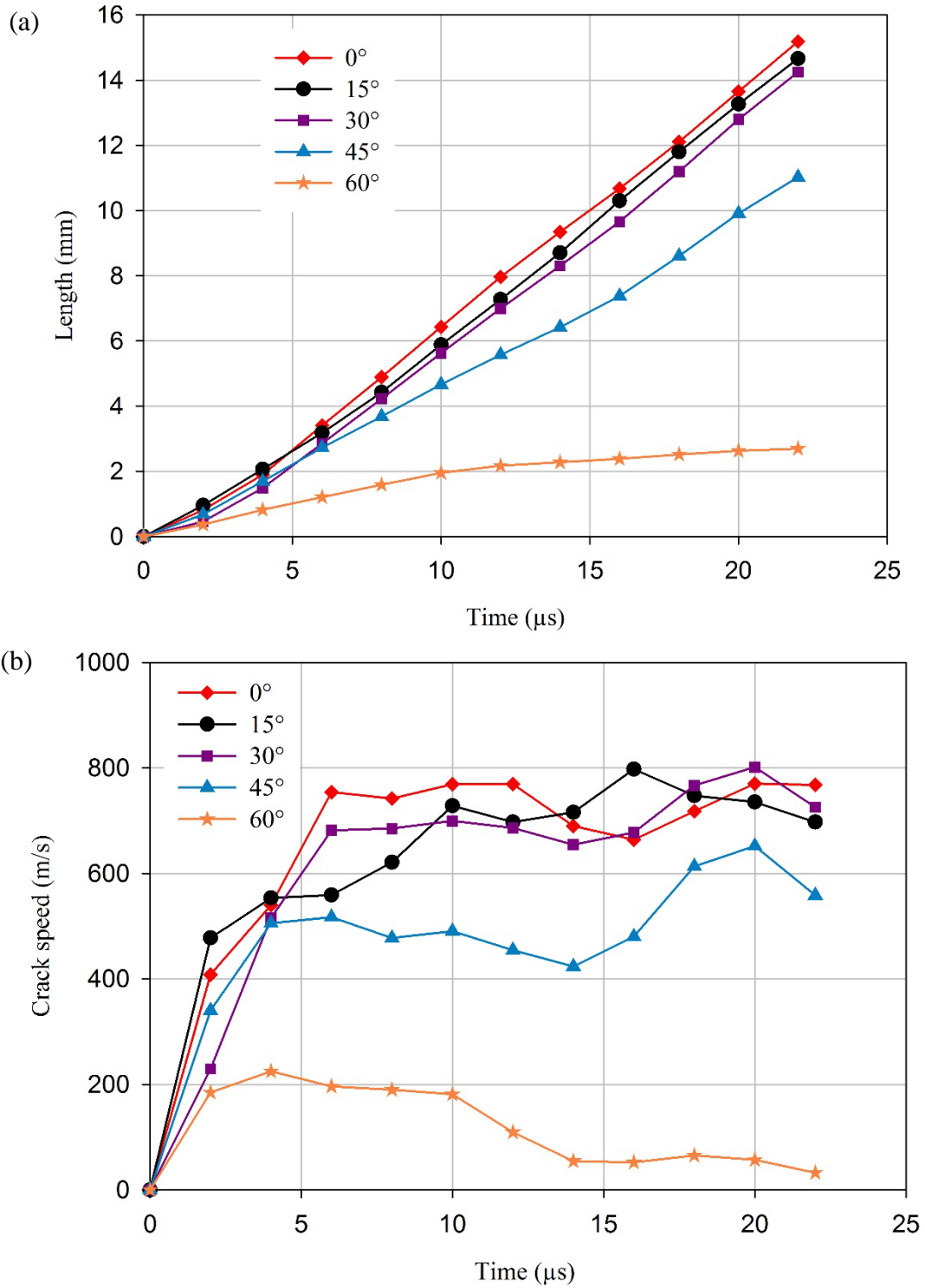


Figure 6.7: Crack growth (a) and velocity (b) histories during dynamic fracture of CFRP with different fiber orientation.

## 6.2 Quasi-Static Fracture

To study the loading rate effect on fracture behaviors of CFRP, quasi-static symmetric 3-point bending experiments were performed on edge notched CFRP coupons using *r*-DGS to measure deformations. Rectangular CFRP specimens of dimensions 152 mm × 56 mm × 6.8 mm with an initial crack of length 10 mm were used. As in the dynamic experiments, the specimens had different fiber orientations<sup>11</sup>,  $\alpha = 0^\circ, 15^\circ, 30^\circ$  and  $45^\circ$ , with respect to the initial crack direction, as shown in Figure 6.8(a). The specimens supported on two anvils (span 127 mm) were loaded using an Instron 4465 universal testing machine operating in displacement-control mode (cross-head speed = 0.007 mm/s). One of the two 152 mm × 56 mm faces of each specimen was made reflective using the aluminum film transfer technique to implement *r*-DGS. The schematic of the static experimental setup is shown in Figure 6.8(b). A beam splitter and the speckle target plate were placed in a  $45^\circ$  holder so that the camera could be focused on the speckles through the beam splitter via the reflective surface of the specimen. The target plate was illuminated by two LED lamps. The distance ( $\Delta$ ) between the mid-plane of the specimen and the target plate was  $\sim 70$  mm. A Nikon D100 digital SLR camera fitted with a 70-300 mm lens and an adjustable bellows was placed in-front of the specimen at  $\sim 1200$  mm ( $L$ ). A small aperture ( $F^\# = 11$ ) was selected for recording the speckles with a good focus. An 8-bit reference image was recorded with a resolution of  $1504 \times 1000$  pixels in the no-load state. While loading, the images corresponding to the deformed state were recorded at a rate of 0.5 frames per second as the anticipated crack speed was low. The speckle images in the deformed state were

---

<sup>11</sup> The load required to initiate the crack in the specimen with  $\alpha = 60^\circ$  exceeded the limit of the loading device and hence static fracture of that configuration was not studied.

correlated with the reference image using ARAMIS<sup>®</sup> image analysis software. For image correlation, a sub-image size of  $35 \times 35$  pixels (scale factor =  $35.08 \mu\text{m}/\text{pixel}$ ) with 25 pixels of overlap was used to extract the local speckle displacements  $\delta_{x;y}$  in the ROI. The displacement fields were then used to compute the two orthogonal surface slopes,  $\frac{\partial w}{\partial x; y}$ .

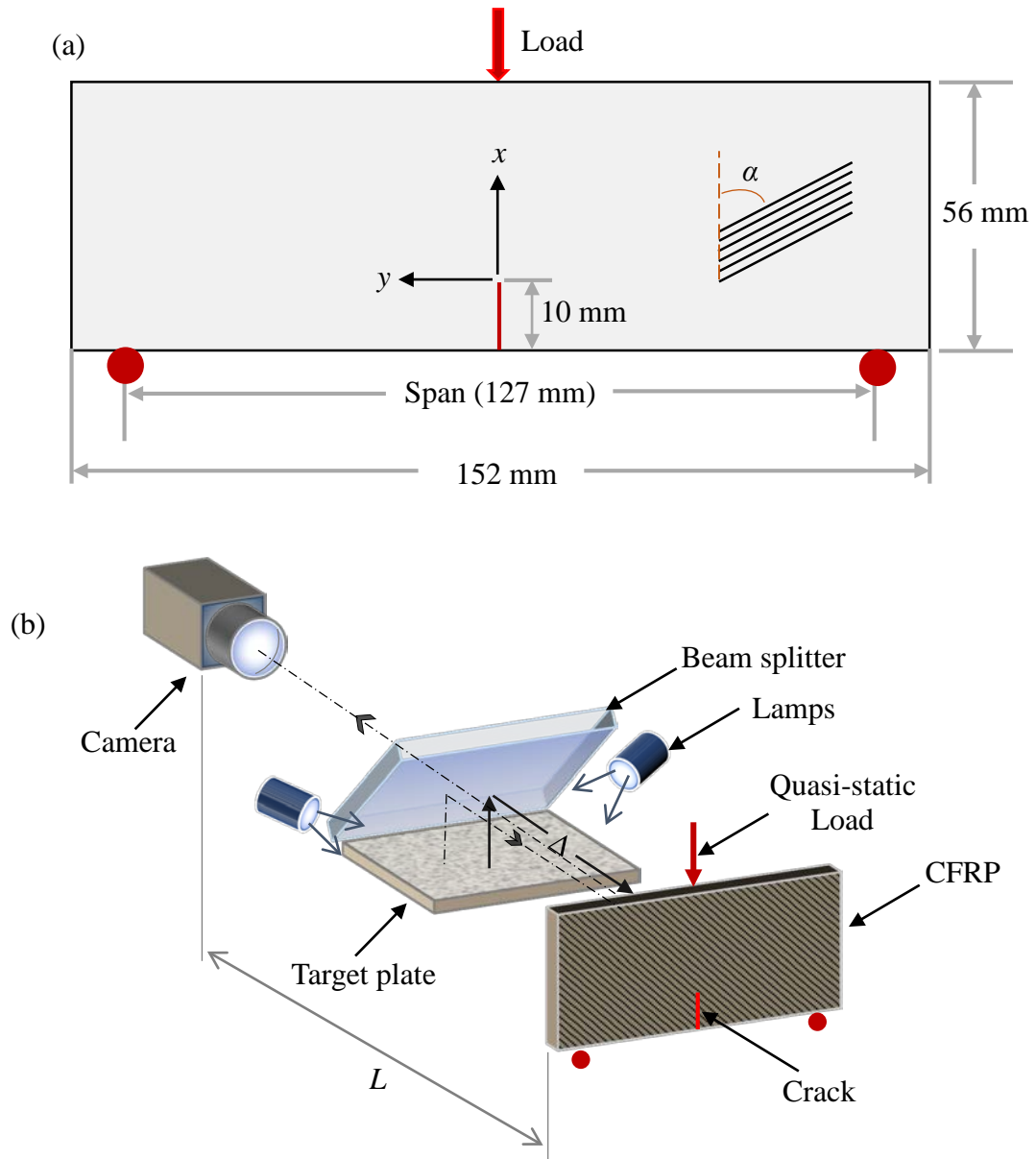


Figure 6.8: Details of quasi-static fracture experiments: (a) Specimen configuration, (b) Schematic of experiment setup.

The measured surface slopes of  $\frac{\partial w}{\partial x}$  around the crack-tip for  $\alpha = 15^\circ$  are shown in Figure 6.9 at a few select time instants. All the contours are plotted in the local crack-tip coordinates  $(x', y')$ ; here the  $x'$ -axis is along the crack propagation direction and the  $y'$ -axis is normal to the crack. Unlike in the dynamic events which last for a couple of hundred microseconds, the rigid body motions could occur during the static experiments as they last several minutes. The failure load histories for quasi-static fracture of CFRP are plotted as a function of the degree-of-anisotropy  $\frac{E_{xx}}{E_{yy}}$  in Figure 6.10(a). It includes two graphs, one for the load at crack initiation ( $t = 0$ ) and the other for the critical/peak load. The complete failure occurred only after the specimens crossed the critical load. It can be observed that the load value after crack initiation for each CFRP coupon is lower than the corresponding critical/peak load. This is attributed to fiber bridging of the crack faces resulting in additional load bearing capacity in each coupon after crack initiation. This is evident in the load-displacement histories for all specimens, plotted in Figure 6.10(b). An enlarged part of the plot for  $\frac{E_{xx}}{E_{yy}} = 19$  (or  $\alpha = 0^\circ$ ) is selected as an example to highlight crack initiation seen as a small kink in otherwise monotonic increase. In the inset, it can be observed that there is a small load drop, highlighted by the dotted circle, before the specimen attained the critical load, marked by the solid circle. The former represents the load at which the crack initiated first but continued to bear load until complete failure occurred after the critical load was attained. Both the critical load and crack initiation load show similar decreasing trends with the degrees-of-anisotropy. *It should be noted that the crack growth was recorded for only 12 s, whereas the specimens took much longer to cross the critical load.*

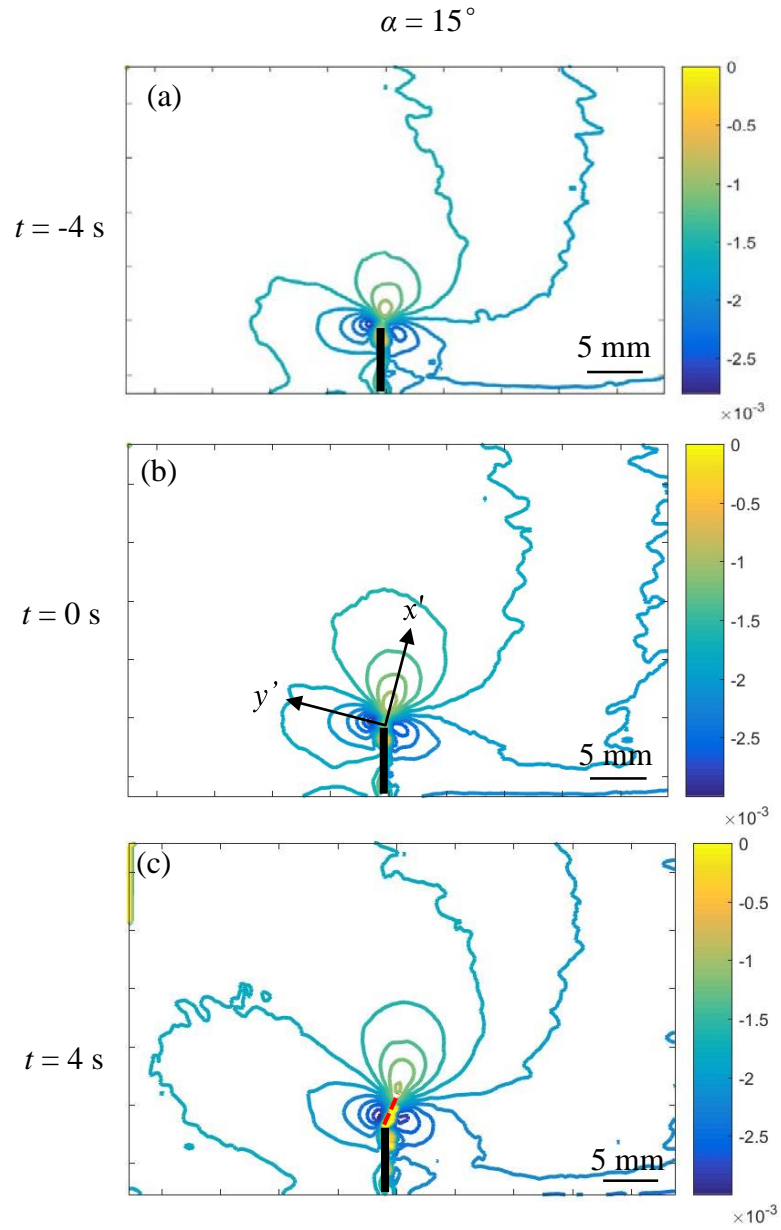


Figure 6.9: Measured surface slopes of  $\frac{\partial w}{\partial x}$  for quasi-static fracture tests on CFRP ( $\alpha = 15^\circ$ ). Contour increments =  $2 \times 10^{-4}$  rad. (Black strips are overlaid to highlight the crack; broken red line suggests kinked crack path.)

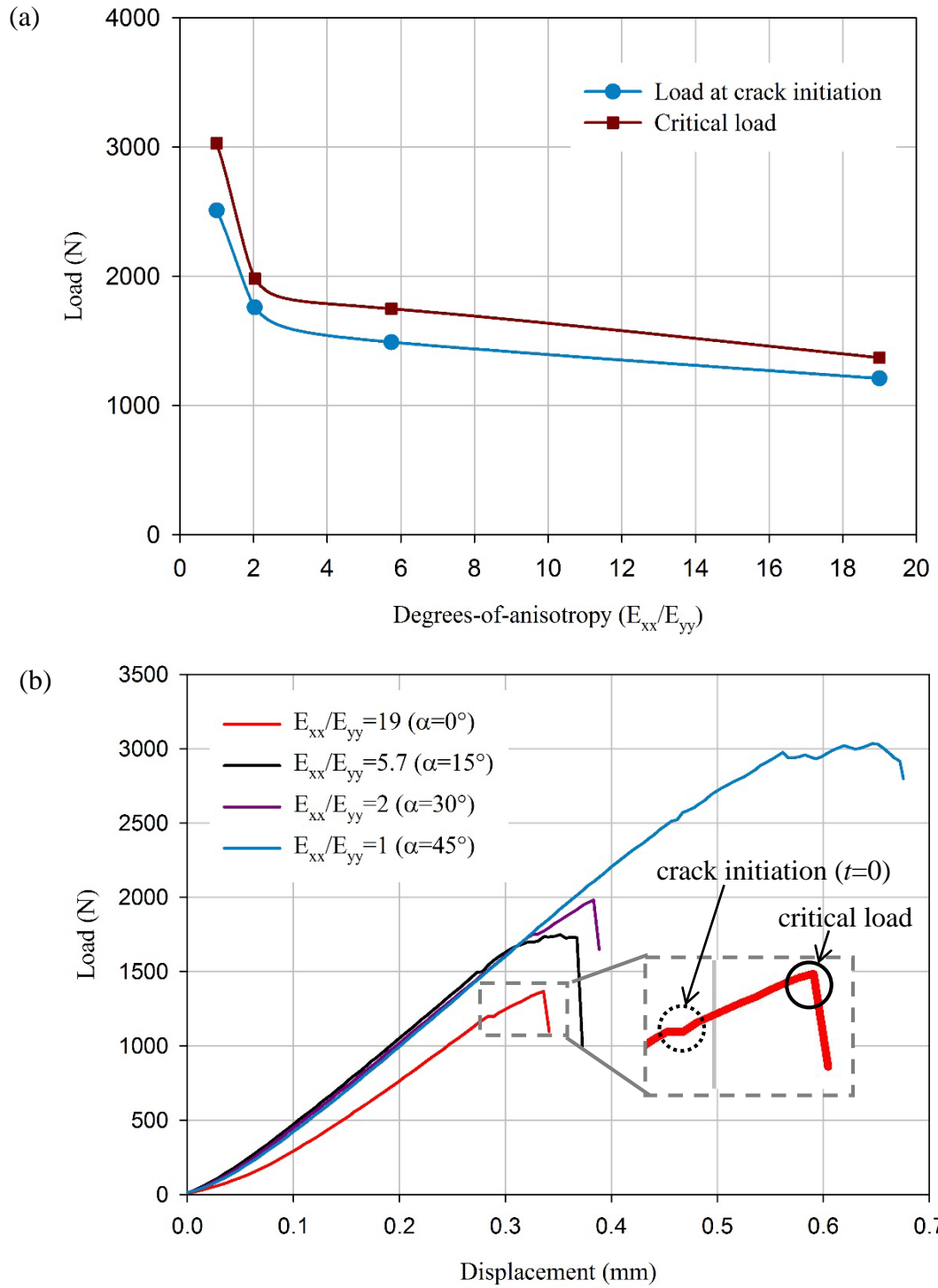


Figure 6.10: (a) Fracture load variations for different fiber orientations, (b) Load vs. load-point deflection histories.

### 6.3 Extraction of Stress Intensity Factors (SIFs)

The measured DGS data in the local crack-tip coordinates  $(x', y')$  are used to extract the mode-I and -II stress intensity factors (SIFs). The corresponding surface slopes  $\frac{\partial w}{\partial x'; y'}$

are expressed in terms of  $\frac{\partial w}{\partial x; y}$  in the global coordinates  $(x, y)$  using transformation equations,

$$\frac{\partial w}{\partial x'} = \frac{\partial w}{\partial x} \cos(\alpha) + \frac{\partial w}{\partial y} \sin(\alpha) \quad (6.1)$$

$$\frac{\partial w}{\partial y'} = -\frac{\partial w}{\partial x} \sin(\alpha) + \frac{\partial w}{\partial y} \cos(\alpha) \quad (6.2)$$

where  $\alpha$  is the fiber orientation angle for each case. An example of these transformations is shown in Figure 6.11. Figure 6.11(a) (same as Figure 6.5(g)) shows the measured surface slope  $\frac{\partial w}{\partial x}$  in the global coordinate system  $(x, y)$  whereas the one in the local coordinate is shown in Figure 6.11(b). The reorientation of the tri-lobed contours as a result of the transformation is readily evident.

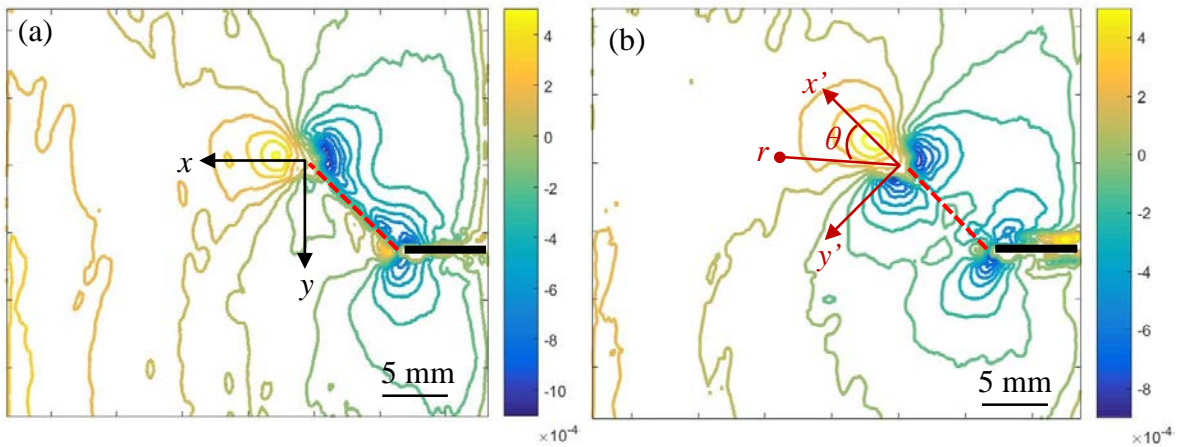


Figure 6.11: Measured surface slopes for  $\alpha = 45^\circ$  in (a)  $\frac{\partial w}{\partial x}$  contours, (b)  $\frac{\partial w}{\partial x'}$  contours. (Black strip highlights the crack; broken red line suggests kinked crack path.)

Now, the measured surface slopes  $\frac{\partial w}{\partial x'; y'}$  for a dynamically growing mixed-mode crack are expressed as follows [104]:

$$\begin{aligned}\frac{\partial w}{\partial x'} &= F_{11}(r, \theta)K_I + F_{12}(r, \theta)K_{II} \\ \frac{\partial w}{\partial y'} &= F_{21}(r, \theta)K_I + F_{22}(r, \theta)K_{II}\end{aligned}\tag{6.3}$$

where

$$\begin{aligned}F_{11} &= -\frac{h}{4\sqrt{2\pi}R(v)} \operatorname{Re} \left\{ \frac{\mu_2 - \lambda_2}{\lambda_1 - \lambda_2} \cdot \frac{\beta_1 - \beta_2 \mu_1 \lambda_1}{(r \cos \theta + \mu_1 r \sin \theta)^{3/2}} - \frac{\mu_1 - \lambda_1}{\lambda_1 - \lambda_2} \cdot \frac{\beta_1 - \beta_2 \mu_2 \lambda_2}{(r \cos \theta + \mu_2 r \sin \theta)^{3/2}} \right\} \\ F_{12} &= \frac{h}{4\sqrt{2\pi}R(v)} \operatorname{Re} \left\{ \frac{\gamma - \lambda \eta^2 \mu_2 \lambda_2}{\lambda_1 - \lambda_2} \cdot \frac{\beta_1 - \beta_2 \mu_1 \lambda_1}{(r \cos \theta + \mu_1 r \sin \theta)^{3/2}} - \frac{\gamma - \lambda \eta^2 \mu_1 \lambda_1}{\lambda_1 - \lambda_2} \cdot \frac{\beta_1 - \beta_2 \mu_2 \lambda_2}{(r \cos \theta + \mu_2 r \sin \theta)^{3/2}} \right\} \\ F_{21} &= -\frac{h}{4\sqrt{2\pi}R(v)} \operatorname{Re} \left\{ \frac{\mu_1(\mu_2 - \lambda_2)}{\lambda_1 - \lambda_2} \cdot \frac{\beta_1 - \beta_2 \mu_1 \lambda_1}{(r \cos \theta + \mu_1 r \sin \theta)^{3/2}} - \frac{\mu_2(\mu_1 - \lambda_1)}{\lambda_1 - \lambda_2} \cdot \frac{\beta_1 - \beta_2 \mu_2 \lambda_2}{(r \cos \theta + \mu_2 r \sin \theta)^{3/2}} \right\} \\ F_{22} &= \frac{h}{4\sqrt{2\pi}R(v)} \operatorname{Re} \left\{ \frac{\mu_1(\gamma - \lambda \eta^2 \mu_2 \lambda_2)}{\lambda_1 - \lambda_2} \cdot \frac{\beta_1 - \beta_2 \mu_1 \lambda_1}{(r \cos \theta + \mu_1 r \sin \theta)^{3/2}} - \frac{\mu_2(\gamma - \lambda \eta^2 \mu_1 \lambda_1)}{\lambda_1 - \lambda_2} \cdot \frac{\beta_1 - \beta_2 \mu_2 \lambda_2}{(r \cos \theta + \mu_2 r \sin \theta)^{3/2}} \right\}\end{aligned}$$

$h$  is the specimen thickness,  $(r, \theta)$  denotes the crack-tip polar coordinates as shown in Figure 6.11(b), and  $K_I$  and  $K_{II}$  are the dynamic stress intensity factors for mode-I and mode-II, respectively. The other parameters in Eq. (6.3) are defined as follows [104]:

$\beta_{1,2}$  are two material constants:  $\beta_1 = S_{31}\eta^2 + S_{32}\gamma$ ;  $\beta_2 = S_{31}\gamma + S_{32}\lambda\eta^2$ ;  $R(v)$  is the

generalized Rayleigh wave function:  $R(v) = \sqrt{\lambda}\eta^2\alpha_1(v)\alpha_s(v) - \frac{\sqrt{\lambda}\eta^2\alpha_1(v) + \gamma^2\alpha_s(v)}{\sqrt{\lambda}\eta^2\alpha_1(v) + \alpha_s(v)}$ ;

$$\lambda_i(v) = \frac{\eta^2\alpha_i^2(v) + \mu_i^2(v)}{(1 + \gamma)\mu_i(v)}, \quad i = 1, 2;$$

$\mu_j (j=1, 2)$  are the two roots with positive imaginary part of the characteristic equation:

$$\mu^4 + \frac{\lambda \eta^4 \alpha_l^2(v) + \alpha_s^2(v) - (1 + \gamma)^2}{\lambda \eta^2} \mu^2 + \frac{\alpha_l^2(v) \alpha_s^2(v)}{\lambda} = 0 \quad \lambda = \frac{\mathbf{S}_{11}}{\mathbf{S}_{22}}, \quad \rho = \frac{2s_{12} + s_{66}}{2\sqrt{s_{11}s_{22}}},$$

$$\kappa = \frac{3\sqrt{s_{11}s_{22}} + s_{12}}{\sqrt{s_{11}s_{22}} - s_{12}}, \quad c_l = \left(\frac{c_{11}}{d}\right)^{1/2}, \quad c_s = \left(\frac{c_{66}}{d}\right)^{1/2}, \quad \alpha_l^2(v) = 1 - \frac{v^2}{c_l^2}, \quad \alpha_s^2(v) = 1 - \frac{v^2}{c_s^2},$$

$$\eta^2 = \left(\frac{c_l}{c_s}\right)^2, \quad \gamma = \sqrt{\lambda} \eta^2 \left(\frac{3 - \kappa}{1 + \kappa}\right), \text{ in which } c_l \text{ is the longitudinal wave speed, } c_s \text{ is the}$$

shear wave speed,  $s_{ij}$  ( $i, j=1, \dots, 6$ ) are the elements of the compliance matrix,  $c_{ij}$  ( $i, j=1, \dots, 6$ ) are the elements of stiffness matrix,  $d$  is mass density,  $v$  is the crack-tip velocity.

As noted earlier, rigid body motions could occur during experiments in general, and quasi-static conditions in particular. These can be tackled by enforcing symmetry and far-field boundary conditions [54] [53] involving mode-I crack problems or by including rigid body motion terms while extracting the fracture parameters. That is, Eq. (6.3) can be modified as,

$$\frac{\partial w}{\partial x'} = F_{11}(r, \theta)K_I + F_{12}(r, \theta)K_{II} + C_1 x' + C_2 y' + C_3$$

$$\frac{\partial w}{\partial y'} = F_{21}(r, \theta)K_I + F_{22}(r, \theta)K_{II} + D_1 x' + D_2 y' + D_3$$

where the bilinear terms with unknown coefficients  $C_1 - C_3$  and  $D_1 - D_3$  account for rigid translations and rotations.

In the analysis,  $\frac{\partial w}{\partial x'}$  data in the region  $0.5 \leq r/h \leq 1.5$  and angular extent of  $-140^\circ \leq$

$\theta \leq 140^\circ$  near the crack-tip were used to calculate SIFs. The choice of the region excluded

triaxial deformations, further lessening the impact of crack-tip location errors on the estimated stress intensity factors. (It should be noted that least-squares over-deterministic SIF extraction showed that coefficients for the rigid rotation terms were significantly smaller, typically two orders of magnitude, relative to the constant term). Recognizing that the above equations degenerate to the quasi-static counterparts in the limit the crack-tip velocity,  $v$ , approaches zero, the equations were utilized for both statically and dynamically loaded stationary crack experiments.

Next, the SIFs were used to evaluate the strain energy release rate,  $G$  [104] as,

$$G = \frac{\eta}{2c_{66}R(v)} \left[ 1 - \left( \frac{1+\gamma}{\sqrt{\lambda}\eta^2\alpha_I(v) + \alpha_s(v)} \right)^2 \right]^{1/2} \left[ \alpha_I(v)K_I^2 + \sqrt{\lambda}\alpha_s(v)K_{II}^2 \right] \quad (6.4)$$

for a moving crack in dynamic fracture case. Further, Eq. (6.4) can be reduced to

$$G = s_{11} \sqrt{\frac{1+\rho}{2}} (\lambda^{-3/4} K_I^2 + \lambda^{-1/4} K_{II}^2) \quad (6.5)$$

for a dynamically loaded stationary crack and quasi-static crack cases.

## 6.4 Results and Discussion

A compilation of mode-I and mode-II stress intensity factor histories evaluated from  $r$ -DGS measurements for dynamically fractured CFRP specimens for different fiber orientations are plotted in Figure 6.12(a). The time axis of each plot was independently shifted so that  $t = 0 \mu\text{s}$  corresponds to crack initiation at the original notch-tip as determined from optically generated contours. The solid and open symbols in Figure 6.12(a) represent  $K_I$  and  $K_{II}$ , respectively. The  $K_I$  histories in all cases increase monotonically prior to crack initiation but drop abruptly once crack initiation occurs. Following the drop, they attain different but nearly steady values during crack propagation period, plotted up to 22  $\mu\text{s}$  after

initiation. As expected, nominally mode-I fracture occurs in  $\alpha = 0^\circ$  case as  $K_{II}$  values oscillate close to zero in the pre- and post-initiation regimes. When mixed-mode fractures occur in other CFRP specimens with fiber orientation  $\alpha = 15^\circ - 60^\circ$ , the  $K_{II}$  values increase in magnitude before crack initiation and further increase abruptly after crack initiation before settling to different but relatively steady values in the crack propagation period. It can be further observed that, with the increase of fiber orientation angle  $\alpha$ , there is an increase in the magnitude of  $K_{II}$  at crack initiation with larger  $\alpha$  resulting in higher plateau value. Additionally, as evident from the plot, it took longer for the crack to initiate with increasing fiber orientation angle; for example, it took approx. 50  $\mu\text{s}$  for  $\alpha = 45^\circ$  whereas it was around  $\sim 25 \mu\text{s}$  for  $\alpha = 15^\circ$ .<sup>12</sup>

A similar compilation of the two stress intensity factor histories for all configurations of quasi-static fracture of CFRP are plotted in Figure 6.12(b). Again, the time axes of the plots were shifted independently so that  $t = 0$  corresponds to crack initiation at the original notch-tip, determined from the optical contours. As noted earlier, the load to initiate the crack in the specimen with  $\alpha = 60^\circ$  exceeded the limit of the testing machine and hence was not studied. The  $K_I$  and  $K_{II}$  histories with  $\alpha = 30^\circ$  and  $45^\circ$  subjected to quasi-static loading have trends quite similar to the dynamic counterparts. That is, the optically extracted  $K_I$  and  $K_{II}$  values increase monotonically and somewhat linearly up to crack initiation. The  $K_I$  values abruptly drop at crack initiation before reaching a plateau. The  $K_I$  histories for  $\alpha = 0^\circ$  and  $15^\circ$ , however, show a slightly different trend after crack initiation.

---

<sup>12</sup> It should be noted that post-initiation variations of stress intensity factors, particularly the  $K_{II}$  histories reported here deviate from the ones in Ref. [110]. This is attributed to multiple differences in experimental details including loading apparatus and hence the loading profiles (drop-tower vs. Hopkinson bar), nature of the recording devise (multi-sensor vs. single sensor ultrahigh-speed camera), temporal resolution used (250 vs. 500 Kfps), and uncertainty associated with the crack tip location (non-singular displacements in DIC vs. singular surface slopes in r-DGS).

A change in the slope of  $K_I$  variation but without an abrupt drop is evident. This is attributed to fibers bridging the crack flanks preventing a significant drop from occurring in the  $K_I$  values at crack initiation in these two cases.

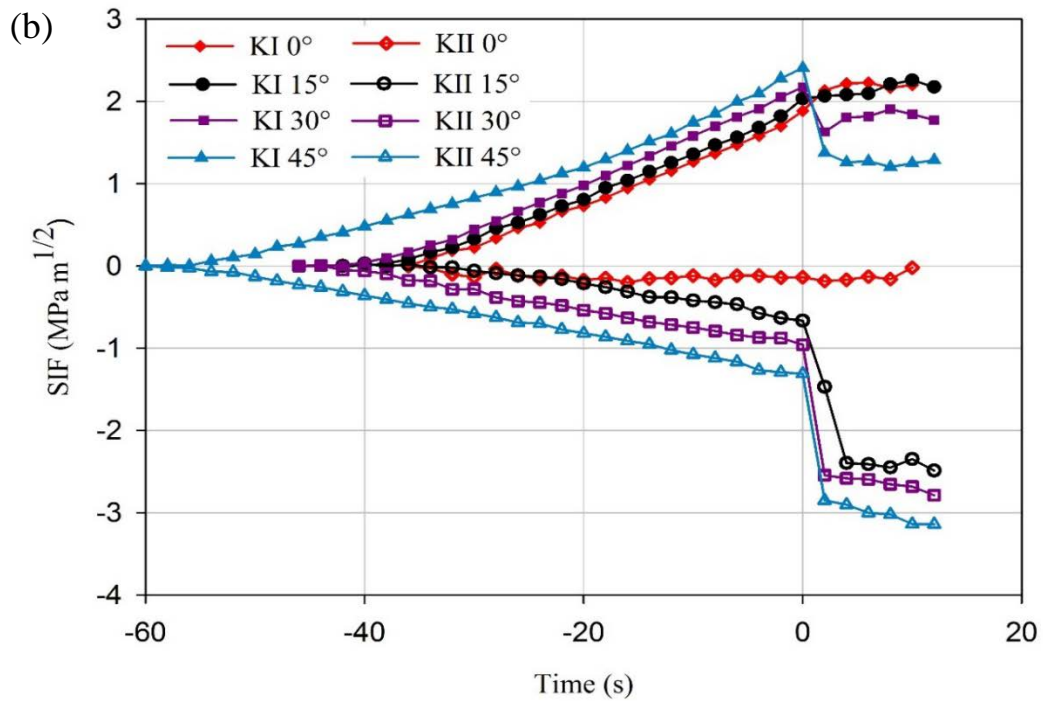
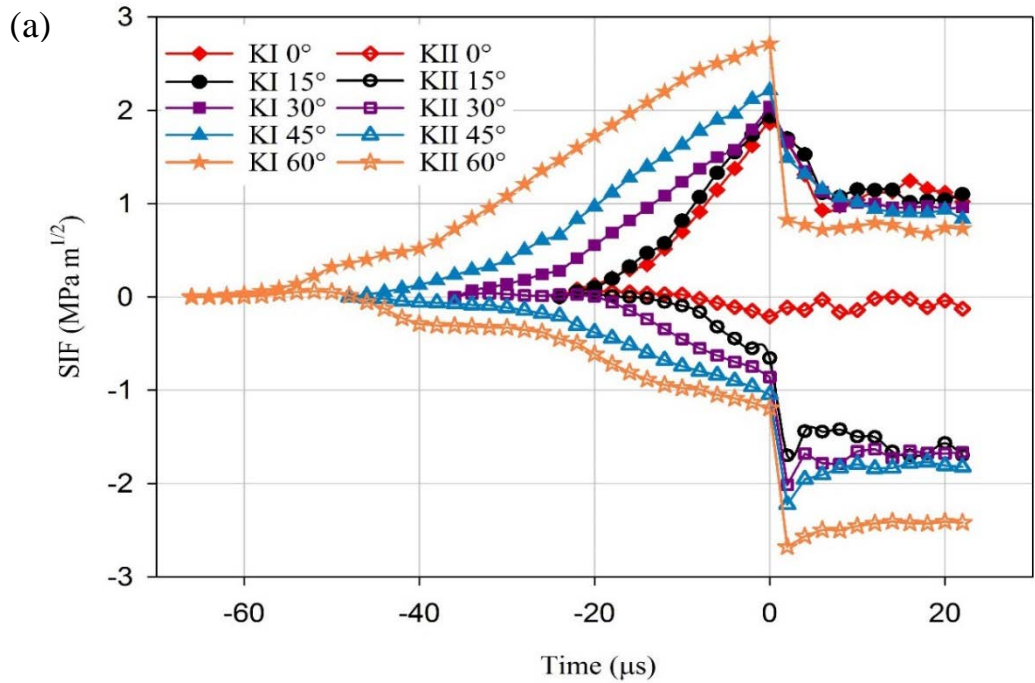


Figure 6.12: Compilation of measured stress intensity factor (SIF) histories for CFRP subjected to (a) dynamic loading and (b) quasi-static loading. ( $t = 0$  corresponds to apparent crack initiation.)

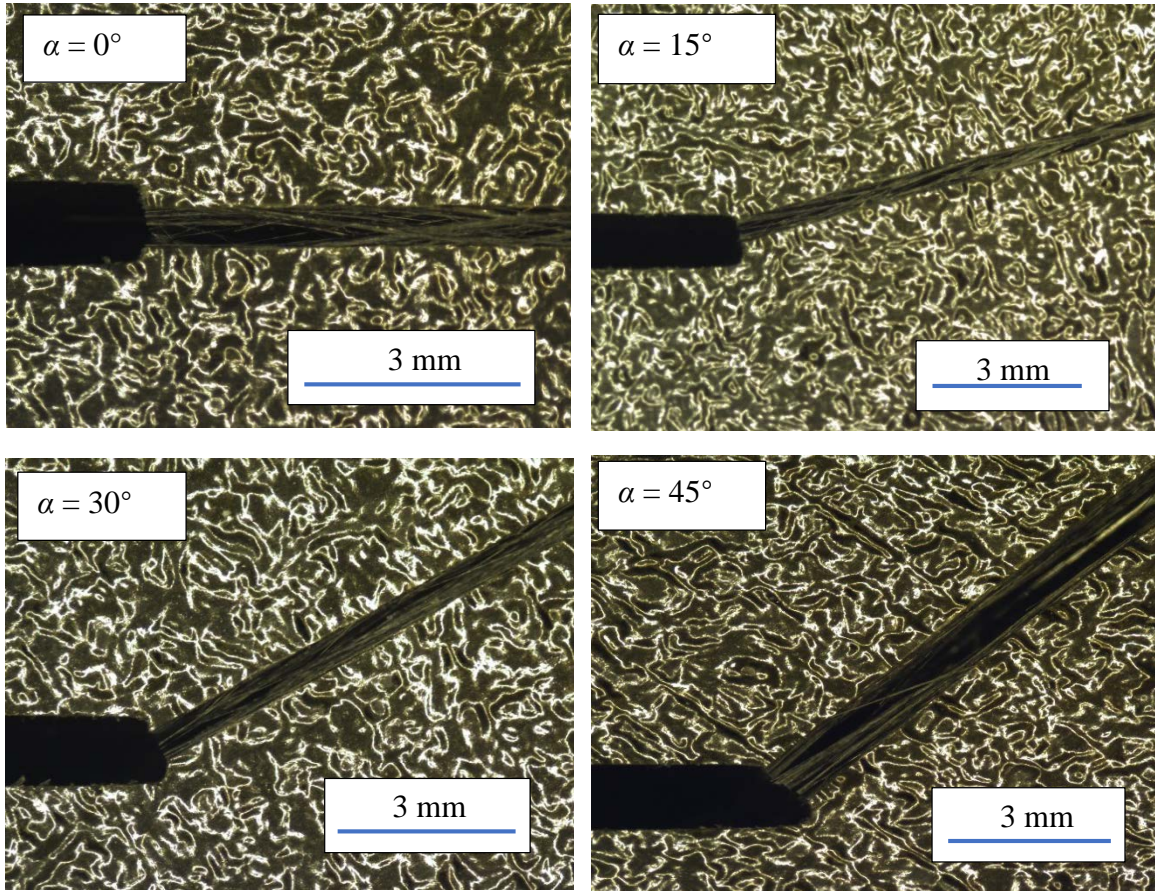


Figure 6.13: Cracked faces bridged by fibers in quasi-static experiments. (The random pattern elsewhere is due to the surface texture and angular illumination)

These crack bridges are evident from the micrographs of the failed samples shown in Figure 6.13. That is, fiber bridges in  $\alpha = 0^\circ$  and  $15^\circ$  cases contribute to a higher percentage of overall crack growth resistance when compared to  $\alpha = 30^\circ$  and  $45^\circ$  cases as load at crack initiation for the former two cases are much smaller than those for the latter ones (see, Figure 6.10(a)). The magnitude of  $K_{II}$  values in all cases (except  $\alpha = 0^\circ$ ) increase monotonically up to crack initiation. Furthermore, as in the dynamic cases, the crack initiation event in these cases is punctuated by an abrupt increase in the magnitude of  $K_{II}$

followed by the values reach different plateaus similar to the  $K_I$  histories. Also, these plateau values of  $K_{II}$  increase with increasing fiber orientation.

The energy release rate,  $G$ , histories were determined from Eqs. (6.4) and (6.5) for both high- and low-rate loading conditions and the results are compiled in Figure 6.14. In the pre-initiation regime, the  $G$  histories monotonically increase up to crack initiation with higher fiber orientation producing higher values at initiation. In the dynamic loading cases (Figure 6.14(a)), the peak value of  $G$  (340-590 N/m; see Table 6-3) occurred either at  $t = 0$  or one time step (2  $\mu$ s) after that, possibly due to the fiber bridging effects noted earlier. Aside this, the  $G$  values drop in all dynamic fracture cases after crack initiation and show a tendency to attain separate plateau values in different cases. The plateau values for different fiber orientations vary between  $\sim 145$  N/m in  $\alpha = 0^\circ$  to  $\sim 300$  N/m in  $\alpha = 45^\circ$ , nearly a half of the (peak) values at crack initiation. In the quasi-static loading cases (Figure 6.14(b)), the values of  $G$  show noticeably different trend in the post-initiation regime although they increase monotonically up to crack initiation for all fiber orientations as in the dynamic cases. Again, the values of  $G$  corresponding to crack initiation increases with fiber angle and are higher than the corresponding dynamic counterparts (Table 6-3). A striking difference in the quasi-static  $G$  histories is in the post-initiation regime where (i) a significant increase in  $G$  values are seen following crack initiation and, (ii) the  $G$  values continue to increase, though at a reduced rate, during the window-of-observation suggesting a relatively graceful failure prior to rapid fracture. This difference relative to the dynamic counterpart is significant as it conveys an important loading rate dependent post-initiation behavior of this CFRP namely dynamic loading produced a weaker post-initiation response relative to the quasi-static counterparts.

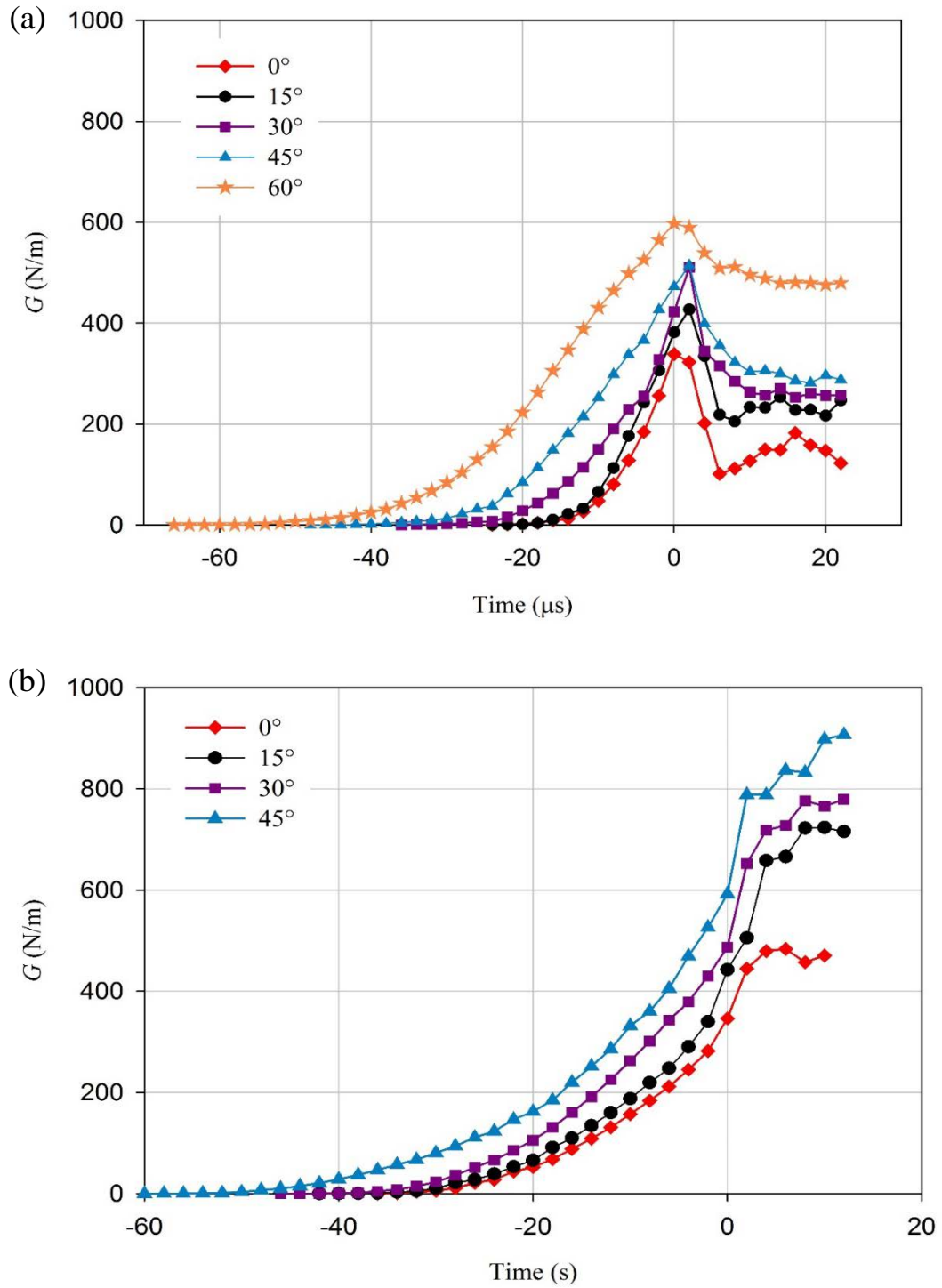


Figure 6.14: Energy release rate histories for CFRP with different fiber orientations (a) dynamic fracture and (b) quasi-static fracture. ( $t = 0$  corresponds to crack initiation.)

Table 6-3: Compilation of energy release rate ( $G$ ), mode-mixity ( $\psi$ ) and time rate of change of effective SIF ( $\dot{K}_{eff}$ )

	$E_{xx}/E_{yy}$	<b>19</b>	<b>5.7</b>	<b>2</b>	<b>1</b>	<b>0.5</b>
<b>Dynamic</b>	$G_{initiation}$ (N/m)	339	382	423	473	598
	$G_{growth}$ (N/m)	144±22	231±15	263±10	298±13	487±11
	$\psi_{initiation}$ (deg.)	-6	-18	-23	-25	-24
	$\psi_{growth}$ (deg.)	-4±3	-55±2	-60±1	-63±2	-73±1
	$\dot{K}_{eff}$ (MPa m <sup>1/2</sup> /s)	12×10 <sup>4</sup>	12×10 <sup>4</sup>	8×10 <sup>4</sup>	6×10 <sup>4</sup>	6×10 <sup>4</sup>
<b>Quasi-static</b>	$G_{initiation}$ (N/m)	346	443	487	592	-
	$G_{growth}$ (N/m)	473±11	697±32	754±28	853±50	-
	$\psi_{initiation}$ (deg.)	-4	-18	-23	-29	-
	$\dot{K}_{eff}$ (MPa m <sup>1/2</sup> /s)	6×10 <sup>-2</sup>	6×10 <sup>-2</sup>	6×10 <sup>-2</sup>	6×10 <sup>-2</sup>	-

A compilation of data for energy release rate,  $G$ , mode-mixity,  $\psi (= \tan^{-1} \left( \frac{K_{II}}{K_I} \right))$ ,

and time rate of change of effective SIF,  $\frac{dK_{eff}}{dt}$  or  $\dot{K}_{eff}$  ( $K_{eff} = \sqrt{K_I^2 + K_{II}^2}$ ), are

summarized in Table 6-3. The  $\dot{K}_{eff}$  for the dynamic experiments are in the 6×10<sup>4</sup> to 12×10<sup>4</sup> MPa√m·s<sup>-1</sup> range whereas they are 6×10<sup>-2</sup> MPa√m·s<sup>-1</sup> for static conditions. The values of  $G$  and  $\psi$  during crack growth are averaged from 8 μs to 22 μs and from 4 s to 12 s in dynamic and quasi-static cases, respectively. These values increase with fiber orientation in case of both the loading rates. It can be observed that energy release rates under quasi-static conditions during crack growth are higher than the corresponding values under dynamic loading conditions suggesting a weaker post-initiation response relative to the quasi-static counterparts.

In the context of the above discussion, it is worth recapping the results of some reports in the literature. Tang *et al.* [94] investigated fracture mechanism of three-dimensional CFRP under static and dynamic loadings, and reported that cracks propagated

as a zigzag pattern in static loading condition, whereas a region of surface ablation occurred seen under dynamic loading conditions. Lee *et al.* [110] studied fracture behavior of unidirectional CFRP under static and dynamic loadings, and reported that fiber bridging in quasi-static loading condition. Mallon *et al.* [113] studied fracture behavior of orthotropic woven glass fiber-reinforced composites under quasi-static and shock loading conditions. Fiber bridging was observed during quasi-static loading, and was associated with higher stress intensity factors. Hoffmann *et al.* [114] reported that the strain-energy release rate of a composite laminate under high-rate loading was lower than its quasi-static counterpart. They also observed a more extensive damage zone under quasi-static conditions than high-rate loading counterparts.

## **Chapter 7. Higher Sensitivity Digital Gradient Sensing Configurations for Transparent Solids**

In this chapter, two modified full-field Digital Gradient Sensing (DGS) methods of higher measurement sensitivity relative to the prevailing ones are described for quantifying small angular deflections of light rays caused by stresses in transparent solids. These methods are devised by combining or altering previously proposed reflection-mode DGS (*r*-DGS) and transmission-mode DGS (*t*-DGS) methods. The working principles of the two new DGS methods will be explained and verified by experiments. The feasibility of application of the two new DGS methods for fracture mechanics is also investigated.

### **7.1 Extensions of *r*-DGS and *t*-DGS Methods**

#### **7.1.1 Double/Dual Transmission Digital Gradient Sensing (*t2*-DGS)**

A schematic of the experimental setup for double/dual transmission Digital Gradient Sensing or simply *t2*-DGS method is similar to the one shown in Figure 2.1. That is, it is similar to the setup for *r*-DGS (Figure 7.1(a)) except a separate/detached reflective planar surface is placed flush with the specimen on its backside, as shown in Figure 7.1(b). (That is, the gap between the additional reflective surface and the rear surface of the specimen is nominally zero.) The light rays, originating from the target plane, pass through the transparent specimen and reach the reflective surface and then get reflected back into

the transparent specimen. Hence, the speckles on the target are recorded by the camera via the additional reflective surface.

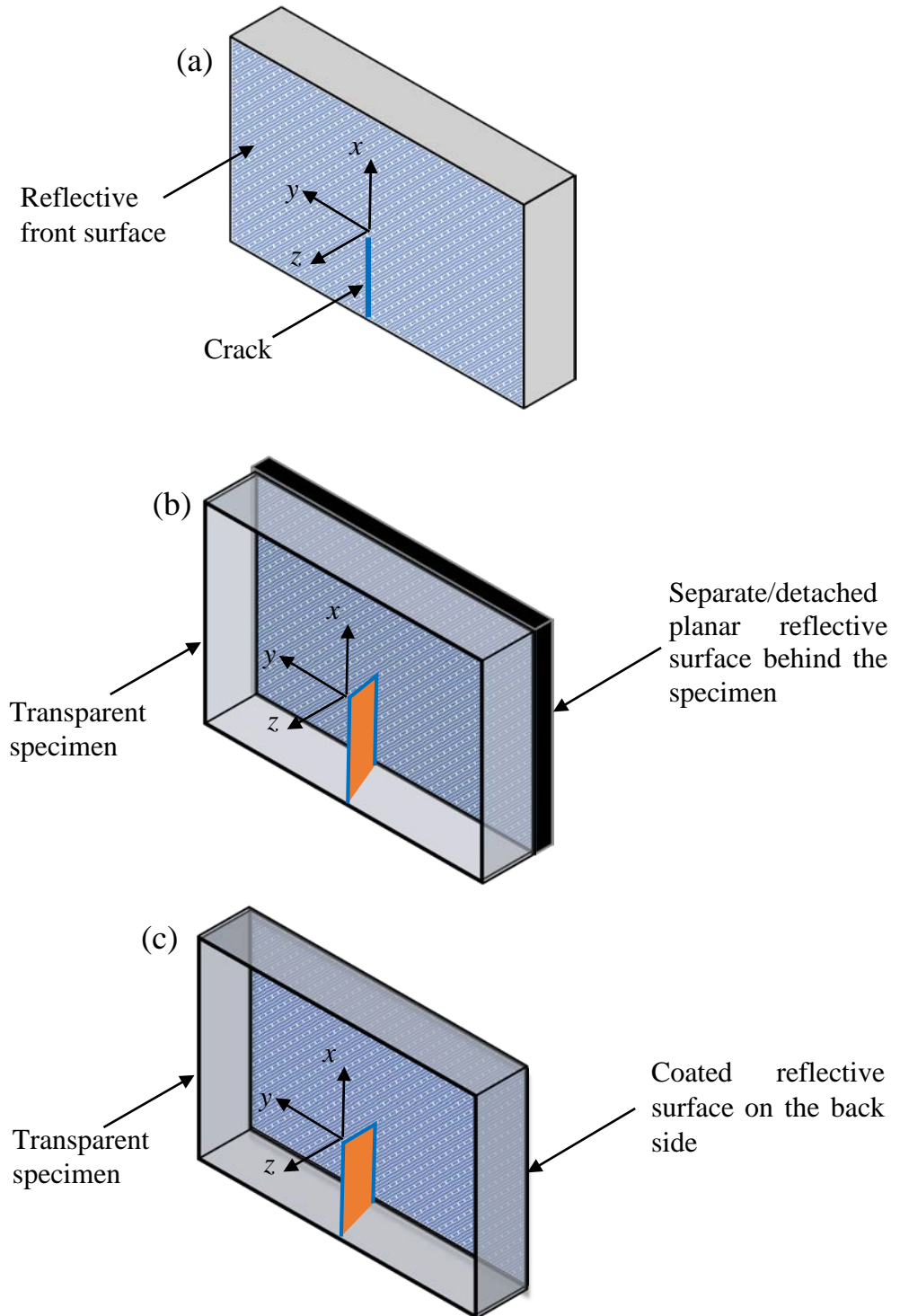


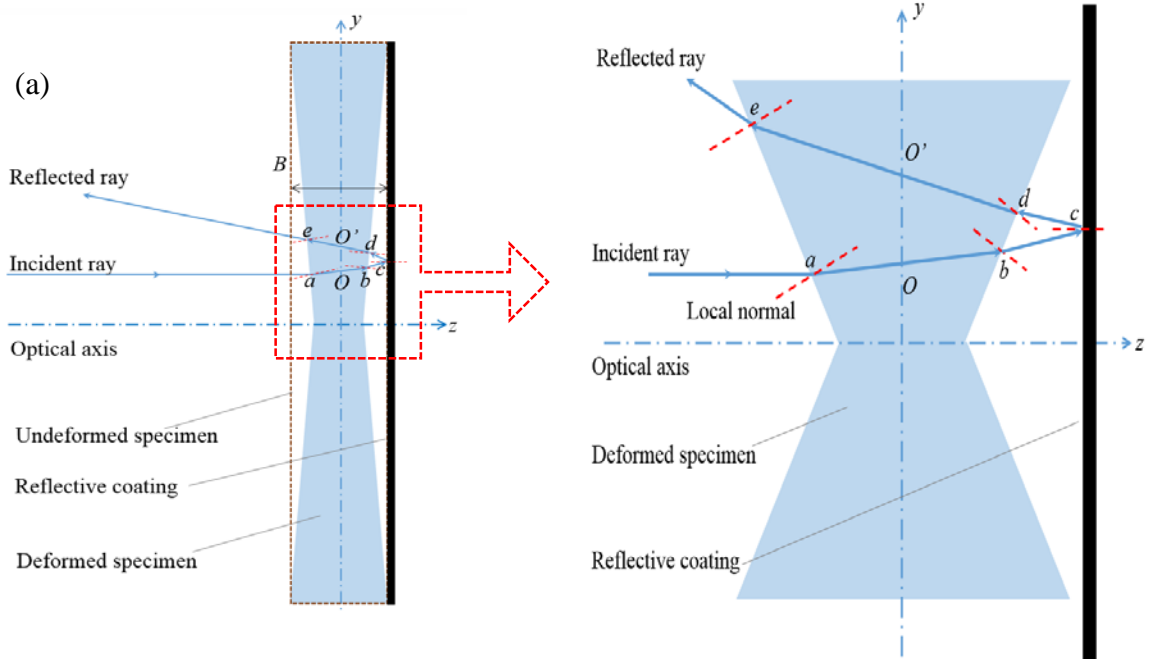
Figure 7.1: Specimen configurations for: (a) *r*-DGS; (b) *t2*-DGS; (c) *tr*-DGS.

As in *r*-DGS, a reference image is recorded first and then the deformed images as the specimen is subjected to load. The local displacements  $\delta_{x;y}$  can be measured by correlating the reference image with the deformed images. Thus, light rays experience the elasto-optical effects over twice the specimen thickness as a result of retro-reflection immediately after leaving the rear face. Hence, the optical path change here is twice that of *t*-DGS,

$$\delta S_{t2-DGS} = 2(\delta S_{t-DGS}) \quad (7.1)$$

$$(\phi_{x;y})_{t2-DGS} = 2(\phi_{x;y})_{t-DGS} = 2C_{\sigma}B \frac{\partial(\sigma_{xx} + \sigma_{yy})}{\partial(x;y)} \quad (7.2)$$

From the above, it is evident that the sensitivity of *t2*-DGS is twice that of *t*-DGS.



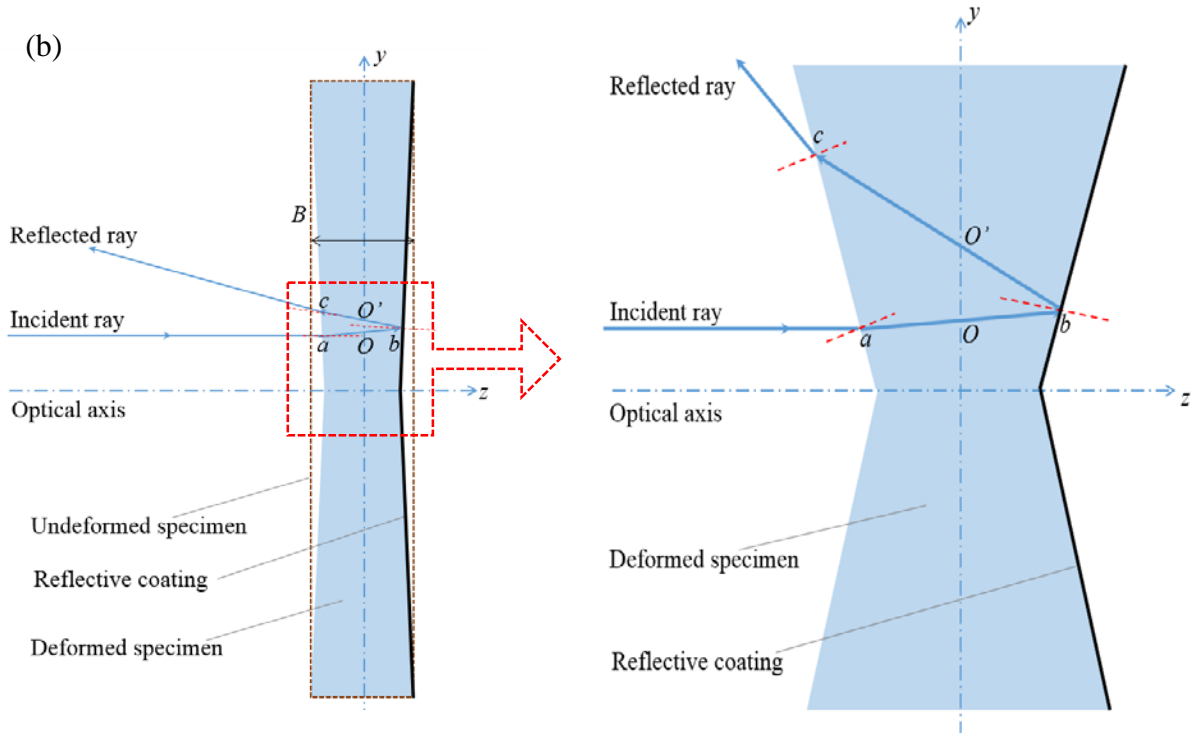


Figure 7.2: Light ray diagrams for  $t_2$ -DGS (a) and  $tr$ -DGS (b).

A planar ray diagram, Figure 7.2(a) is used to depict the path a light ray would take through a deformed specimen in the  $t_2$ -DGS methodology. The above Eq. (7.2) assumes that the specimen is ‘thin’ or ‘stiff’ or both such that the incident and reflected light rays have a negligibly small lateral shift ( $OO'$ ) between them. The exaggerated ray diagram depicts the light path through the specimen for clarity. An incident ray enters the deformed specimen (shaded in blue) and refracts at point ‘a’. Then, it continues to bend progressively<sup>13</sup> as it propagates through-the-thickness due to continuous local refractive index changes, and exits the deformed specimen at point ‘b’. Next, it reflects off the detached reflector at point ‘c’, enters the deformed specimen again and refracts at point ‘d’. After a second transmission through the sample thickness, it exits the specimen at point

<sup>13</sup> considered here as a straight line for depiction purpose and simplicity of analysis

'e'. In  $t$ -DGS, the angular deflection is assumed to occur at point  $O$  along the centerline of the specimen instead of 'a' or 'b' after all the refraction and thickness changes are lumped together. In  $t2$ -DGS, however, the ray reflected off the rear surface reflector passes through  $O'$  during the second transmission. The distance  $OO'$  is assumed to be negligible in the analysis. Obviously, if the detached reflective surface is not kept flush with the specimen, parallelism of the reflector relative to the undeformed specimen cannot be assured and additional errors could occur.

## 7.2 Transmission-Reflection Digital Gradient Sensing ( $tr$ -DGS)

The schematic of the experimental setup for transmission-reflection Digital Gradient Sensing ( $tr$ -DGS) method is again similar to the one shown in Figure 2.1. Furthermore, the experimental setup for  $tr$ -DGS is similar to the one for  $t2$ -DGS. However, in  $tr$ -DGS, the specimen is transparent but its rear face is made reflective by a reflective film deposition, as shown in Figure 7.1(c). The light rays, originating from the target plane, pass through the transparent specimen and then get reflected by the rear surface. The reflected rays then propagate through the transparent specimen for the second time. As in other DGS methods, a reference image is recorded first followed by images in the deformed state of the specimen. That is, gray scale at point  $P$  on the target plate which corresponds to point  $O$  on the specimen plane is recorded. In addition to the refractive index and thickness changes of the specimen, in this case the reflective rear surface of the specimen also deforms due to stress. As a result of these combined effects, light rays deviate from their initial path. In the deformed state of the specimen, an image is recorded. That is, the gray scale at a neighboring point of  $P$ , namely  $Q$  on the target plane, is recorded through  $O$

on the specimen plane. As before, the local speckle displacements  $\delta_{x;y}$  can be quantified by correlating the reference image with the deformed image of the specimen.

In  $r$ -DGS, the reflective surface deforms when the specimen is stressed. In  $t2$ -DGS, the refractive index and thickness of the specimen change when the specimen is stressed. The  $tr$ -DGS method combines  $r$ -DGS and  $t2$ -DGS. That is, in  $tr$ -DGS, the refractive index and thickness of the specimen change, and the reflective rear surface of specimen also deforms when the specimen is stressed, which makes  $tr$ -DGS more sensitive for the same stress field as these effects are additive in nature. Hence, the angular deflections of light rays of  $tr$ -DGS  $(\phi_{x;y})_{tr-DGS}$  is a combination of  $r$ -DGS  $(\phi_{x;y})_{r-DGS}$  and  $t2$ -DGS  $(\phi_{x;y})_{t2-DGS}$ ,

$$(\phi_{x;y})_{tr-DGS} = \frac{\delta_{x;y}}{\Delta} = (\phi_{x;y})_{r-DGS} + (\phi_{x;y})_{t2-DGS} \quad (7.3)$$

As noted earlier,

$$(\phi_{x;y})_{r-DGS} = 2 \frac{\partial w}{\partial(x; y)} \quad (7.4)$$

and for plane stress,  $\varepsilon_{zz} \approx \frac{2w}{B} = -\frac{\nu}{E}(\sigma_{xx} + \sigma_{yy})$ , and hence

$$w \approx -\frac{\nu B}{2E}(\sigma_{xx} + \sigma_{yy}) \quad (7.5)$$

where  $\nu$  is the Poisson's ratio,  $B$  is the undeformed thickness, and  $E$  is the elastic modulus of the specimen. Hence, Eq. (7.3) can be written as,

$$(\phi_{x;y})_{tr-DGS} = \frac{\delta_{x;y}}{\Delta} = \left( 2C_{\sigma} B - \frac{\nu B}{E} \right) \frac{\partial(\sigma_{xx} + \sigma_{yy})}{\partial(x; y)} \quad (7.6)$$

As in  $t2$ -DGS, the above Eq. (7.6) assumes that the specimen is 'thin' or 'stiff' or both such that the incident and reflected light rays have negligible lateral shift ( $OO'$ ), see

Figure 7.2(b), between them. A ray diagram is shown in Figure 7.2(b) to track the bending of a generic light ray through the specimen. An incident ray enters the deformed specimen (shaded in blue) and refracts at point ‘a’. Then, it continues to bend progressively (shown as straight lines for simplicity of depiction and analysis) as it propagates through-the-thickness due to refractive index changes. Next, it reflects off the deformed rear specular surface at point ‘b’ according to the laws of reflection and reenters the specimen. At last, it exits the specimen after refraction at point ‘c’. As in *t2*-DGS, the distance of  $OO'$  can be negligible when the specimen is ‘thin’ or ‘stiff’ or both. The value of  $OO'$  is estimated in next session with the above simplified assumptions.

### 7.2.1 Estimation of Lateral Light Ray Shift in *tr*-DGS

A simplified 2D analysis for estimating the lateral shift of a generic light ray in *tr*-DGS method is attempted to supplement the ray diagram in Figure 7.2 discussed earlier. Referring to Figure 7.3, an incident ray enters the *deformed* specimen (shaded in blue) at point ‘a’ and refracts. Let the angles of incidence and refraction be  $\theta_1$  and  $\theta_2$ , respectively, relative to the surface normal at ‘a’. To enable a geometric ray-optics based analysis,  $\theta_1$  – the local angle between the deformed and undeformed surfaces – is assumed to include the net influence of both the Poisson and stress-optic effects so that progressive bending of light rays through the medium can be avoided in the analysis since it would require *a priori* knowledge of the spatial distribution of stresses in the specimen. From Snell’s law,  $\frac{\sin \theta_1}{\sin \theta_2} = n$  where  $n$  is the locally averaged refractive index of the deformed body. Since  $\theta_1$  and  $\theta_2$  are small,

$$\theta_1 \approx n\theta_2 \quad (7.7)$$

Next, the light ray  $ab$  reflects off point ‘ $b$ ’ on the rear *deformed* surface of the specimen as  $bc$  such that the angles of incidence and reflection are  $\theta_3$ . As noted earlier, in reality, light rays bend progressively when traveling in specimen and are again assumed to be straight lines for estimation purposes.

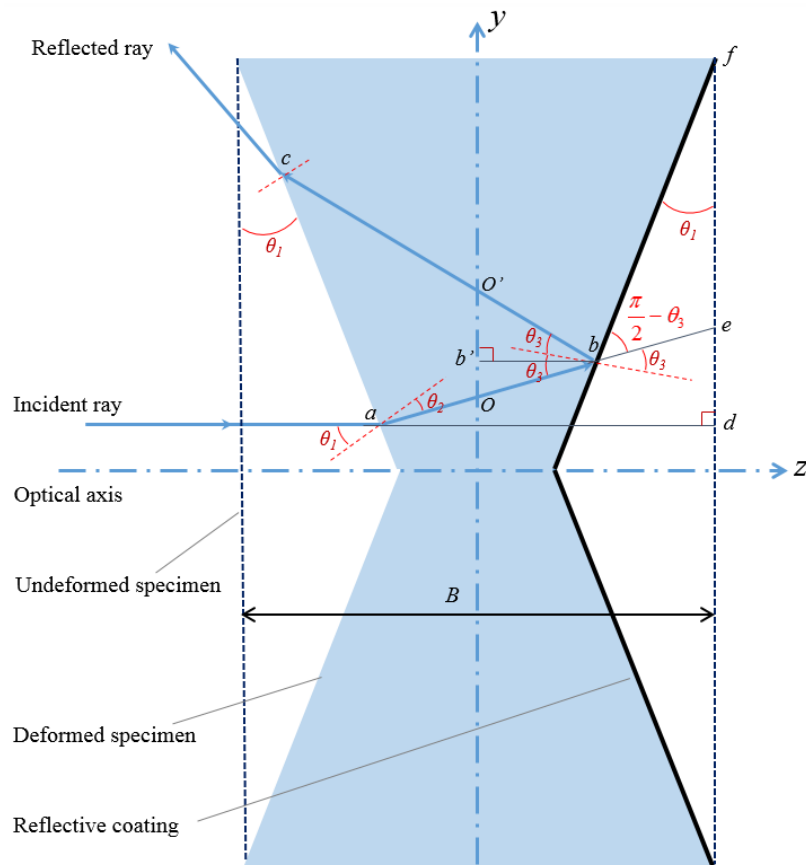


Figure 7.3: Exaggerated light ray diagram for *tr*-DGS.

The incident ray is extended to ‘ $d$ ’ so that  $ad$  is perpendicular to the undeformed rear surface (dark blue dotted line) of the specimen. The ray  $ab$  is also extended beyond ‘ $b$ ’ to ‘ $e$ ’ to the undeformed rear surface. Let ‘ $f$ ’ represent a generic specimen location

where the Poisson deformation is zero or negligible. Now, it can be observed that

$$\angle ead = \theta_1 - \theta_2, \angle bfe = \theta_1 \text{ and } \angle fbe = \frac{\pi}{2} - \theta_3. \text{ Hence, } \angle aed = \angle fbe + \angle bfe = \frac{\pi}{2} - \theta_3 + \theta_1.$$

Further, it can be observed that  $\Delta aed$  is a right angled triangle and hence,

$$\angle ead + \angle aed = \frac{\pi}{2}, \text{ or, } \theta_1 - \theta_2 + \frac{\pi}{2} - \theta_3 + \theta_1 = \frac{\pi}{2}, \text{ and hence,}$$

$$2\theta_1 = \theta_2 + \theta_3 \quad (7.8)$$

In  $\Delta O'bO$ ,  $bb'$  is normal to  $OO'$ ,  $\angle O'bO = 2\theta_3$ ,  $\angle b'bO = \angle ead = \theta_1 - \theta_2$ ,

$\angle b'bO' = 2\theta_3 - (\theta_1 - \theta_2)$ . Hence,

$$(O'b') = (b'b) \tan(2\theta_3 - \theta_1 + \theta_2) \approx (b'b)(2\theta_3 - \theta_1 + \theta_2),$$

and

$$(Ob') = (b'b) \tan(\theta_1 - \theta_2) \approx (b'b)(\theta_1 - \theta_2)$$

for small angles. Therefore,

$$OO' = Ob' + O'b' = 2(b'b)\theta_3 \quad (7.9)$$

Based on Eq. (7.11) and (7.12),  $\theta_3 = (2 - \frac{1}{n})\theta_1$ . Also, note that  $0 \leq 2(b'b) \leq B$ ,

where  $B$  is the undeformed thickness of the specimen. Hence, the approx. value of  $OO'$  at a generic position can be expressed as,

$$0 \leq OO' \leq (2 - \frac{1}{n})B\theta_1 \quad (7.10)$$

For PMMA, assuming  $n \approx 1.5$ ,  $B$  to be of the  $O(10^{-3})$  m, and  $\theta_1$  to be of the  $O(10^{-3})$  radians, the largest value of  $OO'$  would be of the  $O(10^{-6})$  m. Hence the micrometer scale lateral shift  $OO'$  in  $tr$ -DGS could be neglected relative to a typical sub-image to sub-image distance of less than  $O(10^{-3})$  m. Extending similar arguments to  $t2$ -DGS, the lateral shift of  $OO'$  can also be neglected since  $t2$ -DGS is less sensitive than  $tr$ -DGS.

## 7.3 Experimental Verification

### 7.3.1 Dynamic<sup>14</sup> fracture experiment

The working principle for *t2*-DGS is relatively straightforward and hence a separate verification for *t2*-DGS is deemed unnecessary. Instead, a comparative evaluation of *tr*-DGS method with *t2*-DGS is carried out. A cracked PMMA plate undergoing dynamic mode-I fracture is used for this demonstration in which stress gradients in the crack-tip region are measured from the two methods relative to each other. A 152 mm × 76 mm rectangular specimen of 5.8 mm thickness was imaged using ultrahigh-speed digital camera having a single imaging sensor. The specimen configuration as viewed from its backside is shown in Figure 7.4 with its front surface facing the camera. A 10 mm long horizontal pre-notch was cut along the edge in the mid-span of the specimen using a 300  $\mu\text{m}$  thick diamond saw. The top-half of the backside of the specimen was deposited with a thin aluminum film to make it reflective to implement *tr*-DGS. In the bottom-half, a reflective planar surface (mirror) was placed flush with the specimen for implementing *t2*-DGS. The cracked specimen was subjected to symmetric mode-I loading by impacting it on the uncracked long-edge. Thus, during the experiment, stress gradients were measured simultaneously by *tr*-DGS and *t2*-DGS methods in the upper- and lower-halves on the same

---

<sup>14</sup> It is common to perform quasi-static experiments before conducting dynamic counterparts for establishing a new experimental method. When using speckle-based methods, however, the possibility of rigid body motions exists during quasi-static loading events lasting relatively long duration (a few seconds or more). Such issues, on the other hand, are negligible if not completely absent during stress-wave dominant loading events lasting only a few microseconds *and* speckle images being recorded using a single sensor ultrahigh-speed camera (without any moving parts) where both the reference and deformed images are a few microseconds apart and recorded by the same sensor, thus limiting recording issues to the electronic noise. Hence, a dynamic experiment is favored for this demonstration to a quasi-static counterpart to address the primary issue of measurement sensitivity between methods.

specimen with a mode-I crack subjected to the same stress field. The relevant properties of PMMA used in this experiment are listed in Table 7-1.

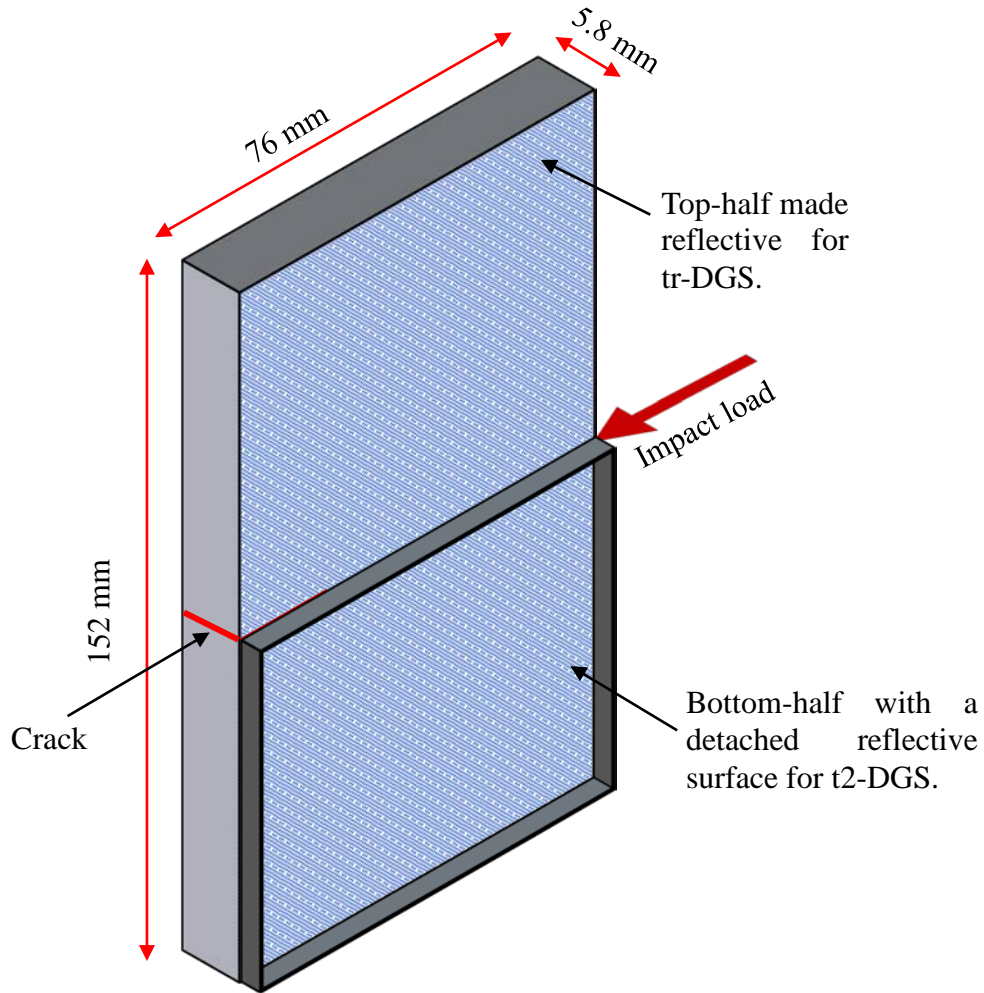


Figure 7.4: Back-side of the specimen with and without reflective coating in the upper-half and lower-half, respectively. (Front-side of the specimen faces the camera).

Table 7-1: Material properties of PMMA [53] [127].

	Dynamic	Static
Density ( $\text{kg/m}^3$ )	1100	1100
Elastic modulus (GPa)	4.92	3.30
Poisson's ratio	0.34	0.34
Elasto-optic constant ( $\text{m}^2/\text{N}$ )	$-1.08 \times 10^{-10}$	$-0.90 \times 10^{-10}$

The schematic of the overall experimental setup used for the dynamic impact experiment is shown in Figure 7.5. A modified Hopkinson pressure bar (or simply a ‘long-bar’) was used for loading the specimen using stress waves. The long-bar was a 1.83 m aluminum rod of 25.4 mm diameter with a tapered rectangular tip (25.4 mm  $\times$  7.5 mm) impacting the unconstrained PMMA plate. A 305 mm long, 25.4 mm diameter aluminum striker placed in the barrel of a gas-gun was aligned co-axially with the long-bar at the start of the experiment. The striker was launched towards the long-bar at a velocity of  $\sim$ 13 m/s during the test. A close-up view of the optical arrangement is also shown in Figure 7.5. Initially, the long-bar was kept in contact with the specimen. The specimen was placed over a rectangular strip of soft putty stuck to a height-adjustable aluminum platform to prevent direct contact with the platform and simulate a ‘free-standing’ specimen configuration. To achieve symmetry in terms of acoustic impedance, a separate putty strip was pressed onto the top edge of the specimen. As noted earlier, the top-half of the backside of the specimen is coated with aluminum film to make it specular. And, a reflective planar mirror was placed flush with the bottom-half. A beam splitter and the speckle target plate were placed in a specially designed 45° holder so that the camera could be focused on the speckles through the beam splitter via the specimen. The speckle images were photographed by a Kirana-05M ultrahigh-speed digital camera assisted by a pair of Cordin-659 high energy flash lamps to illuminate the speckles on the target. The camera is a single sensor camera capable of recording 10-bit gray scale images at a maximum rate of 5 million frames per second and at a fixed spatial resolution of 924  $\times$  768 pixels per image. The camera and the two flash lamps were triggered using a variable delay circuit relative to the

striker impacting the long-bar and knowing the duration required for the stress waves to travel the length of the long-bar.

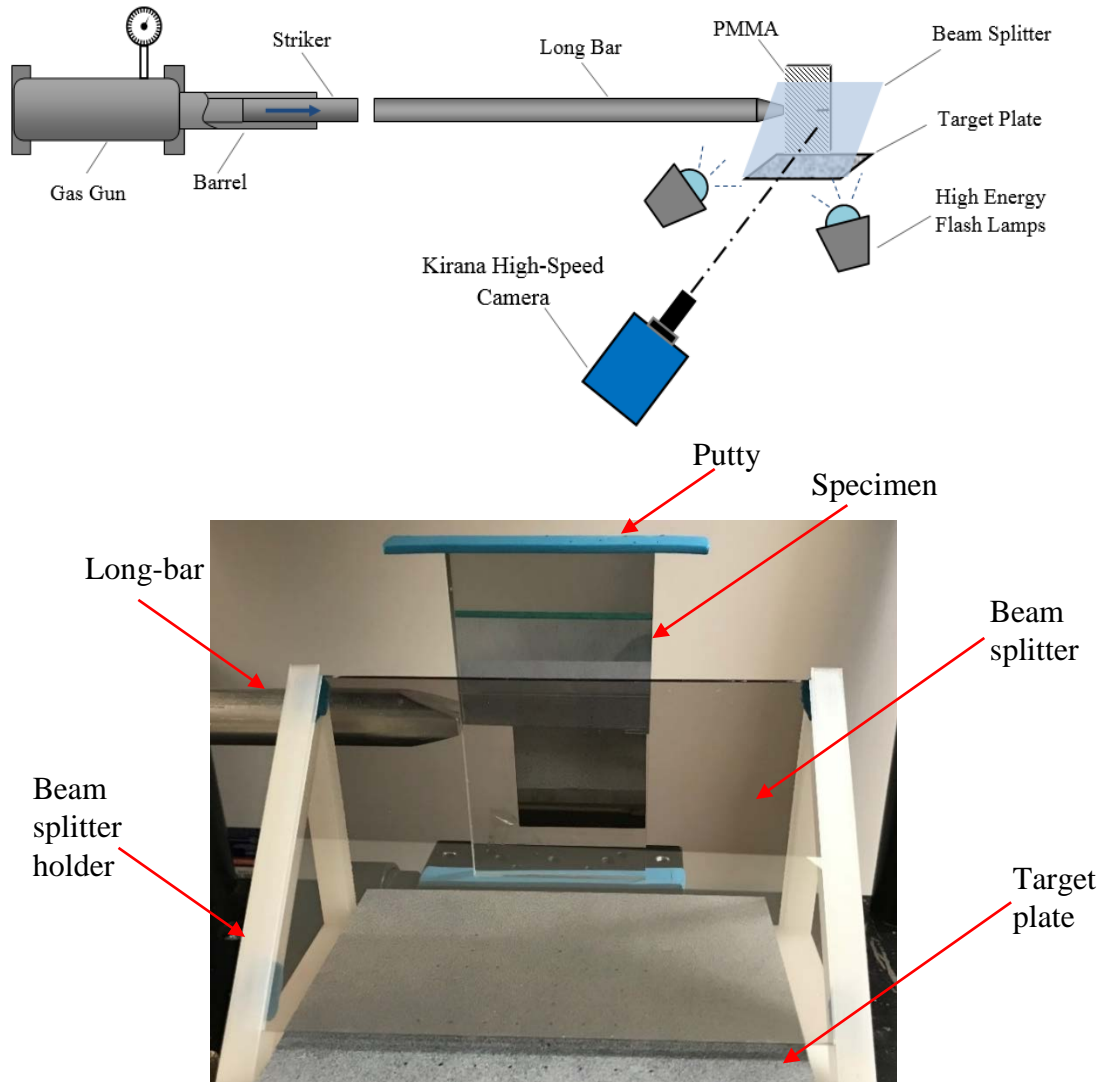


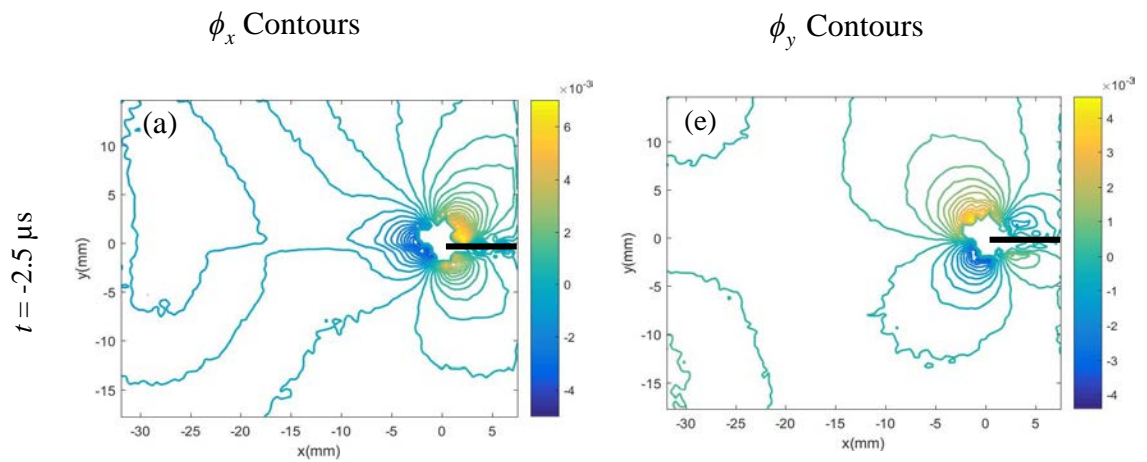
Figure 7.5: Schematic (top) and close-up photography (bottom) of the experimental setup for dynamic plate impact study.

A Nikon 70-300 mm focal length macro zoom lens and adjustable bellows was used with the camera to record the images. A good depth-of-focus over the entire field was achieved by stopping down the lens aperture to  $F^{#}11.0$  after focusing on the speckles. The distance between the specimen and the camera lens plane ( $L$ ) was  $\sim 795$  mm and the one

between the specimen mid-plane and the target plane ( $\Delta$ ) was 72 mm. The camera was focused on a rectangular region of interest (ROI) approximately 40 mm  $\times$  35 mm on the specimen plane in the vicinity of the pre-notch tip. When the long-bar was impacted by the striker, a compressive stress wave generated in the long-bar propagated along its length. Simultaneously a trigger pulse was generated to start recording of images by the camera. A total of 180 images, some corresponding to the undeformed state and others to the deformed state of the specimen, were recorded at 400K frames per second (inter frame period 2.5  $\mu$ s). One of the undeformed images before the start of loading pulse entering the specimen was selected as the reference image. All the deformed images were correlated with that reference image using ARAMIS<sup>®</sup> image analysis software. During image correlation, a sub-image size of 20  $\times$  20 pixels (1 pixel = 48.30  $\mu$ m) with 10 pixels overlap was used to extract the local speckle displacements  $\delta_{x,y}$  in the ROI. The displacement fields were then used to compute the two orthogonal angular deflection fields of light rays ( $\phi_{x,y}$ ) as detailed earlier.

The time-resolved angular deflection contour plots of  $\phi_{x,y}$  in the PMMA plate are shown in Figure 7.6 at a few select time instants. In these plots,  $t = 0 \mu$ s corresponds to crack initiation at the original notch tip. Both  $\phi_x$  and  $\phi_y$  contours increase in number and become denser with the passage of time implying buildup of stresses in the specimen during impact loading event. In each contour plot, the ones in the top-half are measured by *tr*-DGS and the bottom-half by *t2*-DGS methods. The boundary of these two is along the path of mode-I crack growth (or, along the  $x$ -axis). If only one of the two methods were used, the  $\phi_x$  contours should be symmetric in shape and magnitude with respect to the

crack whereas the  $\phi_y$  contours should be symmetric in shape and anti-symmetric in magnitude. In the current implementation, however, the contours of  $\phi_{x;y}$  are not symmetric due to the different measurement sensitivities of these two methods. It can be observed that the contours in the top-half measured by *tr*-DGS are denser and larger than those in the bottom-half measured by *t2*-DGS, indicating qualitatively that *tr*-DGS is more sensitive than *t2*-DGS. In the case of  $\phi_x$  contours at  $t = 15 \mu s$ , the contour lines close to the left hand edge cluster due to the impact occurring over a narrow area of contact. Furthermore, the contours resulting from the impact waves are not as dominant in the *t2*-DGS method while they are rather pronounced in the top-half of the plot. It should be noted here that, although the  $\phi_{x;y}$  contours are different in the top and bottom halves near the crack-tip, they are due to the same stress field. Hence, the values of  $\phi_{x;y}$  along any symmetric angular paths with respect to the crack-tip polar coordinates ( $\pm\theta$ ), measured by *tr*-DGS and *t2*-DGS, can be extracted to directly compare the sensitivities of these two methods.



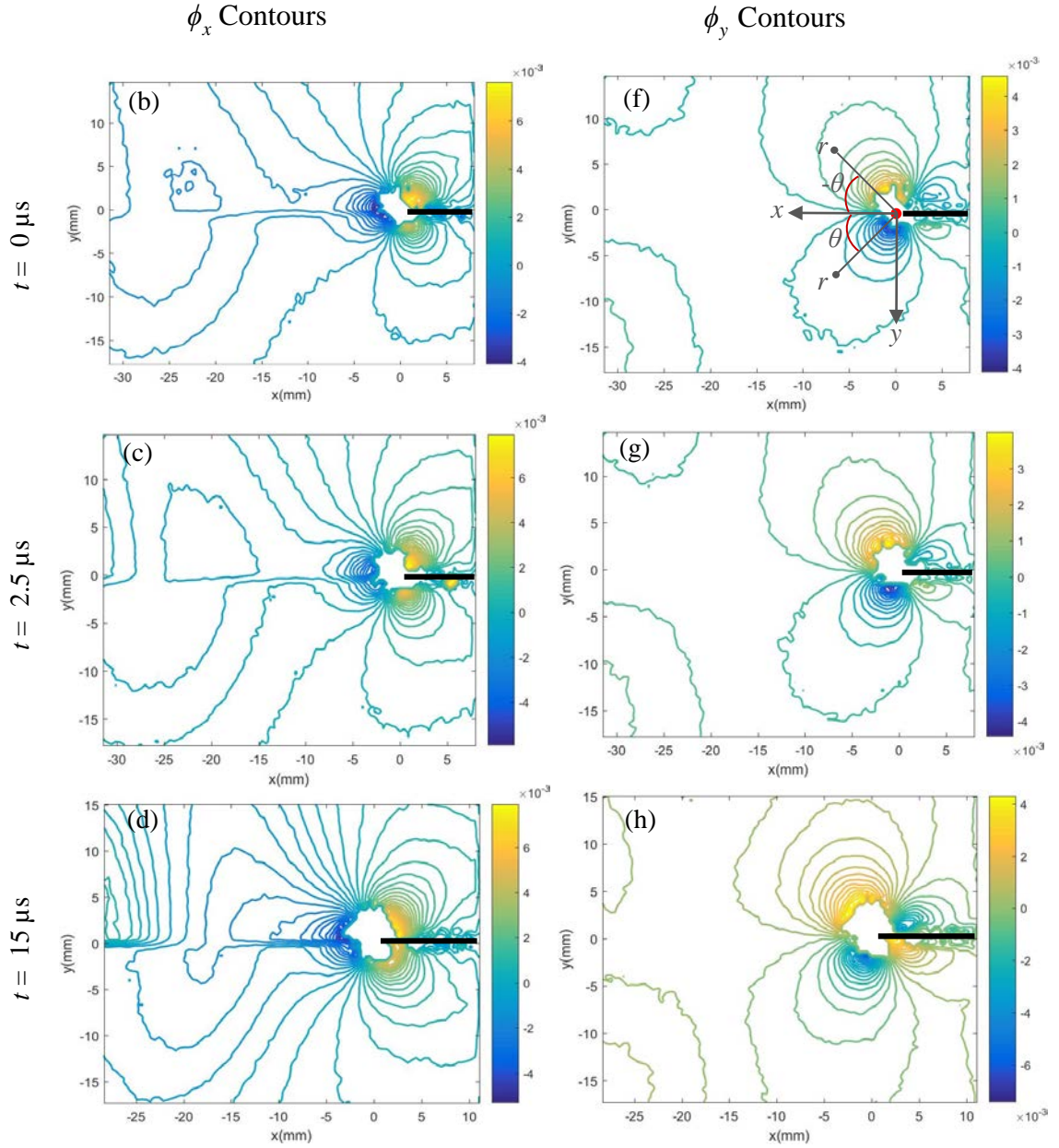


Figure 7.6: Angular deflection contour plots proportional to stress gradients of  $(\sigma_x + \sigma_y)$  in the  $x$ - and  $y$ -directions. Contour increments =  $3 \times 10^{-4}$  rad.

Theoretically, the ratio of values of  $\phi_{x,y}$  measured by  $tr$ -DGS and  $t2$ -DGS, based on Eq. (7.2) and (7.6), can be written as:

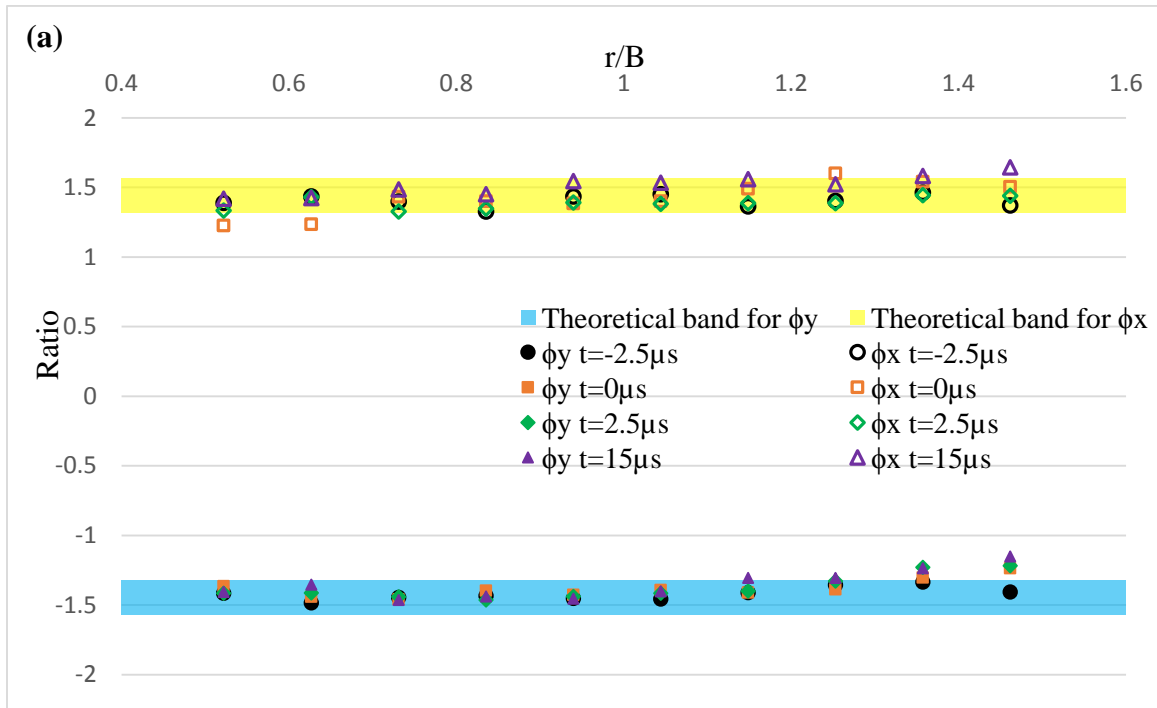
$$\frac{(\phi_{x;y})_{ir-DGS}}{(\phi_{x;y})_{t2-DGS}} = \left( 1 - \frac{\nu}{2C_\sigma E} \right) \quad (7.11)$$

It is evident that this ratio is dependent only on the properties of the specimen material. Based on the properties of PMMA listed in Table-1, the result of Eq. (7.11) in the dynamic loading case should be  $\sim 1.32$  whereas  $\sim 1.57$  for quasi-static loading conditions due to the value of  $C_\sigma$  reported from different sources in the literature [128]. In the region around the crack-tip, discrete angular deflection values of  $\phi_{x;y}$  along  $45^\circ$  and  $90^\circ$  paths in the range  $0.5 \leq r/B \leq 1.5$  were considered. That is,  $(\phi_{x;y})_{ir-DGS}$  along  $-45^\circ$  and  $-90^\circ$ , and  $(\phi_{x;y})_{t2-DGS}$  along  $+45^\circ$  and  $+90^\circ$ , were extracted for comparison. (*It should be noted that the choice of these directions allowed direct use of measured angular deflections without further data interpolation since the shape of the sub-images used during image correlation were squares. Other angles, say,  $\pm 60^\circ$  would require interpolation of sub-image data array and hence avoided.*) The choice of the radial extent ensured that the data was sufficiently close to the crack-tip to capture the singular behavior while minimizing triaxial effects [33] and any uncertainty of locating the origin due to a combination of limited optical aperture, loss of speckle correlation, and edge-effects. The details of the data paths are shown in Figure 7.6(f). The red dot represents the crack-tip,  $r$  is the radial distance from the origin and the heavy black line represents the crack. It can be observed in the  $\phi_y$  plot, the sign of the angular deflection values are opposite with respect to the growing crack path and hence,

the values of  $\frac{(\phi_y)_{ir-DGS}}{(\phi_y)_{t2-DGS}}$  are negative, while the values of  $\frac{(\phi_x)_{ir-DGS}}{(\phi_x)_{t2-DGS}}$  are positive.

The experimental results of  $\frac{(\phi_{x,y})_{tr-DGS}}{(\phi_{x,y})_{r2-DGS}}$  in  $0.5 \leq r/B \leq 1.5$  range along  $\pm 45^\circ$  and

$\pm 90^\circ$  are shown in Figure 7.7(a) and (b), respectively, at a few select time instants corresponding to the plots in Figure 7.6. The blue theoretical band represents the range -1.57 to -1.32, and the yellow one represents the range 1.32 to 1.57. Ratios at  $t = \pm 2.5 \mu s$  indicate the experimental results just before and after crack initiation at  $t = 0 \mu s$ . Three consecutive time instants are selected here as typical examples for comparison. It can be observed from Figure 7.7 that the data points at these time instants are nearly constant and close to the prediction. (The values of three data points of  $t = 15 \mu s$  within  $0.5 \leq r/B \leq 0.7$  in Figure 7.7(b) are zero because  $(\phi_{x,y})_{tr-DGS}$  in that region are zero due to missing data around the crack-tip at  $t = 15 \mu s$ .) It is worth noting that, during analysis, sufficient care was exercised to locate the crack-tip.



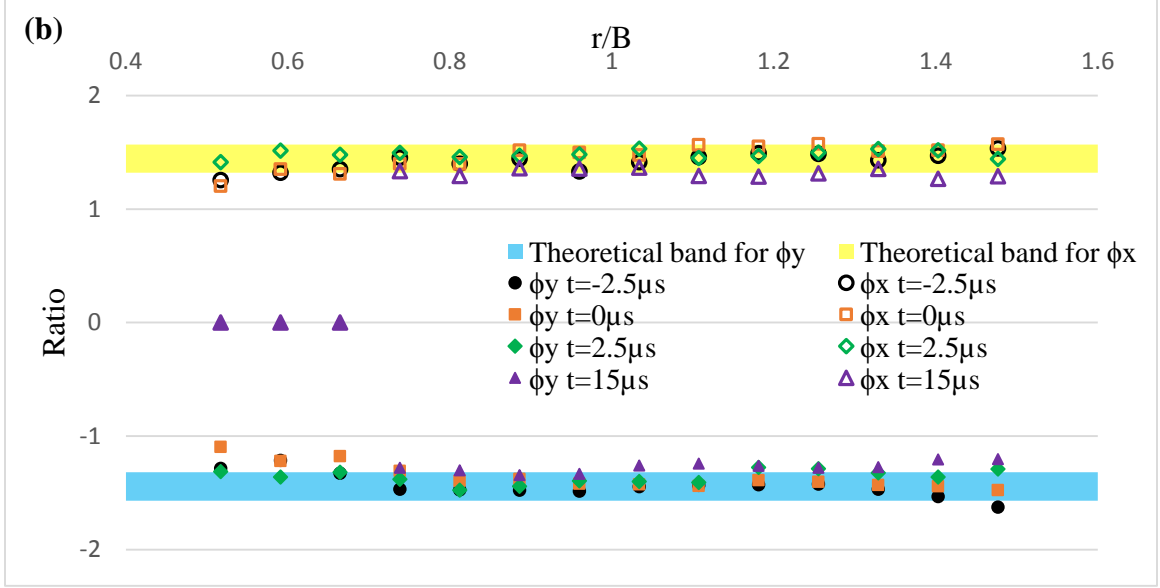


Figure 7.7: Ratio of  $\frac{(\phi_{x,y})_{tr-DGS}}{(\phi_{x,y})_{t2-DGS}}$  within  $0.5 \leq r/B \leq 1.5$ : (a) along  $\pm 45^\circ$ ; (b) along  $\pm 90^\circ$ .

Mode-I stress intensity factor (SIF) histories were evaluated using an overdeterministic least-squares analysis based on the angular deflections fields of  $(\phi_x)$  measured by  $tr$ -DGS and  $t2$ -DGS methods,

$$\phi_x(t) = D \left[ \begin{array}{l} -\frac{1}{2} r_l^{-\frac{3}{2}} \left\{ f(V; C_L; C_S) A_1(t) \cos\left(\frac{3\theta_l}{2}\right) \right\} \\ + \sum_{N=2}^{\infty} \left\{ A_N(t) \left(\frac{N}{2}-1\right) r_l^{\left(\frac{N}{2}-2\right)} \cos\left(\left(\frac{N}{2}-2\right)\theta_l\right) \right\} \end{array} \right] \quad (7.12)$$

where the constant  $D$  varies for each of the DGS methods,  $D_{t2-DGS} = (2C_\sigma B)$  and

$$D_{tr-DGS} = \left( 2C_\sigma B - \frac{\nu B}{E} \right), f \text{ is a function of instantaneous crack velocity, } V, (r_l, \theta_l) \text{ denote}$$

the contracted crack tip polar coordinates for a growing crack (See [117] for details). Mode-I

SIFs  $K_I(t)$  are related to  $A_1(t)$ , as  $A_1(t) = K_I(t) \sqrt{2/\pi}$ . The values of  $(\phi_x)$  measured

by  $tr$ -DGS and  $t2$ -DGS were used to calculate SIFs, respectively, the corresponding SIF

histories are plotted in Figure 7.8. It can be observed that two SIF histories match well with each other.

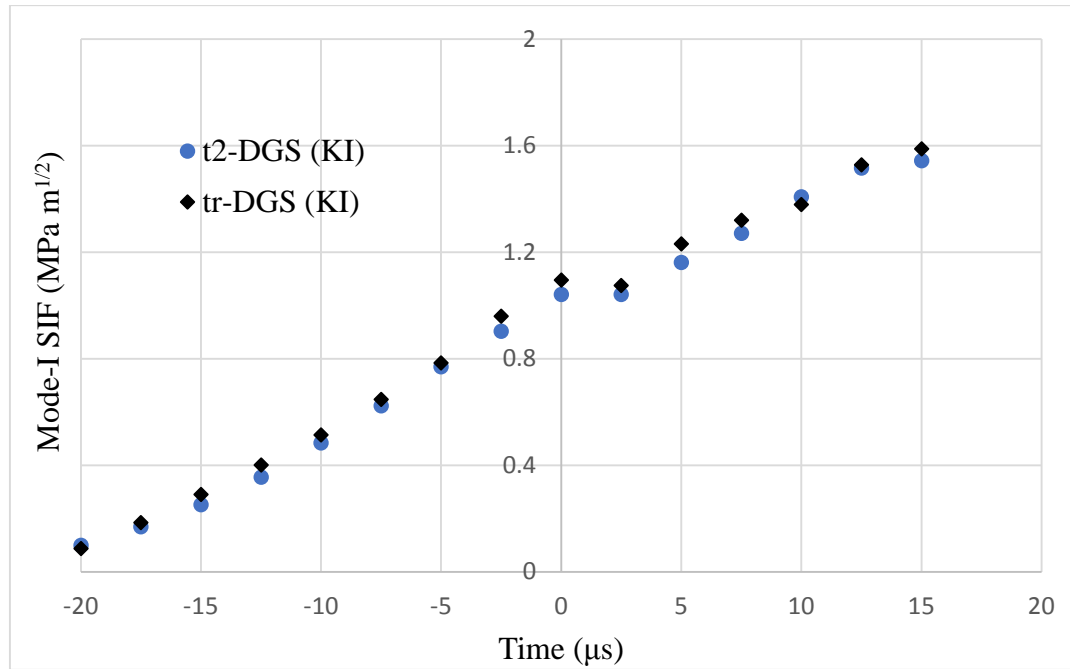


Figure 7.8: Mode-I stress intensity factor histories measured by *tr*-DGS and *t2*-DGS methods.

### 7.3.2 Static Fracture Experiment

To further demonstrate the validity of *tr*-DGS and *t2*-DGS methods for mechanics problems in general, a PMMA beam subjected to a symmetric 3-point bending was considered. A schematic of the experimental setup along with a companion photograph is shown in Figure 7.9. A 152 mm  $\times$  51 mm rectangular PMMA specimen of 5.8 mm thickness, with an initial crack of length 13 mm was used. An Instron 4465 universal testing machine operating in displacement controlled mode (cross-head speed = 0.004 mm/s) was employed to load the specimen supported on two anvils (span 127 mm). In Figure 7.9, the back side of the specimen on its right-half was deposited with a thin aluminum film to

make it reflective for implementing *tr*-DGS. The left-half had a reflective planar surface kept flush against the specimen for *t2*-DGS implementation. Thus, during the experiment, stress gradients were measured by *tr*-DGS and *t2*-DGS methods simultaneously on the same specimen. A beam splitter and the speckle target plate were placed in a specially designed 45° holder, with the camera focused on the speckles through the beam splitter and via the specimen. The target plate was illuminated uniformly by two LED lamps. The distance ( $\Delta$ ) between the specimen mid-plane and the target plate was 80 mm. A Nikon D100 digital SLR camera fitted with a 70-300 mm macro lens and an adjustable bellows was placed in-front of the specimen at a distance of 1350 mm ( $L$ ). An aperture setting of  $F^\# 11$  was selected for recording the speckles with a good depth-of-focus. A computer was used to control both the camera and the loading device during time-lapse photography of speckles.

An 8-bit reference image was recorded with a resolution of  $1504 \times 1000$  pixels before loading the beam ( $F = 0$  N). Subsequently, speckle images were recorded at every 50 N increments up to 300 N. The rigid body motion of speckles in the images was visible in the first increment. To minimize the effect of such motions on the experimental result, the image at  $F = 100$  N was intentionally selected as the reference image. The one at  $F = 300$  N was correlated with the reference image by using ARAMIS® image analysis software. During image correlation, a sub-image size of  $20 \times 20$  pixels (1 pixel = 38.56  $\mu\text{m}$ ) with 10 pixels of overlap was used to extract the local speckle displacements  $\delta_{x,y}$  in the ROI. The displacement fields were then used to compute the two orthogonal angular deflection fields of light rays  $\phi_{x,y}$ .

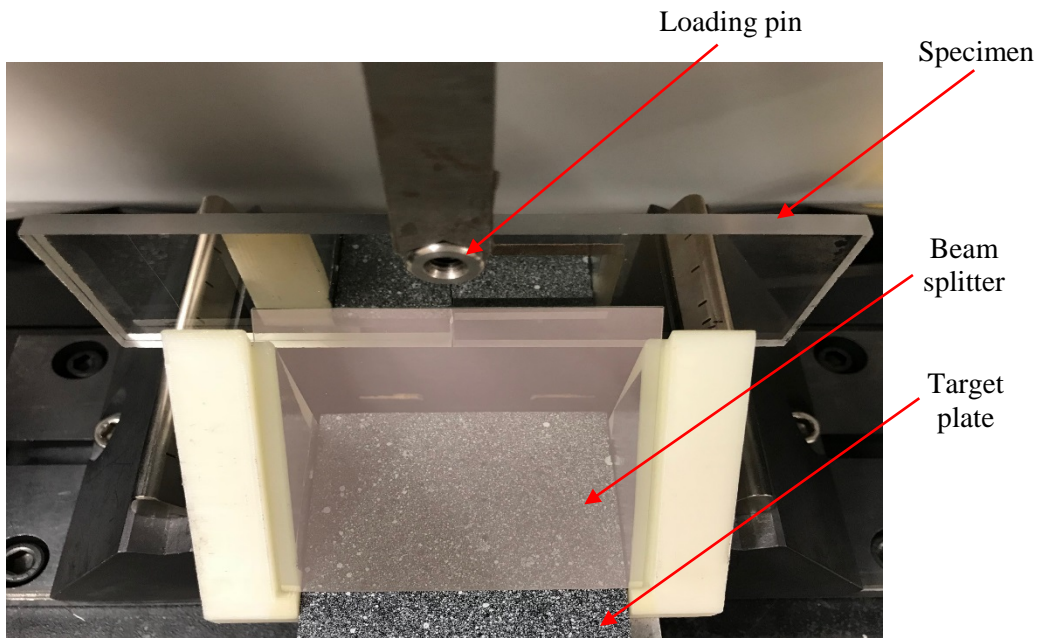
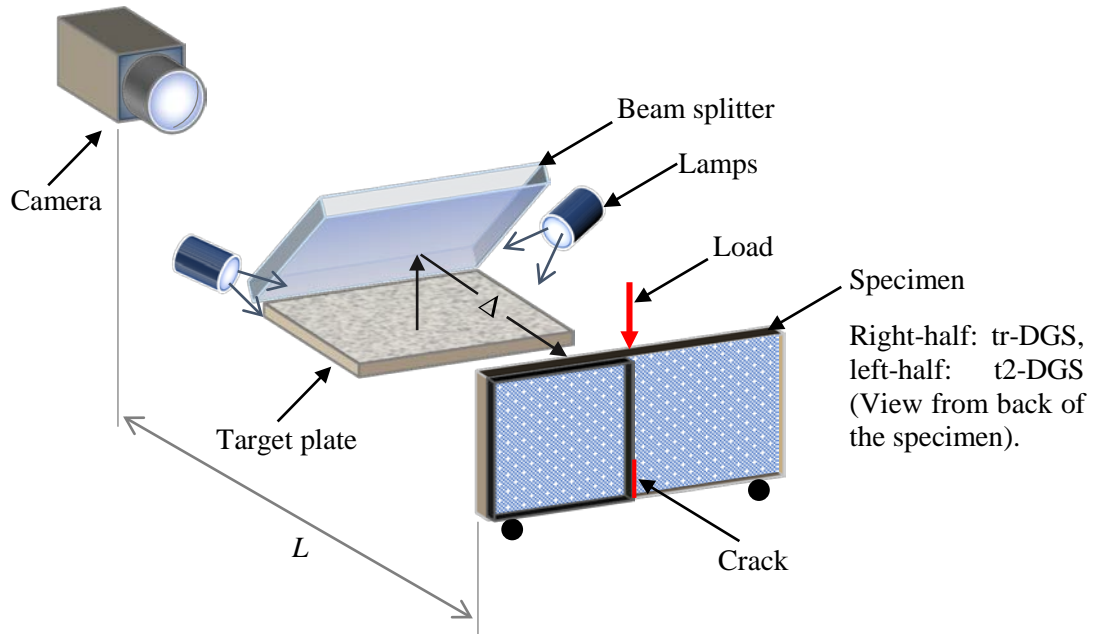


Figure 7.9: Schematic of the experimental setup for static fracture study (top). Close-up view of the optical arrangement (bottom).

The angular deflection contour plots  $\phi_{x,y}$  in the PMMA plate are shown in Figure 7.10(a) and (b). In each contour plot, the left-half are from *tr*-DGS and the right-half are

from  $t2$ -DGS. Similar to the dynamic experiments, it can be observed that the left-half contours are denser and larger in size than the right-half counterparts, indicating higher sensitivity of  $tr$ -DGS relative to  $t2$ -DGS method. The values of  $\phi_y$  measured by  $tr$ -DGS and  $t2$ -DGS in this quasi-static experiment were extracted to compare these two methods and verify the  $tr$ -DGS concept. In the region around the crack-tip, discrete angular deflection values of  $\phi_y$  along the path  $0.5 \leq r/B \leq 1.5$ ,  $(\phi_y)_{tr-DGS}$  along  $+45^\circ$  and  $+90^\circ$ ,  $(\phi_y)_{t2-DGS}$  along  $-45^\circ$  and  $-90^\circ$ , were extracted. Unlike in the dynamic experiment, the rigid body motions cannot be neglected in the static counterparts. Therefore, the measurements were described as,

$$(\phi_y)_{measured} = (\phi_y)_{true} + C \quad (7.13)$$

where  $C$  is the constant representing the rigid body motion,  $(\phi_y)_{true}$  is the one devoid of rigid body motion. (The rigid rotation terms were found to be negligible and hence are not included here for clarity.) Using Eq. (7.13), an over-deterministic least-squares analysis was performed to determine  $C$  and remove the rigid body motion. Then,  $(\phi_y)_{true}$  for  $tr$ -DGS and  $t2$ -DGS methods were used to find the ratio  $\frac{(\phi_y)_{tr-DGS}}{(\phi_y)_{t2-DGS}}$ , and is shown in Figure

7.11. Again, the blue strip indicates the theoretical band from -1.57 to -1.32. It can be observed that the ratios are nearly constant and are located close to if not on the blue strip, thus validating the predictions under quasi-static conditions also. During analysis, care was also exercised to locate the crack-tip from the contours.

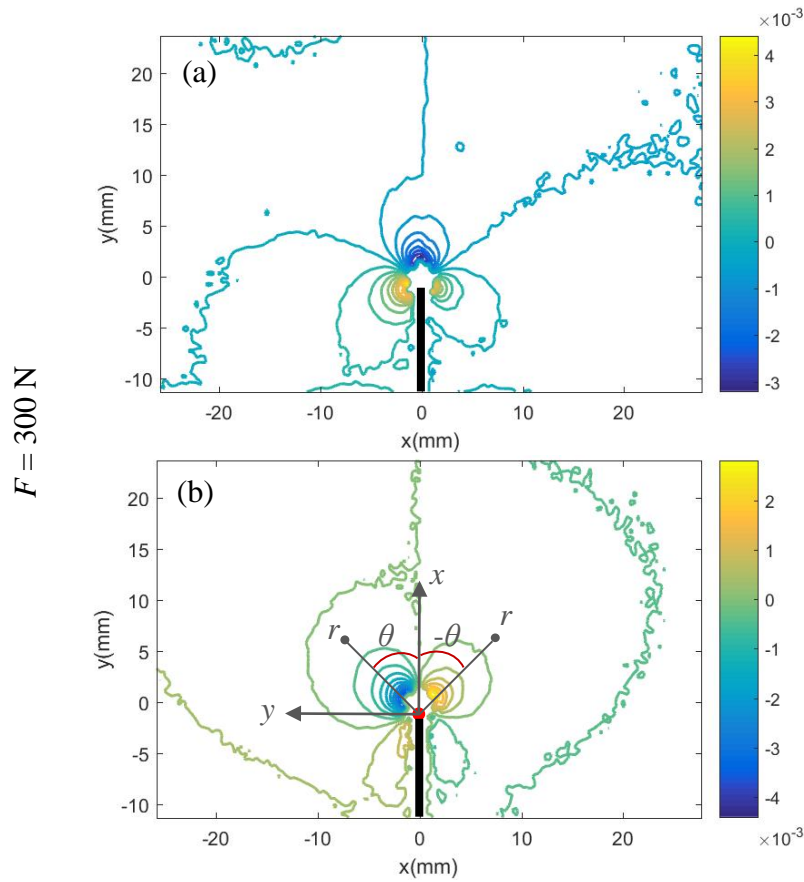


Figure 7.10: Angular deflection contour plots proportional to stress gradients: (a)  $\phi_x$ ; (b)  $\phi_y$ . Contour increments =  $4 \times 10^{-4}$  rad.

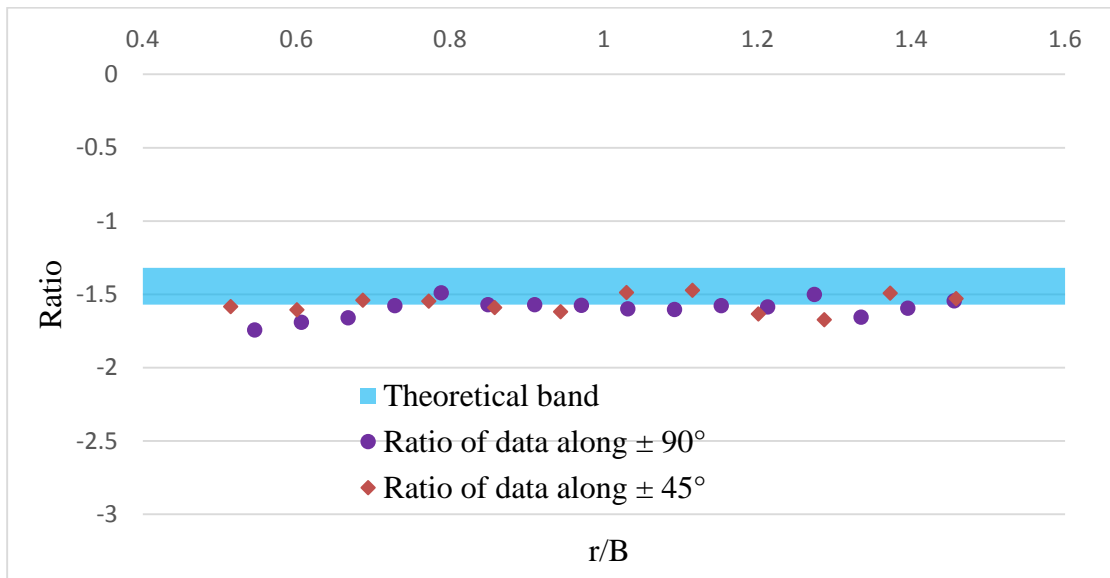


Figure 7.11: Measured ratio of  $\frac{(\phi_y)_{r-DGS}}{(\phi_y)_{r2-DGS}}$  in  $0.5 \leq r/B \leq 1.5$  along  $\pm 45^\circ$  and  $\pm 90^\circ$ .

#### 7.4 Estimation of SIF from *tr*-DGS and *t2*-DGS Methods

As a part of the family of DGS methods, these two approaches of *tr*-DGS and *t2*-DGS were used to measure the crack-tip stress intensity factors of PMMA beams under quasi-static symmetric 3-point bending. The measurements were also done using *t*-DGS and *r*-DGS methods separately for completeness. The experimental setup used is same as the one shown in Figure 7.9. Rectangular PMMA specimens of dimensions 152 mm  $\times$  63.5 mm  $\times$  5.8 mm, with an initial crack of length 13 mm were used in each experiment for different DGS configurations. The other parameters of this experimental setup are same as the one used during verification of *tr*-DGS under quasi-static loading conditions, except the camera distance  $L$  was 1170 mm and  $\Delta$  was 80 mm. All other experimental parameters were same for the four DGS methods. An 8-bit reference image was recorded with a resolution of 1504  $\times$  1000 pixels before loading ( $F = 0$  N). The speckle images were recorded at every 50 N increments up to a maximum load of 500 N. The images in the deformed state were correlated with the reference image as before. During image correlation, a sub-image size of 30  $\times$  30 pixels (1 pixel = 37.86  $\mu$ m) with 10 pixels overlap was used to extract the speckle displacements  $\delta_{x,y}$  in the ROI. The displacement fields were then used to compute the two orthogonal angular deflection fields of light rays ( $\phi_{x,y}$ ).

The angular deflection contour plots  $\phi_{x,y}$  measured by these four DGS methods are plotted in Figure 7.12 at the same load level of 500 N. It can be observed that the contours measured by *t2*-DGS and *tr*-DGS are visually larger and denser than those measured by the other two DGS methods, which indicates higher measurement sensitivity. Furthermore, *tr*-DGS is more sensitive than *t2*-DGS by comparison.

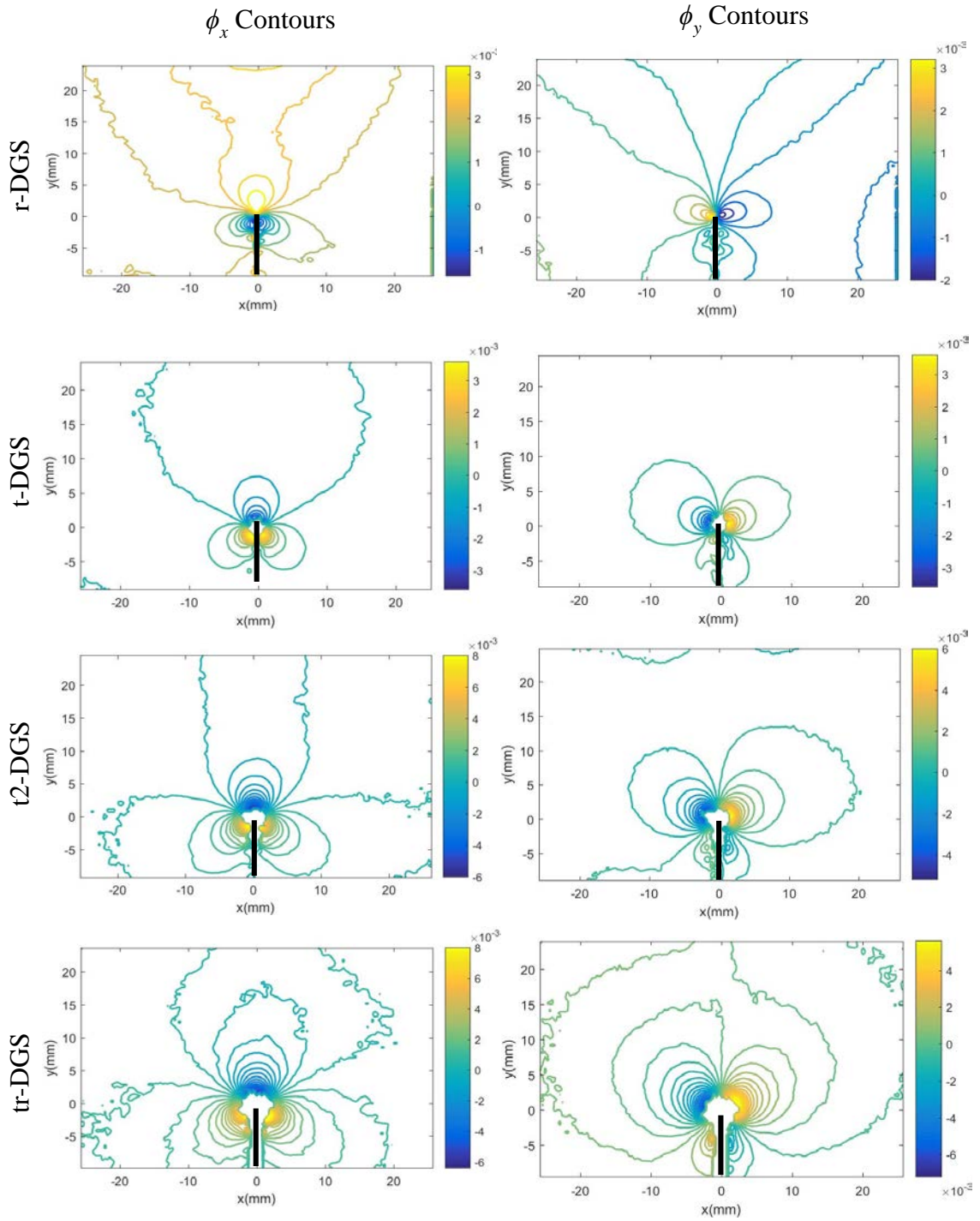


Figure 7.12: Angular deflection contour plots of  $\phi_x$  and  $\phi_y$  for four DGS methods corresponding to load of 500 N. Contour increments =  $4 \times 10^{-4}$  rad.

Based on Williams' asymptotic stress fields for mode-I cracks, the expressions for angular deflections for each of the DGS methods are given by [33] [129] ,

$$(\phi_{x,y}) = D \frac{\partial(\sigma_{xx} + \sigma_{yy})}{\partial(x:y)} = D \sum_{N=1}^{\infty} A_N \left( \frac{N}{2} - 1 \right) r^{\left( \frac{N}{2} - 2 \right)} \frac{\cos\left( \frac{N}{2} - 2 \right) \theta}{\sin\left( \frac{N}{2} - 2 \right) \theta} \quad (7.14)$$

where the constant  $D$  varies for each of the DGS methods:  $D_{r-DGS} = \left( -\frac{\nu B}{E} \right)$  ,

$D_{t-DGS} = (C_{\sigma} B)$ ,  $D_{t2-DGS} = (2C_{\sigma} B)$ , and  $D_{tr-DGS} = \left( 2C_{\sigma} B - \frac{\nu B}{E} \right)$ . In the above equation,

$(r, \theta)$  are the crack-tip polar coordinates and  $A_1 = K_I \sqrt{\frac{2}{\pi}}$  with  $K_I$  being the mode-I stress

intensity factor (SIF). In these experiments,  $\phi_x$  data were used to evaluate SIFs by employing an overdeterministic regression analysis of measurements, and four higher order terms ( $N = 4$ ) in Eq. (7.14). (The use of higher order terms also accounts for any rigid body motion issues when present.) Discrete angular deflections in the region around the crack-tip,  $0.5 \leq r/B \leq 1.5$ ,  $-135^{\circ} \leq \theta \leq 135^{\circ}$ , were used in the regression analysis. This ensured that the data used was sufficiently close to the crack-tip, and also minimized the dominant triaxial effects near the crack-tip [33]. The results obtained are plotted in Fig. 15 for different load levels and measured by all the four DGS methods including  $tr$ -DGS and  $t2$ -DGS. For comparison, the theoretical values of mode-I SIF were also calculated and plotted in Figure 7.13 using [130]:

$$K_I = \frac{F \cdot S}{B \cdot W^{\frac{3}{2}}} \cdot \frac{3 \left( \frac{a}{W} \right)^{\frac{1}{2}} \left[ 1.99 - \frac{a}{W} \left( 1 - \frac{a}{W} \right) \left\{ 2.15 - 3.93 \left( \frac{a}{W} \right) + 2.7 \left( \frac{a}{W} \right)^2 \right\} \right]}{2 \left( 1 + 2 \frac{a}{W} \right) \left( 1 - \frac{a}{W} \right)^{\frac{3}{2}}} \quad (7.15)$$

where  $F$  is the applied load,  $S$  is the span of the beam,  $a$  is the initial crack length,  $B$  is the specimen thickness, and  $W$  is the width. It is evident in Figure 7.13 that there is a good agreement between the experimental and theoretical values of SIF, suggesting the feasible application of  $t2$ -DGS and  $tr$ -DGS for fracture mechanics investigations.

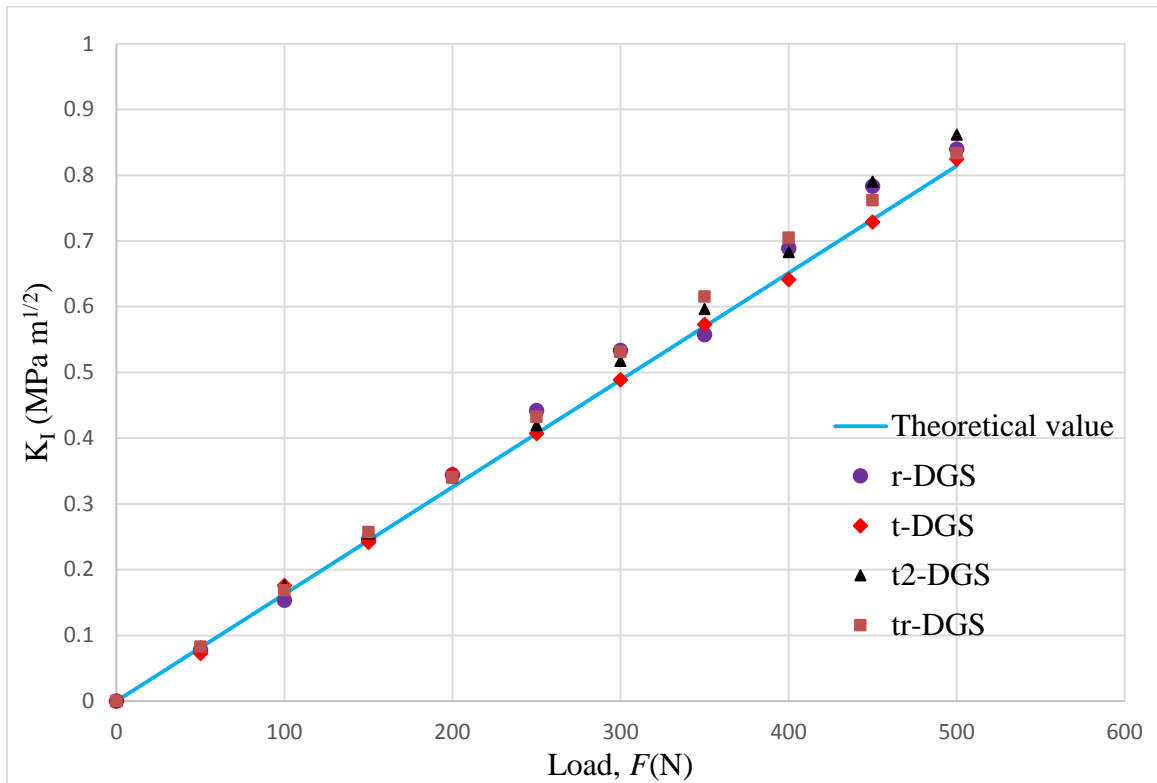


Figure 7.13: Measured mode-I stress intensity factors (symbols) at different loads by different DGS methods. The solid line represents the corresponding theoretical values.

## **Chapter 8. Dynamic Fracture Behavior of Glass Plates using Modified Digital Gradient Sensing Techniques**

In this chapter, fracture mechanics of soda-lime glass plates subjected to dynamic impact loading and studied using the two modified Digital Gradient Sensing (DGS) techniques described in the previous chapters is discussed. First, the feasibility of traditional reflection-mode DGS (*r*-DGS) and its limitation of study fracture mechanics of soda-lime glass are examined. Then the experimental details of applying ultrahigh-speed photography with new DGS methods are described. The results of fracture parameters of crack speed and stress intensity factor (SIF) histories are presented.

### **8.1 Dynamic fracture of soda-lime glass studied using *r*-DGS**

One of the traditional DGS methods, namely, reflection-mode DGS (*r*-DGS), was first applied to study dynamic fracture of soda-lime glass plates. Single edge notched (SEN) specimens of dimensions 152 mm × 76 mm × 9.5 mm plates, as shown in Figure 8.1, were cut from a 9.5 mm thick sheet stock. An initial notch of 12 mm was cut at the middle of the long edge using a 300 μm thick diamond impregnated saw. An impact load was also imposed at the middle of the edge opposite to the cracked edge. One of the two 152 mm × 76 mm faces of the specimen was made reflective by depositing aluminum film to implement *r*-DGS.

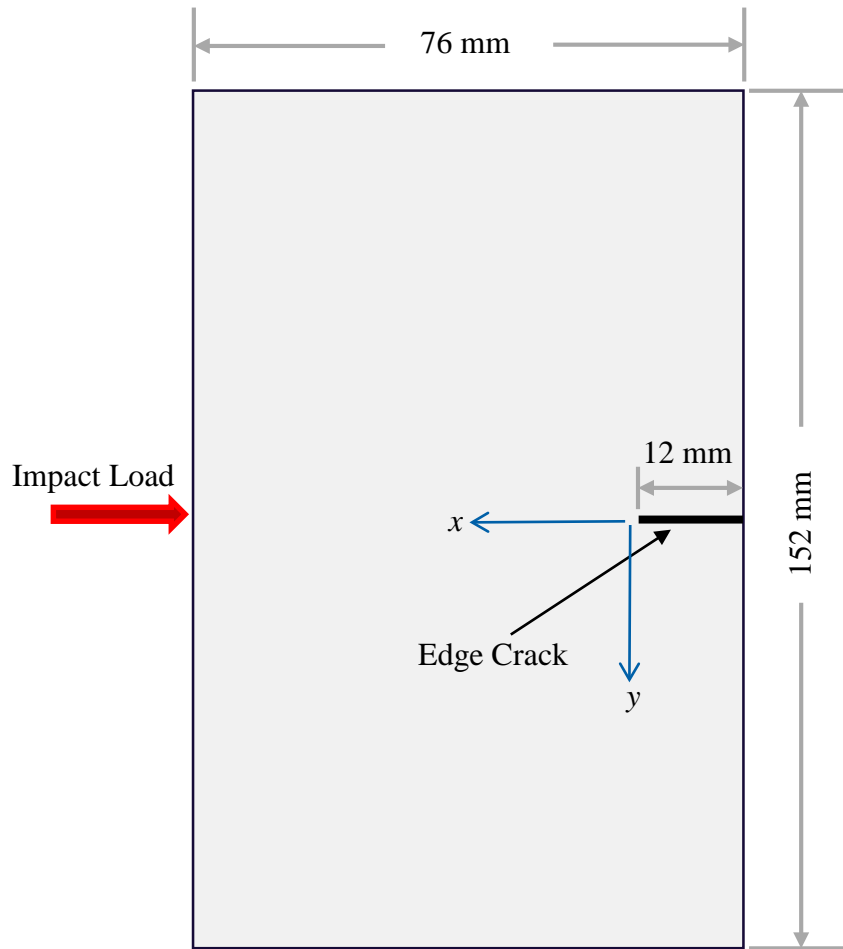
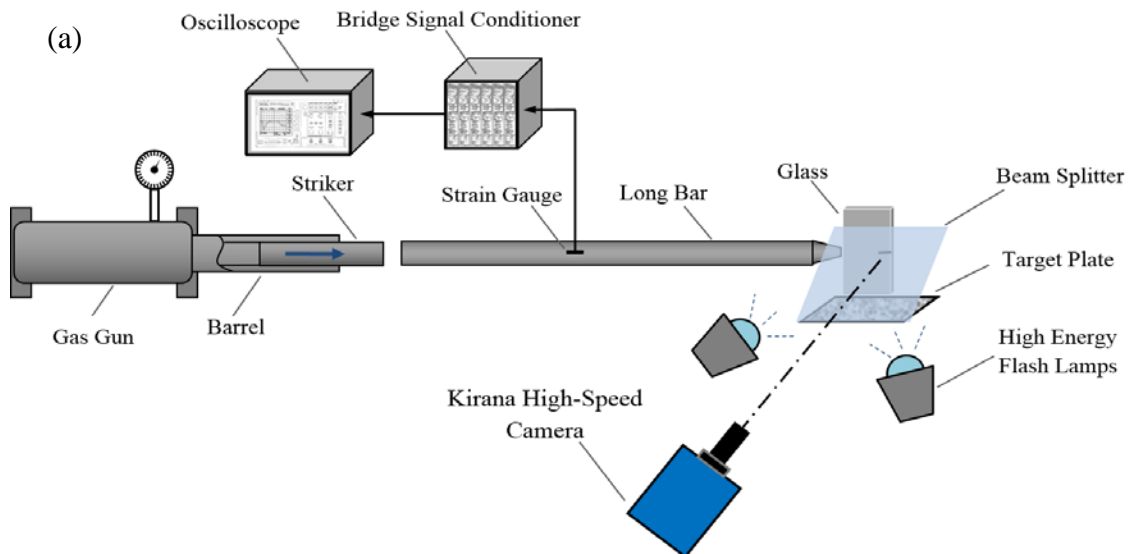


Figure 8.1: Specimen Configuration.

The schematic of the experimental setup used is shown in Figure 8.2. It is same as the one previously described in Chapter 7, (Section 7.3.1) but repeated here for convenience. A modified Hopkinson pressure bar, or a ‘long-bar’, was used for loading the edge-cracked specimens. The long-bar was a 1.83 m steel rod of 25.4 mm diameter with a polished wedge-shaped tip for impacting an unconstrained glass plate on the edge opposite to the cracked edge. A 305 mm long, 25.4 mm diameter steel striker placed in the barrel of a gas-gun was co-axially aligned with the long-bar at the start of the experiment. The striker was launched towards the long-bar at a velocity of approx. 4 m/s during tests. A close-up

of the optical arrangement is also shown in Figure 8.2. Initially, the long-bar tip was kept in contact with the specimen. The specimen was positioned on the platform using a ~1.5 mm thick rectangular soft putty strip to prevent direct contact with the platform. To achieve symmetry in terms of acoustic impedance relative to the loading axis, another identical putty strip was pressed onto the top edge of the specimen. The putty strips isolated the specimen from the adjustable platform to create an approximately ‘free surface’ conditions except the loading surface. A beam splitter and the speckle target plate were placed in a specially designed 45° holder so that the camera could be focused on the speckles through the beam splitter via the reflective specimen surface. The speckle images were photographed by a Kirana-05M ultrahigh-speed digital camera, a single sensor camera capable of recording 180, 10-bit gray scale images at a maximum rate of 5 million frames per second and spatial resolution of  $924 \times 768$  pixels per image. The speckles on the target plate were illuminated using a pair of Cordin-659 high energy flash lamps.



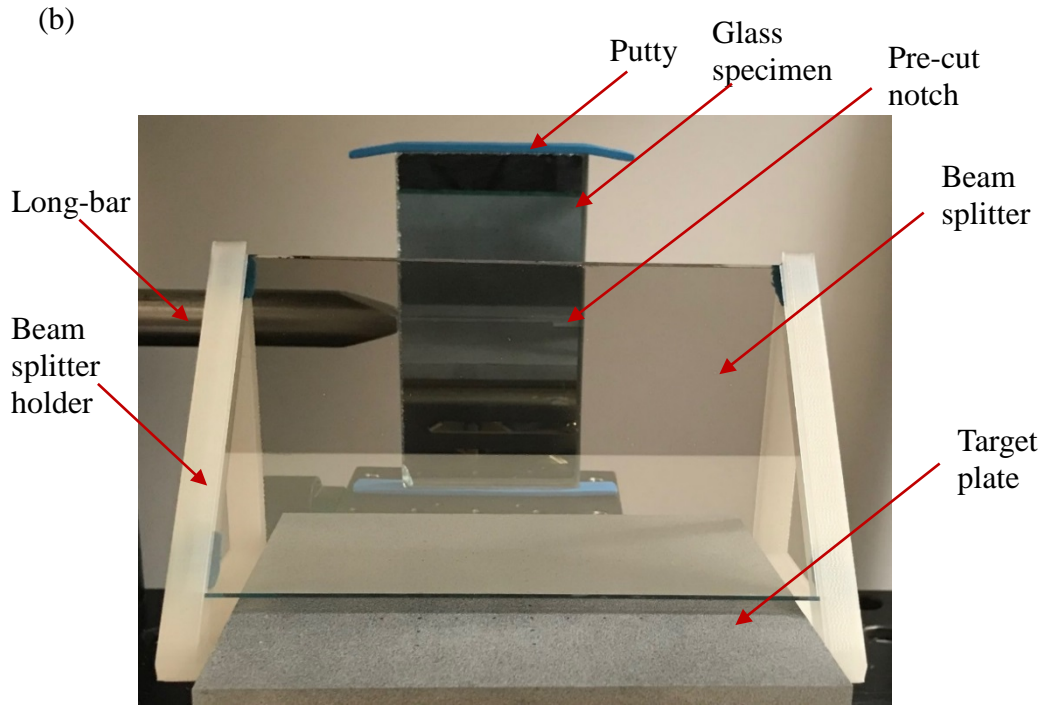


Figure 8.2: Schematic (a) and close-up photograph (b) of the experimental setup used to study dynamic fracture of soda-lime glass.

A Sigma 150-600 mm focal length zoom lens with an adjustable bellows was used with the camera to record the speckle images from a long distance. The distance between the specimen and the lens plane ( $L$ ) was  $\sim 1600$  mm and the one between the specimen mid-plane and the target plane ( $\Delta$ ) was  $\sim 700$  mm. With these settings, the camera recorded information from a rectangular region of approximately  $40 \text{ mm} \times 50 \text{ mm}$  on the specimen plane in the vicinity of the pre-notch tip as the region-of-interest (ROI). When the long-bar was impacted by the striker, a compressive stress wave propagated the entire length of the bar. Also, a trigger pulse was generated at the moment of impact to start recording the speckle images by the camera with a prescribed delay. A total of 180 images, some in the undeformed state and others in the deformed state of the specimen, were recorded at 1,000,000 frames per second (inter frame period  $1 \mu\text{s}$ ). An image just before the start of

deformation was selected as the reference image. Subsequent images corresponding to the deformed state were correlated with the reference image using ARAMIS® image analysis software. During analysis, a sub-image size of  $30 \times 30$  pixels (1 pixel =  $76.88 \mu\text{m}$  on the specimen) with 25 pixels overlap was used to extract the local displacements  $\delta_{x,y}$  in the ROI. The displacement fields were then used to compute the two orthogonal surface slopes,

$$\frac{\partial w}{\partial x; y}$$

where  $w$  is the out-of-plane displacement.

The time-resolved angular deflection contour plots of  $\phi_{x,y}$  ( $\approx 2 \frac{\partial w}{\partial x; y}$ ) around a dynamically loaded mode-I crack in the glass plate are shown in Figure 8.3 at a few select time instants. In these plots,  $t = 0 \mu\text{s}$  corresponds to crack initiation at the original notch-tip. It can be observed that, due to the symmetric nature of mode-I fracture, the crack propagates along a horizontal path (from right to left in these images) and hence the contours are generally symmetric in shape relative to the initial crack. The contours near the left-hand edge in these plots are attributed to the concentration of deformations due to the impact load imposed on that edge (outside the ROI). When compared to the angular deflection contours around a mode-I crack in other materials measured by  $r$ -DGS [131, 132], the singular nature of the crack-tip field which can be measure by  $r$ -DGS is not observed in these contours. This is because, the out-of-plane deformation around the crack-tip in soda-lime glass plate, as a thin and stiff material, is less than  $-100 \text{ nm}$ , and such small out-of-plane deformation was further drowned out by the positive deformation on the left side from the impact load. As a result, the out-of-plane deformation around the crack tip appears diffuse and the singularity has not manifested in the  $r$ -DGS measurements. Hence,

DGS methods of higher measurement sensitivity are required to study dynamic fracture of stiff and low-toughness materials.

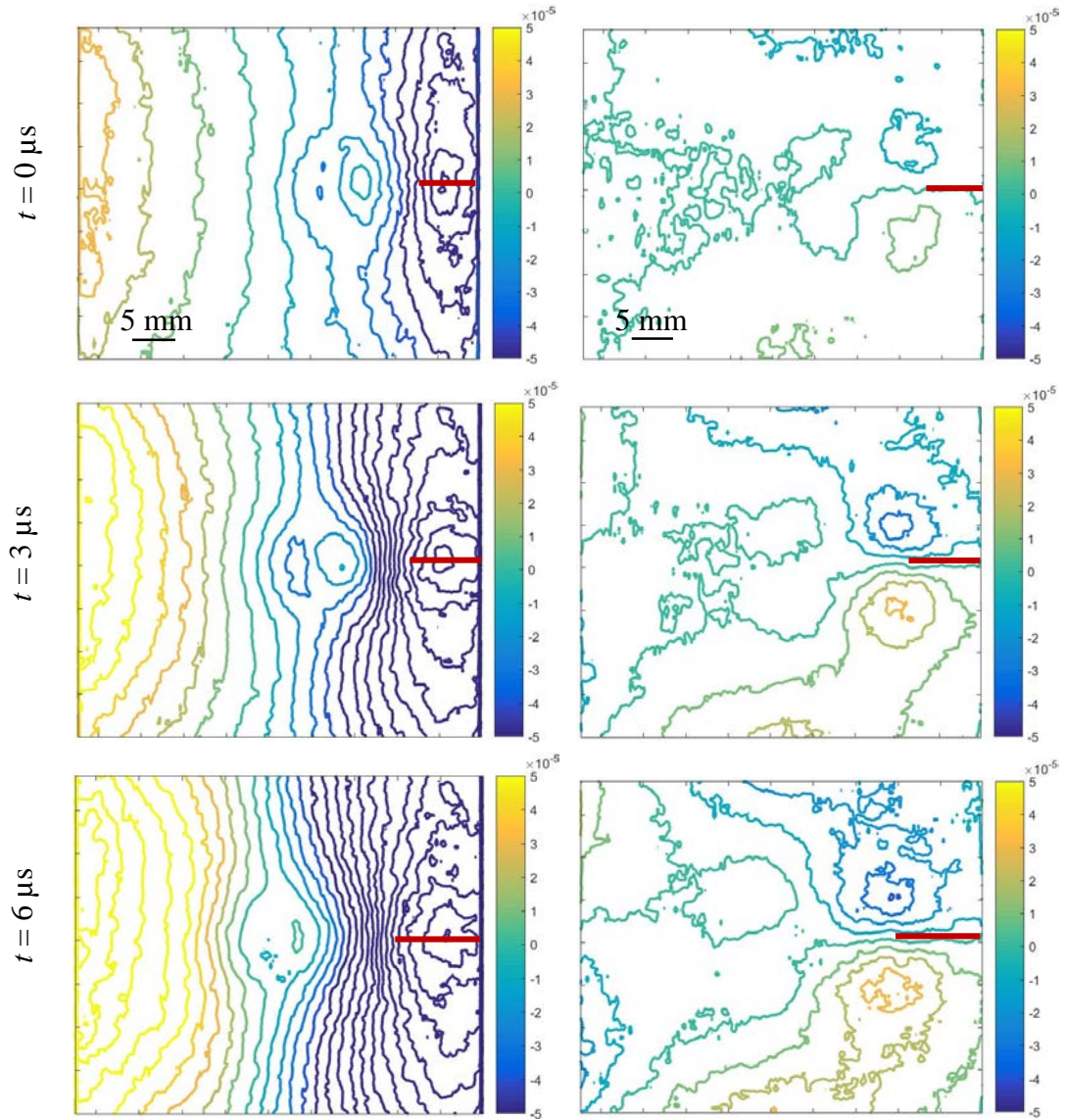


Figure 8.3: Measured angular deflection contours  $\phi_x$  (left column) and  $\phi_y$  (right column) for dynamic fracture of glass using  $r$ -DGS. Contour increment =  $10 \times 10^{-6}$  rad. Red stripes highlight the crack.

## 8.2 Dynamic fracture of soda-lime glass studied using higher sensitivity DGS methods

Recently, the author has proposed two modified DGS methods,  $t2$ -DGS and  $tr$ -DGS, with higher measurement sensitivity, as discussed in Chapter 7. The two new modified DGS methods have experimental setups similar to that for  $r$ -DGS. The  $r$ -DGS method only measures deformations due to the Poisson effect, whereas  $t2$ -DGS measures stress optic effects of transparent materials, and  $tr$ -DGS measures combined Poisson effects and stress optic effects. As a result, the measurement sensitivity of  $t2$ -DGS is double that of  $r$ -DGS, and  $tr$ -DGS is more than triple that of  $r$ -DGS. Hence, the dynamic fracture of soda-lime glass was studied using  $t2$ -DGS and  $tr$ -DGS next.

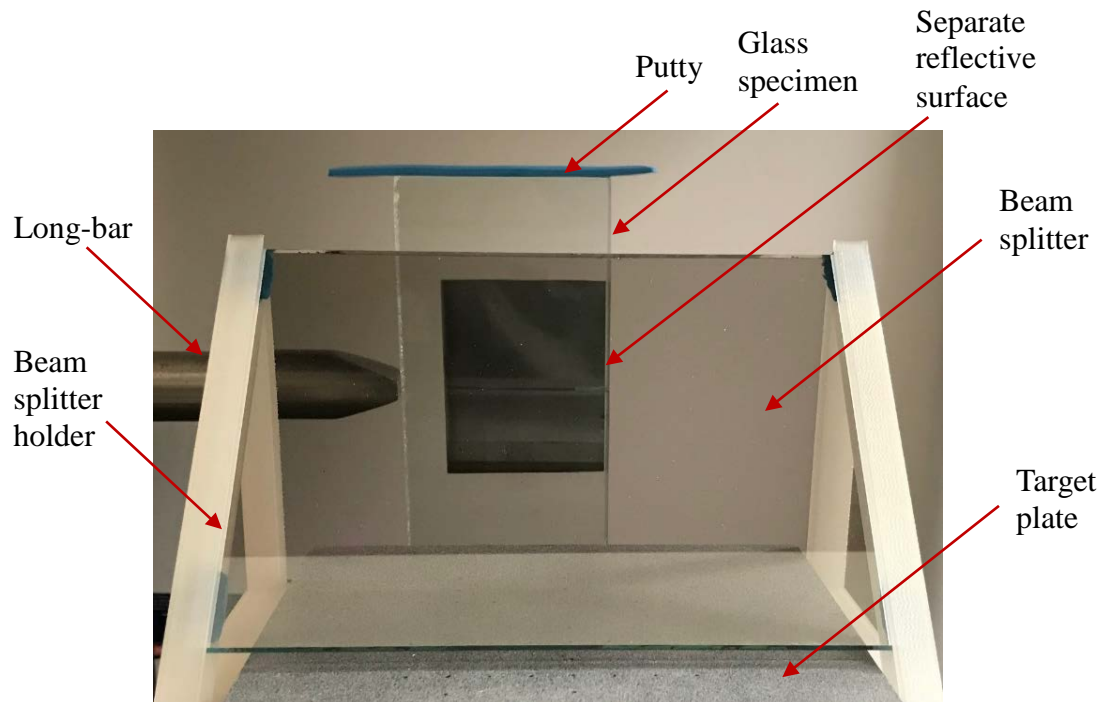


Figure 8.4: Close-up photograph of experimental setup for  $t2$ -DGS.

The specimen configurations and experimental setup used when applying  $t2$ -DGS and  $tr$ -DGS to study glass are the same as the one used in the application of  $r$ -DGS. A close-up of the optical arrangement for  $t2$ -DGS is shown in Figure 8.4, a reflective planar mirror was placed flush with the soda-lime glass specimen. On the other hand, for  $tr$ -DGS, the back surface of specimen is made reflective. The distance between the specimen and the lens plane ( $L$ ) was  $\sim 1300$  mm and the one between the specimen and the target plane ( $\Delta$ ) was  $\sim 200$  mm for both  $t2$ -DGS and  $tr$ -DGS. Note that  $\Delta$  used for  $t2$ - and  $tr$ -DGS were significantly shorter than the one used for  $r$ -DGS ( $\sim 700$  mm).

A few select time-resolved angular deflection contour plots of  $\phi_{x,y}$  around a dynamically loaded mode-I crack in glass plates measured by  $t2$ -DGS and  $tr$ -DGS are shown in Figure 8.5 and Figure 8.6, respectively. In these plots,  $t = 0 \mu s$  corresponds to crack initiation at the original notch-tip. It can be observed that contours in Figure 8.5 and Figure 8.6 are rather well-defined when compared to those in Figure 8.5, especially after crack initiation. This indicates that the higher sensitivity of  $t2$ -DGS and  $tr$ -DGS relative to  $r$ -DGS are helpful for visualizing the singular nature of the crack-tip field quantitatively in soda-lime glass plates. The contour plots in both Figure 8.5 and Figure 8.6 are plotted with the same contour increment of 20 micro-radians. When compared to the contours measured using  $t2$ -DGS in Figure 8.5, those measured by  $tr$ -DGS in Figure 8.6 are larger and denser, which shows that  $tr$ -DGS is more sensitive when compared to  $t2$ -DGS.

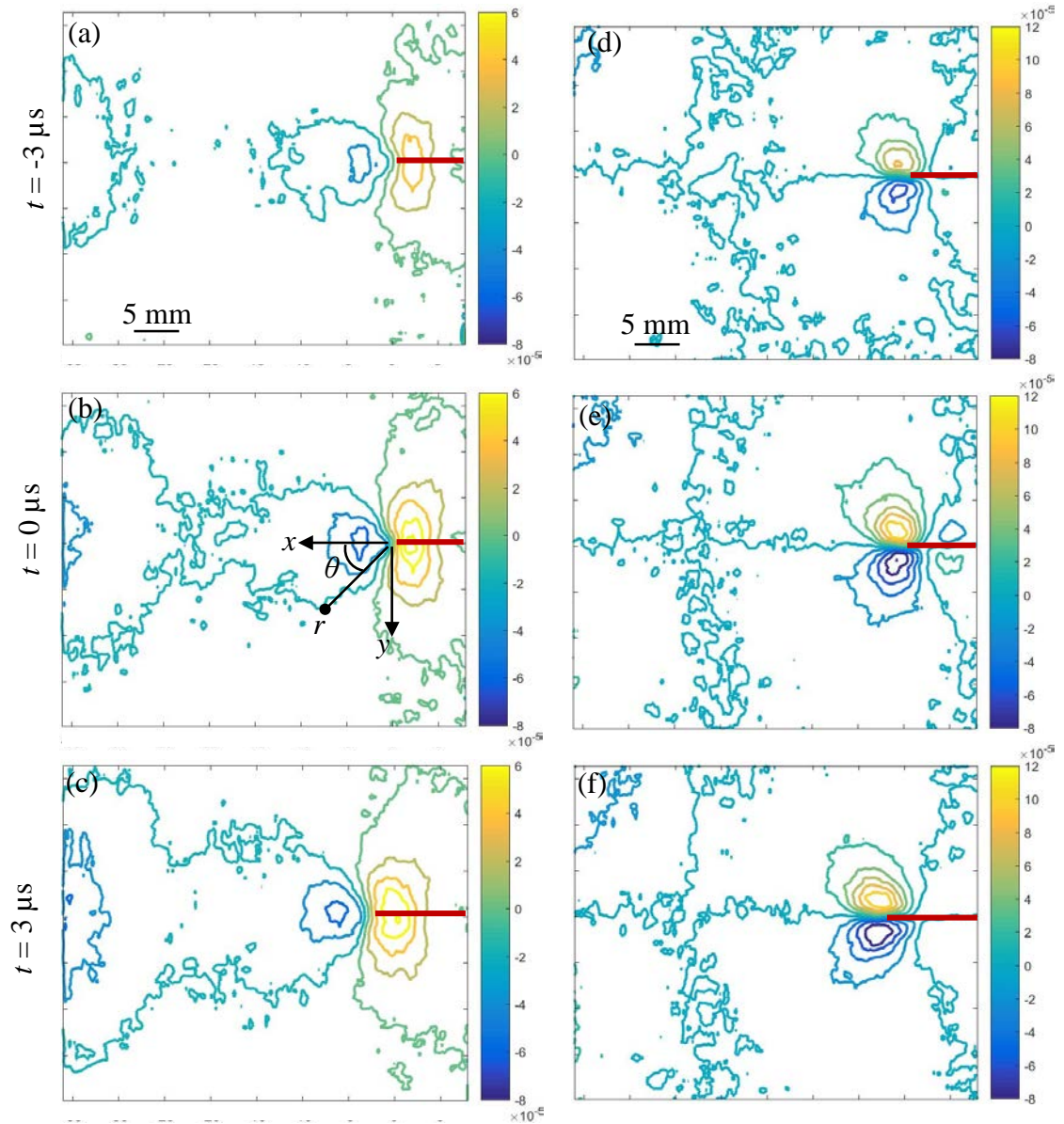


Figure 8.5: Measured angular deflection contours  $\phi_x$  (left column) and  $\phi_y$  (right column) for dynamic fracture of glass using  $t_2$ -DGS. Contour increment =  $20 \times 10^{-6}$  rad. Red stripes highlight the crack.

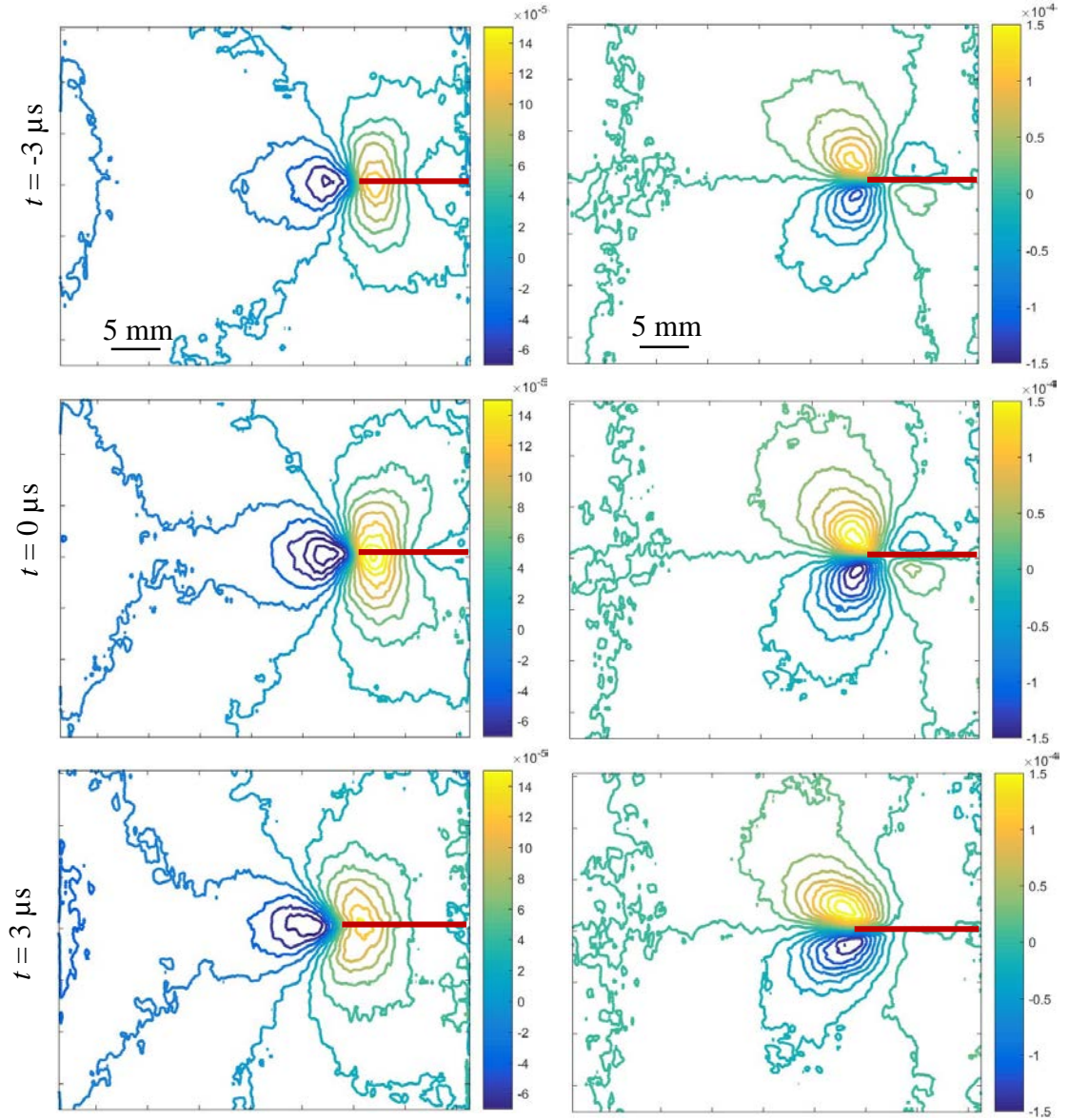


Figure 8.6: Measured angular deflection contours  $\phi_x$  (left column) and  $\phi_y$  (right column) for dynamic fracture of glass using  $tr$ -DGS. Contour increment =  $20 \times 10^{-6}$  rad. Red stripes highlight the crack.

The contours of  $(\sigma_x + \sigma_y)$  computed by 2D integration of stress gradients data from  $t2$ -DGS in conjunction with Higher-order Finite-difference-based Least-squares Integration (HFLI) algorithm [117] (see, Section 3.1) are plotted in Figure 8.7. It is evident that the singular crack-tip stress (positive values) before crack initiation and during crack

growth. As noted earlier in the context of  $r$ -DGS results, the compressive stresses (negative values) on the left edge are attributed to the impact loading.

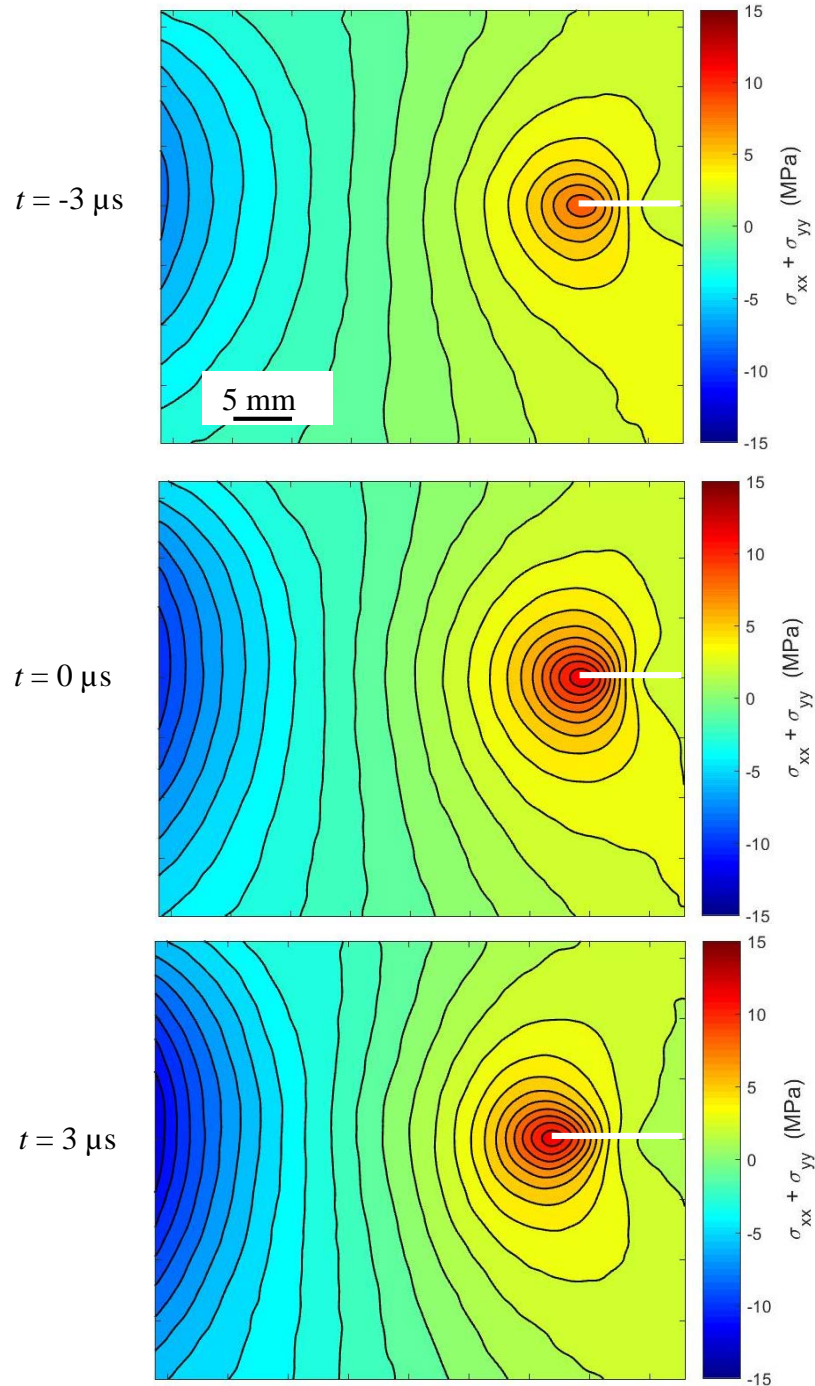


Figure 8.7: Contours of  $(\sigma_x + \sigma_y)$  for dynamic fracture of glass plate at a few select time instants. Contour increment = 1 MPa. White stripes highlight the crack.

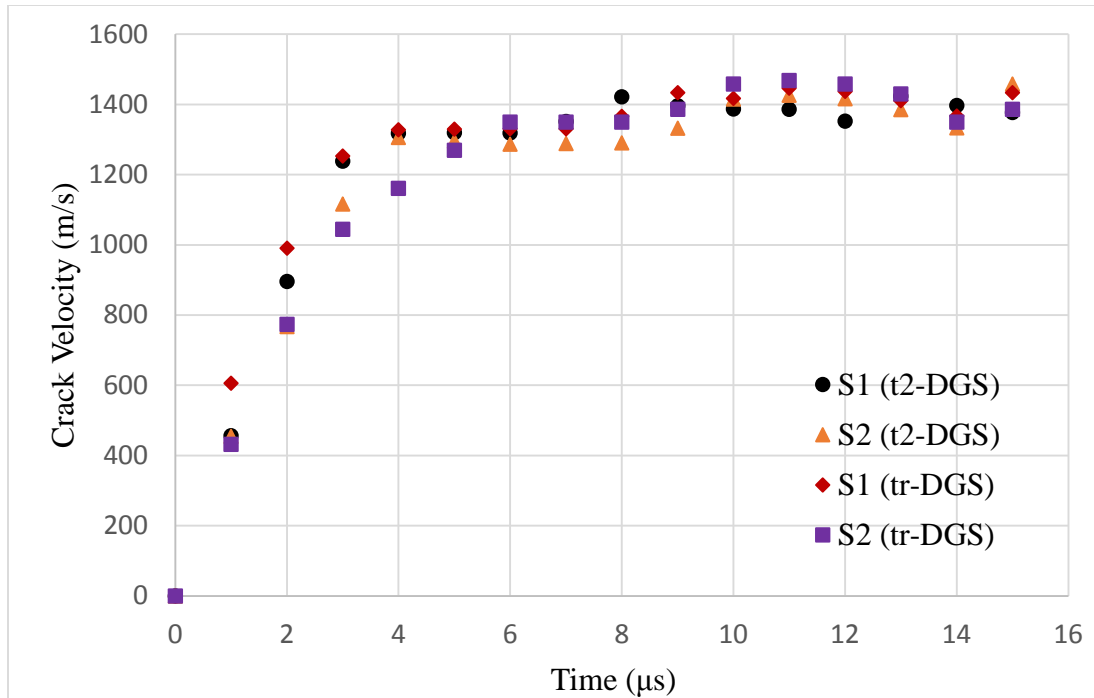


Figure 8.8: Crack velocity histories for specimens measured using  $t2$ -DGS and  $tr$ -DGS.

The crack velocity histories for four different experiments, two specimens each for  $t2$ -DGS and  $tr$ -DGS, obtained from the respective angular deflection contours are shown in Figure 8.8. It can be observed that the velocity histories for all the specimens overlap on each other, indicating the consistency of measurements between  $t2$ -DGS and  $tr$ -DGS methods. All the velocity histories increase from 0 to  $\sim 1300$  m/s in 3-4  $\mu$ s after crack initiation, and then apart from small fluctuations in the histories they become steady at  $\sim 1350$  m/s.

The fractography of crack surface during crack growth is shown in Figure 8.9. The mirror region is observed first at the early stages of crack growth. The rib/arc shaped marks, known as Wallner lines due to interference of emanating crack tip stress waves and reflected stress waves from free surfaces, can be found in the mirror region, which indicate the local crack propagation direction. After the crack grows for a certain distance, the mist

region can be observed. It is followed by the hackle region, where the fracture surface becomes visibly rough. When related to Figure 8.8, it can be seen that the steady crack velocities occur in the mirror region, and then the fluctuations of crack velocities occur in the mist and hackle regions.

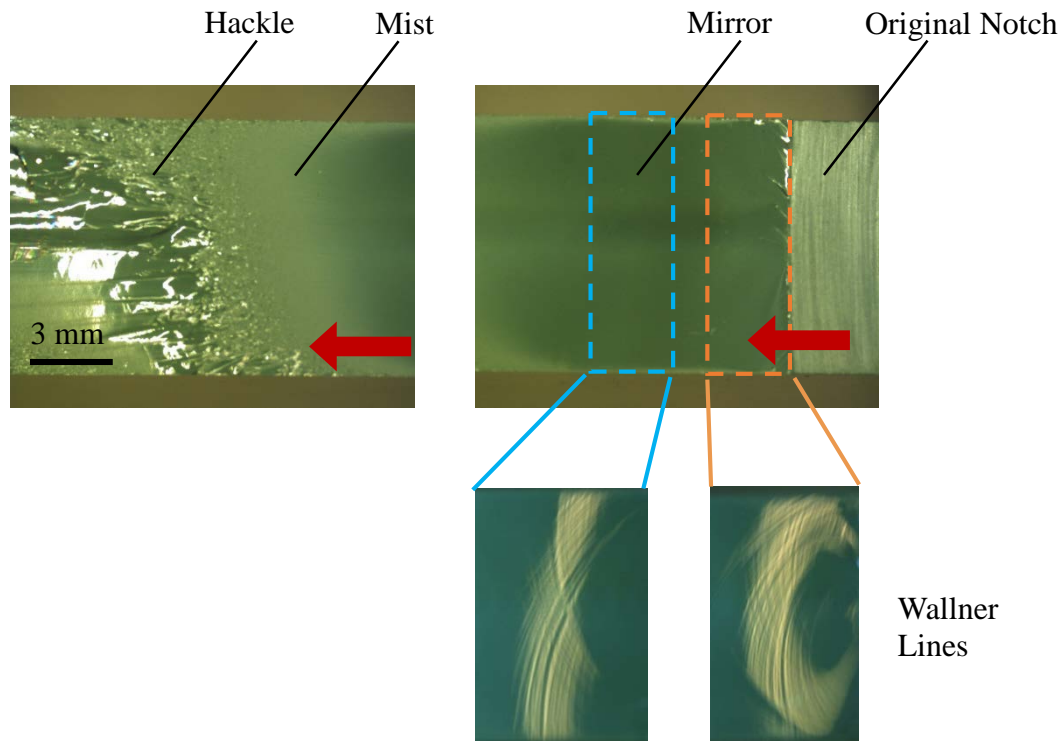


Figure 8.9: Fractography showing ‘mirror’, ‘mist’, and ‘hackle’ features. Red arrows show crack propagation direction.

The stress intensity factor (SIF) histories were evaluated using an overdeterministic least-squares analysis based on the angular deflection fields of ( $\phi_x$ ) measured by *tr*-DGS and *t2*-DGS methods,

$$\phi_x(t) = D \left[ \begin{array}{l} -\frac{1}{2} r^{\frac{3}{2}} \left\{ \begin{array}{l} f(V; C_L; C_S) A_1(t) \cos\left(\frac{3\theta}{2}\right) \\ + g(V; C_L; C_S) D_1(t) \sin\left(-\frac{3\theta}{2}\right) \end{array} \right\} \\ + \sum_{N=2}^{\infty} \left\{ \begin{array}{l} A_N(t) \left(\frac{N}{2}-1\right) r^{\left(\frac{N}{2}-2\right)} \cos\left(\left(\frac{N}{2}-2\right)\theta\right) \\ + D_N(t) \left(\frac{N}{2}-1\right) r^{\left(\frac{N}{2}-2\right)} \sin\left(\left(\frac{N}{2}-2\right)\theta\right) \end{array} \right\} \end{array} \right] \quad (8.1)$$

where the constant  $D$  varies for each of the DGS methods,  $D_{t2-DGS} = (2C_\sigma B)$  and

$$D_{tr-DGS} = \left( 2C_\sigma B - \frac{\nu B}{E} \right), \quad C_\sigma \text{ is the elasto-optic constant of soda-lime glass } (-2.7 \times 10^{-12}$$

$\text{m}^2/\text{N}$ ),  $B$  is its initial thickness,  $E$  and  $\nu$  are elastic modulus and Poisson's ratio,

respectively. Further,  $f$  and  $g$  are the functions of instantaneous crack velocity,  $(r, \theta)$ , as

shown in Figure 8.5(b), denotes the contracted crack-tip polar coordinates for a growing

crack,  $r = \left\{ (x)^2 + \alpha_L^2 (y)^2 \right\}^{1/2}$  and  $\theta = \tan^{-1} \left( \frac{\alpha_L y}{x} \right)$ . Mode-I and mode-II SIFs  $K_I(t)$

and  $K_{II}(t)$  are related to the coefficients of  $A_1(t)$  and  $D_1(t)$ , respectively, as

$A_1(t) = K_I(t) \sqrt{2/\pi}$  and  $D_1(t) = K_{II}(t) \sqrt{2/\pi}$ . Values of  $(\phi_x)$  measured by  $t2$ -DGS and

$tr$ -DGS were used to calculate SIFs, respectively. The functions  $f$  and  $g$  are [117],

$$f(V; C_L, C_S) = \left( \frac{1+\nu}{1-\nu} \right) \frac{(1+\alpha_s^2)(1-\alpha_L^2)}{4\alpha_L\alpha_s - (1+\alpha_s^2)^2} \quad (8.2)$$

$$g(V; C_L, C_S) = \left( \frac{1+\nu}{1-\nu} \right) \frac{2\alpha_s(1-\alpha_L^2)}{4\alpha_L\alpha_s - (1+\alpha_s^2)^2}$$

where  $\alpha_L = \left[1 - \frac{\rho(1-\nu)}{2\mu} V^2\right]^{\frac{1}{2}}$  and  $\alpha_S = \left[1 - \frac{\rho}{\mu} V^2\right]^{\frac{1}{2}}$  for plane stress. The discrete  $\phi_x$  field data in the region around the crack-tip,  $0.4 \leq r/B \leq 1.0$ ,  $-140^\circ \leq \theta \leq 140^\circ$ , were utilized in the analysis. The effect of non-singular far-field deformations on the measured  $K_I$  and  $K_{II}$  was offset by using four higher order terms ( $n = 4$ ) in Eq. (8.2) during least-squares analysis.

To complement the experimental results, an elasto-dynamic 3D model was simulated using ABAQUS® structural analysis software and SIF history prior to crack initiation was verified. The model contained the end of long-bar and the specimen to simulate the stress wave propagating into the specimen. It consisted of 71,775 and 679,174 tetrahedral elements for the long-bar and the specimen, respectively. The mesh in the regions around the impact and the crack tip were refined with elements size of 0.1 mm. The discretized model with the crack opening displacement contours is shown in Figure 8.10(a). The symmetry of these contours about the crack plane are consistent with the mode-I deformations expected from this simulation. Figure 8.10(b) shows the strain history measured using the strain gage on the long-bar during experiment. The particle velocity history calculated from the strain history,  $V_p = c\varepsilon$  (where  $c$  is the bar wave speed in steel and  $\varepsilon$  the measured strain), was used as input to the simulation. The material properties of the specimen and the long-bar used in the simulation are shown in Table 8-1. The apparent mode-I and mode-II SIFs,  $(K_{I:II})_{app}$ , at each time step were calculated from the instantaneous crack opening ( $v$ ) and sliding ( $u$ ) displacements extracted along the two crack faces using [133]:

$$(K_{I;II})_{app} = \frac{E\sqrt{2\pi}}{8\sqrt{r}}(v;u); \quad (r, \theta = \pi) \quad (8.3)$$

The instantaneous values of  $(K_{I;II})$  were determined extrapolating the linear portion of  $(K_{I;II})_{app}$  plotted as a function of the radial distance  $r$  ( $\theta = \pi$ ).

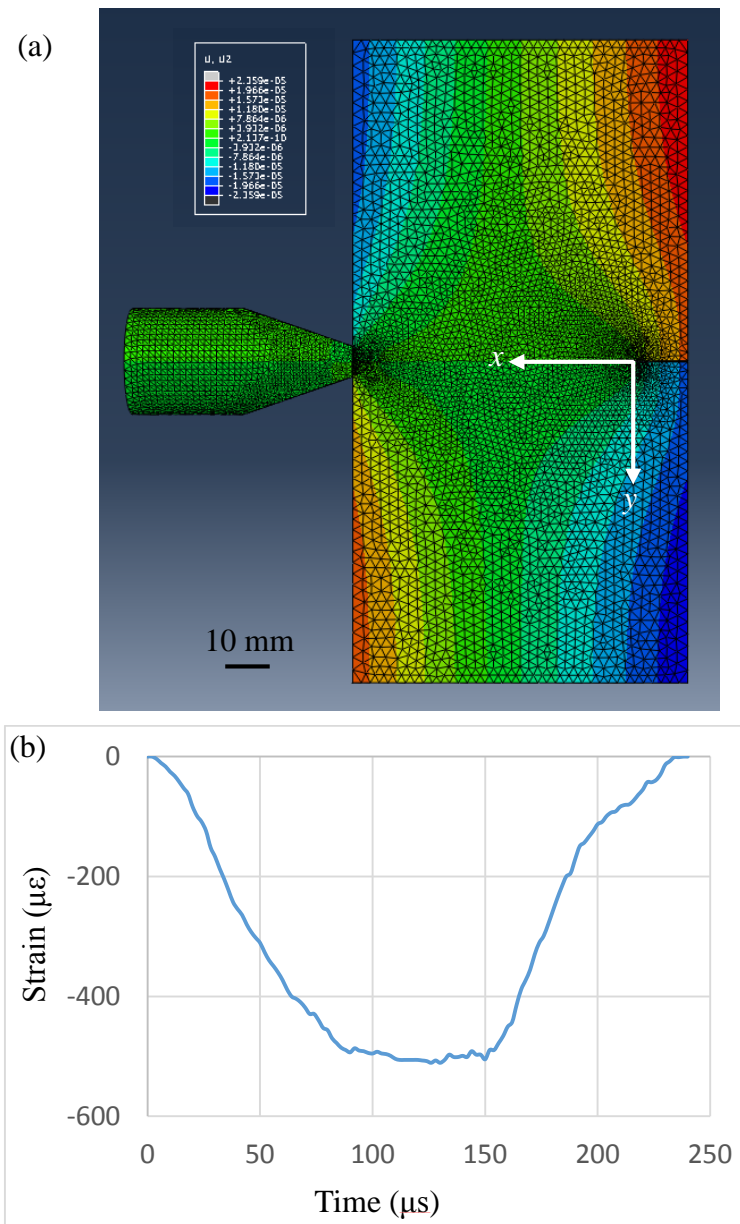


Figure 8.10: (a) Discretized finite element model with crack opening displacement contours. (b) The strain history due to the compressive stress pulse measured using the strain gage on the Hopkinson bar.

Table 8-1 Material properties of maraging steel and soda-lime glass used in the simulation

Properties	Soda-lime Glass	Maraging Steel
$E$ (GPa)	70	200
$\nu$	0.22	0.3
$\rho$ (Kg/m <sup>3</sup> )	2500	8000

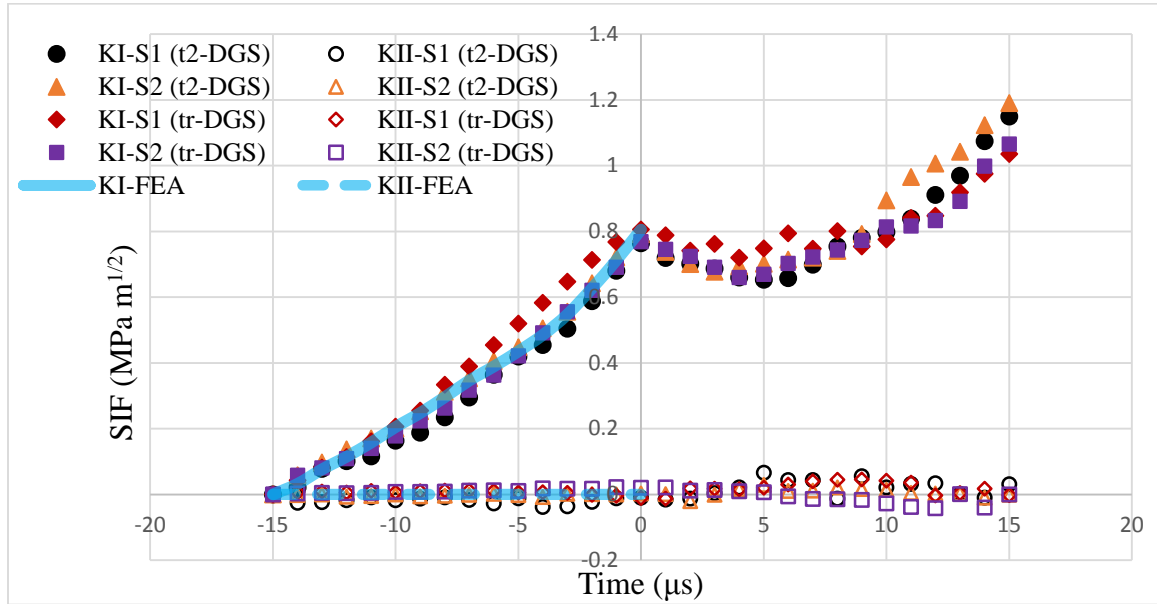


Figure 8.11: Stress intensity factor histories measured by  $t2$ -DGS and  $tr$ -DGS methods, and finite element analysis prior to crack initiation.  $t = 0$  corresponds to crack initiation.

The SIFs obtained from Eq. (8.1) and FEA are plotted in Figure 8.11. Two specimens were studied using each optical method. The time axis of each plot was shifted so that  $t = 0$  corresponds to crack initiation at the original crack-tip. The solid and open symbols in Figure 8.11 represent  $K_I$  and  $K_{II}$ , respectively. The agreement of the SIFs between all the specimens indicates good experimental repeatability and measurement consistency of the two optical methods used. The  $K_I$  histories increase monotonically until crack initiation in all specimens. The dynamic fracture toughness ( $K_I$  at  $t = 0$ ) was recorded as  $0.78 \pm 0.02$  MPa m<sup>1/2</sup>. The time rate of change of  $K_I$ , or  $\frac{dK_I}{dt}$ , was calculated as  $\sim(7.4$

$\pm 1.1) \times 10^4$  MPa m<sup>1/2</sup>/s at crack initiation. There is a visible drop in the  $K_I$  histories after crack initiation, attributed to dynamic unloading at crack initiation. Subsequently,  $K_I$  histories become relatively constant as the crack growth was in the ‘mirror’ region/phase. The apparent  $K_I$  histories then increase monotonically again until the end of the observation window, because (a) the crack propagated towards to compression dominant region caused by the impact on the left edge of the specimen, (b) the crack propagation consumed greater energy as the roughness of crack surface increased, as the ‘mist’ and ‘hackle’ regions shown in Figure 8.9. The apparent  $K_{II}$  histories throughout are nearly zero in both pre- and post-crack initiation regimes due to the nature of mode-I fracture. The nonzero values of  $K_{II}$  suggest potential errors due to the least-squares analysis and crack tip location during data analysis. A good agreement between the SIFs obtained from experiments and FEA can be seen in Figure 8.11.

The dynamic energy release rates for growing cracks can be calculated from the measured crack velocities,  $V$ , and SIFs in Figure 8.8 and Figure 8.11, respectively, using [134]:

$$G^d = \frac{1}{E} \left[ A_I(V) K_I^2 + A_{II}(V) K_{II}^2 \right] \quad (8.4)$$

where  $A_I(V) = \frac{V^2 \alpha_L}{(1-\nu) C_s^2 D}$ ,  $A_{II}(V) = \frac{V^2 \alpha_s}{(1-\nu) C_s^2 D}$ , with  $C_s = \sqrt{\frac{\mu}{E}}$  being the shear wave

speed, and  $D = 4\alpha_L \alpha_s - (1 + \alpha_s^2)^2$ . The plot of dynamic strain energy release rates ( $G^d$ ) with crack velocity ( $V$ ) is shown in Figure 8.12. It can be observed that initially  $G^d$  is nearly a constant, ranging between  $\sim 9$  to  $\sim 7.5$  N/m (J/m<sup>2</sup>), until crack velocity reaches 1300 m/s. Subsequently, the  $G^d$  values rapidly increase to  $\sim 25$  N/m in a narrow velocity range of 1300-1450 m/s.

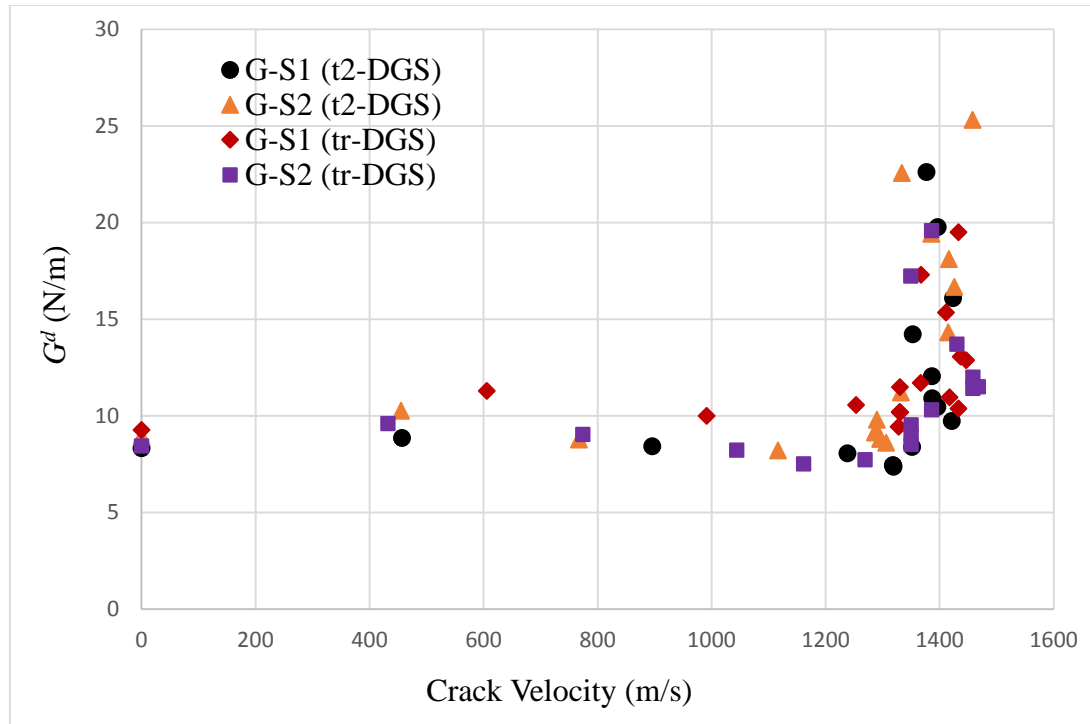


Figure 8.12: Plot of dynamic strain energy release rates ( $G^d$ ) with crack velocity ( $V$ ).

## Chapter 9. Conclusions

In this research, a relatively new optical metrology tool called reflection-mode Digital Gradient Sensor (*r*-DGS) was advanced first to quantify surface topography or profile due to mechanical deformation by coupling it with a robust numerical integration scheme called the Higher-order Finite-difference-based Least-squares Integration or HFLI. This enhanced optical metrology tool was demonstrated for measuring nano- or sub-micron scale out-of-plane deformation over a relatively large ( $\sim 75 \times 75 \text{ mm}^2$ ) field-of-view (FOV) of thin structures. The methodology was next advanced to investigate fracture behavior of carbon fiber reinforced composites (CFRP) by studying loading rate effects. Subsequently, two modified DGS methods of higher measurement sensitivity were advanced specifically for the purpose of performing metrology of high-stiffness and low-toughness transparent ceramics and glass. These two modified DGS methods were applied successfully to study dynamic fracture of soda-lime glass.

The feasibility of surface profile evaluation and stress field mapping from DGS methods were demonstrated first. This was accomplished by coupling DGS output with HFLI scheme implemented in the so-called Southwell configuration. DGS being a digital image correlation-based method capable of providing two orthogonal gradients of a mechanical field simultaneously, it naturally lent itself to the implementation of algorithms in the Southwell configuration to recover the mechanical field. First, the surface profile measurements were successfully extracted using a ‘clamped’ reflective Si wafer subjected

to out-of-plane concentrated loads, applied centrally and eccentrically in two separate sets of experiments. The imposed deflections were recovered using the HFLI scheme with very good accuracy. For  $10 \pm 1 \mu\text{m}$  imposed deflection cases, the recovered values showed approximately 5% deviation from the expected value. Further, reconstruction of  $(\sigma_{xx} + \sigma_{yy})$  stress fields from stress gradients was demonstrated for the case of a dynamically growing crack in a transparent acrylic sheet.

The *r*-DGS methodology coupled with HFLI was also applied to quantitatively visualize both out-of-plane deformations and in-plane stresses in thin composite plates subjected to out-of-plane impact loading. First, the feasibility of measuring micro-radian value surface slopes in two orthogonal directions at microsecond temporal resolution over relatively large regions-of-interest (50-75 mm dia.) was demonstrated using *r*-DGS method via ultrahigh-speed photography. Subsequently, evaluation of micron scale out-of-plane deformations from measurements using HFLI scheme was undertaken. The surface slopes, being just one differentiation away from curvatures and proportional to in-plane stresses according to the plate theory, were numerically differentiated to estimate curvatures and then stresses. Thus, both out-of-plane deformations and in-plane stresses were successfully evaluated.

Subsequently, the accuracy of out-of-plane deformations measured from *r*-DGS used in conjunction with HFLI was investigated. First, the feasibility of detecting deformations over a large FOV was demonstrated using ultrahigh-speed sub-microsecond digital photography with sub-microsecond time-lapse. Next, the validity of those measurements was justified using two methods, one was based on the smallest measurable displacement in 2D DIC, and the other by correlating two speckle images recorded in the

undeformed state with a time-lapse. The verification showed that approx. 10 nm was the smallest measurable out-of-plane deformation using ultrahigh-speed photography at  $10^6$  frames per second. On the other hand, when using slow-speed photography,  $10^1$  frames per second, the smallest measurable out-of-deformation was much higher, yet in the sub-micron range over a large FOV. The difference between ultrahigh-speed photography and slow-speed photography revealed the combined effects of random mechanical vibrations and thermal currents in the optical path. The accuracy of measurement decreased (from  $\sim 10$  nm to  $0.4 \mu\text{m}$  error) at slower speeds or in quasi-static experiments. Hence, it was concluded that *r*-DGS with HFLI could measure nano-scale deformations provided errors from mechanical vibrations and thermal currents are avoided using minimum time-lapse during image capture. Considering the simplicity of the experimental setup, and digital recording and post-processing steps, the potential of this approach to optical metrology of planar substrates (e.g., silicon wafer used in the semiconductor industry) appears to be enormous.

The *r*-DGS technique was advanced successfully to investigate the static and dynamic fracture behaviors of unidirectional CFRP laminates made of T800s/3900-2. Single edge notched coupons subjected to geometrically symmetric loading – quasi-static three-point bending and single-point dynamic impact – were studied. The effect of fiber orientation on crack initiation and growth were examined at two distinctly different loading rates characterized by the rate of change of stress intensity factors,  $10^4 \text{MPa}\sqrt{\text{m}\cdot\text{s}^{-1}}$  and  $10^2 \text{MPa}\sqrt{\text{m}\cdot\text{s}^{-1}}$ , at crack initiation. For dynamic measurements, *r*-DGS was implemented with an ultrahigh-speed single sensor camera. The measured optical fields physically represent small angular deflections of light rays in the  $10^{-5}$  to  $10^{-3}$  radians range and related to two

orthogonal surface slopes in the ROI. Besides visualizing the full-field deformations, the optical measurements were used in concurrence with elasto-static and elasto-dynamic crack-tip fields for orthotropic materials to quantify stress intensity factors, energy release rates, loading rates and crack speeds. Based on the measurements, the following observations were made: (a) The inclined fiber orientation ( $\alpha$ ) relative to the initial crack direction force crack-tip deformations and crack growth occur under mixed-mode conditions despite geometrically symmetric loading configurations. That is, mixed-mode crack growth ensued along the fibers in all non-zero fiber orientation cases. A wide range of speeds, from 800 m/s in the  $\alpha = 0^\circ$  case to less than 200 m/s when  $\alpha = 60^\circ$ , under dynamic impact loading conditions occurred. (b) Under quasi-static loading conditions, crack initiation occurred at a load that continued to increase until a higher peak/critical load was reached. This was attributed to the formation of fiber bridges across the crack flanks. Both crack initiation and critical loads decreased with the degree-of-anisotropy. (c) A monotonic increase in both mode-I and -II stress intensity factors occurred until crack initiation. The crack-tip loading rates in the dynamic cases were of the order of  $10^4 \text{ MPa}\sqrt{\text{m}\cdot\text{s}^{-1}}$  whereas they were six orders of magnitude lower in the quasi-static counterparts. (d) The crack initiation events in the dynamic cases were punctuated by an abrupt drop in  $K_I$  whereas an abrupt increase in  $K_{II}$  magnitude in all non-zero fiber angles. In the quasi-static cases, however, the latter was true in all non-zero fiber angles whereas the former was true for angles  $30^\circ$  and  $45^\circ$  cases as fiber bridges strongly influenced post-initiation behavior in the  $0^\circ$  and  $15^\circ$  cases. It consistently took longer for the crack to initiate when the fiber angles were larger. (e) The energy release rate ( $G$ ) variations showed monotonic increase until crack initiation in both quasi-static and dynamic conditions. The post-initiation

characteristics, however, were quite different. An abrupt drop in  $G$  followed by steady values during the observation window in the dynamic cases contrasted with increasing trends in the static cases. Such a weaker post-initiation crack growth could cause sudden failure under dynamic conditions whereas static loading could result in a more graceful failure. (f) Apart from the zero-degree fiber orientation case, the energy release rate when the crack initiated under dynamic mixed-mode conditions was lower than the corresponding quasi-static cases. During growth, however, the energy release rates were approx. one-half of that at crack initiation in dynamic loading conditions.

In the next part of this research, the concept and the feasibility of two new experimental configurations of DGS methods with enhanced measurement sensitivity for experimental mechanics were examined. The configurations were particularly valuable for studying high-stiffness and low-toughness substrates such as transparent glasses and ceramics. The concept identified as  $tr$ -DGS showed higher than three times the measurement sensitivity of the original  $t$ -DGS method. This was achieved by doubling of the optical path within the specimen besides reflection from the deformed back surface achieved via a reflective coating. For cases where deposition of a reflective coating is not feasible, a simple doubling of the optical path and hence the sensitivity over  $t$ -DGS was achieved in  $t2$ -DGS configuration by using a detached reflector kept flush with the back surface of the specimen. A dynamic mode-I crack initiation and growth experiment involving  $tr$ -DGS and  $t2$ -DGS measurements performed simultaneously on the same specimen above and below the crack-line were comparatively examined by exploiting the symmetry of the problem. The fact that the rigid body motion of speckles was negligible under stress wave loading conditions was taken advantage of using a single sensor

ultrahigh-speed camera where reference and deformed speckle images were recorded only a few microseconds apart. The measured sensitivity ratio of angular deflections of light rays from *tr*-DGS and *t2*-DGS methods matched well with those from opto-mechanical predictions. A single edge notched beam bending experiment in a 3-point symmetric bending configuration was used to implement four different variants of DGS – *t*-DGS, *r*-DGS, *t2*-DGS and *tr*-DGS – to measure crack-tip stress gradient fields and extract mode-I SIF. The measured SIF values matched well with the predictions.

Finally, the above two modified DGS methods were applied successfully to quantitatively visualize stress gradient fields around the crack-tip in single-edge-notched soda-lime glass plates subjected to dynamic impact loading. The measured stress gradients fields were again numerically integrated using HFLI scheme to obtain  $(\sigma_{xx} + \sigma_{yy})$  stress fields. The higher measurement sensitivities of both *t2*-DGS and *tr*-DGS were very attractive to detect the stress gradients around the mathematically sharp crack-tip without using a relatively large  $\Delta$ , and hence the optical errors due to thermal currents and vibrations were reduced relative to traditional *r*-DGS and *t*-DGS methods. By employing ultrahigh speed photography at 1 Mfps, the crack speed was clocked at ~1350 m/s. The stress intensity factor histories were also calculated during pre- and post-crack initiation regimes. The dynamic fracture toughness was recorded as  $0.78 \pm 0.02$  MPa m<sup>1/2</sup>. The dynamic strain energy release rates,  $G^d$ , were also extracted and plotted as a function of crack velocity. The plot shows a rapid increase in  $G^d$  values from ~9 to ~25 N/m when the crack reached ~1400 m/s. The results obtained from *t2*-DGS and *tr*-DGS matched with each other indicating good consistency of these two optical methods. The good agreement

between the results obtained from experiments and FEA further supported the validity of these two optical methods.

## 9.1 Future work

In this research, *r*-DGS was advanced to study mechanical behaviors of CFRP under dynamic out-of-plane impact. Therefore, the optical technique could be used to evaluate compression after impact (CAI) of CFRP. The two orthogonal slopes can be integrated using HFLI to reconstruct the surface topography of damaged CFRP.

*r*-DGS method can also be modified by projecting a speckle image onto the specimen surface. The speckles on the target plate can be photographed and stored in a computer, so that the speckle image can be projected onto specimens as large as  $\sim 1 \text{ m}^2$  or larger. *t*-DGS being an optical method to study transparent material, there is potential for a tomographic approach which needs to be explored.

*tr*-DGS, as the most sensitive of all the DGS methods, has been applied to study dynamic fracture mechanics of transparent ceramics. It could be modified to study opaque ceramics. To accomplish this, a transparent thin acrylic sheet with a reflective surface (coating) can be adhered to the opaque ceramics. The strain on the opaque ceramics, transferred to the adhered coating could be used to infer mechanical fields in the opaque substrate.

## Reference

- [1] D. Malacara-Doblado and I. Ghozeil, "Hartmann, Hartmann–Shack, and Other Screen Tests," in *Optical Shop Testing*, Wiley, 2007.
- [2] M. Strojnik, G. Paez and M. Mantravadi, "Lateral shear interferometers," in *Optical Shop Testing*, Wiley, 2007.
- [3] R. Ragazzoni, "Pupil plane wavefront sensing with an oscillating prism," *J. Mod. Opt.*, vol. 43, pp. 289-293, 1996.
- [4] S. Ettl, J. Kaminski, M. Knauer and G. Häusler, "Shape reconstruction from gradient data," *Appl Opt*, vol. 47, pp. 2091-2097, 2008.
- [5] J.-M. Thomassin, C. Jerome, T. Pardoen, C. Bailly, I. Huynen and C. Detrembleur, "Polymer/carbon based composites as electromagnetic interference (EMI) Shielding materials," *Materials Science and Engineering R*, vol. 74, pp. 211-232, 2013.
- [6] C. Soutis, "Fibre reinforced composites in aircraft construction," *Progress in Aerospace Sciences*, vol. 41, pp. 143-151, 2005.
- [7] G. Williams, R. Trask and I. Bond, "A self-healing carbon fibre reinforced polymer for aerospace applications," *Composites: Part A*, vol. 38, pp. 1525-1532, 2007.
- [8] S. H. Lee and A. M. Waas, "Compressive response and failure of fiber reinforced unidirectional composites," *International Journal of Fracture*, vol. 100, pp. 275-306, 1999.
- [9] S. Sanchez-Saez, E. Barbero, R. Zaera and C. Navarro, "Compression after impact of thin composite laminates," *Composite Science and Technology*, vol. 65, pp. 1911-1919, 2005.
- [10] L. Walker, M.-S. Sohn and H. Xiao-Zhi, "Improving impact resistance of carbon-fibre composites through interlaminar reinforcement," *Composites: Part A*, vol. 33, pp. 893-902, 2002.
- [11] F. K. Ligtenberg, "The Moire Method: A New Experimental Method for the Determination of Moments in Small Slab Models," *Proceedings of the Society for Experimental Stress Analysis*, vol. 12, pp. 83-98, 1954.
- [12] G. Rieder and R. Ritter, "Krümmungsmessung an belasteten Platten nach dem Ligtenbergschen Moiré-Verfahren," *Forschung im Ingenieurwesen A*, Vols. 33-44, p. 31, 1965.
- [13] F. P. Chiang and G. Jaisingh, "Dynamic moiré methods for the bending of plates," *Experimental Mechanics*, vol. 13, pp. 168-171, 1973.
- [14] A. Asundi, "Novel techniques in reflection moiré," *Experimental Mechanics*, vol. 34, pp. 230-242, 1994.

- [15] H. Ding, R. E. Powell, C. R. Hanna and I. C. Ume, "Warpage measurement comparison using shadow moiré and projection moiré methods," *IEEE Transactions on Components and Packaging Technologies*, vol. 25, pp. 714-721, 2002.
- [16] J. N. Butters and J. A. Leendertz, "Holographic and Video Techniques Applied to Engineering Measurement," *Measurement and Control*, vol. 4, pp. 349-354, 1971.
- [17] A. Macovski, S. D. Ramsey and L. F. Schaefer, "Time-Lapse Interferometry and Contouring Using Television Systems," *Applied Optics*, vol. 10, pp. 2722-2727, 1971.
- [18] M. C. Shellabear and J. R. Tyrer, "Application of ESPI to Three-Dimensional Vibration Measurements," *Optics and Lasers in Engineering*, vol. 15, pp. 43-56, 1991.
- [19] N. K. Mohan, H. Saldner and N. -E. Molin, "Electronic speckle pattern interferometry for simultaneous measurement of out-of-plane displacement and slope," *Optics Letters*, vol. 18, pp. 1861-1863, 1993.
- [20] P. K. Rastogi, "Measurement of curvature and twist of a deformed object by electronic speckle-shearing pattern interferometry," *Optics Letters*, vol. 21, pp. 905-907, 1996.
- [21] D. Findeis and J. Gryzagoridis, "A Comparison of the Capabilities of Portable Shearography and Portable Electronic Speckle Pattern Interferometry," in *Proceedings of SPIE*, San Diego, 2004.
- [22] D. Francis, R. P. Tatam and R. M. Groves, "Shearography technology and applications: a review," *Measurement Science and Technology*, vol. 21, p. 102001, 2010.
- [23] H. M. Shang, Y. Y. Hung, W. D. Luo and F. Chen, "Surface profiling using shearography," *Optical Engineering*, vol. 39, pp. 23-31, 2000.
- [24] Y. Y. Hung, J. L. Turner, M. Tafraian, J. D. Hovanesian and C. E. Taylor, "Optical method for measuring contour slopes of an object," *Applied Optics*, vol. 17, 1978.
- [25] Y. Y. Hung and C. Y. Liang, "Image-shearing camera for direct measurement of surface strains," *Applied Optics*, vol. 18, 1979.
- [26] Y. Y. Hung and A. J. Durelli, "Simultaneous measurement of three displacement derivatives using a multiple image-shearing interferometric camera," *Journal of strain analysis*, vol. 14, 1979.
- [27] P. Rastogi, "Determination of surface strains by speckle shear photography," *Optics and Lasers in Engineering*, vol. 29, pp. 103-116, 1998.
- [28] Y. Y. Hung, "Applications of digital shearography for testing of composite structures," *Composites: Part B*, vol. 30, p. 765-773, 1999.
- [29] Y. Y. Hung and J. Wang, "Dual-beam phase shift shearography for measurement of in-plane strains," *Optics and Lasers in Engineering*, vol. 24, pp. 403-413, 1996.
- [30] Y. Hung, H. Shang, Y. Lin, L. Zhang and X. Wen, "Evaluation of residual stresses in plastics and composites by shearography," in *SAE International Congress and Exposition*, Detroit, 1999.

- [31] Y. Y. Hung and W. Luo, "Shearography for rapid nondestructive evaluation of bonded composite structure," in *SAE International Congress and Exposition*, Detroit, 1999.
- [32] H. V. Tippur, S. Krishnaswamy and A. J. Rosakis, "A Coherent Gradient Sensor for Crack Tip Deformation Measurements: Analysis and Experimental Results," *International Journal of Fracture*, vol. 48, pp. 193-204, 1991.
- [33] H. V. Tippur, S. Krishnaswamy and A. J. Rosakis, "Optical mapping of crack tip deformations using the methods of transmission and reflection coherent gradient sensing: a study of crack tip K-dominance," *International Journal of Fracture*, vol. 52, pp. 91-117, 1991.
- [34] H. V. Tippur and A. J. Rosakis, "Quasi-Static and Dynamic Crack Growth along Bimaterial Interfaces: A Note on Crack Tip Field Measurements Using Coherent Gradient Sensing," *Experimental Mechanics*, vol. 31, pp. 243-251, 1991.
- [35] J. Kimberley and J. Lambros, "Dynamic Crack Kinking from a PMMA/Homalite Interface," *Experimental Mechanics*, vol. 44, p. 158-166, 2004.
- [36] S. Krishnaswamy, H. V. Tippur and Rosakis, "Measurement of Transient Crack Tip Deformation Fields Using the Method of Coherent Gradient Sensing," *Journal of the Mechanics and Physics of Solids*, vol. 40, p. 339-372, 1992.
- [37] C. E. Rousseau and H. V. Tippur, "Evaluation of crack tip fields and stress intensity factors in functionally graded elastic materials: Cracks parallel to elastic gradient," *International Journal of Fracture*, vol. 114, pp. 87-111, 2002.
- [38] M. S. Kirugulige and H. V. Tippur, "Mixed-Mode Dynamic Crack Growth in Functionally Graded Glass-Filled Epoxy," *Experimental Mechanics*, vol. 46, pp. 269-281, 2006.
- [39] M. Kirugulige and H. V. Tippur, "Mixed-Mode Dynamic Crack Growth in a Functionally Graded Particulate Composite: Experimental Measurements and Finite Element Simulations," *Journal of Applied Mechanics*, vol. 75, pp. 1-14, 2008.
- [40] R. Kitey and H. V. Tippur, "Dynamic Crack Growth Past a Stiff Inclusion: Optical Investigation of Inclusion Eccentricity and Inclusion-matrix Adhesion Strength," *Experimental Mechanics*, vol. 48, pp. 37-54, 2008.
- [41] G. G. Stoney, "The tension of metallic films deposited by electrolysis," *Proceedings of the Royal Society of London. Series A, Containing Papers of a Mathematical and Physical Character*, vol. 82, pp. 172-175, 1909.
- [42] A. J. Rosakis, R. P. Singh, Y. Tsuji, E. Kolawa and N. R. Moore Jr, "Full field measurements of curvature using coherent gradient sensing: application to thin film characterization," *Thin Solid Films*, vol. 325, pp. 42-54, 1998.
- [43] H. Lee, A. J. Rosakis and L. B. Freund, "Full-field optical measurement of curvatures in ultra-thin-film-substrate systems in the range of geometrically nonlinear deformations," *Journal of Applied Physics*, vol. 89, p. 6116-6129, 2001.
- [44] T. S. Park, S. Suresh, A. J. Rosakis and J. Ryu, "Measurement of full-field curvature and geometrical instability of thin film-substrate systems through CGS interferometry," *Journal of the Mechanics and Physics of Solids*, vol. 51, pp. 2191-2211, 2003.

- [45] M. A. Brown, T.-S. Park, A. Rosakis, E. Ustundag, Y. Huang, N. Tamura and B. Valek, "A Comparison of X-Ray Microdiffraction and Coherent Gradient Sensing in Measuring Discontinuous Curvatures in Thin Film: Substrate Systems," *Journal of Applied Mechanics*, vol. 73, pp. 723-729, 2006.
- [46] X. Dong, X. Feng, K.-C. Hwang, S. Ma and Q. Ma, "Full-field measurement of nonuniform stresses of thin films at high temperature," *Optics Express*, vol. 19, p. 13201–13208, 2011.
- [47] X. Dong, C. Zhang, X. Feng and K. -C. Hwang, "Full-field Measurement of Topography and Curvature by Coherent Gradient Sensing Method at High Temperature," *Experimental Mechanics*, vol. 53, p. 959–963, 2013.
- [48] C. Liu, X. Zhang, J. Zhou, Y. Zhou and X. Feng, "The coherent gradient sensor for film curvature measurements at cryogenic temperature," *Optics Express*, vol. 21, pp. 26352-26362, 2013.
- [49] D. Mishra, S. L. Wong, J. P. Longtin, R. P. Singh and V. Prasad, "Development of a coherent gradient-sensing tomographic interferometer for three-dimensional refractive index-based measurements," *Optics Communications*, vol. 212, pp. 17-27, 2002.
- [50] M. Budyansky, C. Madormo, J. L. Maciaszek and G. Lykotrafitis, "Coherent gradient sensing microscopy (micro-CGS): A microscale curvature detection technique," *Optics and Lasers in Engineering*, vol. 49, pp. 874-879, 2011.
- [51] K. Ma and H. Xie, "A Novel Phase Shifting Technique of Coherent Gradient Sensing Method for Measuring Crack-tip K-Dominance," *Experimental Mechanics*, vol. 57, p. 1239–1248, 2017.
- [52] K. Ma and H. Xie, "Spatially-Phase-Shifted Coherent Gradient Sensor for Full-Field Measurement of Surface Slope and Curvature," *Experimental Mechanics*, vol. 56, p. 1073–1082, 2016.
- [53] C. Periasamy and H. V. Tippur, "Full-field digital gradient sensing method for evaluating stress gradients in transparent solids.," *Applied Optics*, vol. 51, no. 12, pp. 2088-2097, 2012.
- [54] C. Periasamy and H. V. Tippur, "A full-field reflection-mode digital gradient sensing method for measuring orthogonal slopes and curvatures of thin structures.," *Measurement Science and Technology*, vol. 24, p. 025202, 2013.
- [55] T. C. Chu, W. F. Ranson, M. A. Sutton and W. H. Peters, "Application of digital-image-correlation techniques to experimental mechanics," *Experimental Mechanics*, vol. 25, no. 3, pp. 232-244, 1985.
- [56] D. J. Chen, F. P. Chiang, Y. S. Tan, H. Don and S., "Digital speckle-displacement measurement using a complex spectrum method," *Appl Opt* , vol. 32, no. 11, pp. 1839-1849, 1993.
- [57] M. A. Sutton and J. J. Ortu, Image correlation for shape, motion and deformation measurements, New York, NY, USA: Springer, 2009.
- [58] B. Pan, K. Qian, H. Xie and A. Asundi, "Two-dimensional digital image correlation for in-plane displacement and strain measurement: a review," *Measurement Science and Technology*, vol. 20, p. 062001, 2009.

- [59] A. Giachetti, "Matching techniques to compute image motion," *Image and Vision Computing*, vol. 18, pp. 247-260, 2000.
- [60] W. Tong, "An evaluation of digital image correlation criteria for strain mapping applications," *Strain*, vol. 41, pp. 167-175, 2005.
- [61] B. Pan, H. M. Xie, Z. Q. Guo and T. Hua, "Full-field strain measurement using a two-dimensional Savitzky–Golay digital differentiator in digital image correlation," *Optical Engineering*, vol. 46, p. 033601, 2007.
- [62] C. Periasamy and H. V. Tippur, "Measurement of Orthogonal Stress Gradients Due to Impact Load on a Transparent Sheet using Digital Gradient Sensing Method," *Experimental Mechanics*, vol. 53, pp. 97-111, 2013.
- [63] C. Periasamy and H. V. Tippur, "Nondestructive evaluation of transparent sheets using a full-field digital gradient sensor," *NDT&E International*, vol. 54, pp. 103-106, 2013.
- [64] W. Hao, C. Tang, Y. Yuan, X. Yao and Y. Ma, "Experimental study on the fiber pull-out of composites using digital gradient sensing technique," *Polymer Testing*, vol. 41, pp. 239-244, 2015.
- [65] C. Zhang, Z. Qu, X. Fang, X. Feng and K.-C. Hwang, "Full-field measurement of surface topographies and thin film stresses at elevated temperatures by digital gradient sensing method," *Applied Optics*, vol. 54, pp. 721-727, 2015.
- [66] A. S. Jain and H. V. Tippur, "Mapping Static and Dynamic Crack-Tip Deformations Using Reflection-Mode Digital Gradient Sensing: Applications to Mode-I and Mixed-Mode Fracture," *Journal of Dynamic Behavior of Materials*, vol. 1, p. 315–329, 2015.
- [67] A. S. Jain and H. V. Tippur, "Extension of reflection-mode digital gradient sensing method for visualizing and quantifying transient deformations and damage in solids," *Optics and Lasers in Engineering*, vol. 77, pp. 162-174, 2016.
- [68] R. K. A. Pasumarthy and H. V. Tippur, "Mechanical and optical characterization of a tissue surrogate polymer gel," *Polymer Testing*, vol. 55, pp. 219-229, 2016.
- [69] X. Dai, H. Yun, X. Shao, Y. Wang, D. Zhang, F. Yang and X. He, "Thermal residual stress evaluation based on phase-shift lateral shearing interferometry," *Optics and Lasers in Engineering*, vol. 105, pp. 182-187, 2018.
- [70] N. E. Coleman and R. Jain, "Obtaining 3-dimensional shape of textured and specular surfaces using four-source photometry," *Comput Vision Graph*, vol. 18, pp. 309-328, 1982.
- [71] G. Healey and R. Jain, "Depth recovery from surface normals," *Int Conf Pattern Recognition*, vol. 2, pp. 894-896, 1984.
- [72] Z. Wu and L. Li, "A line-integration based method for depth recovery from surface normals," *Comput Vision Graph*, vol. 43, pp. 53-66, 1988.
- [73] R. T. Frankot and R. Chellappa, "A method for enforcing integrability in shape from shading algorithms," *IEEE Trans. Pattern Anal. Mach. Intell*, vol. 10, pp. 439-451, 1988.
- [74] R. H. Hudgin, "Wave-front reconstruction for compensated imaging," *J Opt Soc Am*, vol. 67, pp. 375-378, 1977.

- [75] L. Huang and A. Asundi, "Improvement of least-squares integration method with iterative compensations in fringe reflectometry," *Appl Opt*, vol. 51, pp. 7459-7465, 2012.
- [76] W. H. Southwell, "Wave-front estimation from wave-front slope measurements," *Journal of the Optical Society of America*, vol. 70, pp. 998-1006, 1980.
- [77] G. Li, Y. Li, K. Liu, X. Ma and H. Wang, "Improving wave front reconstruction accuracy by using integration equations with higher-order truncation errors in the Southwell geometry," *Journal of the Optical Society of America A*, vol. 2013, pp. 1448-1459, 2013.
- [78] R. Klette and K. Schlüns, "Height data from gradient fields," in *SPIE 2908, Machine Vision Applications, Architectures, and Systems Integration V*, Boston, Massachusetts, 1996.
- [79] L. Huang, M. Idir, C. Zuo, K. Kaznatcheev, L. Zhou and A. Asundi, "Comparison of two-dimensional integration methods for shape reconstruction from gradient data," *Optics and Lasers in Engineering*, vol. 64, pp. 1-11, 2015.
- [80] L. Ye, Y. Lu, Z. Su and G. Meng, "Functionalized composite structures for new generation airframes: a review," *Composites Science and Technology*, vol. 65, pp. 1436-1446, 2005.
- [81] R. F. Gibson, "A review of recent research on mechanics of multifunctional composite materials and structures," *Composite Structures*, vol. 92, p. 2793–2810, 2010.
- [82] M. Grediac, "The use of full-field measurement methods in composite material characterization: interest and limitations," *Composites: Part A*, vol. 35, pp. 751-761, 2004.
- [83] J. P. Quinn, A. T. McIlhagger and R. McIlhagger, "Examination of the failure of 3D woven composites," *Composites: Part A*, vol. 39, pp. 273-283, 2008.
- [84] F. Bosia, J. Botsis, M. Facchini and G. Philippe, "Deformation characteristics of composite laminates—part I: speckle interferometry and embedded Bragg grating sensor measurements," *Composites Science and Technology*, vol. 62, pp. 41-54, 2002.
- [85] H. V. Tippur, "Simultaneous and real-time measurement of slope and curvature fringes in thin structures using shearing interferometry," *Opt Eng*, vol. 43, pp. 3014-3020, 2004.
- [86] R. Ritter, "Reflection moire methods for plate bending studies," *Opt Eng*, vol. 21, pp. 663-671, 1982.
- [87] D. S. Cairns, P. J. Minguet and M. G. Abdallah, "Theoretical and experimental response of composite laminates with delaminations loaded in compression," *Composite Structures*, vol. 24, pp. 431-437, 1994.
- [88] K. Karthikeyan, B. P. Russell, N. A. Fleck, H. N. G. Wadley and V. S. Deshpande, "The effect of shear strength on the ballistic response of laminated composite plates," *European Journal of Mechanics A/Solids*, vol. 42, pp. 35-53, 2013.
- [89] H. Koerber, J. Xavier and P. P. Camanho, "High strain rate characterisation of unidirectional carbon-epoxy IM7-8552 in transverse compression and in-plane

- shear using digital image correlation," *Mechanics of Materials* , vol. 42, pp. 1004-1019, 2010.
- [90] M. Yamada, Y. Tanabe, A. Yoshimura and T. Ogasawara, "Three-dimensional measurement of CFRP deformation during high-speed impact loading," *Nuclear Instruments and Methods in Physics Research A*, vol. 646, pp. 219-226, 2011.
- [91] M. Pankow, B. Justusson and A. M. Waas, "Three-dimensional digital image correlation technique using single high-speed camera for measuring large out-of-plane displacements at high framing rates," *Applied Optics* , vol. 49, pp. 3418-27, 2010.
- [92] L. Yu and B. Pan, "Single-camera stereo-digital image correlation with a four-mirror adapter: optimized design and validation," *Optics and Lasers in Engineering*, vol. 87, pp. 120-128, 2016.
- [93] B. Pan, L. Yu, Y. Yang, W. Song and L. Guo, "Full-field transient 3D deformation measurement of 3D braided composite panels during ballistic impact using single-camera high-speed stereo-digital image correlation," *Composite Structures* , vol. 157, pp. 25-32, 2016.
- [94] G. Tang, Y. Yan, X. Chen, J. Zhang, B. Xu and Z. Feng, "Dynamic damage and fracture mechanism of three-dimensional braided carbon fiber/epoxy resin composites," *Materials and Design*, vol. 22, pp. 21-25, 2001.
- [95] Q. Liu and M. Hughes, "The fracture behaviour and toughness of woven flax fibre reinforced epoxy composites," *Composites: Part A*, vol. 39, p. 1644–1652, 2008.
- [96] M. Arai, Y. Noro, K.-i. Sugimoto and M. Endo, "Mode I and mode II interlaminar fracture toughness of CFRP laminates toughened by carbon nanofiber interlayer," *Composites Science and Technology*, vol. 68, pp. 516-525, 2008.
- [97] M. May, "Measuring the rate-dependent mode I fracture toughness of composites - A review," *Composites: part A*, vol. 81, pp. 1-12, 2016.
- [98] G. W. Beckermann and K. L. Pickering, "Mode I and Mode II interlaminar fracture toughness of composite laminates interleaved with electrospun nanofibre veils," *Composites: Part A*, vol. 72, pp. 11-21, 2015.
- [99] A. T. Seyhan, M. Tanoglu and K. Schulte, "Mode I and mode II fracture toughness of E-glass non-crimp fabric/carbon nanotube (CNT) modified polymer based composites," *Engineering Fracture Mechanics*, vol. 75, pp. 5151-5162, 2008.
- [100] A. Shukla, B. Agarwal and B. Bhushan, "Determination of stress intensity factor in orthotropic composite materials using strain gages," *Engineering Fracture Mechanics* , vol. 32, pp. 469-477, 1989.
- [101] S. Khanna and A. Shukla, "On the use of strain gages in dynamic fracture mechanics," *Engineering Fracture Mechanics*, vol. 51, pp. 933-948, 1995.
- [102] J. L. F. Freire, R. A. Antonelli, Y. Dror and A. S. Voloshin, "Application of Reflection Orthotropic Photoelasticity to Laminated Composites," *Journal of Composite Materials* , vol. 23, pp. 42-57, 1989.
- [103] A. Shukla and S. K. Khanna, "Effect of Fiber Reinforcement on Dynamic Crack Growth in Brittle Matrix Composites," *Journal of Engineering Materials and Technology*, vol. 115, pp. 140-145, 1993.

- [104] C. Liu, A. J. Rosakis and M. G. Stout, "Dynamic Fracture Toughness of a Unidirectional Graphite/Epoxy Composite," in *Proceedings of the Symposium on "Dynamic Effects in Composite Structures"*, IMECE 2001, New York, 2001.
- [105] C. Liu, A. J. Rosakis, R. W. Ellis and M. G. Stout, "A Study of the Fracture Behavior of Unidirectional Fiber- Reinforced Composite Using Coherent Gradient Sensing (CGS) Interferometry," *International Journal of Fracture*, vol. 90, pp. 355-382, 1998.
- [106] H. Hatta, M. S. Aly-Hassan, Y. Hatsukade, S. Wakayama, H. Suemasu and N. Kasai, "Damage detection of C/C composites using ESPI and SQUID techniques," *Composites Science and Technology*, vol. 65, pp. 1098-1106, 2005.
- [107] W. Mekky and P. S. Nicholson, "The fracture toughness of Ni/Al<sub>2</sub>O<sub>3</sub> laminates by digital image correlation I: Experimental crack opening displacement and R-curves," *Engineering Fracture Mechanics*, vol. 73, pp. 571-582, 2006.
- [108] M. S. Kirugulige and H. V. Tippur, "Measurement of Fracture Parameters for a Mixed-Mode Crack Driven by Stress Waves using Image Correlation Technique and High-Speed Digital Photography," *Strain*, vol. 45, pp. 108-122, 2009.
- [109] M. S. Kirugulige, H. V. Tippur and T. S. Denney, "Measurement of transient deformations using digital image correlation method and high-speed photography: application to dynamic fracture," *Applied Optics*, vol. 46, no. 22, pp. 5083-5096, 2007.
- [110] D. Lee, H. Tippur and P. Bogert, "Quasi-static and dynamic fracture of graphite/epoxy composites: An optical study of loading-rate effects," *Composites: Part B*, vol. 41, pp. 462-474, 2010.
- [111] D. Lee, H. Tippur and M. Kirugulige, "Experimental Study of Dynamic Crack Growth in Unidirectional Graphite/Epoxy Composites using Digital Image Correlation Method and High-speed Photography," *Journal of Composite Materials*, vol. 43, pp. 2081-2108, 2009.
- [112] R. W. Bedsole, P. B. Bogert and H. V. Tippur, "An experimental investigation of interlaminar and intralaminar dynamic fracture of CFRPs: Effect of matrix modification using carbon nanotubes," *Composite Structures*, vol. 132, pp. 1043-1055, 2015.
- [113] S. Mallon, B. Koohbor, A. Kidane and M. A. Sutton, "Fracture Behavior of Prestressed Composites Subjected to Shock Loading: A DIC-Based Study," *Experimental Mechanics*, vol. 55, p. 211-225, 2015.
- [114] J. Hoffmann, H. Cui and N. Petrinic, "Determination of the strain-energy release rate of a composite laminate under high-rate tensile deformation in fibre direction," *Composites Science and Technology*, vol. 164, pp. 110-119, 2018.
- [115] H. V. Tippur, "Optical Techniques in Dynamic Fracture Mechanics," in *Dynamic Fracture Mechanics*, World Scientific Publications, 2006.
- [116] D. JW and R. WF, Experimental stress analysis. 4th ed., College House Enterprises, 2005.

- [117] C. Miao, B. M. Sundaram, L. Huang and H. V. Tippur, "Surface profile and stress field evaluation using digital gradient sensing method," *Measurement Science and Technology*, vol. 27, p. 095203, 2016.
- [118] D. Malacara, *Optical shop testing*, John Wiley and Sons, 1992.
- [119] E. Ventsel and T. Krauthammer, *Thin Plates and Shells: Theory, Analysis, and Applications*, CRC Press, 2001.
- [120] B. M. Sundaram and H. V. Tippur, "Dynamic Crack Growth Normal to an Interface in Bi-Layered Materials: An Experimental Study Using Digital Gradient Sensing Technique," *Experimental Mechanics*, vol. 56, pp. 37-57, 2015.
- [121] P. C. Paris and G. C. Sih, *Stress Analysis of Cracks, Fracture Toughness Testing and its Applications*, Philadelphia: American Society for Testing and Materials STP 381, 1964.
- [122] O. A. Bauchau and J. I. Craig, "Kirchhoff plate theory," in *Structural Analysis. Solid Mechanics and Its Applications*, Dordrecht, Springer, 2009, pp. 819-914.
- [123] R. Bedsole and H. V. Tippur, "Dynamic Fracture Characterization of Small Specimens: A Study of Loading Rate Effects on Acrylic and Acrylic Bone Cement," *Journal of Engineering Materials and Technology*, vol. 135, pp. 031001-10, 2013.
- [124] T. Tran, D. Simkins, S. H. Lim, D. Kelly, G. Pearce, B. G. Prusty, J. Gosse and S. Christensen, "Application of a Scalar Strain-Based Damage Onset Theory to the Failure of a Complex Composite Specimen," in *28th Congress of the International Council of the Aeronautical Sciences*, Brisbane, Australia, 2012.
- [125] J. H. Mathews and K. K. Fink, *Numerical Methods Using Matlab*, 4th Edition, New Jersey: Prentice-Hall Inc, 2004.
- [126] K. C. Jajam and H. V. Tippur, "Quasi-static and dynamic fracture behavior of particulate polymer composites: A study of nano- vs. micro-size filler and loading-rate effects," *Composites: Part B*, vol. 43, pp. 3467-3481, 2012.
- [127] C. Periasamy and H. V. Tippur, "Measurement of orthogonal stress gradients due to impact load on a transparent sheet using digital gradient sensing method.," *Experimental Mechanics*, vol. 53, pp. 97-111, 2013.
- [128] L. Xu, H. Tippur and C.-E. Rousseau, "Measurement of contact stresses using real-time shearing interferometry," *Optical Engineering*, vol. 38, pp. 1932-7, 1999.
- [129] M. L. Williams and P. Calif, "On the stress distribution at the base of a stationary crack," *Journal of applied mechanics*, vol. 24, p. 109-114, 1959.
- [130] M. Janssen, J. Zuidema and R. Wanhill, *Fracture mechanics*. 2nd ed., VSSD, 2006.
- [131] J. A. S and H. V. Tippur, "Mapping Static and Dynamic Crack-Tip Deformations Using Reflection-Mode Digital Gradient Sensing: Applications to Mode-I and Mixed-Mode Fracture," *Journal of Dynamic Behavior of Materials*, vol. 1, pp. 315-329, 2015.
- [132] C. Miao and H. V. Tippur, "Fracture behavior of carbon fiber reinforced polymer composites: An optical study of loading rate effects," *Engineering Fracture Mechanics*, vol. 207, pp. 203-221, 2019.

- [133] C. Periasamy and H. V. Tippur, "Measurement of crack-tip and punch-tip transient deformations and stress intensity factors using Digital Gradient Sensing technique," *Engineering Fracture Mechanics*, vol. 98, pp. 185-199, 2013.
- [134] K. Ravi-Chandar, *Dynamic fracture*, San Diego: Elsevier, 2004.
- [135] C. Miao and H. V. Tippur, "Reflection-mode digital gradient sensing method: measurement accuracy," *Optical Engineering*, vol. 58, pp. 044101-14, 2019.
- [136] H. V. Tippur, "Simultaneous and real-time measurement of slope and curvature fringes in thin structures using shearing interferometry," *Optical Engineering*, vol. 43, pp. 3014-3020, 2004.
- [137] A. S. Jain and H. V. Tippur, "Mapping Static and Dynamic Crack-Tip Deformations Using Reflection-Mode Digital Gradient Sensing: Applications to Mode-I and Mixed-Mode Fracture," *Journal of Dynamic Behavior of Materials*, vol. 1, pp. 315-329, 2015.
- [138] C. Miao and H. V. Tippur, "Higher sensitivity Digital Gradient Sensing configurations for quantitative visualization of stress gradients in transparent solids," *Optics and Lasers in Engineering*, vol. 108, pp. 54-67, 2018.
- [139] C. Miao and H. V. Tippur, "Measurement of Sub-micron Deformations and Stresses at Microsecond Intervals in Laterally Impacted Composite Plates Using Digital Gradient Sensing," *Journal of Dynamic Behavior of Materials*, vol. 4, no. 3, pp. 336-358, 2018.

## Appendix A

### A.1 Disadvantages of current experimental setup of *r*-DGS

The experimental setup and working principle of *r*-DGS are shown in Figure 2.1, Figure 2.2, respectively. The reflective specimen is positioned vertically relative to the target plate containing speckles. A 50/50 beam splitter is utilized here to image on the random speckles on the target plate via the reflective surface of the specimen. As a result, a large amount of light is lost due to the beam splitter, as shown in Figure A1. When a light ray originated from the target plate reaches the beam splitter, half of the light ray passes through the beam splitter, and the other half is reflected towards to the specimen. Then, the light ray is reflected back towards to the beam splitter. Again, only one half of that passes through the beam splitter to be captured by the camera. Thus, under ideal conditions only 25% of the light is captured by the camera. In reality, however, the light ray captured by camera would be much lower. Such a huge loss of light may not be a problem for recording low-speed events. However, it introduces difficulties to ultrahigh-speed photography reaching  $10^6$  frames per second or higher. Also, the beam splitter adds to the complexity of the *r*-DGS experimental setup. Considering the core principle of *r*-DGS that the camera needs to be focused on the target plate via the reflective specimen surface to record speckles, and the beam splitter is an auxiliary optical element in the traditional setup, and hence, it is possible to design a simpler variant of *r*-DGS method without using beam

splitter. Furthermore, the measurement precision increases when the number of optical elements is minimized in an optical setup, thus avoiding any additional optical aberrations.

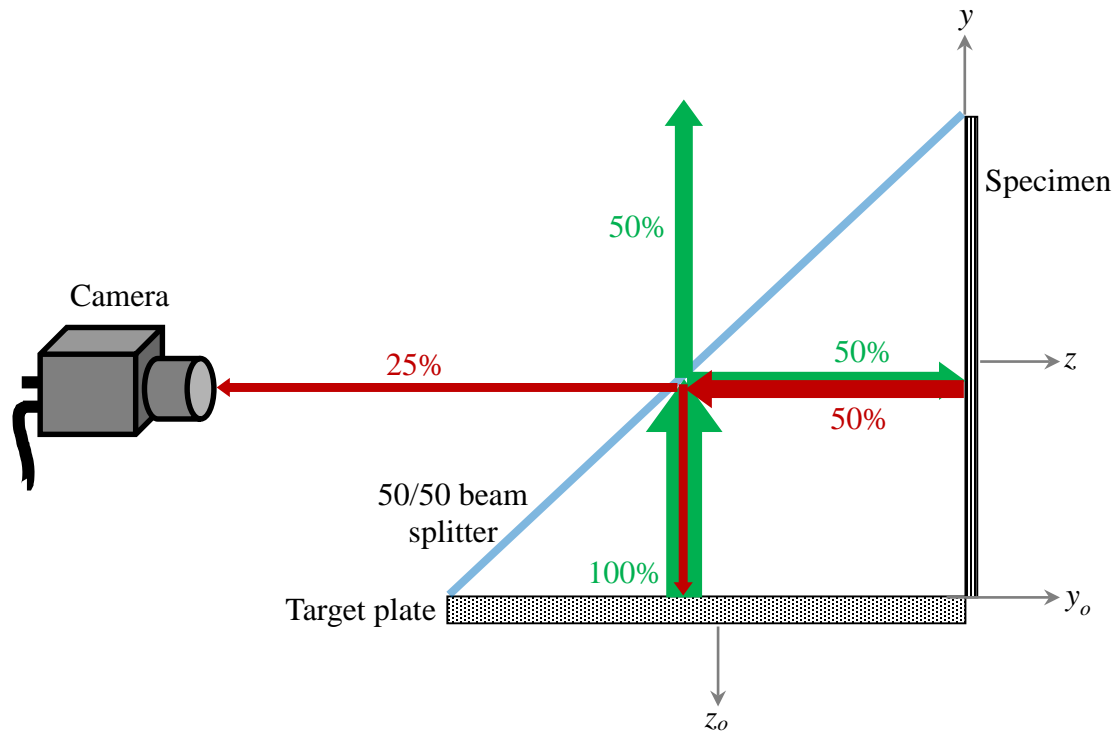


Figure A1: Light ray diagram of traditional *r*-DGS depicting loss of light in the apparatus due to the beam splitter.

## A.2 Simplified *r*-DGS setup without beam splitter

The sideview of the experimental setup for *r*-DGS without the beam splitter is shown in Figure A2. Let  $(y, z)$  and  $(y_o, z_o)$  be the in-plane coordinates of the specimen and target planes, respectively. The schematic here is similar to the setup for traditional *r*-DGS, except the specimen is rotated about the  $x$ -axis relative to the target plate at  $\alpha = 45^\circ$ . The light rays, originating from the target plate, get reflected by the specimen surface towards the camera. Hence, the speckles on the target plate are recorded by the camera directly via the reflective specimen surface. Unlike the traditional *r*-DGS, in this simplified *r*-DGS

method, the gap between the specimen plane and the target, also defined as  $\Delta$ , is continuously changing from  $\Delta_M$  to  $\Delta_N$ , as shown in Figure A2. The appropriate local measurement of  $\Delta$  will be explained in the experimental section. As in regular  $r$ -DGS, the distance from the center of specimen to the camera is defined as  $L$ .

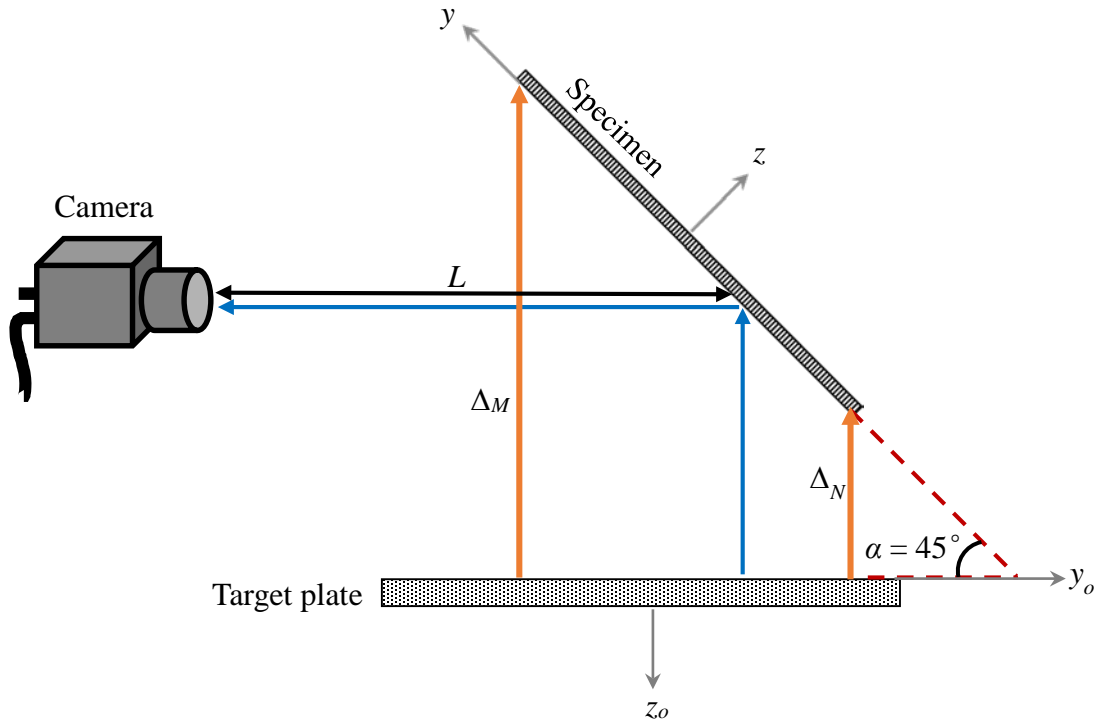


Figure A2: Schematic of experimental setup for simplified  $r$ -DGS without beam splitter.

The angular deflections of light rays are shown in Figure A3. When the specimen is in the undeformed state, the gray scale at a generic point  $P$  on the target plate is photographed by a camera pixel through point  $O$  on the specimen plane. Thus recorded image at that time instant and/or load level is the reference image. After the specimen suffers deformation, say, due to the applied load (the load needs not be along the  $z$ -direction), the gray scale at a neighboring point of  $P$ , namely  $Q$  on the target plate is photographed by the same pixel through the same point  $O$  on the specimen surface. The corresponding image of the specimen in the deformed state is recorded next. The local

orthogonal speckle displacements  $\delta_{y_0;x_0}$  can be obtained by performing a 2D image correlation of the reference and deformed images. The corresponding angles  $\phi_{y';x'}$  represent two orthogonal angular deflections of light rays. It should be noted that, the out-of-plane deformation ( $w$ ) is along the  $z$ -axis of the specimen coordinates ( $y, z$ ), however, the images recorded by the camera are in the plane with coordinates of ( $y', z'$ ). The details of these two coordinate systems are shown in the inset of Figure A3. It can be observed that

$$\frac{w'}{w} = \frac{y'}{y} = \cos \alpha (= 45^\circ) = \frac{1}{\sqrt{2}}; \quad x' = x \quad (\text{A1})$$

Hence,  $\phi_{y';x'}$  is related to  $\frac{\partial w'}{\partial y';x'}$ :

$$\frac{\partial w'}{\partial y';x'} = \frac{1}{2} \tan(\phi_{y';x'}) \approx \frac{1}{2} (\phi_{y';x'}) \approx \frac{1}{2} \left( \frac{\delta_{y_0;x_0}}{\Delta_p} \right) \quad (\text{A2})$$

where  $\Delta_p$  is the gap between the specimen and target planes at point  $P$ . The Eq. (A2) is

similar to the governing equation for traditional  $r$ -DGS. Next,  $\frac{\partial w'}{\partial y';x'}$  needs to be

transformed to obtain the specimen surface slopes,  $\frac{\partial w}{\partial y;x}$ , using the two equations above:

$$\frac{\partial w}{\partial y} = \frac{\partial(\sqrt{2}w')}{\partial(\sqrt{2}y')} = \frac{\partial w'}{\partial y'} \approx \frac{1}{2} \left( \frac{\delta_{y_0}}{\Delta_p} \right); \quad (\text{A3})$$

$$\frac{\partial w}{\partial x} = \frac{\partial \sqrt{2}w'}{\partial x'} = \sqrt{2} \frac{\partial w'}{\partial x'} \approx \frac{\sqrt{2}}{2} \left( \frac{\delta_{x_0}}{\Delta_p} \right) = \frac{1}{\sqrt{2}} \left( \frac{\delta_{x_0}}{\Delta_p} \right)$$

It should be noted that the experimental setup shown here rotates about the  $x$ -axis, which means  $x = x'$ ;  $y = \sqrt{2}y'$ , but  $\frac{\partial w}{\partial y} = \frac{\partial w'}{\partial y'}$ ;  $\frac{\partial w}{\partial x} = \sqrt{2} \frac{\partial w'}{\partial x'}$ . Also, it can be concluded that when the experimental setup is rotated about the  $y$ -axis instead, the governing equations will be  $x = \sqrt{2}x'$ ;  $y = y'$ , and  $\frac{\partial w}{\partial y} = \sqrt{2} \frac{\partial w'}{\partial y'}$ ;  $\frac{\partial w}{\partial x} = \frac{\partial w'}{\partial x'}$ . Note that, in this simplified  $r$ -DGS method, the angle  $\alpha$ , between the specimen and target planes is selected to be  $45^\circ$ . It should be pointed that any other more convenient angle,  $0^\circ < \alpha < 90^\circ$ , is theoretically acceptable, but  $45^\circ$  is relatively straightforward and often more suitable.

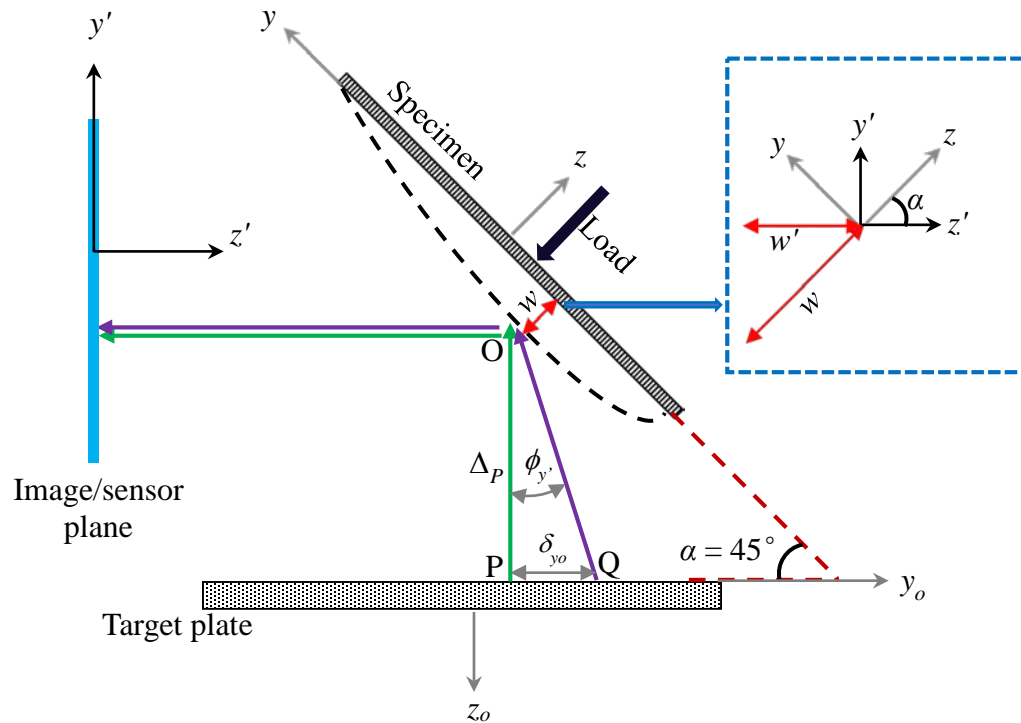


Figure A3: Working principle of simplified  $r$ -DGS without beam splitter. Inset shows relation between specimen and global coordinate systems.

It is important to note that the coordinates of the specimen plane are utilized for describing the governing equations and the camera is focused on the target plane during photography. Therefore, a coordinate mapping is needed to transfer the target plane locations to the specimen plane. This can be done using the pin-hole camera approximation,

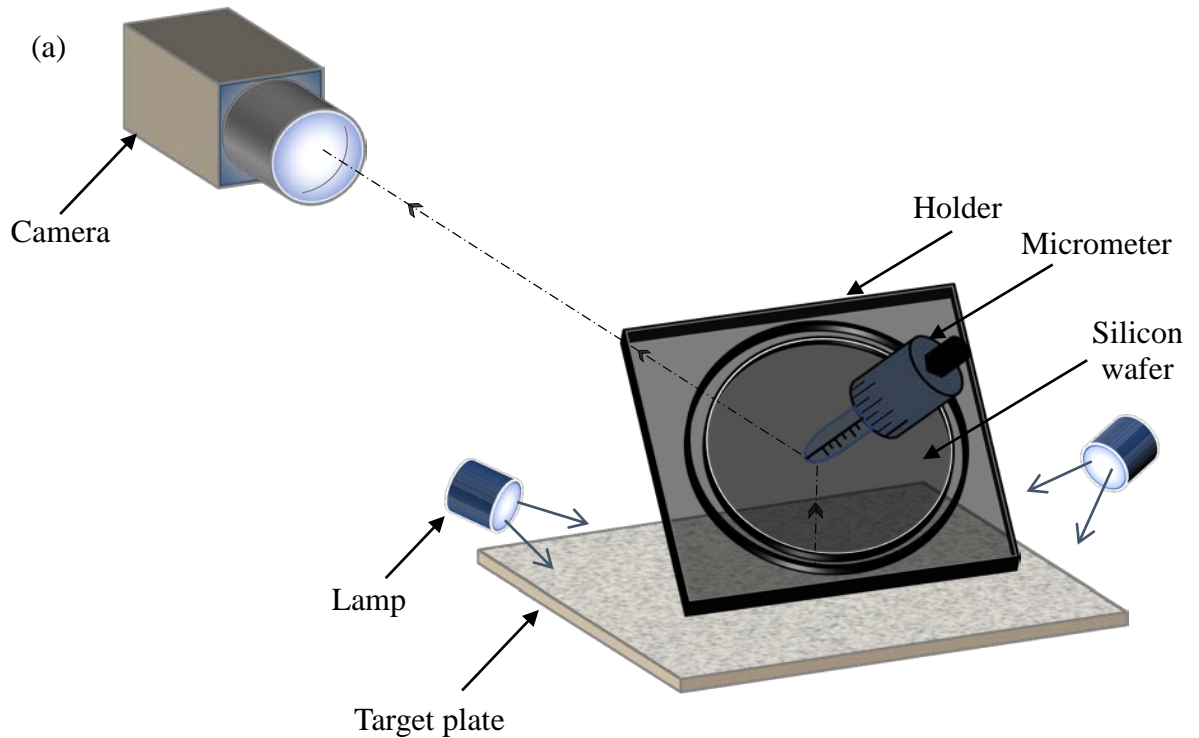
$$(x; y) = \frac{L}{L + \left(\frac{\Delta_M + \Delta_N}{2}\right)} (x_o; y_o), \text{ where } (x; y) \text{ and } (x_o; y_o) \text{ represent the coordinates of}$$

the specimen and target planes, respectively [53].

### **A.3 Demonstration: Silicon wafer subjected to central loading**

The feasibility of this new method to measure surface slopes of deformed thin silicon wafer is demonstrated next. A schematic of experimental setup and a photograph of the close-up view for silicon wafer subjected to central loading are shown in Figure A4. The specimen used here is similar to the one used in Chapter 3 and [117, 135], a single-face polished 360  $\mu\text{m}$  thick silicon wafer of diameter 50.8 mm was used in the experiment. The unpolished face was glued to a thick steel washer with a circular aperture of 30 mm using epoxy. Another steel plate fitted with a micrometer (least count = 10  $\mu\text{m}$ ) at its center was positioned directly behind the silicon wafer. These two steel plates were secured in a holder. A target plate, decorated with random black and white speckles, was placed horizontally at 45° to the silicon wafer (the specimen). A Nikon D100 digital SLR camera was focused on the target via the polished face of the silicon wafer. The camera was fitted with a 70-300 mm lens and an adjustable bellows. A small aperture ( $F^\# = 22$ ) was selected to record the speckles with a good depth-of-focus. The distance between the center of silicon wafer and the end of lens ( $L$ ) along the optical axis of the setup was ~1448 mm

(Note that  $L$  at other generic locations are different; while the value of  $L + \Delta$  is nearly constant at any location,  $L + \left(\frac{\Delta_M + \Delta_N}{2}\right)$  is  $\sim 1506$  mm in this experiment). An 8-bit reference image was recorded with a resolution of  $1504 \times 1000$  pixels before the silicon wafer was subjected to central deflection. Subsequently, three different out-of-plane displacements,  $w = 10, 20, 30 \mu\text{m}$ , were imposed manually using the micrometer during the experiment. The corresponding speckle images in the deformed state were recorded. The close-up view of the experimental setup in Figure A4(b) and Figure A4(c) show the simplicity of this new method.



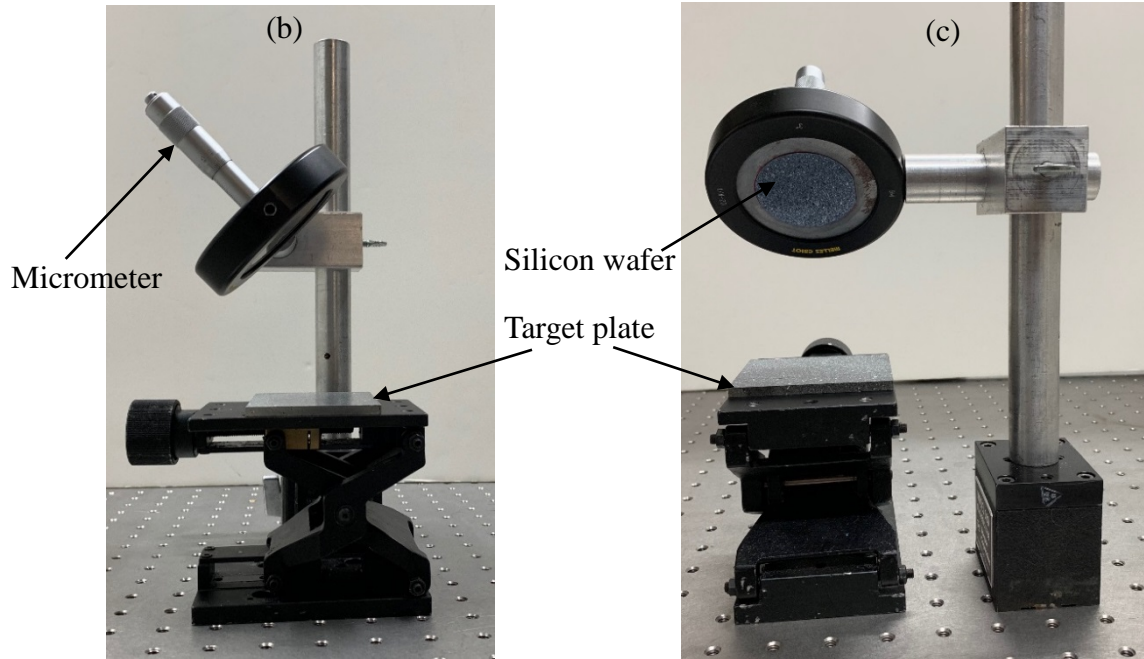


Figure A4: Schematic of the experimental setup for silicon wafer subjected to central loading (a). Images of side view (b) and front view (c) for the setup. (The target plane speckles are visible in bottom-right photograph because the Si wafer surface is reflective.)

The speckle images in the reference and deformed states of the silicon wafer subjected to central out-of-plane deformation of  $10\ \mu\text{m}$  are shown in Figure A5(a) and Figure A5(b), respectively. In the experiment, the silicon wafer is circular with a diameter of  $50.8\ \text{mm}$ . As the coordinate system of image plane is different from that of wafer plane, it can be observed that the recorded speckle images here are in elliptical shape, and are contracted in the  $y'$  direction. Before performing the experiment, two dots,  $A$  and  $B$ , were marked on the speckle target to be along the  $y'$  (or  $y_o$ ) direction. The distance  $AB$  was selected as  $10\ \text{mm}$ , hence, the scale factor (SF) of the speckle images was  $33.56\ \mu\text{m}/\text{pixel}$  in this experiment. The dashed line connecting  $A$  and  $B$  was extended to the top edge of image at point  $M$ , and the bottom edge of image at point  $N$ . Distances of  $MA$  and  $AN$  can be calculated based on the scale factor used. During the experiment,  $\Delta_A$ , shown in Figure

A5(c), was measured as 68 mm, then the  $\Delta_M (= \Delta_A + MA)$  and  $\Delta_N (= \Delta_A - AN)$  can be calculated based on the distance  $MA$  and  $AN$ , and  $\alpha = 45^\circ$ . Hence,  $\Delta$  at any location along the  $y'$  direction can be calculated. It should be noted that  $\Delta$  is constant along the  $x'$  direction since this experimental setup is tilted about the  $x'$ -axis.

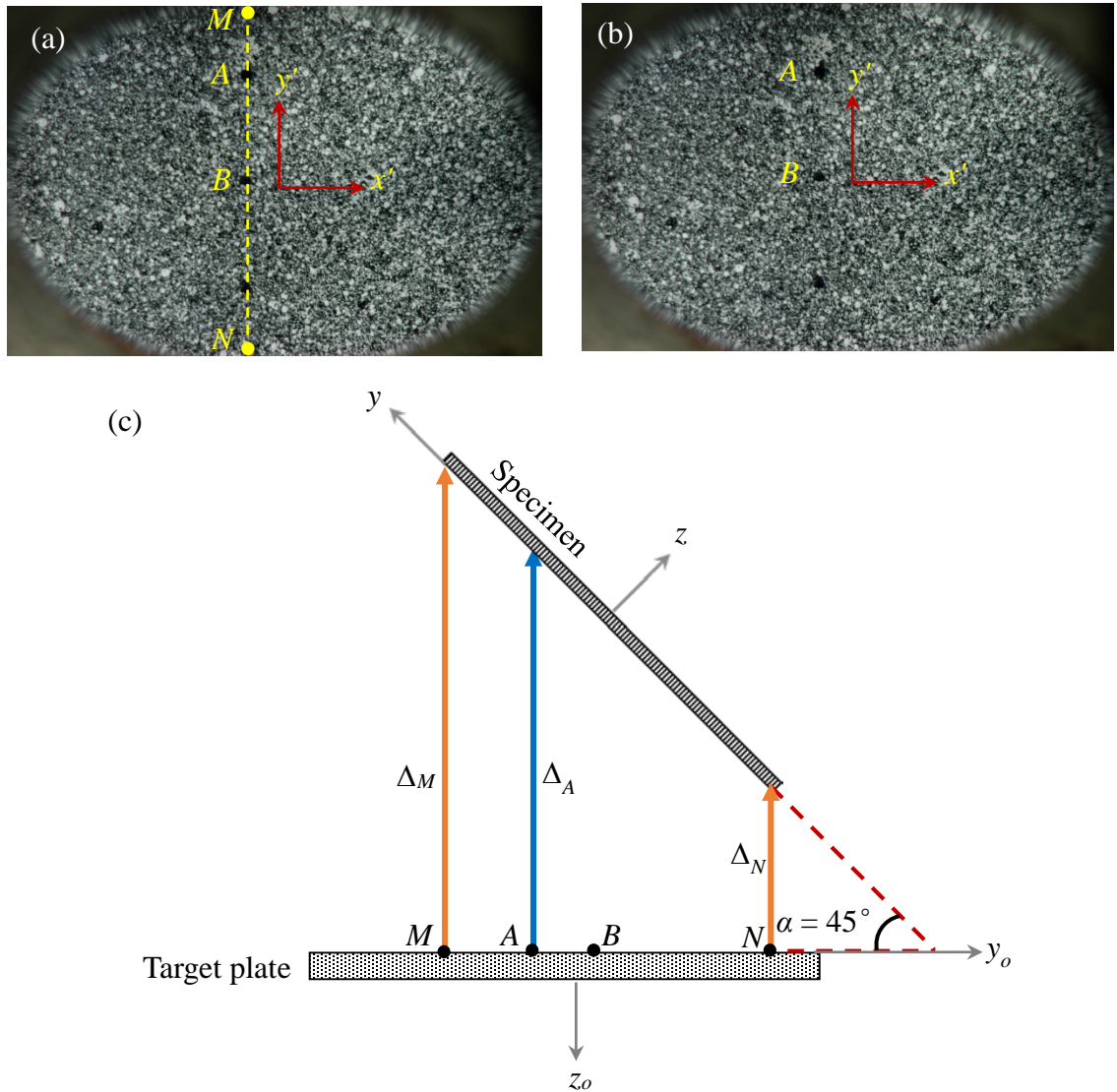


Figure A5: Speckle images in the reference (a) and deformed (b) states of the silicon wafer subjected to central out-of-plane deformation of  $10 \mu\text{m}$ ; (c) illustration for the measurement of  $\Delta$ .

All the deformed images were correlated with the same reference image to measure the local speckle displacements/shifts  $\delta_{y_0, x_0}$  in the region-of-interest (ROI). During correlation (using ARAMIS image analysis software), a sub-image size of  $20 \times 20$  pixels with 10 pixels overlap was used, and it resulted in  $97 \times 148$  matrix of slope data points in the field. The local displacements were used to calculate  $\frac{\partial w}{\partial y; x}$  based on Eq. (A3). Thus

obtained surface slope contours,  $\frac{\partial w}{\partial y; x}$ , are shown in Figure A6, for different out-of-plane deformations imposed. It can be observed that contours are symmetric relative to the horizontal or vertical axes in terms of magnitude with a high concentration in the vicinity of the loading point. Furthermore, both are antisymmetric relative to the vertical and horizontal axes with the origin at the loading point. The contours become denser with larger out-of-plane deflection. There are no contours in the portion of the Si wafer glued to the steel washer as the Si wafer there is essentially ‘clamped’.

To verify the measurements from this new method, the slope contours are compared directly with the analytical solutions for an elastic thin circular plate with a clamped boundary subjected to a centrally applied deflection using [117],

$$\frac{\partial w}{\partial(x; y)} = \frac{4(x; y)w}{R^2} \log \left( \frac{\sqrt{x^2 + y^2}}{R} \right); \quad (\text{A4})$$

where  $w$  is the out-of-plane deformation and  $R$  is the radius of the circular plate. The comparisons made between the experimental and analytical data sets along the  $x$ - and  $y$ -axes for all three out-of-plane deformations are shown in Figure A7. It can be observed that there is a very good agreement between all the experimental and analytical data.

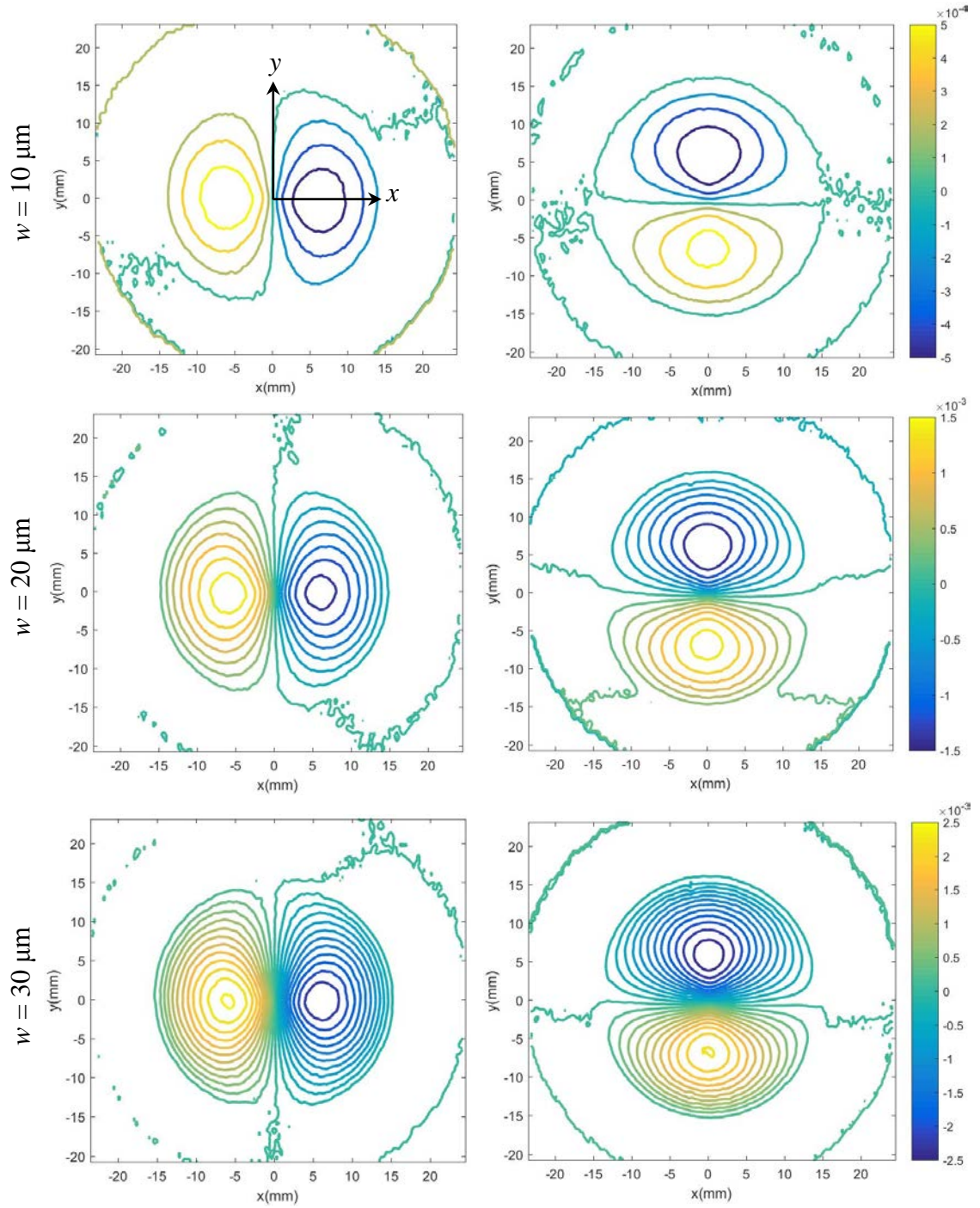


Figure A6: Surface slopes  $w_{,x}$  (left column) and  $w_{,y}$  (right column) for a clamped silicon wafer subjected to out-of-plane deformations. Note:  $(0, 0)$  is made to coincide with the center of silicon wafer. Contour increments =  $2 \times 10^{-4}$  rad.

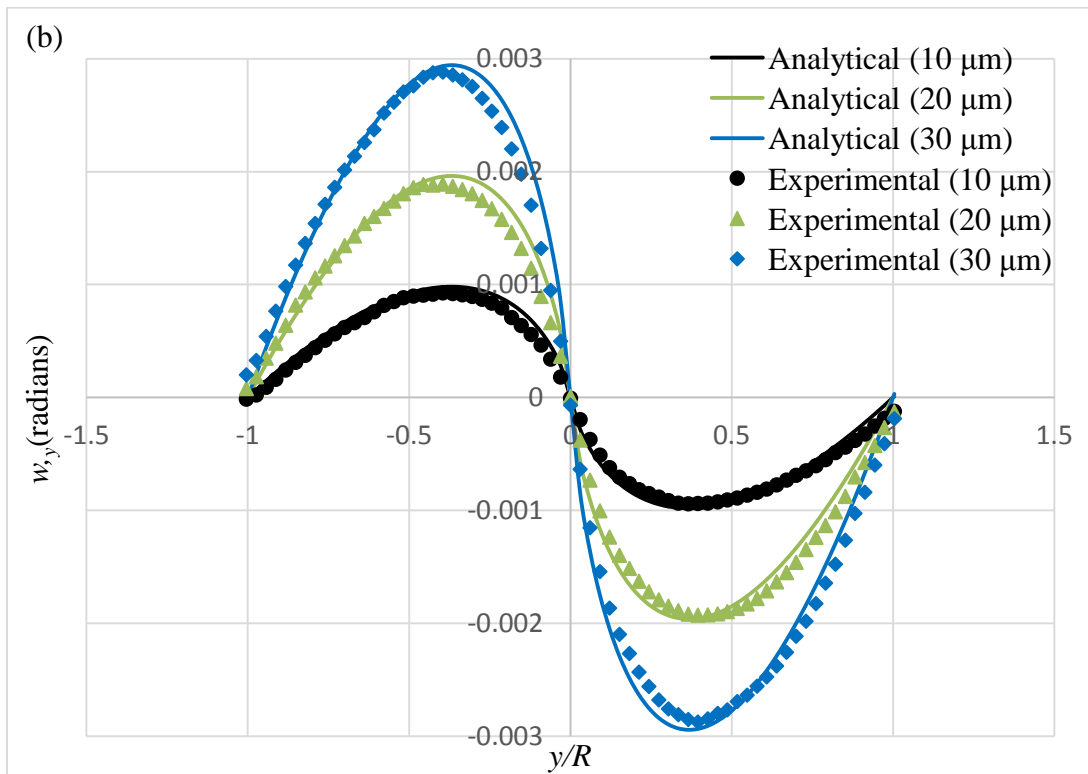
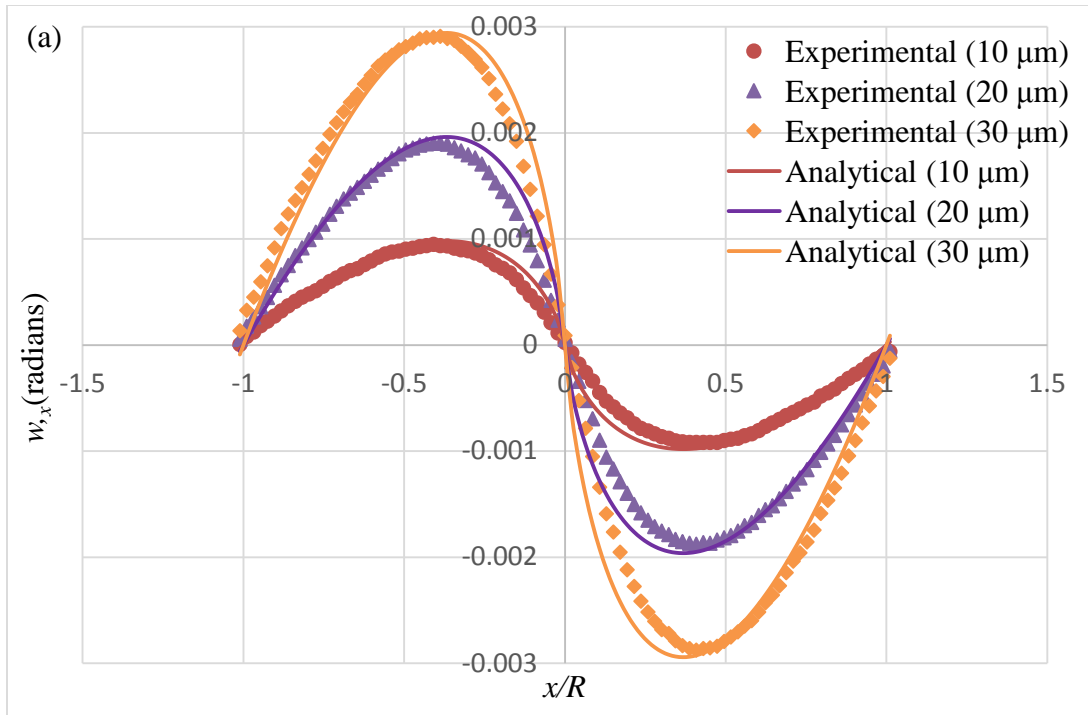


Figure A7: Comparison of analytical data and experimental data of  $w_x$  along the  $x$ -axis (a), and  $w_y$  along the  $y$ -axis (b) corresponding to three different imposed out-of-plane deformations.

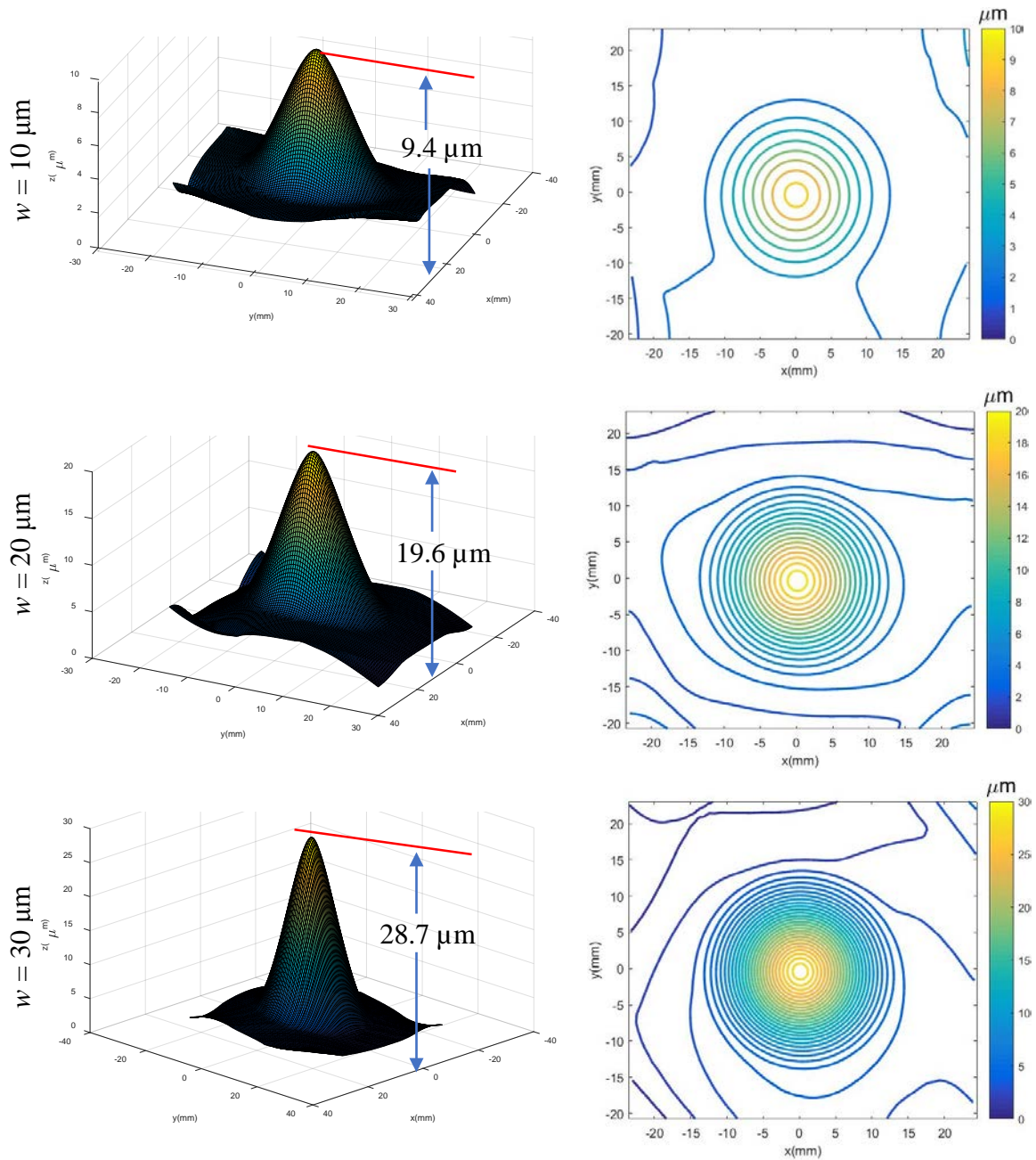


Figure A8: Surface topography obtained from integrating surface slopes using HFLI method for a clamped silicon wafer subjected to out-of-plane deformations. Left column: 3D surface; Right column: out-of-plane displacement ( $w$ ) contours (1  $\mu\text{m}$  increment).

It is shown in [117] that the two orthogonal surface slopes obtained from traditional  $r$ -DGS can be numerically integrated to reconstruct the surface topography using Higher-order Finite-difference-based Least-squares Integration or the HFLI method; see, Chapter

3. It is also worthwhile to use HFLI to integrate the two orthogonal surface slopes obtained from this simplified  $r$ -DGS method. The reconstructed surface topography and the corresponding contours of out-of-plane displacements ( $w$ ) are shown in Figure A8. The peak values of the height of the reconstructed topography are 9.4, 19.6 and 28.7  $\mu\text{m}$  with errors ranging from 2% to 6%. Given the uncertainty of the imposed deflection of  $\pm 1 \mu\text{m}$ , the resulting accuracy is very good. The circular contours in the right column of Figure A8 show that the shape of the reconstructed figures match well with the reality of the experiment both qualitatively and quantitatively. The results here are similar to the results in Ref. [117], which demonstrated that it is feasible to apply this new method with HFLI to reconstruct the surface topography of Si wafer.

For the semiconductor industry, curvatures of Si wafer are also critical, since stress can be directly calculated from curvatures based on elastic plate theory. Hence, the curvatures obtained by differentiating the slope with respect to the local coordinates are plotted in Figure A9. It can be observed that all the curvature contours rapidly increase the vicinity of the loading point in the direction of differentiation. Unlike integration, numerical differentiation exaggerates noise in the experimental data. Hence, the curvature contours in Figure A9 are less smooth compared to the contours in Figure A6 and Figure A8. For comparison, the curvature contours are compared directly with the analytical solutions given by [136]:

$$\frac{\partial^2 w}{\partial(x^2; y^2)} = \frac{4w}{R^2} \log\left(\frac{\sqrt{x^2 + y^2}}{R}\right) + \frac{4(x^2; y^2)w}{R^2(x^2 + y^2)}; \quad (\text{A5})$$

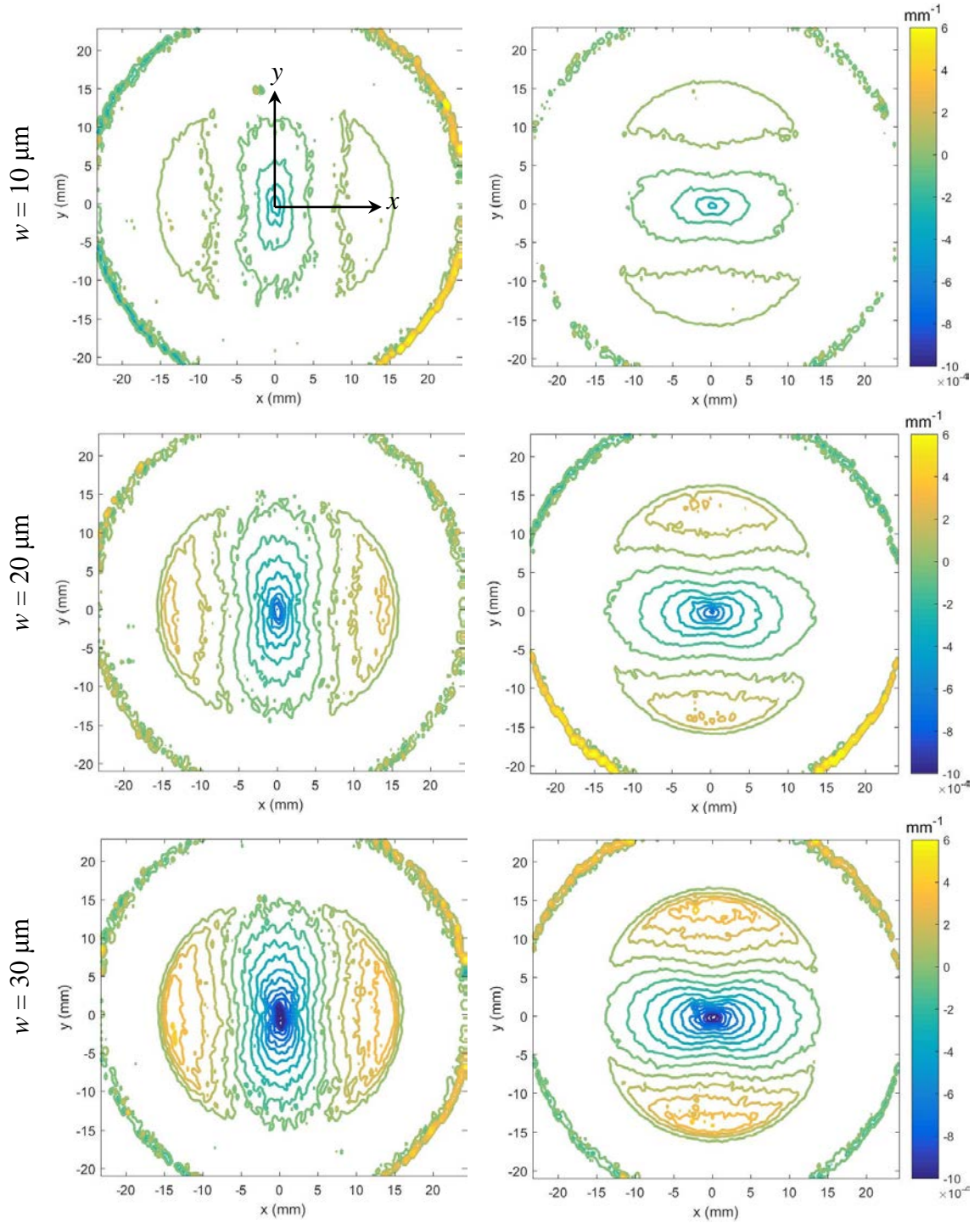


Figure A9: Curvatures  $w_{,xx}$  (left column) and  $w_{,yy}$  (right column) for a clamped silicon wafer subjected to out-of-plane deformations. Note:  $(0, 0)$  is made to coincide with the center of silicon wafer. Contour increments =  $9.3 \times 10^{-5} \text{mm}^{-1}$ .

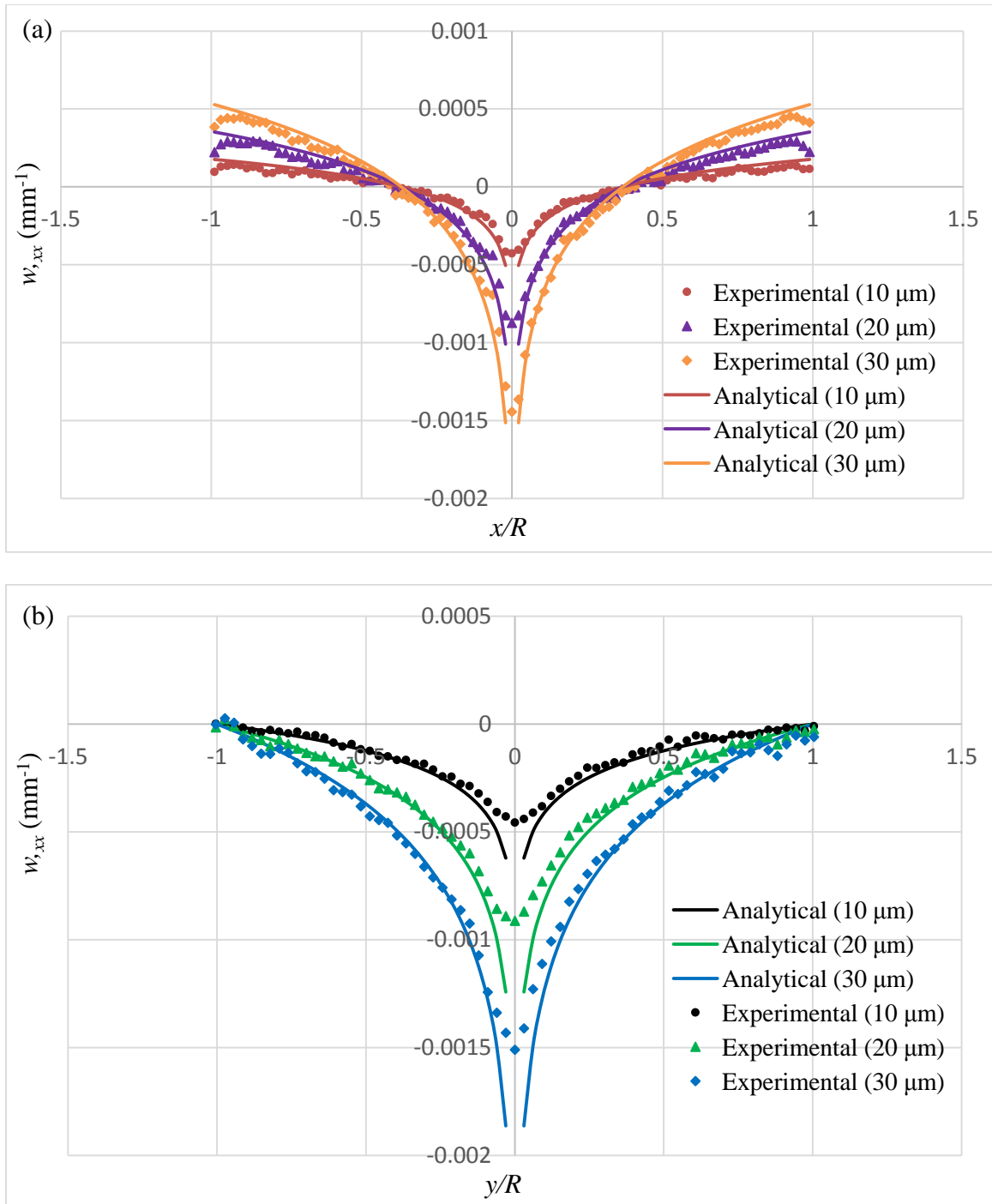


Figure A10: Comparison of analytical data and experimental data of  $w_{,xx}$  along the  $x$ -axis (a), and along the  $y$ -axis (b) corresponding to three different imposed out-of-plane deformations.

The curvatures of  $\frac{\partial^2 w}{\partial x^2}$  were selected to make the comparison between experimental and analytical data sets along the  $x$ - and  $y$ -axes for all three levels of out-of-plane deflection, as shown in Figure A10. It can be clearly observed that there is a good agreement between the experimental and analytical data in each case. Some deviations can be observed close to the center and edge of the Si wafer, where the surface slopes are approaching zero, hence numerical differentiation introduced larger errors.

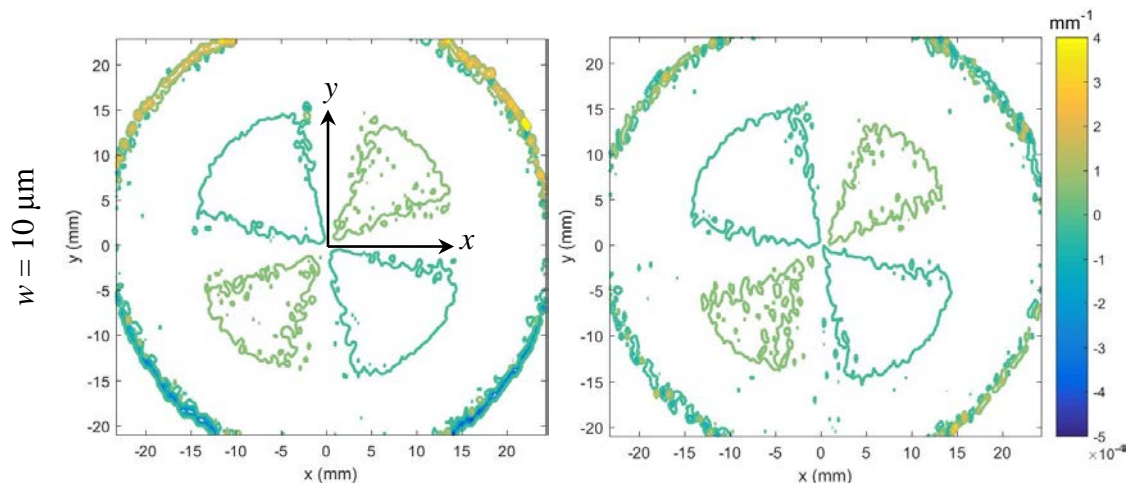
For completeness, the curvatures of  $\frac{\partial^2 w}{\partial xy}$  and  $\frac{\partial^2 w}{\partial yx}$  obtained by differentiating

$\frac{\partial w}{\partial x}$  and  $\frac{\partial w}{\partial y}$  with respect to the  $y$ - and  $x$ -variables, respectively, are plotted in Figure

A11. It can be observed that all the fields representing the twist are skewed along  $\pm 45^\circ$  directions with dual, equidistant positive and negative contours away from the origin. It is

evident that the twist fields of  $\frac{\partial^2 w}{\partial xy}$  are nearly identical with those of  $\frac{\partial^2 w}{\partial yx}$  both

qualitatively and quantitatively.



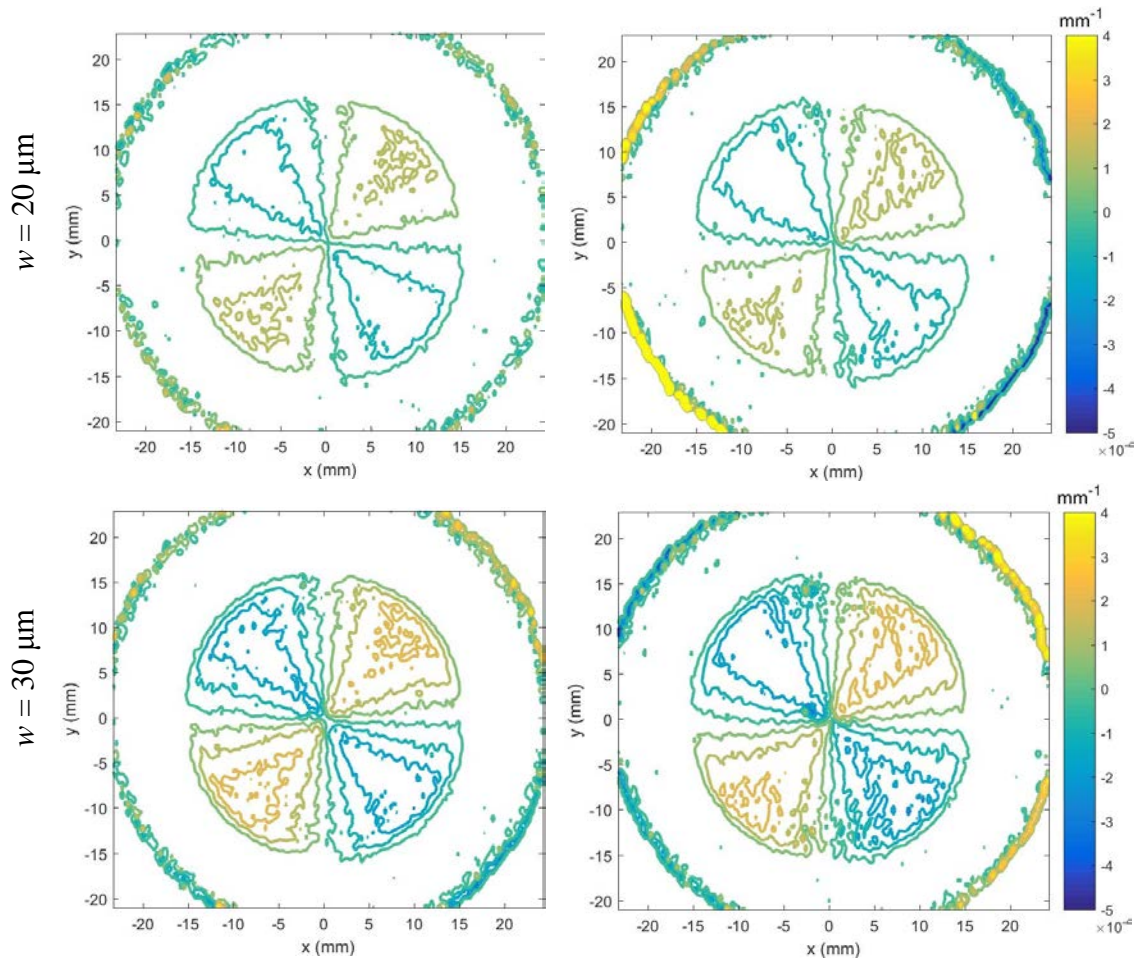
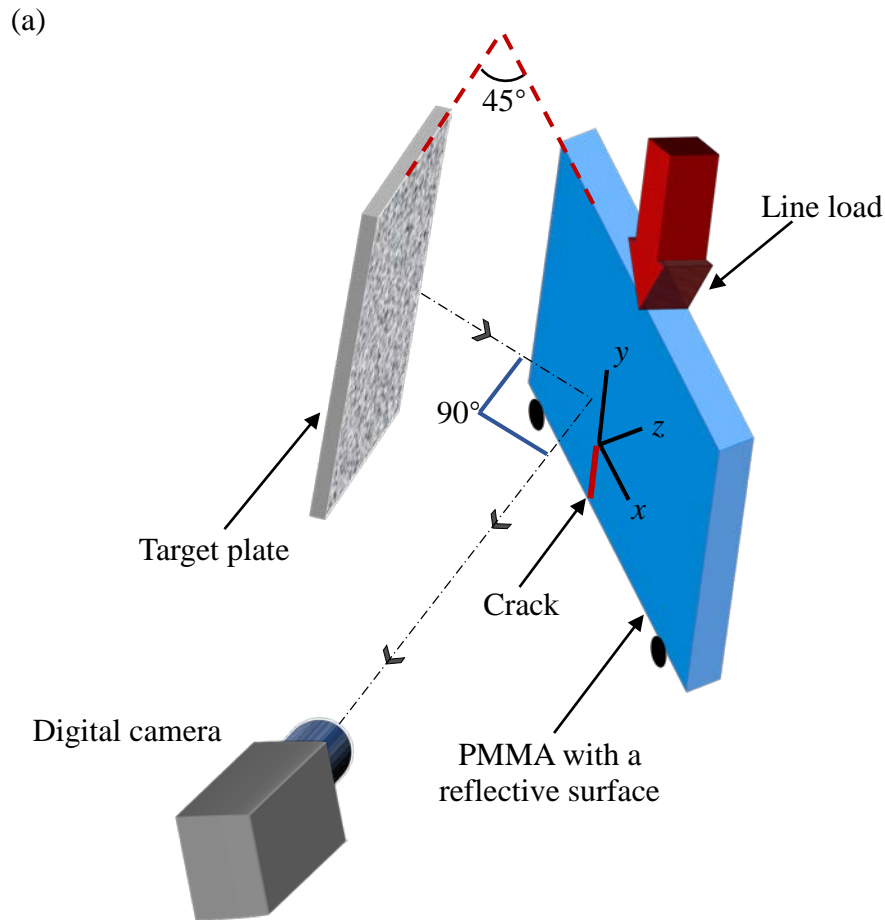


Figure A11: Curvatures  $w_{,xy}$  (left column) and  $w_{,yx}$  (right column) for a clamped silicon wafer subjected to out-of-plane deformations. Note:  $(0, 0)$  is made to coincide with the center of silicon wafer. Contour increments =  $7.5 \times 10^{-5} \text{ mm}^{-1}$ .

#### A.4 Application to fracture mechanics

The traditional  $r$ -DGS has been applied to study fracture mechanics problems [132, 137]. It is therefore important to demonstrate the feasibility of this simplified  $r$ -DGS methodology to study a fracture mechanics problem. A PMMA beam subjected to a symmetric three-point bending was carried out. A schematic of the experimental setup along with a photograph is shown in Figure A12.

A 152 mm × 51 mm × 8.6 mm PMMA specimen, with an initial crack of length 13 mm was used. One of the 152 mm × 51 mm faces was made reflective by depositing with a thin aluminum film to implement this new method. The single edge notched (SEN) specimen was supported on two anvils (span 127 mm), and loaded using an Instron 4465 universal testing machine operating in displacement controlled mode (cross-head speed = 0.004 mm/s). A Nikon D100 digital SLR camera was focused on the target via the reflective surface of PMMA. The camera was fitted with a 70-300 mm lens and an adjustable bellows. A small aperture ( $F^{\#} = 22$ ) was selected to record the speckles with a good depth-of-focus. The distance between the center of PMMA specimen and the end of lens ( $L$ ) was ~1320 mm. The largest and smallest distances,  $\Delta_M$  and  $\Delta_N$ , were 75 mm and 24 mm, respectively.



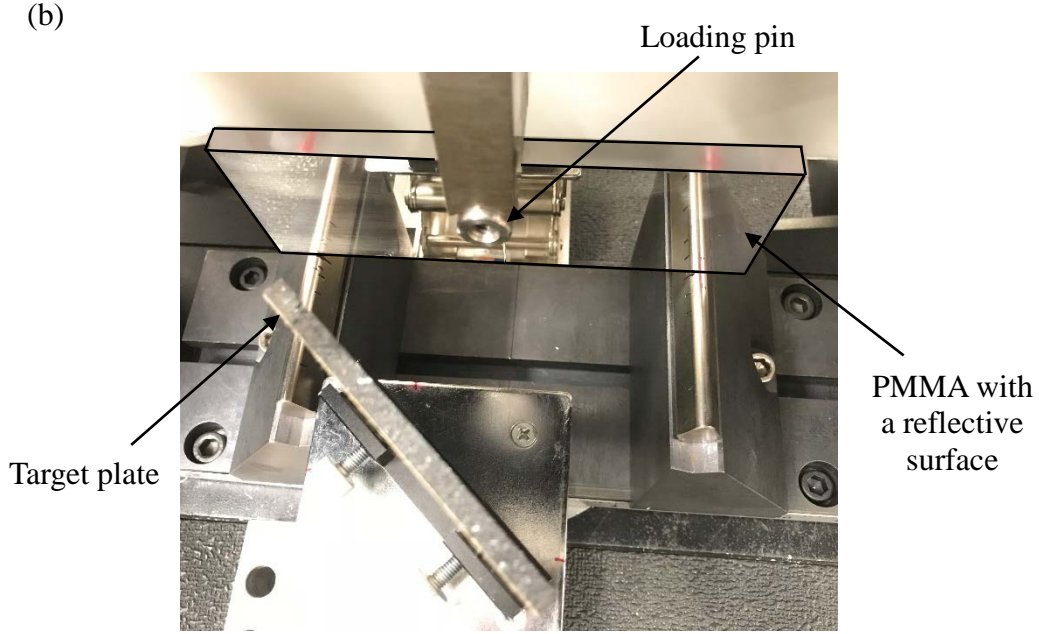


Figure A12: Schematic of the experimental setup for static fracture study (a). Image of top-view of the setup (b).

An 8-bit reference image was recorded with a sensor resolution of  $1504 \times 1000$  pixels before loading ( $F = 0$  N). The speckle images were recorded at every 50 N increments up to a maximum load of 500 N. The images in the deformed state were correlated with the reference image as before. During image correlation, a sub-image size of  $30 \times 30$  pixels (1 pixel =  $35.18 \mu\text{m}$ ) with 10 pixels overlap was used to extract the speckle displacements  $\delta_{y_0; x_0}$  in the ROI. The displacement fields were then used to

compute the two orthogonal surface slopes  $\frac{\partial w}{\partial y; x}$ . It should be noted that, the experimental

setup in Figure A12 rotated about the  $y$ -axis, unlike the one in Figure A4 which was rotated

about the  $x$ -axis. Hence, appropriate attention was be paid when transforming  $\frac{\partial w'}{\partial y'; x'}$  to

$$\frac{\partial w}{\partial y; x}$$

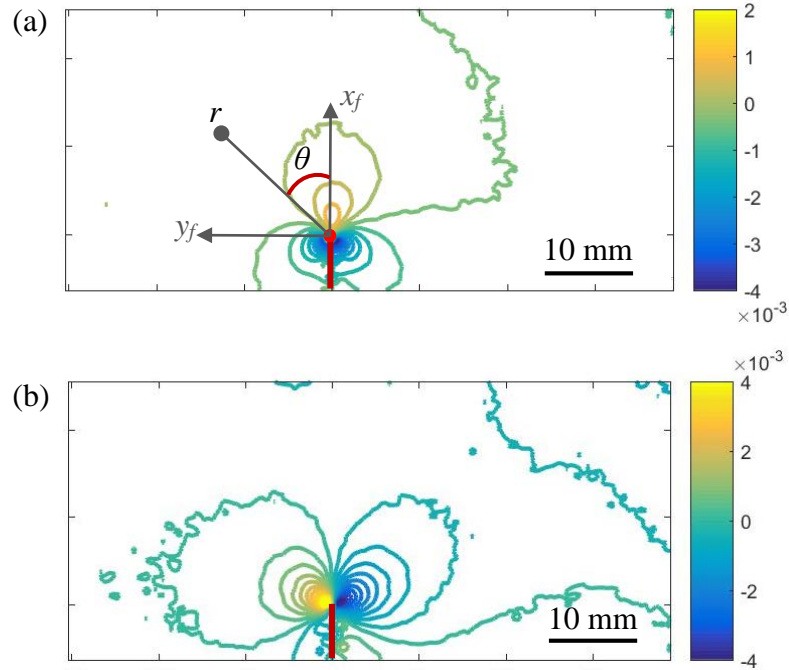


Figure A13: Mode-I crack tip contours of surface slopes  $w,x$  (a) and  $w,y$  (b) corresponding to load of 500 N in 3-point bend PMMA specimen. Contour increments =  $4 \times 10^{-4}$  rad.

The surface slopes of  $\frac{\partial w}{\partial y; x}$  measured by this new method at a load level of 500 N

are plotted in Figure A13. It can be observed that the contours of  $\frac{\partial w}{\partial x}$  are symmetric in

shape and magnitude with respect to the initial crack, the contours of  $\frac{\partial w}{\partial y}$  are symmetric in

shape and antisymmetric in magnitude with respect to the initial crack. These features are similar with the traditional  $r$ -DGS counterparts [137, 138].

The stress intensity factor (SIF) histories were evaluated using an over-deterministic least-squares analysis based on surface slope  $\frac{\partial w}{\partial x}$  measured by this new

method. The asymptotic expression for  $\frac{\partial w}{\partial x}$  field around the crack-tip can be expressed as [33, 138]:

$$\frac{\partial w}{\partial x} = -\frac{\nu t}{2E} \left\{ \begin{array}{l} \sum_{N=1}^{\infty} A_N \left(\frac{N}{2}-1\right) r_f^{\left(\frac{N}{2}-2\right)} \cos\left(\frac{N}{2}-2\right)\theta_f \\ + \sum_{N=1}^{\infty} B_N \left(\frac{N}{2}-1\right) r_f^{\left(\frac{N}{2}-2\right)} \sin\left(\frac{N}{2}-2\right)\theta_f \end{array} \right\} \quad (\text{A6})$$

where  $\nu$  is the Poisson's ratio (= 0.34 for PMMA),  $B$  the sample thickness (= 8.6 mm), and  $E$  the elastic modulus (= 3.3 GPa),  $(r, \theta)$  denotes the crack-tip polar coordinates as shown in Figure A13(a). Mode-I and mode-II SIFs,  $K_I$  and  $K_{II}$ , are related to the coefficients of

$A_1$  and  $B_1$ , respectively, as  $A_1 = K_I \sqrt{\frac{2}{\pi}}$  and  $B_1 = K_{II} \sqrt{\frac{2}{\pi}}$ . Here, the analysis utilized

discrete  $\frac{\partial w}{\partial x}$  data in the region around the crack-tip,  $0.5 \leq \frac{r}{t} \leq 1.5$ ,  $-135^\circ \leq \theta \leq 135^\circ$  in

order to minimize the uncertainty associated with triaxial effects near the crack-tip as well as uncertainty associated with crack-tip location. The resulting effects of non-singular far-field deformations on the measured  $K_I$  and  $K_{II}$  was offset by using four higher order terms ( $N = 4$ ) in Eq. (A6) during least-squares analysis. The results obtained are plotted in Figure A14 for different load levels for two different specimens. The mode-I SIFs obtained from the experiment were compared to the theoretical counterparts using [130]:

$$K_I = \frac{F \cdot S}{t \cdot W^{\frac{3}{2}}} \cdot \frac{3 \left(\frac{a}{W}\right)^{\frac{1}{2}} \left[ 1.99 - \frac{a}{W} \left(1 - \frac{a}{W}\right) \left\{ 2.15 - 3.93 \left(\frac{a}{W}\right) + 2.7 \left(\frac{a}{W}\right)^2 \right\} \right]}{2 \left(1 + 2 \frac{a}{W}\right) \left(1 - \frac{a}{W}\right)^{\frac{3}{2}}} \quad (\text{A7})$$

where  $F$  is the applied load,  $S$  is the span of the beam,  $a$  is the initial crack length,  $t$  is the specimen thickness, and  $W$  is the width. The comparison is shown in Figure A14. A good agreement between the experimental and theoretical values of SIF is evident, suggesting the feasibility of simplified  $r$ -DGS method to study challenging fracture mechanics problems containing sharp discontinuities and stress singularities. The mode-II SIF values are also plotted in this figure for completeness even though the loading was nominally mode-I. The resulting values of  $K_{II}$  therefore are nearly zero and deviations from zero are due to errors from the least-squares analysis approach.

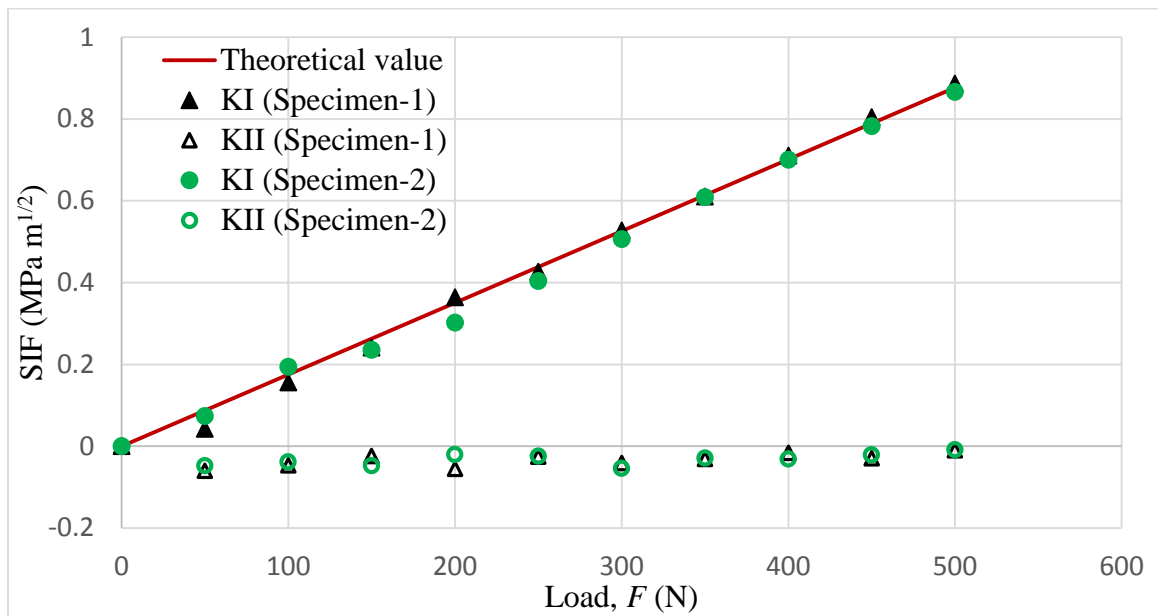


Figure A14: Measured stress intensity factors (symbols) from simplified  $r$ -DGS at different load levels. The solid line represents the theoretical prediction.